



HAL
open science

Phase field and Plasticity

Kais Ammar

► **To cite this version:**

Kais Ammar. Phase field and Plasticity. Mechanics of materials [physics.class-ph]. Mines Paris PSL, 2024. tel-04582936

HAL Id: tel-04582936

<https://hal.science/tel-04582936>

Submitted on 22 May 2024

HAL is a multi-disciplinary open access archive for the deposit and dissemination of scientific research documents, whether they are published or not. The documents may come from teaching and research institutions in France or abroad, or from public or private research centers.

L'archive ouverte pluridisciplinaire **HAL**, est destinée au dépôt et à la diffusion de documents scientifiques de niveau recherche, publiés ou non, émanant des établissements d'enseignement et de recherche français ou étrangers, des laboratoires publics ou privés.



**HABILITATION À DIRIGER
DES RECHERCHES**

DE L'UNIVERSITÉ PSL

Présentée à Mines Paris

**Phase field and Plasticity
Champ de phases et plasticité**

Soutenue par

Kais AMMAR

07 Mai 2024

École doctorale n°621

**Ingénierie des Systèmes,
Matériaux, Mécanique,
Energétique**

Spécialité

Mécanique

Composition du jury :

Henry HERVE CNRS Researcher, École Polytechnique	<i>Reviewer</i>
Yann LE BOUAR Director of Research, Onera	<i>Reviewer</i>
Julien RETHORE Director of Research, École Centrale Nantes	<i>Reviewer</i>
Anna ASK Research engineer, Onera	<i>Examiner</i>
Michel CORET Professor, École Centrale Nantes	<i>Examiner</i>
Samuel FOREST Director of Research, Mines Paris- Université PSL	<i>Examiner</i>



Avant-propos

Ce dossier de candidature en vue de l'obtention de l'Habilitation à Diriger des Recherches comprend trois parties.

- La première est dédiée à mon dossier personnel en français, qui contient un curriculum vitae étendu, une liste de mes publications, mes activités d'enseignement et d'encadrement ainsi que mes activités contractuelles avec l'industrie.
- La deuxième partie de ce manuscrit, rédigée en Anglais, constitue le cœur du manuscrit. Elle présente une synthèse de mes travaux de recherches et qui porte sur le couplage de la méthode de champs de phases avec la plasticité pour l'étude de les évolutions micro-structurales dans les matériaux métalliques.
- La dernière partie est consacrée à mon projet de recherche et l'ensemble de mes perspectives, qui présentent soit des travaux en cours soit des thèmes, qui seront développés au cours des prochaines années.

Notations

The notations used throughout this work are the following :

Notation

a	Scalar
$\underline{\mathbf{a}}, a_k$	Vector
$\underline{\mathbf{a}}, a_{ij}$	Second order tensor
$\underline{\underline{\mathbf{a}}}, a_{ijkl}$	Fourth order tensor
$[\mathbf{a}], a_{ij}$	Matrix
$\{\underline{\mathbf{x}}, \underline{\mathbf{y}}, \underline{\mathbf{z}}\}, \{\underline{\mathbf{r}}\}$	Orthonormal set

Operators

\cdot	Scalar product
$:$	Tensor inner product
\otimes	Tensor outer product
$\nabla \cdot \underline{\mathbf{a}}$	Divergence
$\nabla \underline{\mathbf{a}}$	Gradient
$\Delta \underline{\mathbf{a}}$	Laplacian
$\dot{\underline{\mathbf{a}}}$	Time derivative
$\tilde{\underline{\mathbf{a}}}$	Normalized value

Formula

$x = \underline{\mathbf{a}} \cdot \underline{\mathbf{b}}$	$x = a_i b_i$
$\underline{\mathbf{x}} = \underline{\mathbf{a}} \cdot \underline{\mathbf{b}}$	$x_i = a_{ij} b_j$
$\underline{\underline{\mathbf{x}}} = \underline{\mathbf{a}} \cdot \underline{\underline{\mathbf{b}}}$	$x_{ij} = a_{ik} b_{kj}$
$x = \underline{\mathbf{a}} : \underline{\mathbf{b}}$	$x = a_{ij} b_{ij}$
$\underline{\underline{\mathbf{x}}} = \underline{\underline{\mathbf{a}}} : \underline{\underline{\mathbf{b}}}$	$x_{ij} = a_{ijkl} b_{kl}$
$\underline{\mathbf{x}} = \underline{\mathbf{a}} \times \underline{\mathbf{b}}$	$x_i = \varepsilon_{ijk} a_j b_k$
$\underline{\underline{\mathbf{x}}} = \underline{\mathbf{a}} \otimes \underline{\mathbf{b}}$	$x_{ij} = a_i b_j$
$\underline{\underline{\underline{\mathbf{x}}}} = \underline{\underline{\mathbf{a}}} \otimes \underline{\underline{\mathbf{b}}}$	$x_{ijkl} = a_{ij} b_{kl}$
Δx	$x_\alpha - x_\beta$

Symbols

a_α, a_β	Equilibrium concentrations
A	Gradient coefficient related to plastic gradient
b, b_α, b_β	Height of the free energy barrier
C, D	Isotropic hardening coefficients
$c_\gamma, c_{\gamma'}$	Equilibrium concentration
$c, c_\alpha, c_\beta, c_0, c_{\text{ox}}, c_\gamma$	Coherent concentrations
$\underline{\underline{C}}, \underline{\underline{C}}_\alpha, \underline{\underline{C}}_\beta, \underline{\underline{C}}_{\text{eff}}$	Fourth-order tensor of elasticity moduli
d	Damage internal variable
D_α, D_β	Chemical diffusivities
D^{GB}	Grain boundary diffusivity
E, E_α, E_β	Young's modulus
F	Total free energy functional
$f, f_\alpha, f_\beta, f_{\text{ox}}, f_\gamma$	Free energy densities
f^ϕ	Interface free energy
f^{ch}	Chemical free energy density
$f^e, f_\alpha^e, f_\beta^e$	Elastic free energy density
$f^p, f_\alpha^p, f_\beta^p$	Plastic free energy density
f^{vp}	Viscoplastic energy density
f^u	Mechanical free energy density
f^{GB}	Grain boundary free energy
E^{coh}	Coherence energy
g, g_α, g_β	Yield function
H	Isotropic hardening modulus
J_2	Yield surface
\underline{J}	Diffusion flux
k, k_α, k_β	Curvature of the free energy density
L	Kinetic Onsager coefficient
L_p	Characteristic plastic length
N, K	Positive Norton parameters
$R^0, R_\alpha^0, R_\beta^0$	Initial yield stress
R, R_α, R_β	Scalar variables of isotropic hardening
r_α, r_β	Isotropic hardening variables
p	Accumulated plastic strain
\underline{n}	Normal unit vector
M	Kinetic parameter related to the interface mobility
t	Time
T	Temperature
\underline{r}	Position vector
\mathcal{S}	Area
\underline{u}	Displacement field
V, \mathcal{V}	Material representative volume element
V_k	Internal variable
W	Height of double-well barrier
β	Gradient energy coefficient for concentration

c	Gradient energy coefficient for phase field
ϕ	Phase field variable
η	Grain boundary phase field
θ	Orientation field
$\underline{\epsilon}, \underline{\epsilon}_\alpha, \underline{\epsilon}_\beta, \underline{\epsilon}_{\text{ox}}, \underline{\epsilon}_\gamma$	Total strain
$\underline{\epsilon}^e, \underline{\epsilon}_\alpha^e, \underline{\epsilon}_\beta^e$	Elastic strain tensor
$\underline{\epsilon}^p, \underline{\epsilon}_\alpha^p, \underline{\epsilon}_\beta^p, \underline{\epsilon}_{\text{ox}}^p$	Plastic strain tensor
$\underline{\epsilon}^*, \underline{\epsilon}_\alpha^*, \underline{\epsilon}_\beta^*$	Stress-free strain tensor
$\underline{\epsilon}^d, \underline{\epsilon}_\phi^d$	Damage strain tensor
$\mathcal{B}, \mathcal{C}, \mathcal{D}$	Constants
$\underline{\sigma}, \underline{\sigma}_\alpha, \underline{\sigma}_\beta, \underline{\sigma}_{\text{ox}}, \underline{\sigma}_\gamma$	Cauchy stress tensor
$\underline{\sigma}^{\text{dev}}, \underline{\sigma}_{\text{ox}}^{\text{dev}}$	Deviatoric stress
$\underline{X}_\alpha, \underline{X}_\beta$	Tensor variables of kinematic hardening
$\sigma^{\text{eq}}, \sigma_\alpha^{\text{eq}}, \sigma_\beta^{\text{eq}}$	Von Mises equivalent stress
σ^H	Hydrostatic stress
$\underline{\alpha}, \underline{\alpha}_\alpha, \underline{\alpha}_\beta$	Kinematic hardening variables
$\nu, \nu_\alpha, \nu_\beta$	Poisson's ratios
$\mu, \mu_\alpha, \mu_\beta, \mu_{\text{ox}}, \mu_\gamma$	Chemical potentials
$\omega_\alpha, \omega_\beta$	Grand potentials
Ω	Convex dissipation potential
$\Omega_u, \Omega_{u\alpha}, \Omega_{u\beta}$	Mechanical dissipation potentials
γ	Disordered phase
γ'	Ordered phase
λ	Lattice mismatch
Λ	Interfacial energy
δ	Interfacial thickness
Δf	Energy density scale
ℓ	Thickness of γ' layers
s	Thickness of γ channels
$\tau_{\gamma'}$	Volume fraction



Table des matières

1	Dossier personnel	3
1.1	Curriculum vitae étendu	5
1.2	Production scientifique	9
1.3	Activités pédagogiques	13
1.4	Activités d'encadrement	17
1.5	Mes relations avec le monde de l'entreprise	34
2	Introduction	37
3	Phase field and Continuum Plasticity	41
3.1	Introduction	43
3.2	Model description	44
3.2.1	Helmholtz free energy density	44
3.2.1.1	Partition of free energy	44
3.2.1.2	Chemical contribution	44
3.2.1.3	Mechanical contribution	45
3.2.2	Coupling between phase-field model and plasticity	45
3.2.2.1	Interpolation model	45
3.2.2.2	Multiphase approach : homogenisation method	47
3.2.3	Governing equations	51
3.3	Application : Splitting of dissolving precipitates during plastic shear	52
3.3.1	Introduction	52
3.3.2	Parameters and conditions for FE calculations	53
3.3.3	Results	54
3.3.4	Conclusion	66
3.4	Inheritance of plastic deformation during migration of phase boundaries	67
3.4.1	Introduction	67
3.4.2	Parameters and conditions for FE calculations	68
3.4.3	Results	69
3.4.3.1	Growth of a spherical precipitate	69
3.4.3.2	Microstructural evolution coupled to plastic activity	75
3.4.4	Conclusion	75
4	Phase field and strain gradient visco-plasticity	79

4.1	Introduction	81
4.2	Model description	81
4.2.1	Ginzburg-Landau free energy	81
4.2.1.1	Chemical free energy	82
4.2.1.2	Elastic energy	82
4.2.1.3	Evolution equations	83
4.2.2	Strain gradient Mesoscale Plasticity Model	83
4.3	Results	85
4.3.1	Plasticity in a static microstructure	85
4.3.1.1	1D : Analytical solution	85
4.3.1.2	Global mechanical behavior	87
4.3.2	Microstructural evolution coupled to a viscoplastic activity	89
4.3.2.1	Initial cuboidal microstructure and elastic parameters	89
4.3.2.2	Rafting under creep	90
4.3.2.3	Influence of the plastic length scale	90
4.4	Conclusion	95
5	Phase field and Crystal Plasticity	97
5.1	Introduction	99
5.2	Oxidation induced damage	100
5.3	Stress oxidation phase field model	101
5.3.1	Phase field variables	101
5.3.2	Free energy potential	102
5.3.3	Grain boundary description	103
5.3.4	Mechanical contribution to the free energy potential	103
5.3.5	Damage strain	104
5.3.6	Homogenisation and evolution equations	105
5.4	Simulation of intergranular oxide growth	107
5.4.1	Initial and boundary conditions	107
5.4.2	Materials parameters	108
5.4.3	Accelerated growth along a grain boundary	108
5.4.4	Concentration fields of oxygen and chromium	109
5.5	Intergranular oxide growth, and crack initiation	111
5.5.1	Oxidation-induced internal stresses	111
5.5.2	Effect of a creep load on the damage behaviour	115
5.6	Conclusions	115
6	Perspectives - Mon projet de recherche	119
	Bibliographie	123
	Appendices	135
A	Analytical solution of the model in 1D	137

CHAPITRE

1

Dossier personnel

Contents

1.1	Curriculum vitae étendu	5
1.2	Production scientifique	9
1.3	Activités pédagogiques	13
1.4	Activités d'encadrement	17
1.5	Mes relations avec le monde de l'entreprise	34

1.1 Curriculum vitae étendu

Kais AMMAR

Docteur Ingénieur en Sciences et Génie des Matériaux

Date et lieu de naissance : 09 Août 1980 à Béja (TUNISIE)
Nationalité : Tunisienne/Française
Adresse : Centre des matériaux, MINES ParisTech, CNRS UMR 7633
63-65 Rue Henri Auguste Desbruères,
BP 87, 91003 Evry Cedex France
Tél. : (33) 6 45 70 89 02 / (33) 1 60 76 30 78
Fax. : (33) 1 60 76 31 50
E-mail : kais.ammar@minesparis.psl.eu
ResearcherID : U-2622-2018
ORCID : <http://orcid.org/0000-0003-1318-6003>
<http://scholar.google.fr/kais.ammar>
<http://matperso.mines-paristech.fr/Personnel/kais.ammar>

Compétences techniques

- | | |
|--|--|
| Théorique | <ul style="list-style-type: none">● Mécanique du solide; Comportement et fatigue des matériaux.● Transformation et caractérisation microstructurale; Méthode des champs de phases. |
| Modélisation/
Expérimentale | <ul style="list-style-type: none">● Implémentation d'outils et de méthodes numériques; Simulation numérique en calcul scientifique.● Développement, implémentation et identification de lois de comportement et de critères de fatigue couplés; Préparation de campagnes d'essais mécaniques. |
| Informatique | <ul style="list-style-type: none">● Algorithmique avancée; Utilisation avancée des langages de programmation : C/C++, Python, Matlab, Fortran.● Maîtrise des codes de calcul par éléments finis : Z-set, Abaqus, ANSYS LS-DYNA. |

Formation

- | | |
|------------------|---|
| 2006-2009 | Thèse de Doctorat en Sciences et Génie des Matériaux - Mines Paris-PSL. |
| 2005-2006 | Master en Mécanique et Ingénierie des Systèmes - Université Pierre et Marie Curie. |
| 2001-2004 | Diplôme d'Ingénieur en Génie Mécanique - École Nationale d'Ingénieurs de Tunis. |
| 1999-2001 | Classes Préparatoires - Institut Préparatoire aux Études d'Ingénieurs de Nabeul. |
| 1992-1999 | Baccalauréat Scientifique, Section Mathématiques - Lycée Ibn El Haithem Béja. |

Expériences professionnelles

- Jan. 17/Actuel** **Enseignant Chercheur au Centre des Matériaux, Mines Paris-PSL.**
- Méthode des champs de phases; Transformation et caractérisation micro-structurale; Lois de comportement et critères de fatigue; Homogénéisation; Identification.
- Sep. 11/Dec. 16** **Ingénieur de Recherche et Développement en Calcul Scientifique et Simulation Numérique, dans la cellule de Valorisation ARMINES.**
- Activités contractuelles pour les partenaires académiques et industriels.
 - Industrialisation et valorisation du code de calcul par éléments finis Z-set.
 - Activités de support pour les utilisateurs.
- Jan. 10/Juin 11** **Ingénieur de Recherche (post-doctorant) à l'ONERA (LEM)/Mines Paris-PSL**
- Développement et implémentation du couplage entre changement de phases et plasticité cristalline continue par la méthode des champs de phases.
- Intervenants :** B. Appolaire, S. Forest, A. Finel, Y. Le Bouar et M. Cottura
- Sep. 06/Déc. 09** **Ingénieur de Recherche (doctorant) au Centre des Matériaux, Mines Paris-PSL**
- Modélisation et simulation du couplage changement de phases-mécanique par la méthode des champs de phase (projet ANR COUPHIN).
- Directeurs de thèse :** G. Cailletaud, S. Forest et B. Appolaire
Jury : J.-B. Leblond, A. Finel, T. Antretter et M. Plapp
- Jan. 06/Juil. 06** **Stage de Master au Laboratoire Mécanique et Technologie (LMT Cachan)**
- Implémentation assistée par ordinateur de lois de comportement couplées.
- Responsables :** S. Pommier, N. Schmitt et H. Leclerc

Principaux projets réalisés lors de mes expériences professionnelles

- **Identification des lois de comportement non-linéaires complexes (élasto-visco-plastique, écrouissage, vieillissement, restauration, mémoire...) et des critères de fatigue anisothermes (modèles de fatigue en contrainte et en énergie, interaction fatigue-fluage...)**
 - Études réalisées pour les comptes de : MONTUPET, FAURECIA, HONEYWELL.
- **Méthodologie de prédiction de la durée de vie de structure en matériaux plastiques.**
 - Étude réalisée pour le compte de : RENAULT.
- **Conception et préparation de campagnes d'essais mécaniques en vue de l'identification d'une loi de comportement.**
 - Études réalisées pour le compte de : MONTUPET.
- **Développement et implémentation d'un nouveau modèle énergétique de fatigue de type Charaluk pour une utilisation en anisotherme.**
 - Étude réalisée pour le compte de : RENAULT.

- **Développement et implémentation d'un outil pour estimer rapidement l'état élastoplastique d'une structure "Notch Concentration Plastic Correction" pour des chargements multiaxiaux complexes.**
 - Étude réalisée pour le compte de : SAFRAN Aircraft Engines.
- **Implémentation et validation d'un comportement non-linéaire complexe pour les matériaux haute température (chambres de combustion).**
 - Étude réalisée pour le compte de : SAFRAN Aircraft Engines.

Activités d'enseignement

- 2015/2023** **Simulations multi-échelles des matériaux et des structures**
Cours doctoraux destinés aux ingénieurs et aux doctorants (30 heures)
Centre des Matériaux - Mines Paris-PSL
- 2019/2023** **Lois de comportement avancées : Développement et implémentation**
Formation destinée aux doctorants et aux chercheurs (15 heures)
Centre des Matériaux - Mines Paris-PSL
- 2010/2011** **Méthodes numériques pour la mécanique**
Cours de licence L3 Sciences et Technologie (30 heures)
Université de Versailles Saint-Quentin-en-Yvelines UVSQ
Chargé de Cours et de TD.
- 2009/2011** **Comportement inélastique des matériaux (plasticité, visco-plasticité)**
Cours de Mastère spécialisé DMS (ex-CoMaDiS) (25 heures/an)
Centre des Matériaux - Mines Paris-PSL
Chargé de Cours.
- Mai 2009** **Physics and mechanics of random media**
Cours doctoraux destinés à des élèves-ingénieurs et des doctorants (40 heures)
Mines Paris-PSL
Chargé de TP.

Formation pour les industriels

- Décembre 2014** **Identification d'une loi de comportement élasto-visco-plastique de type Chaboche et modélisation d'un collecteur de gaz d'échappement**
Pour le compte de FAURECIA.
- Novembre 2014** **Calibration d'une loi de comportement élasto-plastique**
Pour le compte de NEXTER.
- Juillet 2013** **Implémentation et identification d'une loi de comportement**
Pour le compte de FAURECIA.
- Décembre 2012** **Calibration d'une loi de comportement élasto-plastique**
Pour le compte d'AREVA.

Organisation d'événements

- 2019** **Séminaire du département "Mécanique et Matériaux" de Mines Paris-PSL,**
4-5 Avril 2019, Fréjus.
- 2017** **Séminaire du département "Mécanique et Matériaux" de Mines Paris-PSL,**
21-22 Septembre 2017, Dammarie les Lys.
- 2013** **11st CSMA Conference on Computational Mechanics,**
Organisation des sessions logiciels
13-17 Mai 2013, Giens.

Synthèse de production scientifique

Articles dans des revues internationales à comité de lecture	25
Chapitres dans des ouvrages	3
Conférences avec proceedings ou actes de congrès	17
Conférences sans proceedings	10

1.2 Production scientifique

Articles dans des revues internationales à comité de lecture (22)

- [1] F. Ghiglione, A. Ask, **K. Ammar**, B. Appolaire and S. Forest, **Cosserat-phase-field modeling of grain nucleation in plastically deformed single crystals**, submitted.
- [2] V. De Rancourt, B. Appolaire, S. Forest and **K. Ammar**, **Phase field study of the role of stress relaxation of oxides on the delayed brittle cracking of oxide intrusions**, submitted.
- [3] **K. Ammar**, S. Forest, H. Ben Kahla, D. Mereib and M. Laurent-Brocq , **Unravelling the extra-hardening in chemically architected high entropy alloys**, *Computational Materials Science*, vol. 233, pp. 167–194, 2024.
- [4] H.E. Chaieb, V. Maurel, **K. Ammar**, S. Forest, A. Tanguy, E. Hériprié, F. Nozahic, J.-M. Mategne and J. De Strycker, **In-situ localization of damage in a Zn-Al-Mg coating deposited on steel by continuous hot-dip galvanizing**, *Scripta Materialia*, vol. 243, 2024.
- [5] M. Abatour, S. Forest, **K. Ammar**, C. O. Rodas, N. Osipov and S. Quilici, **Toward robust scalar-based gradient plasticity modeling and simulation at finite deformations**, *Acta Mechanica*, 2022, <https://doi.org/10.1007/s00707-022-03411-3>.
- [6] M. Abatour, **K. Ammar**, S. Forest, C. O. Rodas, N. Osipov and S. Quilici, **A generic formulation of anisotropic thermo-elastoviscoplasticity at finite deformations for Finite Element codes**, HAL E-Prints, 03462216, 2021.
- [7] M. Lindroos, T. Pinomaa, **K. Ammar**, A. Laukkanen, N. Provatas and S. Forest, **Dislocation density in cellular rapid solidification using phase field modeling and crystal plasticity**, *International Journal of Plasticity*, vol. 148, pp. 103-139, 2022., doi.org/10.1016/j.ijplas.2021.103139.
- [8] T. Pinomaa, M. Lindroos, P. Jreidini, M. Haapalehto, **K. Ammar**, L. Wang, S. Forest, N. Provatas and A. Laukkanen, **Multiscale analysis of crystalline defect formation in rapid solidification of pure aluminium and aluminium-copper alloys**, *Phil. Trans. R. Soc. A*, vol. 380, pp. 20200319, 2022, doi.org/10.1098/rsta.2020.0319.
- [9] **K. Ammar**, B. Appolaire and S. Forest, **Splitting of dissolving precipitates during plastic shear : A phase field study**, *Comptes Rendus. Physique*, 2021, doi.org/10.5802/crphys.82.
- [10] S.D. Schmidt, **K. Ammar**, W. Dornisch, S. Forest and R. Müller, **Phase field model for the martensitic transformation : comparison of the Voigt/Taylor and Khachaturyan approach**, *Continuum Mechanics and Thermodynamics*, vol. 33, pp. 2075–2094, 2021. doi.org/10.1007/s00161-021-01007-1.
- [11] L. Lu-Tuan, **K. Ammar** and S. Forest, **Efficient simulation of single and poly-crystal plasticity based on the pencil glide mechanism**, *Comptes Rendus Mécanique*, vol. 202, pp. 532-551, 2020, doi.org/10.5802/crmeca.44.
- [12] A. Ask, S. Forest, B. Appolaire and **K. Ammar**, **Microstructure evolution in deformed polycrystals predicted by a diffuse interface Cosserat approach**, *Adv. Model. and Simul. in Eng. Sci*, vol. 7 :9, 2020.
- [13] A. Ask, S. Forest, B. Appolaire and **K. Ammar**, **A Cosserat-phase-field theory of crystal plasticity and grain boundary migration at finite deformation**, *Continuum Mechanics and Thermodynamics*, vol. 31, pp. 1109-1141, 2019. doi.org/10.1007/s00161-018-0727-6
- [14] A. Ask, S. Forest, B. Appolaire and **K. Ammar**, **Cosserat crystal plasticity with dislocation driven grain boundary migration**, *Journal of Micromechanics and Molecular Physics*, vol. 3, pp. 1840009, 2018.
- [15] A. Ask, S. Forest, B. Appolaire, **K. Ammar** and O.U. Salman, **A Cosserat crystal plasticity and phase field theory for grain boundary migration**, *Journal of the Mechanics and Physics of Solids*, vol. 115, pp. 167–194, 2018.

- [16] M. Beranger, J.M. Fiard, **K. Ammar** and G. Cailletaud, **A new fatigue model including thermal ageing for low copper aluminum-silicon alloys**, *Procedia Engineering*, vol. 213, pp. 720–729, 2018.
- [17] W. Maktouf, **K. Ammar**, I. Ben Naceur and k. sai, **Multiaxial high-cycle fatigue criteria and life prediction : application to gas turbine blade**, *Int. Journal of Fatigue*, vol. 92, pp. 25–35, 2016.
- [18] V. De Rancourt, **K. Ammar**, B. Appolaire and S. Forest, **Homogenization of viscoplastic constitutive laws within a phase field approach**, *Journal of mechanics and physics of solid*, vol. 88, pp. 291–319, 2016.
- [19] **K. Ammar**, B. Appolaire, S. Forest, M. Cottura, Y. Le Bouar and A. Finel, **Modelling inheritance of plastic deformation during migration of phase boundaries using a phase field method**, *Meccanica*, vol. 49, pp. 2699-2717, 2014.
- [20] A. Villani, E.P. Busso, **K. Ammar**, S. Forest and M.G.D. Geers, **A fully coupled diffusional mechanical formulation : numerical implementation, analytical validation and effects of plasticity on equilibrium**, *Archive of Applied Mechanics*, vol. 84, pp. 1647-1664, 2014.
- [21] M. Cottura, Y. Le Bouar, A. Finel, B. Appolaire, **K. Ammar**, S. Forest, **A Phase field mode incorporating strain gradient viscoplasticity : Application to rafting in Ni-base superalloys**, *Journal of the Mechanics and Physics of Solids*, vol 60, pp. 1243-1256, 2012.
- [22] **K. Ammar**, B. Appolaire, G. Cailletaud and S. Forest, **Phase field modeling of elasto-plastic deformation induced by diffusion controlled growth of a misfitting spherical precipitate**, *Philosophical Magazine Letters*, vol. 91, pp. 164-172, 2011.
- [23] **K. Ammar**, B. Appolaire, G. Cailletaud and S. Forest, **Combining phase field approach and homogenization methods for modelling phase transformation in elastoplastic media**, *European Journal of Computational Mechanics*, vol. 18(5-6), pp. 485-523, 2009.
- [24] **K. Ammar**, B. Appolaire, G. Cailletaud, F. Feyel and S. Forest, **Finite element formulation of a phase field model based on the concept of generalized stresses**, *Computational Materials Sciences*, vol. 45, pp. 800-805, 2009.

Chapitres dans des ouvrages (3)

- [25] S. Forest, **K. Ammar**, B. Appolaire, V. De Rancourt and S. Wulfinghoff, **Generalized continua and phase-field models : application to crystal plasticity**, *In : Mesarovic S., Forest S., Zbib H. (eds) Mesoscale Models. CISM International Centre for Mechanical Sciences, Springer*, vol. 587, pp. 299-344, 2018.
- [26] S. Forest, **K. Ammar**, B. Appolaire, N. Cordero and A. Gaubert, **Micromorphic approach to crystal plasticity and phase transformation**, *In Plasticity and beyond, Springer*, pp. 131-198, 2014.
- [27] S. Forest, **K. Ammar** and B. Appolaire, **Micromorphic vs. phase-field approaches for gradient viscoplasticity and phase transformations**, *In Advances in Extended and Multifield Theories for Continua, Lecture Notes in Applied and Computational Mechanics 59, Springer*, pp. 69-88, 2011.

Conférences avec proceedings ou communications à des congrès avec actes (17)

- [28] T. Pinomaa, M. Lindroos, P. Jreidini, M. Haapalehto, **K. Ammar**, L. Wang, S. Forest, N. Provasas and A. Laukkanen, **Formation of crystal defects in rapid solidification**, *The Additive Manufacturing Benchmarks AM-Bench 2022*, 14-18 Août 2022, Bethesda, Maryland, États-Unis.
- [29] O. Fandeur, T. Helfer, D. Siedel, **K. Ammar** and S. Forest, **Une approche micromorphe de l'endommagement de matériaux quasi-fragiles : implémentation numérique et lien avec la méthode par champ de phase**, *15^{ème} colloque national en calcul des structures CSMA2022*, 16-20 mai 2022, Giens, France.
- [30] M Abatour, S Forest, **K. Ammar**, C Ovalle and N Osipov, **Méthode systématique de régularisation des lois thermo-élastoviscoplastiques en grandes déformations**, *15^{ème} colloque national en calcul des structures CSMA2022*, 16-20 mai 2022, Giens, France.

- [31] M. Lindroos and al., **Micromechanical modeling of length scale effects and performance of SLM stainless steel microstructures**, *TMS 2020 Annual Meeting & Exhibition*, 23-27 February 2020, California, USA.
- [32] M. Beranger, J.M. Fiard, **K. Ammar** and G. Cailletaud, **A new fatigue model including thermal ageing for low copper aluminum-silicon alloys**, *7th edition of the International conference on fatigue design*, 29-30 November 2017, Senlis, France.
- [33] **K. Ammar**, S. Forest, B. Appolaire, M. Cottura, Y. Le Bouar and A. Finel, **Numerical Modelling of Phase Transformation-Mechanics Coupling Using a Phase Field Method : Inheritance of plastic deformation during migration of phase boundaries**, *International symposium on plasticity PLASTICITY2015*, 4-9 Janvier 2015, Montego Bay, Jamaica.
- [34] **K. Ammar**, M. beranger, JM. fiard, D. missoum and S. quilici, **Anisothermal energetic approach to predict thermomechanical fatigue lifetime on exhaust manifold**, *13th International Spring Meeting on FATIGUE BEHAVIOUR : FROM SPECIMEN TO STRUCTURE JIP2013*, 22-23 Mai 2013, Paris, France.
- [35] V. De Rancourt, **K. Ammar**, B. Appolaire, EP. Busso and S. Forest, **Modelling stress-diffusion controlled phase transformations : application to stress corrosion cracking**, *11^{ème} colloque national en calcul des structures CSMA2013*, 13-17 Mai 2013, Giens, France.
- [36] **K. Ammar**, B. Appolaire and S. Forest, **Inheritance of plastic deformation during migration of phase boundaries using a phase field method**, *11^{ème} colloque national en calcul des structures CSMA2013*, 13-17 mai 2013, Giens, France.
- [37] **K. Ammar**, B. Appolaire, S. Forest, M. Cottura, Y. Le Bouar and A. Finel, **Phase field and plasticity**, *6th international conference on Multiscale Modeling of Materials MMM2012*, 15-19 Octobre 2012, Biopolis, Singapore.
- [38] **K. Ammar**, S. Forest and B. Appolaire, **A phase field model incorporating strain gradient plasticity**, *6th European Congress of Computational Methods in Applied Sciences and Engineering ECCOMAS2012*, 10-14 Septembre 2012, Vienna, Austria.
- [39] **K. Ammar**, B. Appolaire, G. Cailletaud, S. Forest, Y. Le Bouar and A. Finel, **Phase field modeling of dissolution of precipitates after and during plastic shear**, *European Congress and Exhibition on Advanced Materials and Processes Euromat2011*, 12-15 Septembre 2011, Montpellier, France.
- [40] **K. Ammar**, B. Appolaire, G. Cailletaud and S. Forest, **Influence of plasticity on diffusive phase transformations kinetics investigated by phase field**, *International Conference on Solid-to-Solid Phase Transformation in Inorganic Materials PTM2010*, 6-10 juin 2010 , Avignon, France.
- [41] **K. Ammar**, B. Appolaire and S. Forest, **Combining phase field approach and homogenization methods for modeling phase transformation in elastoplastic media**, *European Congress on Computational Mechanics : Solids, Structures and Coupled Problems in Engineering ECCM2010*, 16-21 mai 2010, Paris, France.
- [42] **K. Ammar**, B. Appolaire, G. Cailletaud and S. Forest, **Modélisation du couplage changement de phase-mécanique par la méthode des champs de phases et les techniques d'homogénéisation**, *9^e Colloque national en calcul des structures GIENS2009*, 25-29 Mai 2009, Giens, France.
- [43] **K. Ammar**, B. Appolaire, G. Cailletaud and S. Forest, **Finite element formulation of an elastoplastic phase-field model for binary alloys based on the concepts of generalized stresses and homogenization methods**, *International symposium on plasticity PLASTICITY2009*, 3-8 Janvier 2009, St. Thomas, US Virgin Islands.
- [44] **K. Ammar**, B. Appolaire, G. Cailletaud, F. Feyel and S. Forest, **Formulation éléments finis des modèles de champ de phases basée sur la théorie de l'équilibre des microforces**, *École "Mécanismes et Mécanique des Interactions Plasticité-Environnement" PlastOx2007*, 19-25 mai 2007, Argelès-sur-Mer, France, *EDP Sciences*, p. 117-129, DOI : <http://dx.doi.org/10.1051/ptox/2009009>.

Conférences sans proceedings (10)

- [45] **K. Ammar**, S. Forest and B. Appolaire, **Numerical Modelling of Phase Transformation Mechanics Coupling Using a Phase Field Method : Inheritance of plastic deformation during migration of phase boundaries**, *16th European Mechanics of Materials Conference*, 26-28 Mars 2018, Nantes, France.
- [46] **K. Ammar**, S. Forest and B. Appolaire, **Phase field approach and strain gradient plasticity**, *In Professor Dr. Hans Georg und Liselotte Hahn Workshop on Phase Field Modeling, organized by R. Muller and B. Markert*, 20–22 Février 2013, Freudenstadt, Germany.
- [47] **K. Ammar**, F. Azzouz, D. Missoum-Benziane, V. Chiaruttini, J.D. Garaud, F. Feyel, S. Feld-Payet, N. Osipov, S. Quilici, J.Rannou, A. Roos and D. Ryckelynck, **Z-set : une suite logicielle pour la mécanique des matériaux et le calcul de structures**, *11^{ème} colloque national en calcul des structures CSMA2013*, 13-17 Mai 2013, Giens, France.
- [48] **K. Ammar**, S. Forest, B. Appolaire, M. Cottura, Y. Le Bouar and A. Finel, **Modélisation du couplage changement de phase-élastoplasticité par la méthode des champs de phases**, *Journées Annuelles en Transformations de phase à l'état solide SF2M*, 29-31 octobre 2012, Paris, France.
- [49] **K. Ammar**, B. Appolaire, G. Cailletaud, S. Forest, Y. Le Bouar and A. Finel, **Phase field modeling of dissolution of precipitates after and during plastic shear**, *2nd International conference on Material Modeling ICMM2*, 31 Août-02 September 2011, Paris, France.
- [50] **K. Ammar**, B. Appolaire, G. Cailletaud and S. Forest, **Phase field modeling of dissolution of precipitates after and during plastic shear**, *europa congress and exhibition on advanced materials and processes euromat2011*, 12-15 September 2011, Paris, France.
- [51] **K. Ammar**, B. Appolaire, G. Cailletaud and S. Forest, **Modélisation du couplage changement de phase-élastoplasticité par la méthode des champs de phases et les techniques d'homogénéisation**, *Colloque national Mecamat*, 26-30 janvier 2009, Aussois, France.
- [52] **K. Ammar**, B. Appolaire, G. Cailletaud and S. Forest, **Implémentation par éléments finis d'un modèle de champ de phases avec plasticité dans le cadre de la théorie d'équilibre des microforces**, *GdR champ de phases « Champs de phases et mécanique »*, 23-24 avril 2008, Paris, France.
- [53] **K. Ammar**, B. Appolaire, G. Cailletaud and S. Forest, **Formulation éléments finis des modèles de champ de phases basée sur la théorie d'équilibre des microforces**, *Premier Congrès Tunisien de Mécanique*, 17-19 Mars 2008, Hammamet, Tunisie.
- [54] **K. Ammar**, B. Appolaire, G. Cailletaud and S. Forest, **Finite element formulation of a phase field model based on the concept of generalized stresses**, *17th International Workshop on Computational Mechanics of Materials IWCMM17*, 22-24 août 2007, Paris, France.

1.3 Activités pédagogiques

Méthodes Numériques pour la Mécanique :

Pendant l'année universitaire 2010/2011, j'ai assuré le cours "Méthodes Numériques pour la Mécanique" à l'université de Versailles Saint-Quentin-en-Yvelines UVSQ. Ce cours est destiné aux étudiants en L3 Sciences et Technologie, Mention : Sciences Pour l'Ingénieur SPI Mécanique. L'enseignement a été dispensé sous forme de : 12h de cours, 18h de travaux dirigés et 54h de travaux pratiques. Dans le cadre de ce module, j'ai assuré les séances de cours et de TD ainsi que le suivi des projets d'étude en binôme.

Année	Matière	Nature/Nbre heures			Niveau	Institution
		cours	TD	TP		
2010/2011	Méthodes Numériques pour la Mécanique	12 h	18 h	54 h	Licence L3 SPI	UVSQ

Descriptif :

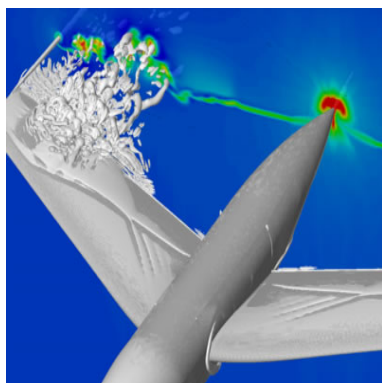
Cette unité d'enseignement a pour objectif la mise en œuvre informatique par les étudiants des méthodes numériques pour la résolution de problèmes mécaniques ciblés :

- (i) mise en données informatiques d'un problème de mécanique.
- (ii) algorithmique associé à la résolution du problème.
- (iii) implémentation de cette stratégie à l'aide du langage de programmation C.
- (iv) visualisation et caractérisation des solutions obtenues.



Programme :

- Informatique : Présentation des techniques de visualisation informatiques ; Utilisation du logiciel Lab-Windows.
- Problèmes mécaniques : Présentation de problèmes mécaniques ciblés et liés à la résolution de systèmes linéaires, d'équations aux dérivées partielles, d'équation d'onde et de problèmes aux valeurs propres ; Application algorithmique des problèmes précédents.
- Mise en données : Présentation du logiciel Lab-Windows ; Réalisation d'un projet visuel.



Comportement inélastique des matériaux :

J'ai assuré, durant mon travail Post-doctoral, le cours "Comportement inélastique des matériaux (plasticité, visco-plasticité)". Cette unité d'enseignement est destinée aux étudiants du Mastère professionnel spécialisé "Design des Matériaux et des Structures DMS" (ex-COMADIS).

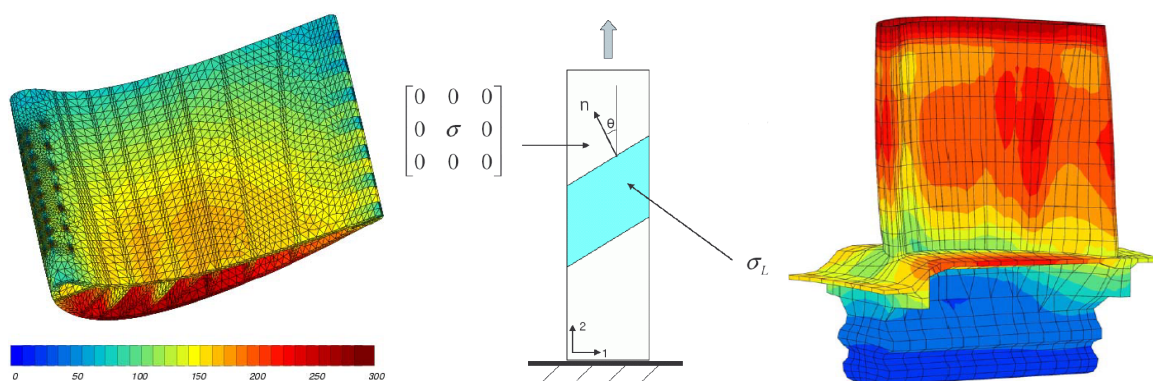
Année	Matière	Nature/Nbre heures			Niveau	Institution
		cours	TD	TP		
2009/2011	Comportement inélastique des matériaux	20 h/an	5 h/an	–	Mastère spécialisé DMS (ex-CoMaDiS)	Centre des Matériaux Mines Paris-PSL

Descriptif :

Pour comprendre le comportement mécanique des matériaux et en particulier leur plasticité, on souhaite corrélérer leur microstructure interne à diverses échelles et leurs lois de comportement macroscopique. Ce cours se fixe pour objectifs de présenter les éléments microstructuraux les plus typiques associés à des essais mécaniques simples ainsi que la forme sous laquelle les lois de comportement peuvent être écrites.



- Aspects microstructuraux :
 - Configurations stables de dislocations, échelles et microstructures.
 - Déformation du monocristal en traction uniaxiale.
 - Facteur de Schmid, cission critique.
 - Comportement des polycristaux.
 - Microstructures en fatigue oligocyclique.
- Approche phénoménologique :
 - Modèles rhéologiques uniaxiaux.
 - Critères de plasticité, Lois d'écoulement.
 - Lois de comportement élasto-viscoplastiques 3D.
 - Écrouissages isotrope et cinématique.



Physics and Mechanics of Random Media :

C'était une semaine de cours doctoraux, principalement destinée pour les élèves-ingénieurs et les doctorants dans le domaine des matériaux. Dans le cadre du programme ATHENS de Mines Paris-PSL, j'étais chargé d'assurer des séances des travaux dirigés.

Année	Matière	Nature/Nbre heures			Niveau	Institution
		cours	TD	TP		
Mai 2009	Physics and Mechanics of Random Media	30 h	-	10 h	Elèves-ingénieurs Doctorants	ENSMP Mines Paris-PSL

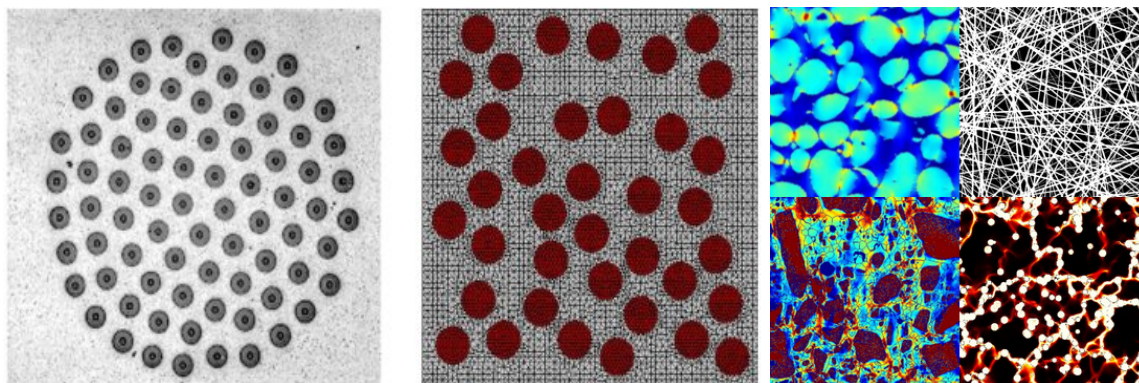
Descriptif :

Many solid media and materials (composites, granular media, metals, biomaterials, porous media, soils, rocks, etc...) encountered in materials sciences, geophysics, environmental sciences, energetics, hydrogeology,... display microstructures and structures of several length scales, showing often a non-deterministic disorder. A better understanding and prediction of the resulting multiscale and random nature of materials' mesoscopic and/or macroscopic properties requires a modeling approach based on a combination of probabilistic concepts with methods of physics and mechanics. The course, which aims to provide an introduction to this subject, is given in a self-contained series of lectures and training sessions on computers.



Programme :

Motivated by a review of advanced experimental techniques for the microstructure description, and by typical results involving fluctuations present in plasticity, damage, fracture, and flows phenomena in porous media, basic tools of applied probability and random processes are recalled. Probabilistic tools for the description random media and models together with their simulation are introduced. Physics and mechanics of random media are first presented from the standpoint of approximate solutions of partial differential equations with random coefficients. The use of numerical techniques (like Finite Elements), to provide an estimation of homogenized properties of random media from Monte Carlo type simulations is introduced. Bounds and numerical techniques are then extended to non linear behaviours, like the plasticity of polycrystals.



Simulations multi-échelles des matériaux et des structures :

C'est une semaine de cours doctoraux, dont les publics cibles sont les élèves-ingénieurs, les doctorants et les ingénieurs travaillant dans le domaine des matériaux et/ou des structures. L'enseignement est dispensé sous forme de cours et de travaux pratiques. J'étais chargé d'assurer, avec Benoît APPOLAIRE et Victor DE RANCOUR, les travaux pratiques.

Année	Matière	Nature/Nbre heures			Niveau	Institution
		cours	TD	TP		
2015/2023	Simulations multi-échelles des matériaux et des structures	15 h	-	15 h	Ingénieurs Doctorants	Centre des Matériaux Mines Paris-PSL

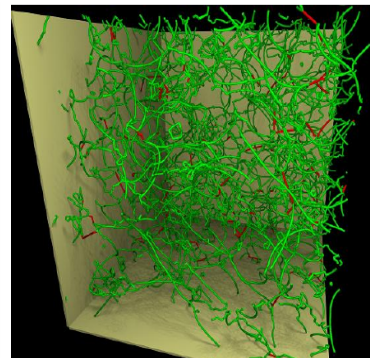
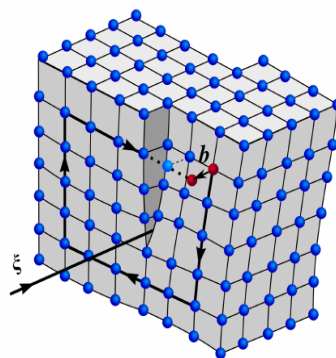
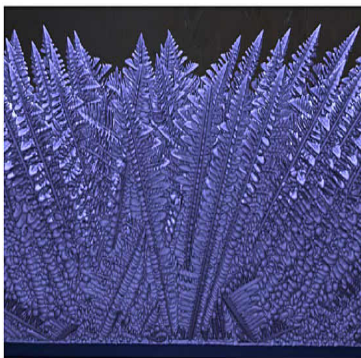
Descriptif :

Le monde de la simulation numérique du comportement mécanique des matériaux s'est enrichi de nombreux outils tels que la dynamique moléculaire et des dislocations, dans le cas discret, et la méthode des champs de phases et des éléments finis pour les problèmes continus. L'objectif du cours est de présenter les bases théoriques du couplage mécanique et la physico-chimie des solides, et de mettre en pratique ces techniques. L'enseignement s'appuiera en particulier sur la thermodynamique des milieux continus incluant les approches à gradient et de champs de phases. Les applications concernent la plasticité des métaux et alliages, le vieillissement des matériaux et des structures, les changements de phase sous conditions thermomécaniques.



Programme :

- (i) Couplage mécanique diffusion.
- (ii) Mécanique et changement de phase.
- (iii) Méthodes numériques :
 - dynamique moléculaire.
 - dynamique discrète de dislocations.
 - éléments finis.
 - champs de phases.
 - calcul de diagrammes de phases.



1.4 Activités d'encadrement

Masters & Stages :

- 2015/2016** **Hichem ABERBACHE**
Etude de la nocivité de défauts dans les structures produites par fabrication additive.
Master recherche M2 "MAterials and EnGIneering Sciences MAGIS", Mines Paris-PSL.
- 2018/2019** **Mohamed Naceur BERRABAA**
Simulation du grenailage d'un super alliage base nickel pour disques de turbine.
Mastere spécialisé "Design des Matériaux et des Structures DMS", Centre des Matériaux - Mines Paris-PSL/Onera/Safran Snecma.

Doctorant :

- 2011/2015** **Aurelien VILLANI**
Modélisation multiphysique de l'endommagement par irradiation de laminés nanocristallins.
Centre des Matériaux - Mines Paris-PSL, Projet européen RADINTERFACE.
Thèse présentée et soutenue publiquement le 12 février 2015.
- 2011/2015** **Victor DE RANCOURT**
Modélisation de l'oxydation des aciers 316 polycristallins par une approche en champs de phases couplée avec la mécanique.
Centre des Matériaux - Mines Paris-PSL/Chaire EDF R&D.
Thèse présentée et soutenue publiquement le 12 juin 2015.
- 2017/2020** **Hazmil HASBULLAH**
Comportement mécanique et rupture de filtres céramiques à haute porosité.
Centre des Matériaux - Mines Paris-PSL/Corning.
Thèse arrêtée suite à un problème de santé du doctorant.
- 2018/2021** **Housseem Eddine CHAIEB**
Approche multiéchelles du comportement mécanique de revêtements Zn-Al-Mg de tôles d'acier galvanisées au trempé.
Centre des Matériaux - Mines Paris-PSL/Arcelor-Mittal.
Thèse présentée et soutenue publiquement le 08 février 2022.
- 2019/2022** **Mohamed ABATOUR**
Méthode de régularisation automatique pour la simulation par éléments finis de la plasticité et de l'endommagement en grandes déformations.
Centre des Matériaux - Mines Paris-PSL/Transvalor.
Thèse présentée et soutenue publiquement le 16 Novembre 2022.
- 2019/2023** **David SIEDEL**
Description de la fissuration des combustibles nucléaires par champs de phase.
Centre des Matériaux - Mines Paris-PSL/CEA Saclay.

- 2020/2023** **Wajih JBARA**
Analyse du couplage transformation de phase et endommagement en conditions anisothermes par la méthode des champs de phase : cas du cyclage thermique dans les revêtements de diffusion.
Centre des Matériaux - Mines Paris-PSL.
- 2020/2023** **Flavien GHIGLIONE**
Modélisation de la recristallisation dans les polycristaux par un modèle couplé champ de phase et milieux de Cosserat.
Centre des Matériaux - Mines Paris-PSL/CNRS.
- 2021/2024** **Régis NGOUADJE KENKO**
Simulation numérique avancée pour la compréhension des points bas en résilience des aciers forgés.
Centre des Matériaux - Mines Paris-PSL/Framatome.
- 2022/2025** **Khadija EL JEDAYNY**
Mécanique de l'oxydation des alliages de zirconium : déformation, ondulation d'interface et fissuration.
Centre des Matériaux - Mines Paris-PSL/Framatome.
- 2022/2025** **Mikel BENGOETXEA ARISTONDO**
Multiscale investigation of the forming and mechanical properties of temper rolled Zn-Al-Mg coatings on steel sheets.
Centre des Matériaux - Mines Paris-PSL/Arcelor-Mittal.
- Post-doctorant :**
-
- 2013/2014** **Abderrahim EL KHABBAZ**
Solutions matériaux architecturés pour le contrôle vibratoire des tubes GV.
Centre des Matériaux - Mines Paris-PSL/Chaire AREVA.
- 2015/2016** **Anna ASK**
Modélisation des évolutions microstructurales lors de processus de transformation faisant intervenir la recristallisation.
Université Paris 13/Onera/Centre des Matériaux - Mines Paris-PSL, Projet CNRS "Coup de pouce F2M" 2015 .
- 2016/2018** **Anna ASK**
Cosserat phase field modelling and simulation of viscoplasticity induced grain boundary migration and recrystallisation in metallic polycrystals.
Centre des Matériaux - Mines Paris-PSL, Projet européen MIGRATE.
- 2018/2019** **Tuan Lu LE**
New titanium alloys with a combination of high strength, strain hardening and high ductility, induced by TRIP and TWIP effects.
Centre des Matériaux - Mines Paris-PSL, Projet ANR TITWIP.
- 2020/2021** **Hiba BEN KAHLA**
Chemically Architected MEtalic aLloys, towards a new strengthening mechanism.
Centre des Matériaux - Mines Paris-PSL/ICMPE-CNRS, Projet CAMEL.

Thèse d'Aurélien VILLANI (Octobre 2011 - Février 2015) :

Sujet : Modélisation multiphysique de l'endommagement par irradiation de laminés nanocristallins.

Encadrement : E.P. Busso (Onera) (33%), S. Forest (Mines Paris-PSL) (33%) et K. Ammar (Mines Paris-PSL) (33%).

Partenariat : Projet européen RADINTERFACE.

Date de la soutenance : 12 février 2015.

Les nano-composites multicouches métalliques cristallins sont capables d'évacuer les défauts ponctuels produits par irradiation, grâce à leur densité d'interface élevée. Ils permettent de retarder le gonflement et de minimiser le fluage, qui mènent à la ruine du matériau. Il est donc impératif de comprendre l'endommagement par irradiation de laminés nanocristallins afin de garantir la sécurité des réacteurs nucléaires. L'objectif de cette thèse est de développer un cadre thermodynamique à l'échelle continue meso et nanoscopique, rendant compte des principaux phénomènes physiques à l'œuvre dans ces laminés irradiés. Principalement trois points sont abordés : le couplage diffusion-mécanique et le fluage, la nucléation et croissance de cavités sous irradiation, et le comportement mécanique des multicouches. La micro-structure du matériau est ici entièrement modélisée, afin de rendre compte de son influence sur le comportement du matériau. Le fluage par diffusion est traité via une approche originale où le tenseur des vitesses de déformation est directement relié au gradient du flux de lacunes. Un modèle de type Cahn-Hilliard est utilisé afin de prédire la nucléation et la croissance des cavités. Dans les systèmes multicouches, une zone affectée par l'interface est définie, dans laquelle les dislocations peuvent être annihilées.

Le modèle est implémenté numériquement via la méthode des éléments finis. Des simulations de fluage couplé à la diffusion de lacunes sont pour la première fois réalisées sur des agrégats polycristallins, prédisant des champs de déformation intra-granulaire fortement hétérogènes (Fig. 1.1). De plus, la vitesse de fluage macroscopique obtenue met en évidence les dépendances classiques à la taille de grain ainsi qu'à la contrainte appliquée. Lors des simulations d'irradiation de multicouches, des zones libres de cavités sont prédites de part et d'autre des interfaces, en accord avec les observations expérimentales. Enfin, des essais de traction sont simulés sur des systèmes Cu-Nb en 3D, mettant en évidence un mode de déformation complexe, et un effet moindre de l'anisotropie élastique.

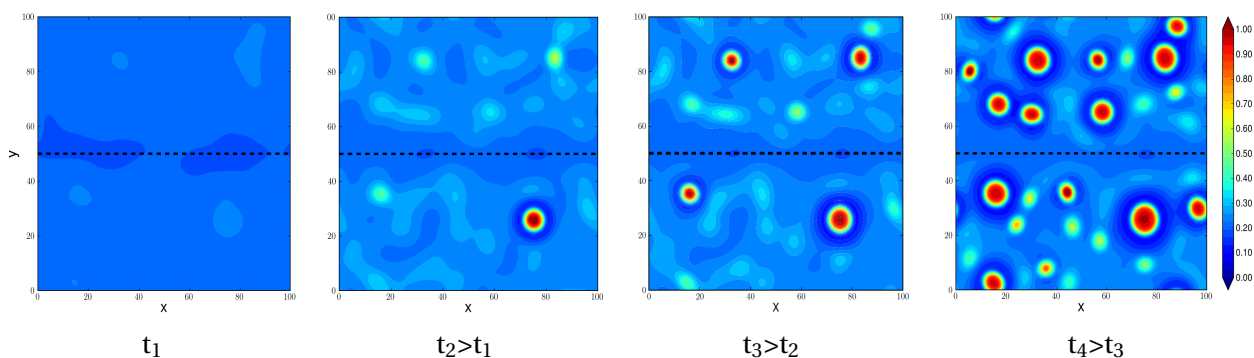


FIGURE 1.1 – Évolution temporelle de la concentration de lacunes

Cette étude a fait l'objet d'une publication dans une revue internationale à comité de lecture [20].

Thèse de Victor DE RANCOURT (Octobre 2011 - Juin 2015) :

Sujet : Modélisation de l'oxydation des aciers inoxydables polycristallins par une approche en champs de phases couplée avec la mécanique.

Encadrement : S. Forest (Mines Paris-PSL) (33%), B. Appolaire (Onera) (33%) et K. AMMAR (Mines Paris-PSL) (33%)

Partenariat : T. Couvant, Chaire EDF R&D (cifre).

Date de la soutenance : 12 juin 2015.

Les aciers austénitiques et les alliages à base de nickel sont des matériaux de choix pour leurs propriétés mécaniques à haute température. L'enrichissement en chrome améliore leur durabilité de par la formation d'une couche d'oxyde protectrice. Il est néanmoins établi que l'oxydation réduit de manière notable leur durée de vie en fatigue. En effet, la croissance d'oxyde peut être accompagnée d'une introduction de défauts (lacunes, éléments délétères comme l'hydrogène) mais également de contraintes résiduelles. Les micromécanismes de fissuration sont ainsi régis par des interactions complexes entre l'environnement et la surface du métal. Aujourd'hui, les enjeux de sécurité et de compétitivité font de la prévision de la durée de vie de ces alliages une nécessité pour l'industrie nucléaire. L'augmentation de la dimension des modèles permet de prendre en compte de manière explicite les interactions multiphysiques du couple oxyde/métal sous l'action d'un chargement mécanique.

La thèse s'est inscrite dans cette démarche et a proposé une formulation d'un modèle de champs de phases couplé avec la mécanique et fondé sur les principes de la thermodynamique des milieux continus. Le comportement effectif de l'interface est présentement obtenu via des méthodes d'homogénéisation permettant de combiner des comportements mécaniques dissemblables, à l'image d'un substrat ductile et de son oxyde fragile. Les contraintes induites par la formation d'oxyde et également par le chargement mécanique peuvent être relaxées viscoplastiquement, de manière isotrope et anisotrope, dans l'oxyde et dans le substrat. Des simulations par éléments finis de l'oxydation généralisée ainsi que de l'oxydation intergranulaire sous chargement mécanique ont été effectuées (Fig. 1.2). Ces dernières mettent en évidence la possibilité d'un phénomène d'oxydation catastrophique par la génération de contraintes de tensions dans l'oxyde fragile, lesquelles peuvent être localisées le long des intrusions d'oxyde dans les joints de grains.

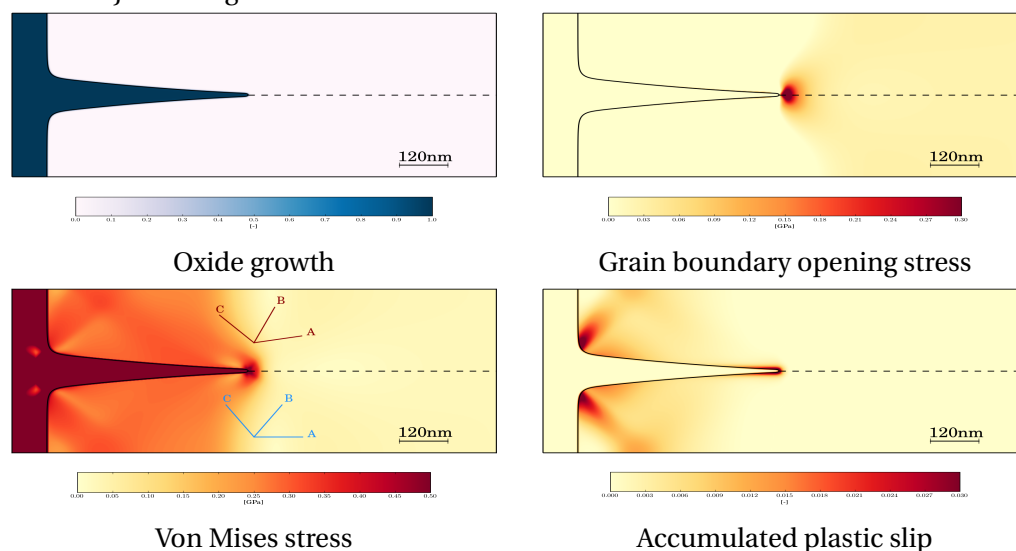


FIGURE 1.2 – Simulation de l'oxydation aux joints de grains

Cette étude a fait l'objet de deux articles dans des revues internationales à comité de lecture [2, 18], un chapitre [25] ainsi que plusieurs communication dans des conférences internationales [35].

Thèse de Hazmil HASBULLAH (Juin 2017 - Septembre 2020) :

Sujet : Comportement mécanique et rupture de filtres céramiques à haute porosité.

Encadrement : M. Boussuge (Mines Paris-PSL) (50%) et K. Ammar (Mines Paris-PSL) (50%).

Partenariat : K. Layouni, Corning (Cifre).

Cette étude s'est arrêtée suite à un problème de santé du thésard.

Pour répondre au respect des réglementations des émissions de polluants automobiles, Corning a développé, depuis des années, des filtres à particules et des substrats à base de cordiérite et de titanate d'aluminium. Pour améliorer les performances de filtration, des produits à haute porosité sont développés, afin de pouvoir augmenter la quantité de catalyseur supporté, tout en minimisant la perte de charge. L'augmentation de la porosité exige une maîtrise croissante des performances mécaniques pour assurer la fiabilité des produits. D'un point de vue plus général, la réduction drastique des émissions de particules polluantes par l'utilisation de filtres performants constitue un enjeu écologique d'une importance majeure à l'échelle planétaire. Les filtres à particules en céramique, objets de cette étude, se présentent sous forme d'une structure cylindrique de type nid d'abeilles (Fig. 1.3), obtenue par extrusion d'une pâte céramique à grande porosité. A la périphérie de cette structure mécaniquement orthotrope se trouve une «peau», également en céramique, chargée de transmettre les efforts de frottement exercés lors de l'introduction de cette structure dans son enveloppe métallique. Les propriétés des céramiques poreuses constituant ces structures sont elles-mêmes actuellement peu connues.

Le sujet proposé consiste à l'étude du comportement mécanique et des mécanismes de rupture des filtres céramiques à haute porosité en visant à caractériser les propriétés mécaniques des filtres à différentes échelles, de la céramique constitutive des produits (parois de cellules filtrantes et peau) au matériau homogène anisotrope équivalent. Différents essais seront réalisés au Centre des Matériaux de MINES-ParisTech, aboutiront au développement d'un modèle de comportement et d'endommagement pour le matériau homogène équivalent constituant le «cœur» du filtre. Le comportement mécanique de la structure nid d'abeilles sera construit par une technique d'homogénéisation périodique. Plusieurs simulations numériques par éléments finis permettent de valider le modèle proposé, par confrontation avec les résultats d'essais réalisés sous des sollicitations variées et plus ou moins complexes, notamment multiaxiales. La compréhension multiéchelles de la rupture fragile des filtres céramiques avec une structure périodique, qui s'avère être à priori un problème plus délicat, en particulier en raison du caractère fragile des céramiques constitutives, représente un enjeu scientifique majeur de la thèse. La mécanique de l'endommagement fragile sera couplée à l'homogénéisation périodique afin de détecter la rupture locale au sein de plusieurs motifs représentatifs et de simuler par éléments finis sa propagation pouvant conduire à une rupture macroscopique.

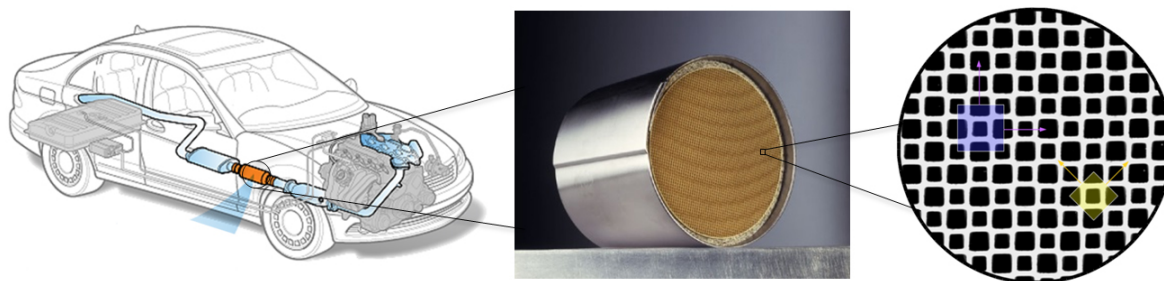


FIGURE 1.3 – Filtre à particules en céramique se présentent sous forme d'une structure de type nid d'abeilles

Thèse de Housseem Eddine CHAIEB (Octobre 2018 - Septembre 2021) :

Sujet : Approche multiéchelles du comportement mécanique de revêtements Zn-Al-Mg de tôles d'acier galvanisées au trempé.

Encadrement : S. Forest (Mines Paris-PSL) (33%), V. Maurel (Mines Paris-PSL) (33%) et K. Amar (Mines Paris-PSL) (33%).

Partenariat : J-M. Mataigne et F. Gilbert (ArcelorMittal Global R&D) (Cifre).

Date de la soutenance : 08 février 2022.

Arcelor-Mittal est engagé dans un programme de recherches visant à caractériser la formabilité et les propriétés mécaniques des revêtements Zn-Al-Mg de tôles d'acier galvanisées au trempé, en fonction de leur microstructure de solidification. La stratégie de la thèse s'articule autour de 5 axes : choix des matériaux d'études, méthodes avancées de caractérisation, propriétés mécaniques macroscopiques des revêtements, modélisation des propriétés à l'échelle de la microstructure ainsi que la mise en œuvre d'une démarche multiéchelles afin d'identifier les mécanismes de déformation et d'endommagement intra et intergranulaires des différentes phases. Trois types de revêtements de tôles galvanisées ont été sélectionnés avec différentes compositions en Zn, Al et Mg.

Des essais de traction *in situ* seront réalisés sur les trois matériaux, permettent d'observer aisément les hétérogénéités de déformation et les fissures sur des surfaces représentatives et d'extraire des informations concernant les limites d'élasticité et les contraintes de clivage de différentes phases. Les observations comprendront (i) les mesures de champs de déformation par corrélation d'images (DIC), (ii) la caractérisation des réseaux de fissures en fonction de la déformation appliquée et (iii) l'étude de la distribution finale de fissures. La microscopie optique à haute résolution, ainsi que la microscopie électronique à balayage, seront utilisées pour différencier les modes de déformation et d'endommagement des différentes phases à l'échelle macroscopique (densités et tailles de fissures) et mésoscopique.

La modélisation et la simulation accompagneront de manière systématique l'étude expérimentale (Fig. 1.4). En particulier, les analyses par éléments finis au plan macroscopique seront utiles à la préparation et à l'analyse des essais en optimisant les rayons d'entaille pour étudier l'influence de la triaxialité sur les modes d'endommagement. Des éprouvettes en croix permettront de solliciter les tôles sous chargement équi-biaxial et de déterminer les réseaux de fissures correspondants. Des approches à champs complets, à partir des images 3D FIB, aideront également à l'identification des lois de comportement des phases. Des modèles d'interface de type zones cohésives seront identifiés pour les joints de grains, les joints de phase et l'interface acier-revêtement dans le but d'analyser les conditions pour lesquelles des fissures nées en surface peuvent progresser vers l'interface avec le substrat et s'y propager.

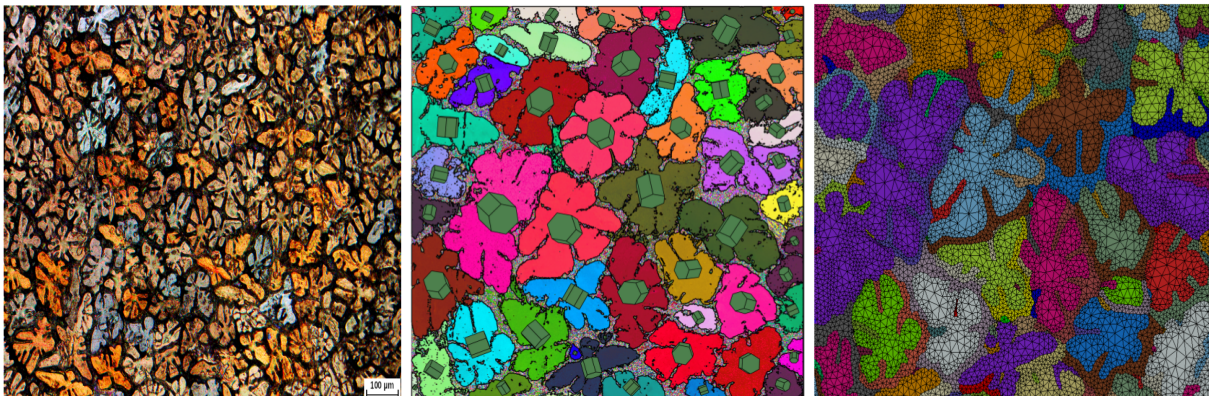


FIGURE 1.4 – Observation du revêtement de Zn-Al-Mg sous lumière polarisée (gauche); Réseau cristallin, superposé à la carte IPF-Z (Milieu); Maillage EF (droite)

Cette étude a fait l'objet d'une publication dans une revue internationale à comité de lecture [4].

Thèse de Mohamed ABATOURE (Octobre 2019 - Septembre 2022) :

Sujet : Méthode de régularisation automatique pour la simulation par éléments finis de la plasticité et de l'endommagement en grandes déformations.

Encadrement : S. Forest (Mines Paris-PSL) (50%) et K. Ammar (Mines Paris-PSL) (50%).

Partenariat : S. Quilici (Transvalor) et N. Osipov (Transvalor) (Cifre).

Date de la soutenance : 16 Novembre 2022.

La simulation numérique par éléments finis des phénomènes de localisation de la déformation plastique et de l'endommagement s'accompagne en général avec une forte dépendance au maillage ainsi que les algorithmes utilisés (Fig. 1.5). Cette difficulté est liée au caractère mal posé du problème aux limites dans le cas d'un fort adoucissement à cause de la perte d'ellipticité des équations différentielles en jeu. L'enjeu principal de cette thèse est de proposer et implémenter une méthode systématique permettant de régulariser ce genre de simulations, en s'appuyant sur les théories actuelles pour les milieux micromorphes et à gradient. Cela nécessite une formulation cohérente et robuste intégrant l'élastoplasticité en transformations finies. La plupart des codes industriels et de recherche existants s'appuient sur des formulations hypoélastiques définies à l'aide des dérivées objectives. Ces lois, ne garantissant pas l'existence d'un potentiel d'élasticité, engendrent des artefacts vu leur caractère non conservatif. Par exemple, dans le cas d'un chargement cyclique fermé de déformations, les contraintes qui en résultent constituent un cycle non fermé. En plus, quelques dérivées objectives entraînent des comportements non physiques tels que des oscillations, soit en élasticité ou en élastoplasticité, dans le cas du cisaillement simple. D'un autre côté, il existe une bibliothèque riche de modèles thermo-élastoviscoplasticité pour différents types de matériaux établies en petites déformations. Ces modèles sont facilement introduits dans les formulations corotationnelles basées sur une décomposition additive de la déformation. La description de l'anisotropie, à l'aide de ces formulations, reste limitée vu que les axes d'anisotropie tournent avec le repère corotationnel et l'absence de la notion du taux de rotation des directeurs de la matière appelé plastic spin.

Par conséquent, il est nécessaire de formuler une méthode d'extension systématique des lois de comportement établies dans le cadre des petites déformations aux transformations finies. Cette méthode doit être formulée de façon à faciliter la tâche aux utilisateurs qui ne sont pas forcément familiers avec la théorie des grandes déformations. L'approche préconisée se base sur la décomposition multiplicative du gradient de déformation et sur les principes de la thermodynamique. Les informations requises pour l'extension des lois formulées en petites déformations sont le choix d'un potentiel hyperélastique, un potentiel de dissipation viscoplastique, les types d'écroûissage et l'évolution du plastic spin.

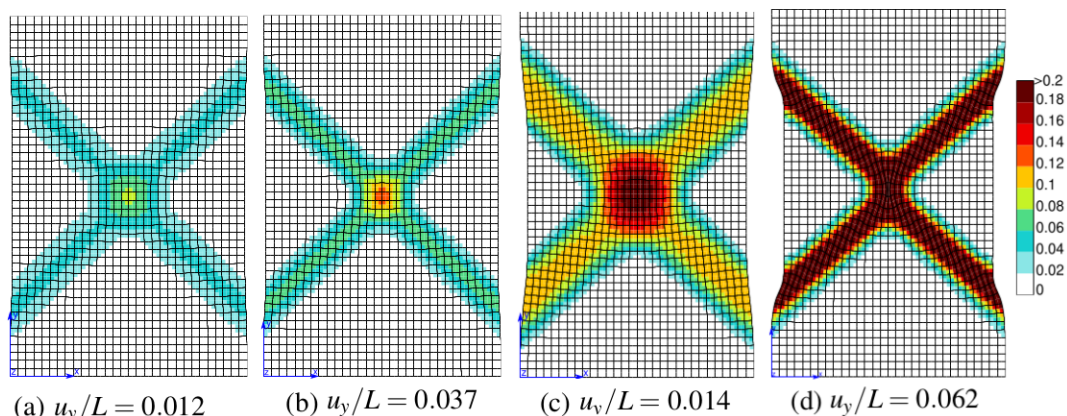


FIGURE 1.5 – Exemple de l'élargissement de la bande de localisation en grandes déformations

Cette étude a fait l'objet de deux publications dans des revues internationales [5, 6].

Thèse de David SIEDEL (décembre 2019 - Janvier 2023) :

Sujet : Description de la fissuration des combustibles nucléaires par champs de phase.

Encadrement : J. Besson (Mines Paris-PSL) (33%), S. Forest (Mines Paris-PSL) (33%) et K. Ammar (Mines Paris-PSL) (33%).

Partenariat : O. Fandeur (CEA Saclay) et T. Helfer (CEA Saclay) (Cifre).

L'objectif de l'étude est de contribuer à la modélisation traitent des phénomènes mécaniques complexes intervenant dans la pastille combustible des combustibles des réacteurs à eau pressurisée (Fig. 1.6). Dans ce cas, ces simulations peuvent avoir à traiter, sur une structure de (4mm) de rayon : la formation instable d'un réseau de fissures complexe (lors de la 1ère montée en puissance) la formation d'un réseau secondaire de fissures en situation incidentelle.

Des écoulements viscoplastiques importants (de l'ordre de 10%) pouvant conduire au comblement des évidements en situations incidentelles La solution retenue dans le cadre de la thèse de D. Siedel est d'employer des éléments finis de type «Hybrid High Order» (HHO) récemment développés dans la thèse de N. Pignet (EdF R&D) couplé à un comportement intégrant un endommagement régularisé. Les éléments HHO permettent en particulier de mieux traiter la quasi-incompressibilité des matériaux et ainsi d'évaluer plus correctement la pression qui est un facteur essentiel dans les phénomènes de rupture. Compte tenu de la complexité et de la nouveauté de ces éléments, le CdM développera de manière complètement indépendante ces éléments dans le code Zset. Il sera ainsi possible de comparer deux implantations indépendantes qui se valideront mutuellement. Le CdM testera également une méthode désormais plus «classique» et reposant sur les techniques «phase fields».

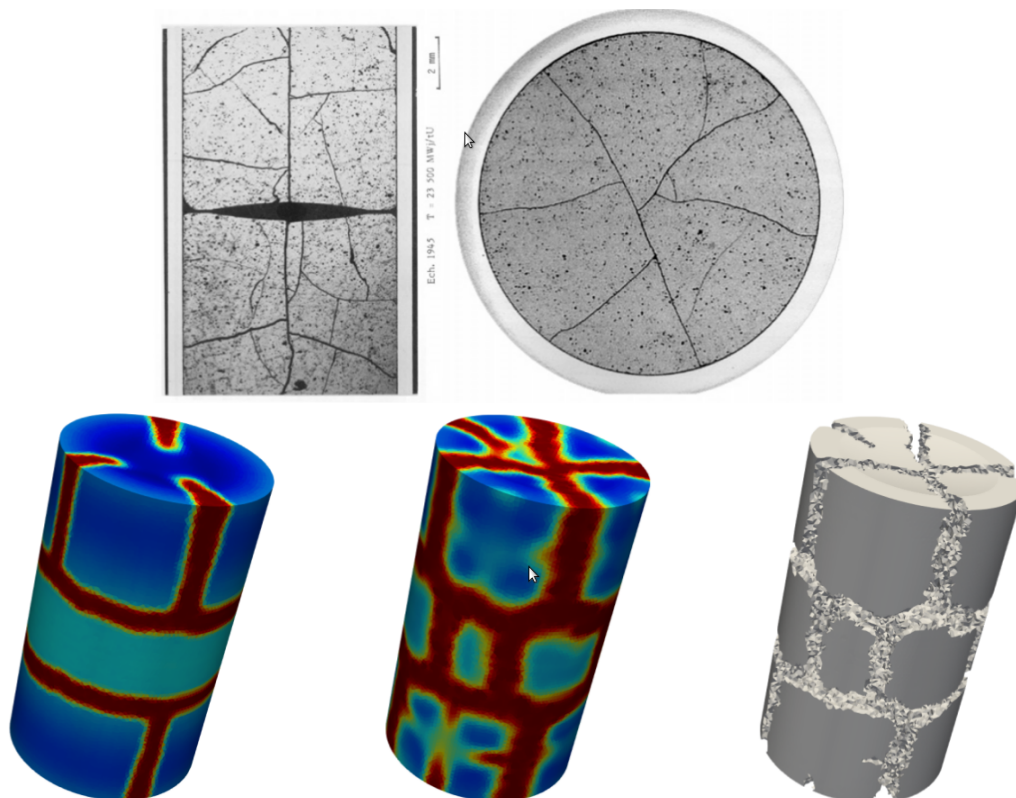


FIGURE 1.6 – Exemple d'études de fissuration de la pastille combustible

Cette étude a fait l'objet d'une communications dans un colloque national [29].

Thèse de Wajih JBARA (October 2020 - Septembre 2023) :

Sujet : Analyse du couplage transformation de phase et endommagement en conditions anisothermes par la méthode des champs de phase : cas du cyclage thermique.

Encadrement : V. Maurel (Mines Paris-PSL) (50%) et K. Ammar (Mines Paris-PSL) (50%).

Pour les applications hautes températures (par exemple barrière thermique), on utilise comme couche de passivation des revêtements de diffusion (Ni,Pt)Al ou plus récemment des revêtements dits $\gamma - \gamma'$ où seul le Pt est utilisé en apport sur un superalliage base Ni. Ces revêtements sont le siège de transformations de phases couplées aux conditions de chargement relevant de la fatigue thermo-mécanique en condition oxydante. L'analyse de la diffusion comme seul moteur de transformation de phase ne permet ni de reproduire les cinétiques de transformation observées expérimentalement ni a fortiori de tenir compte des couplages mécaniques/endommagement dans ces transformations. En effet, l'endommagement par écaillage d'un oxyde de croissance modifie considérablement les transformations de phase. De plus, le désaccord dilatométrique entre oxyde, revêtement, substrat et les différentes phases en présence conduit aux modifications de la cinétique et de la localisation des transformations de phase probablement pilotées par le couplage mécanique/diffusion (ou encore germination-croissance de phase).

Les outils de champs de phase, efficaces pour l'analyse du couplage oxydation/mécanique doivent permettre de lever ces verrous. Les résultats expérimentaux disponibles montrent la complexité des morphologies des phases et l'extrême rugosité des surface induites par le couplage cyclage thermique et oxydation. L'approche par champs de phase est particulièrement adaptée à la description de l'évolution morphologique des phases et la cinétique associée. L'approche proposée intègrera un modèle de diffusion à plusieurs éléments utilisant des potentiels adaptés, une équation de champ de phase caractérisant l'oxydation et un couplage direct avec la mécanique (comportement élasto-visco-plastique endommageable).

Pour parvenir à une telle modélisation, cette étude devra lever les verrous scientifiques suivants :

- Améliorer la robustesse des couplages forts mécanique/transformation de phase pour des cas complexes (multicomposants, multiphasés, anisotherme, non-linéarité mécanique) (Fig. 1.7) ;
- Réaliser l'interfaçage avec les bases de données Calphad pour traiter les cas anisothermes pour des alliages complexes ;
- Optimiser les temps de calcul (remaillage, réduction de modèles...);
- Comprendre les couplages transformation de phase/chargement thermo-mécanique observés dans les revêtements de diffusion en condition anisotherme ;

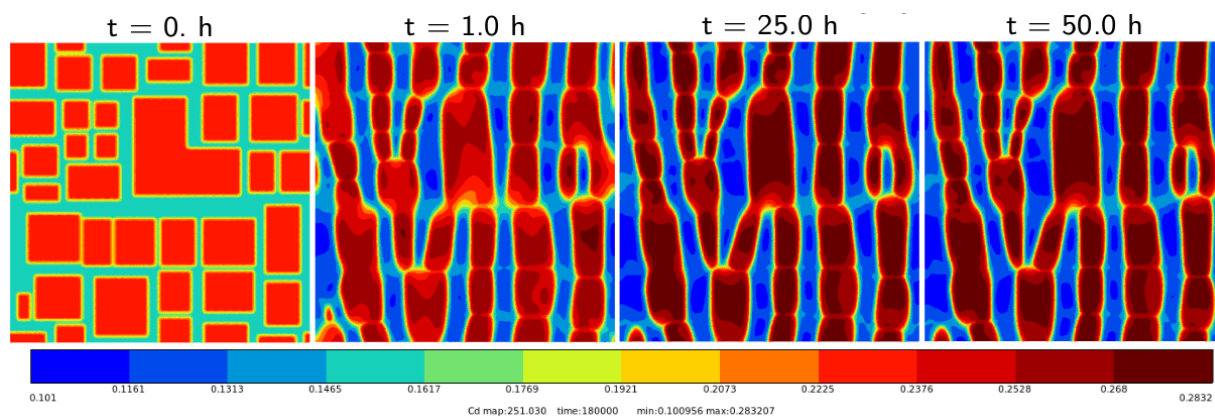


FIGURE 1.7 – Simulation de l'évolution de microstructure γ/γ' en utilisant la méthode de champs de phases

Thèse de Flavien GHIGLIONE (October 2020 - Septembre 2023) :

Sujet : Phase field Cosserat crystal plasticity towards modelling nucleation in recrystallization.

Encadrement : S. Forest (Mines Paris-PSL) (40%), B. Appolaire (Université de Lorraine) (30%) et K. Ammar (Mines Paris-PSL) (30%).

Partenariat : A. Ask (Onera).

The microstructure of materials has a tremendous influence on their macroscopic properties, which naturally leads to seeking to tailor microstructures to reach wanted features. In the case of metals, it has been long recognized that grain boundaries control the macroscopic mechanical properties. Throughout the years, the so called grain boundary engineering, which aims at designing grain boundaries through metallurgical and thermomechanical processes, has been developed. Controlling the grain size at will requires a thorough understanding of the physical and mechanical phenomena occurring during thermomechanical processes such as annealing, especially the phenomenon of recrystallization.

Recrystallization can be roughly said to be composed of two steps : nucleation and growth of the newly nucleated grains. While grain growth can be relatively well modelled, nucleation is still a challenging topic. The Kobayashi-Warren-Carter (KWC) phase field model is thought to be able to naturally account for such phenomena. It has been extended recently by Ask et al. in a new model with full coupling for material and lattice rotations, which also accounts for the evolution of dislocation densities. Though very promising, this model has only been implemented in a 2D, small strain and rotations framework.

In this work, we aim at illustrating the capabilities of the modelling framework to handle grain nucleation occurring during recrystallization. Hence, we will consider conditions generating high lattice curvatures and stored energies such as slip or kink bands that are likely to promote nucleation of new grains. We intend on tackling the limitations of the model proposed by Ask et al., mostly due to a 2D, small strain and rotations framework. To do so, the model is extended through :

- The implementation of a 3D, small strain and rotations version of the finite element model, to perform more realistic simulations ;
- The development of a finite strain and rotations finite element for a Cosserat medium coupled with the phase field method (1D and 2D), following the theoretical formulation of Ask. Simple loading cases, such as torsion, will be tested on single and poly-crystals to trigger grain nucleation (Fig. 1.8).

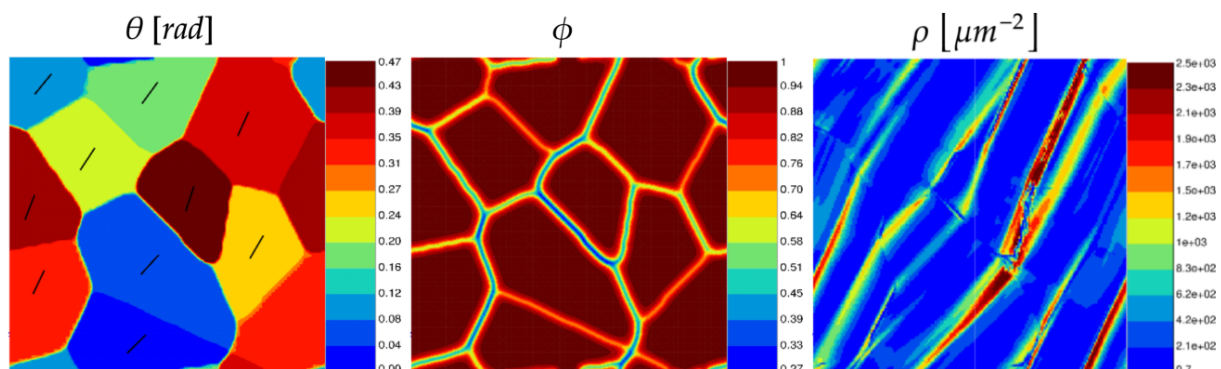


FIGURE 1.8 – Subgrain formation due to slip bands under shear loading of a periodic polycrystal with a single slip system per grain

Thèse de Régis NGOUADJE KENKO (Octobre 2021 - Octobre 2024) :

Sujet : Simulation numérique avancée pour la compréhension des points bas en résilience des aciers forgés.

Encadrement : J. Besson (Mines Paris-PSL) (35%), P. Kerfriden (Mines Paris-PSL) (35%) et K. Ammar (Mines Paris-PSL) (30%).

Partenariat : Framatome et ARMINES (Cifre).

Les essais de résilience Charpy sont utilisés dans l'industrie nucléaire pour certifier les pièces forgées. Cependant, les résultats de ces essais présentent une variabilité forte dans certaines configurations de forgeage sur des pièces de très grandes dimensions réalisés par Framatome à l'usine du Creusot. Des études préliminaires ont montré que, dans certaines zones des pièces forgées l'acier est fortement hétérogène à l'échelle millimétrique. Les hétérogénéités, due à la micro-ségrégation de certains éléments chimiques pendant la solidification des lingots, puis transformées par la succession de procédés thermomécaniques mis-en jeu lors du forgeage et des traitements thermiques, sont la cause principale de la variabilité observée sur les résultats d'essais de résilience. L'enjeu de la thèse est de permettre à Framatome de mieux appréhender cette variabilité par une approche alliant simulation numérique et méthodes statistiques.

L'objectif scientifique de la thèse est développé un outil de simulation numérique performant permettant de mieux appréhender la variabilité en résilience des aciers de forge. En particulier :

1. On développera un simulateur statistique permettant de générer numériquement un ensemble de microstructures hétérogènes représentatives de celles observées par tomographie. Il s'agira de se rapprocher de la réalité par rapport aux simulateurs existants, en représentant la variabilité des formes et des positions relatives des hétérogénéités de manière statistique.
2. On développera un simulateur mécanique permettant de prédire la rupture mécanique, les hétérogénéités microstructurales étant déterminées (par tomographie, ou générées synthétiquement). La compétition entre les mécanismes de clivage et de rupture, qui n'a fait l'objet que d'études préliminaires jusqu'à présent intergranulaire), sera l'objet d'une modélisation fine.
3. Des études statistiques seront menées, rendues possibles par une méthode d'accélération des calculs appropriée (réduction de modèle, zoom numérique méta-modélisation), permettant de gagner en compréhension sur la variabilité en résilience des aciers de forge, et de caractériser la relation statistique entre résilience, microstructure et ténacité mécanique (Fig. 1.9).

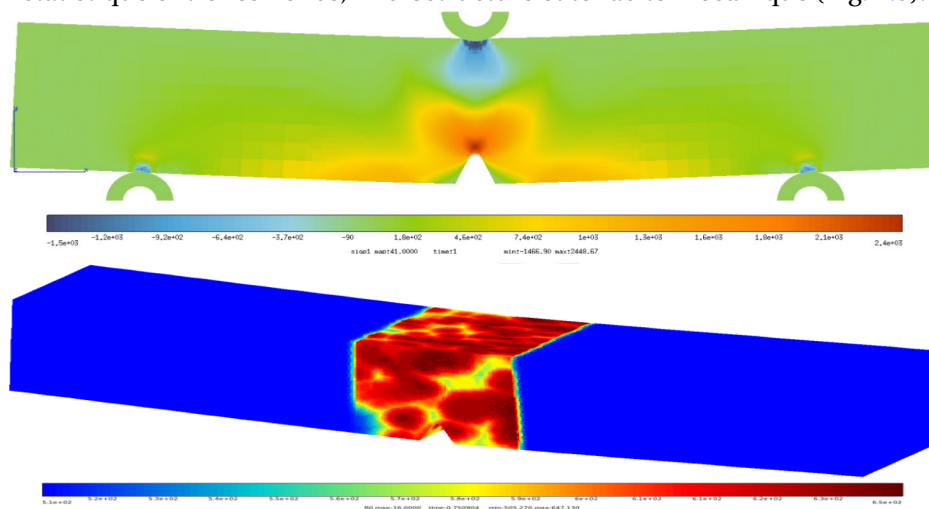


FIGURE 1.9 – Simulation numérique des aciers forgés, Essai de résilience (Charpy)

Thèse de Khadija EL JEDAYNY (Octobre 2022 - Octobre 2025) :

Sujet : Mécanique de l'oxydation des alliages de zirconium : déformation, ondulation d'interface et fissuration.

Encadrement : V. Maurel (Mines Paris-PSL) (50%) et K. Ammar (Mines Paris-PSL) (50%).

Partenariat : Framatome (Cifre).

Les tubes gaines produits par Framatome sont soumis lors de leur séjour en réacteur nucléaire à la corrosion par l'eau à haute température et forte pression. Une couche d'oxyde se développe, dont l'épaisseur atteint quelques dizaines de micromètres en quelques années. A cause de la diminution du volume molaire lors de la transformation métal-oxyde, associée à une déformation dite de croissance, cette couche d'oxyde naît en compression et induit des contraintes de traction dans le métal et donc une déformation des composants. En outre, l'interface métal-oxyde ne reste pas plane mais développe une ondulation qui crée des hétérogénéités de contraintes et in fine une fissuration de la couche (Fig. 1.10).

L'objectif de la thèse est de développer une modélisation de ces phénomènes (croissance de la couche d'oxyde par diffusion, aspect mécanique...) en utilisant le logiciel par éléments finis COMSOL Multiphysics, en y intégrant une approche champ de phases, et en confrontant ces résultats à des modélisations analogues sur d'autres logiciels. Les données expérimentales existant dans la littérature ouverte ou en propre Framatome permettront d'ajuster certains paramètres du modèle et ainsi de le valider. Les études paramétriques portant sur l'influence de la température, de la vitesse d'oxydation, des propriétés mécaniques de l'alliage permettront de mieux comprendre les phénomènes de corrosion.

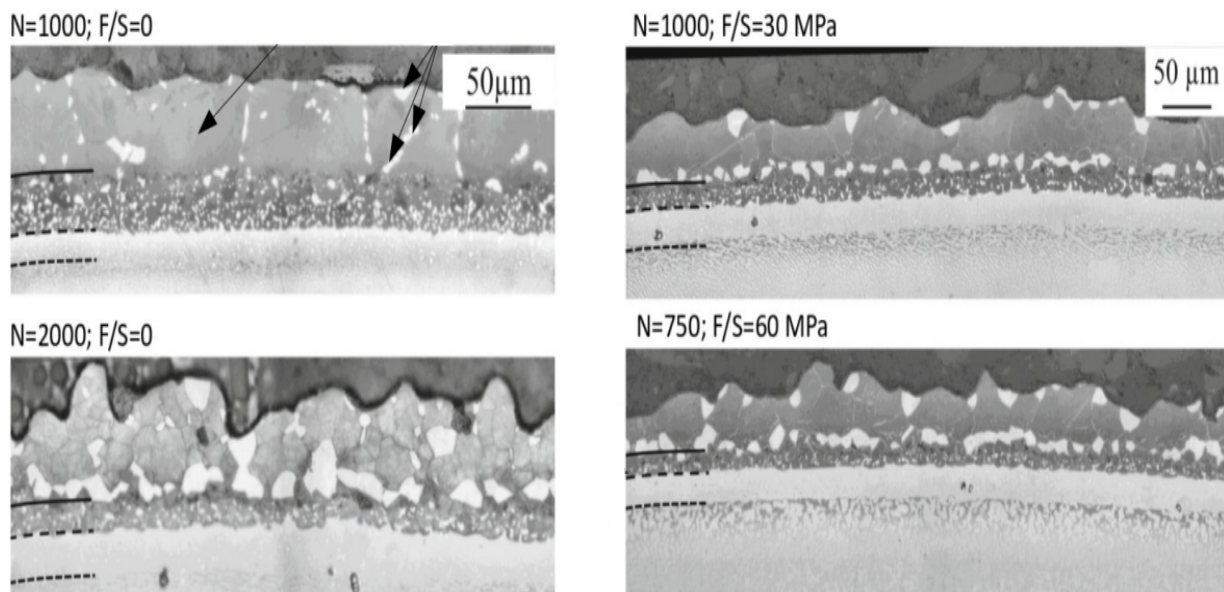


FIGURE 1.10 – Oxydation cyclique/100-1100°C + effort en phase à haute température

Thèse de Mikel BENGOTXEA ARISTONDO (Octobre 2022 - Octobre 2025) :

Sujet : Multiscale investigation of the forming and mechanical properties of temper rolled Zn-Al-Mg coatings on steel sheets.

Encadrement : S. Forest (Mines Paris-PSL) (40%), V. Maurel (Mines Paris-PSL) (30%) et K. Ammar (Mines Paris-PSL) (30%).

Partenariat : J-M. Mataigne (ArcelorMittal Global R&D) et H. Chaieb (OCAS) (Cifre).

ArcelorMittal is carrying out a research program aiming at determining the forming and mechanical properties of temper rolled Zn-Al-Mg coatings on hot-dip galvanized steel sheets, depending on the solidification microstructures of the coatings and the rheology of the underlying steel substrate. ArcelorMittal has selected two types of coatings on steel sheets having different compositions in Al and Mg. These coatings exhibit complex multiphase microstructures. Some of the phases can exhibit brittle behaviour and alter the rheology of the coating. Tensile tests will be performed on the two materials to identify the respective deformation and damage modes at the macroscopic scale (crack density and size) and at the mesoscopic scale (SEM analysis). One material will then be selected to perform the full proposed multiscale analysis.

The research strategy is developed along 5 lines : material selection, advanced characterization techniques (Fig. 1.11), macroscopic mechanical properties of coatings, mesoscale modelling of microstructures and identification of deformation and inter- and transgranular damage mechanisms.

The proposed PhD project aims at applying advanced characterization and modelling techniques for a better understanding of the mechanical properties of Zn-Al-Mg coating along the previous lines. The objective is to draw from these observations new guidelines for the microstructure optimization. In a nutshell, this ambitious PhD project lies on a tight connection between in situ characterization of strain and damage localization (understanding the associated mechanisms), and assessment of the coating behavior as a function of both loading and composition of the coating based on systematic finite element simulations requiring identification of constitutive models.

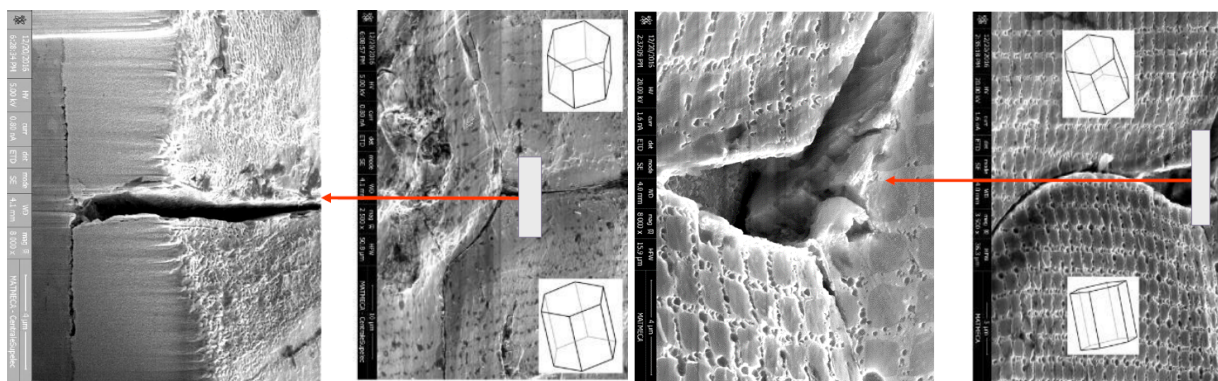


FIGURE 1.11 – 3D FIB-SEM characterization of damage zones inside zinc coatings

Travail Post-doctoral d'Abderrahim EL KHABBAZ (Septembre 2013 - Août 2014) :

Sujet : Solutions matériaux architecturés pour le contrôle vibratoire des tubes GV.

Encadrement : S. Forest (Mines Paris-PSL) (70%) et K. Ammar (Mines Paris-PSL) (30%).

Partenariat : G. Perrin (chaire AREVA).

L'optimisation de structures est une des préoccupations essentielles pour la conception des systèmes dans l'industrie mécanique (génie civil, aéronautique, automobile...). Les bureaux d'études ne se contentent pas d'améliorer les performances mécaniques des pièces qu'ils conçoivent, mais ils cherchent également à optimiser leur poids, leur encombrement ainsi que leur coût de réalisation. Déterminer la géométrie ou la forme appropriée d'un objet représente un défi quotidien de première importance pour l'ingénieur. L'optimisation intervient de façon primordiale dans l'augmentation des performances, la maîtrise des techniques de conception des systèmes ainsi que la réduction des coûts de fabrication et d'exploitation.

Ce projet s'inscrit dans le cadre du développement des nouveaux matériaux architecturés dédiés spécialement pour des applications nucléaires. L'objectif de ce travail est d'adapter et d'appliquer la méthode d'optimisation de formes en utilisant la méthode de champ de phases applicable à la conception des tubes des générateurs de vapeur. Ces derniers ont pour fonction principale de faire l'échange thermique entre l'eau du circuit primaire et secondaire. Plusieurs exemples numériques classiques ont été proposés pour bien valider la méthode numérique suggérée, tel que le cas d'un cantilever bidimensionnel, soumis à une force ponctuelle verticale au milieu de la côte droite avec une conditions aux limites d'encastrement sur le bord gauche (Fig. 1.12).

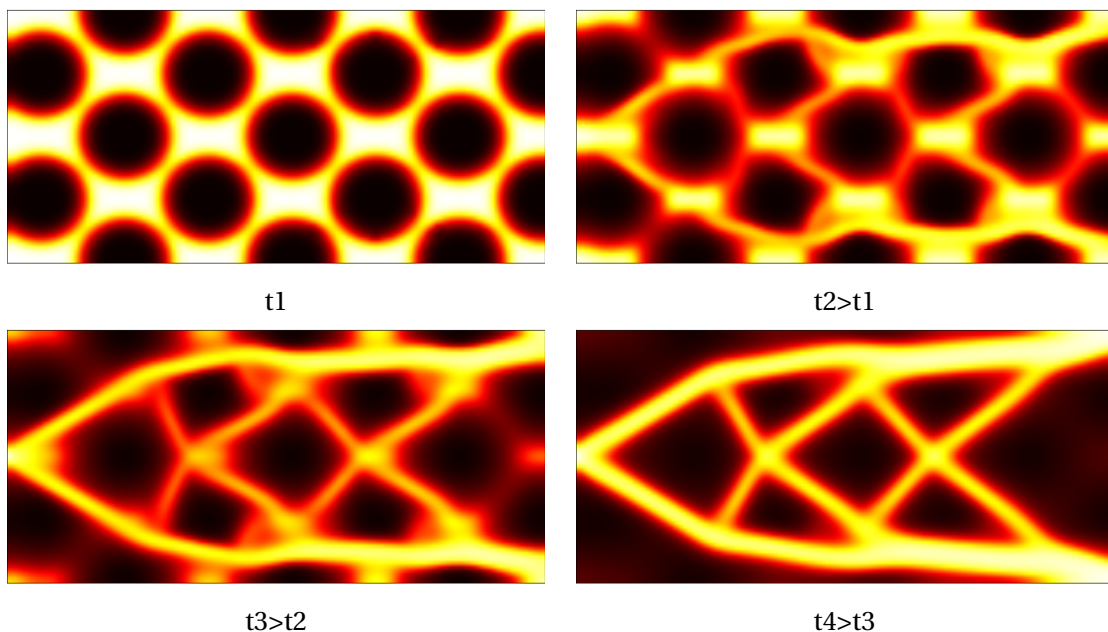


FIGURE 1.12 – Forme optimisée d'un cantilever bidimensionnel

Travail Post-doctoral d'Anna ASK (Septembre 2015 - Octobre 2018) :

Sujet : Modélisation de la recristallisation en utilisant la méthode des champs de phases.

Encadrement : S. Umut (Université Paris-XIII) (33%), K. Ammar (Mines Paris-PSL) (33%) et B. Appolaire (Onera) (33%).

Partenariat : Projet CNRS "Coup de pouce F2M" 2015 (entre 2015 et 2016).

S. Forest (Mines Paris-PSL), projet européen MIGRATE (entre 2016 et 2018).

La recristallisation est un phénomène complexe que l'on rencontre durant l'évolution de la microstructure des alliages métalliques soumis à des chargements combinés thermiques et mécaniques, et qui a pour effet majeur de transformer totalement la microstructure du matériau et notamment son degré d'anisotropie. Elle se produit généralement en même temps que d'autres sources de modification de l'état microstructural du matériau comme l'écroutissage, la restauration statique et dynamique et la croissance de grains. La compréhension et la prévision de ces mécanismes est nécessaire pour un contrôle rigoureux des propriétés mécaniques des composants industriels et de leur optimisation, pourtant la tâche est particulièrement complexe vu que les phénomènes cités impliquent tous les défauts des structures cristallines monophasées, lacunes, dislocations, joints de grains, etc et ce à toutes les échelles. À l'heure actuelle, tous les modèles existants, à savoir les modèles qualitatifs reposant sur des grandeurs moyennes et scalaires ou les modèles en champ complet ne sont pas actuellement en mesure d'englober tous ces aspects et surtout de définir des lois de germination et de migration.

L'objectif de ce projet est de développer un cadre de modélisation, formulé comme une théorie des champs mécaniques et physiques sur une base thermodynamique cohérente et intégrant les mécanismes principaux impliqués dans la recristallisation, à savoir la déformation viscoplastique, la restauration et le mouvement des joints de grains.

Le projet s'est articulé donc en deux parties sur une démarche à deux échelles, menées en parallèle :

- La mise en place d'un modèle mésoscopique opérationnel pour étudier les phénomènes de la recristallisation dans un cadre théorique unique, sans recours à des couplages entre méthodes de natures différentes avec les difficultés numériques afférentes. Il est basé sur l'enrichissement du modèle de champ de phase, développé précédemment au centre des matériaux (Fig. 1.13a), par un modèle de Cosserat à l'échelle mésoscopique pour tenir compte de la désorientation du réseau cristallin et la cristallinité, liée à celle déduite des calculs de plasticité.

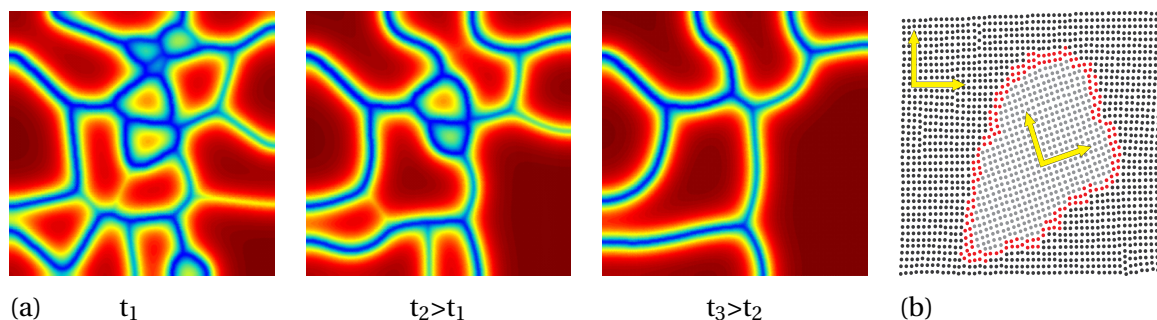


FIGURE 1.13 – (a) Évolution du champ de cristallinité (b) Simulation préliminaire d'un nanograin obtenue par minimisation de l'énergie élastique construite par réduction de Lagrange sur une grille atomistique.

- La mise en œuvre d'une nouvelle approche à une échelle plus fine, basée sur un formalisme à la Landau, permettant d'étudier l'auto-organisation des dislocations et de prendre en compte les rotations associées aux joints de grains (Fig. 1.13b).

Cette étude a fait l'objet de deux articles dans des revues internationales à comité de lecture [12, 13, 14, 15] ainsi que plusieurs communications dans des conférences internationales.

Travail Post-doctoral de LU Tuan LE (Janvier 2018 - Septembre 2019) :

Sujet : New titanium alloys with a combination of high strength, strain hardening and high ductility, induced by TRIP and TWIP effects.

Encadrement : S. Forest (Mines Paris-PSL) (50%) et K. Ammar (Mines Paris-PSL) (50%).

Partenariat : F. Prima (IRCP Chimie ParisTech), projet ANR TITWIP.

The objective of the research is to develop constitutive models describing the mechanical behaviour of a new generation of titanium alloys with promising properties for aeronautic applications. The multiscale model will include plastic slip and twinning mechanisms that are active in these alloys at room temperature. For that purpose, two types of approaches will be proposed. The first one is based on non-linear homogenisation techniques recently developed for metallic polycrystals (Fig. 1.14). This model will be extended to twinning mechanisms and to large deformations within efficient algorithms for the computation of a large number of grains to represent the texture of the material. The second approach is dedicated to the plasticity and twinning at the grain scale within polycrystalline aggregates. Continuum crystal plasticity models will be used to compute the heterogeneous deformation field inside the grains and the interaction with neighbouring grains depending on grain misorientations. The development of twins inside the grains will be accounted for using phase field methods coupled with crystal plasticity. Comparisons will be drawn, on the one hand, with experimental observations of the deformation mechanisms and, on the other hand, with phase field simulations of twinning and phase transformation performed by the two other partners of the project. Special attention will be paid to the optimization of strain hardening of these new materials by controlling the relative importance of the various deformation mechanisms and their interaction, as evidenced by experimental observations. Implications for the ultimate strength of these materials are drawn .

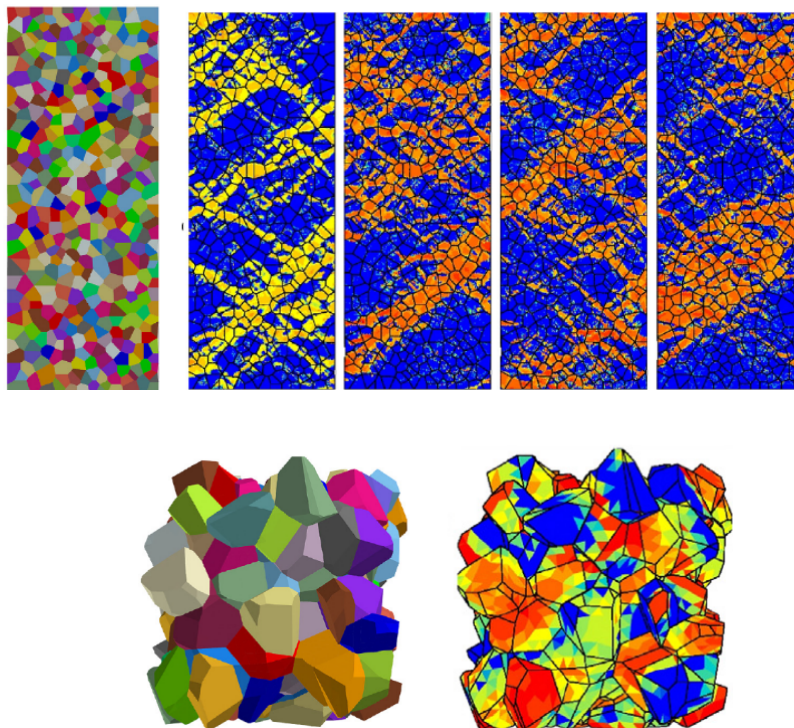


FIGURE 1.14 – 2D and 3D Finite element computations of polycrystalline titanium aggregates.

Cette étude a fait l'objet d'un article a dans une revue internationale à comité de lecture [11].

Travail Post-doctoral de Hiba BEN KAHLA (Mars 2020 - Septembre 2021) :

Sujet : Chemically Architected MEtallic aLloys, towards a new strengthening mechanism.

Encadrement : S. Forest (Mines Paris-PSL) (50%) et K. Ammar (Mines Paris-PSL) (50%).

Partenariat : M. Laurent-Brocq (ICMPE-CNRS) et M. Bletry (ICMPE-CNRS), projet CAMEL.

Chemical architecturation is a new concept of multi-scale microstructure, in which two phases are separated by a 3D network of composition fluctuations. The chemical fluctuations are proposed as a new strengthening mechanism at the mesoscale. At the microscopic and atomic scale, grain boundaries and solid solution also provide conventional strengthening mechanism. This concept has already been successfully applied to high entropy alloys, by applying spark plasma sintering (SPS) on a powder mixture (Ni)-(CoCrFeMnNi). The objectives of this work are to evidence that composition fluctuation is indeed a strengthening mechanism and to study the interactions between all strengthening mechanisms (Fig. 1.15).

The microstructures and mechanical behavior were characterized in detail, including scanning electron microscopy coupled with energy dispersive microscopy and electron backscatter diffraction, nanoindentation, and compression tests. Focus was made on the chemical fluctuations, which are named interphase, and the resulting local strengthening, as well as on grain boundaries. To identify the main strengthening mechanism, finite element modelling was performed with various approaches (two-phased and three-phase models, strain gradient plasticity, addition of a new chemical gradient effect). Then, interphase characteristics were tuned by controlling the SPS parameters, to maximize the strengthening. To do so, new samples were processed and characterized. Finally, for the most promising microstructures, tensile and ductile shearing tests were performed in order to assess the fracture behavior.

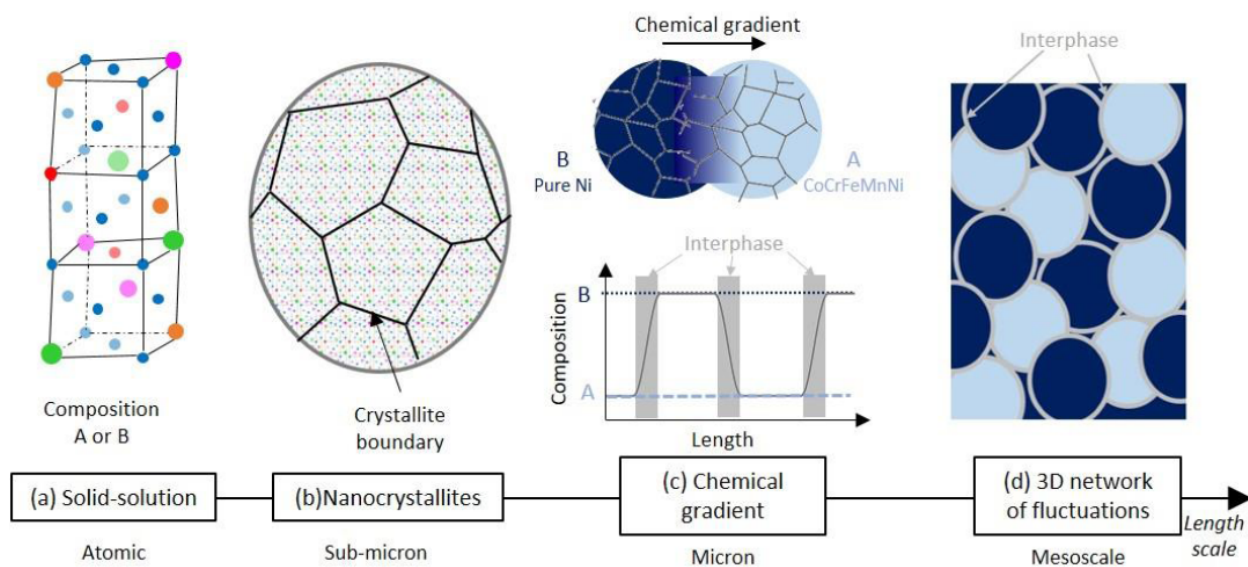


FIGURE 1.15 – Multi-scale microstructure of chemically architected high entropy alloys.

1.5 Mes relations avec le monde de l'entreprise

En tant qu'ingénieur de recherche et développement en calcul scientifique et simulation numérique au sein de l'équipe valorisation entre 2011 et 2016, j'étais chargé d'assurer l'industrialisation et la valorisation de l'ensemble de la suite logicielle Z-set Software ainsi que l'activité de support aux utilisateurs industriels et académiques. Également, j'étais amené à gérer des activités contractuelles pour l'industrie en assurant le montage, la négociation et les gestions administrative et financière de projets de coopération scientifique et de recherches subventionnées (Fig. 1.16). Un récapitulatif de mes principaux projets réalisés est présenté ci-dessous :

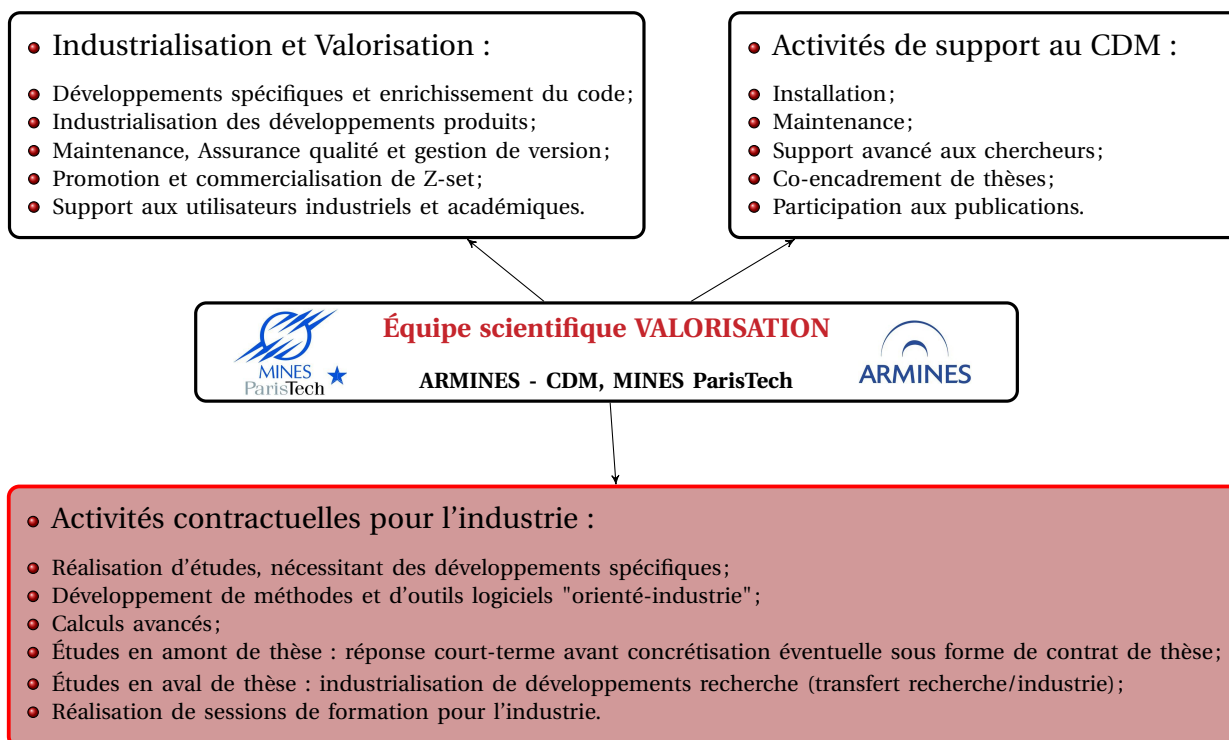





FIGURE 1.16 – Mes activités réalisées durant mon expérience professionnelle





Principaux projets réalisés lors de mes expériences professionnelles

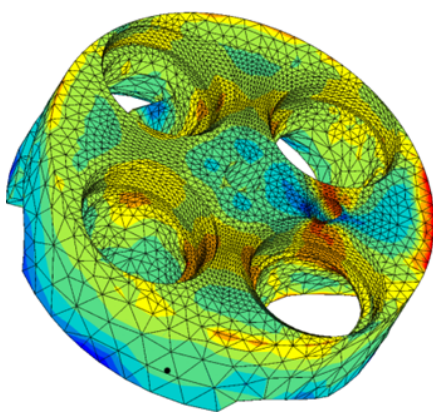
05/15-05/16 (5mois)	Solutions matériaux architecturés pour le contrôle vibratoire Pour le compte de <i>CHAIRE AREVA</i> (25% de participation)	
07/15-08/15 (1mois)	Développement d'une interface LS-DYNA/Z-mat Pour le compte de <i>METRONIC</i> Contrat industriel : 7.5K € (75% de participation)	
02/15-05/15 (3mois)	Loi de comportement et critère de fatigue pour l'alliage d'aluminium à base de cuivre AS7G (Figs. 1.17a et 1.17b) Pour le compte de <i>RENAULT</i> Contrat industriel : 17.5K € (100% de participation) Cette étude a fait l'objet d'un article dans une revue internationale à comité de lecture [16] et d'une communication dans une conférence internationale [32].	

<p>10/14-02/15 (5mois)</p>	<p>Développement et implémentation d'un outil pour estimer rapidement l'état élastoplastique d'une structure "Notch Concentration Plastic Correction" pour des chargements multiaxiaux complexes Pour le compte de <i>SAFRAN Aircraft Engines</i> Contrat industriel : 32K € (50% de participation)</p>	
<p>06/14-09/14 (3mois)</p>	<p>Développement et implémentation d'un nouveau modèle énergétique anisotherme de type Charkaluk afin de prédire la durée de vie de la fatigue thermomécanique, appliquée sur un turbocompresseur (Fig. 1.17c) Pour le compte de <i>RENAULT</i> <i>Contrat industriel : 45K € (90% de participation)</i> Cette étude a fait l'objet d'une communication dans une conférence internationale [34].</p>	
<p>01/13-05/14 (6mois)</p>	<p>Implémentation et validation de comportements complexes pour les matériaux sous haute température (chambres de combustion) (projet PRC-chaud) Pour le compte de <i>SAFRAN Aircraft Engines</i> <i>Contrat industriel : 300K € (10% de participation)</i></p>	
<p>01/13-12/13 (4mois)</p>	<p>Conception et préparation de campagnes d'essais mécaniques en vue de l'identification d'une loi de comportement Pour le compte de <i>RENAULT</i> <i>Contrat industriel : 50K € (75% de participation)</i></p>	
<p>05/13-08/13 (3mois)</p>	<p>Caractérisation du comportement mécanique du matériau AS10 Pour le compte de <i>MONTUPET</i> <i>Contrat industriel : 38K € (100% de participation)</i></p>	
<p>01/13-04/13 (3mois)</p>	<p>Méthodologie de prédiction de la durée de vie de structure en matériaux plastiques (Fig. 1.17d) Pour le compte de <i>RENAULT</i> <i>Contrat industriel : 50K € (50% de participation)</i></p>	
<p>10/12-11/12 (15 jours)</p>	<p>Calibration d'une loi de comportement non-linéaire élasto-plastique Pour le compte de <i>AREVA</i> <i>Contrat industriel : 5K € (100% de participation)</i></p>	
<p>05/12-07/12 (2 mois)</p>	<p>Modélisation du comportement d'un matériau composite à fibres courtes de verre (Application automobile) Pour le compte de <i>RENAULT</i> <i>Contrat industriel : 12.5K € (50% de participation)</i></p>	
<p>01/12-03/12 (2 mois)</p>	<p>Calibration of a visco-plastic behavior and fatigue life criterion to apply in a benchmark calculation of an exhaust manifold component (Fig. 1.17e) Pour le compte de <i>TENNECO AUTOMOTIVE</i> <i>Contrat industriel : 12.5K € (50% de participation)</i></p>	
<p>09/11-11/11 (2 mois)</p>	<p>Calibration of the M15 material parameters Pour le compte de <i>HONEYWELL</i> <i>Contrat industriel : 25K € (100% de participation)</i></p>	

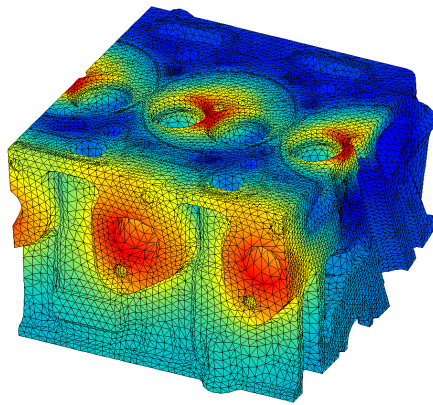
J'ai aussi assuré des sessions de formation professionnelle pour des industriels tels que le groupe d'ingénierie et de production d'équipements automobiles FAURECIA, le groupe industriel NEXTER ainsi que la multinationale française du secteur de l'énergie AREVA :

Formation pour les industriels

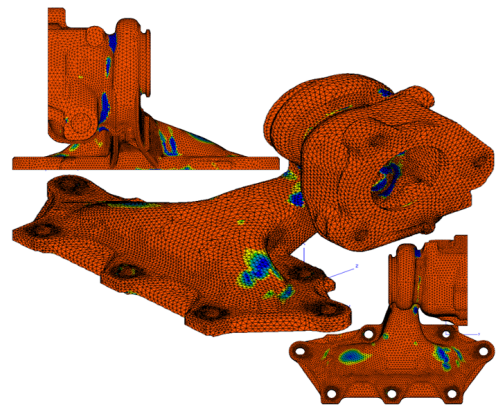
Décembre 2014	Identification d'une loi de comportement élasto-visco-plastique de type Chaboche et modélisation d'un collecteur Pour le compte de <i>FAURECIA</i> (Une journée).	
Novembre 2014	Calibration d'une loi de comportement élasto-plastique Pour le compte de <i>NEXTER</i> (Deux journées).	
Juillet 2013	ZsimOpt training session : Implémentation et identification d'une loi de comportement Pour le compte de <i>FAURECIA</i> (Une journée).	
Décembre 2012	Calibration d'une loi de comportement élasto-plastique Pour le compte de <i>AREVA</i> (Une journée).	



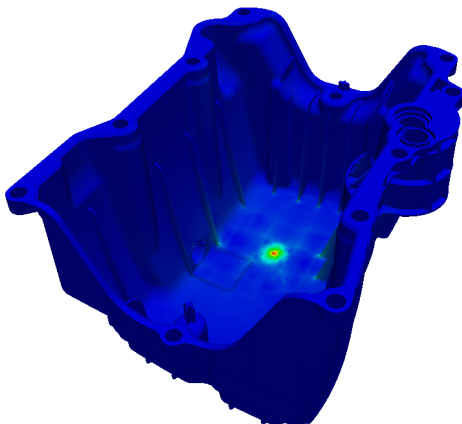
(a) Fatigue thermomécanique avec effet de vieillissement du chambre des combustions.



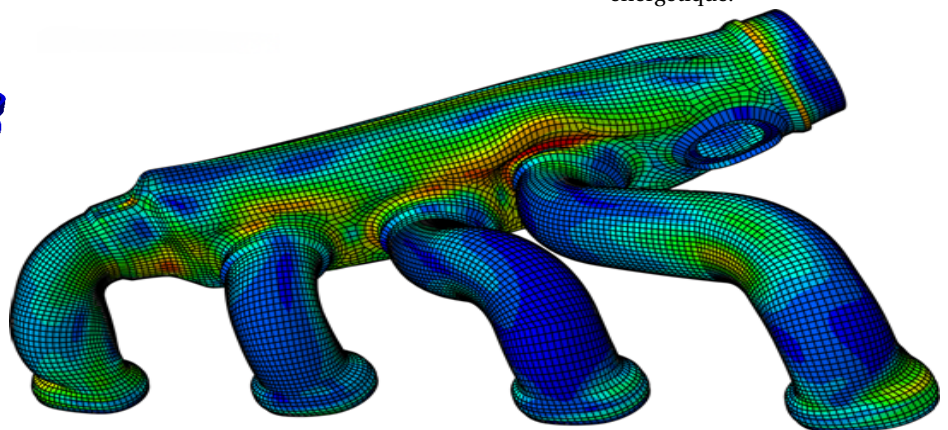
(b) Simulation du vieillissement en appliquant un champ de température maximale sur la culasse.



(c) Estimation de la durée de vie de la fatigue thermomécanique d'un turbocompresseur en utilisant un modèle énergétique.



(d) Simulation de l'impact d'un projectile sur la surface extérieure d'un carter d'huile.



(e) Prédiction de la durée de vie de la fatigue thermomécanique d'un collecteur d'échappement.

FIGURE 1.17 – Quelques résultats obtenus durant mes activités contractuelles pour l'industrie.

Introduction

Ce mémoire en vue de l'obtention de l'habilitation à diriger des recherches présente une synthèse de mes travaux de recherche que j'ai effectués au Centre des Matériaux de l'École des Mines de Paris durant les dix dernières années. Ces activités de recherche, inscrites dans la continuité de mes travaux de thèse, portent sur la modélisation du couplage entre les évolutions microstructurales et la mécanique, et plus particulièrement la plasticité, dans les matériaux métalliques en utilisant la méthode de champs de phases.

Les propriétés mécaniques des matériaux sont fortement contrôlées par leurs microstructures, à savoir la forme et la disposition spatiale de différentes phases présentes. Il est donc primordial, d'un point de vue à la fois fondamental et appliqué, de comprendre et de maîtriser les évolutions microstructurales. Dans de nombreux matériaux métalliques, les microstructures sont souvent issues de changements de phase à l'état solide se déroulant pendant des traitements thermiques et thermomécaniques, où des contraintes et des déformations sont généralement générées par l'hétérogénéité de structure cristalline et sont accommodées par relaxation plastique. Cette plasticité influence en retour les morphologies et les cinétiques. D'autre part, à l'échelle du micromètre et en dessous, la plasticité s'avère dépendre de la taille des zones impliquées, comme l'ont montré de nombreux travaux en mécanique des matériaux : généralement, plus la plasticité est confinée, moins le matériau se plastifie. La plasticité est donc impactée par l'évolution des microstructures.

En se basant sur mes compétences acquises durant mes travaux de recherche et mes activités d'encadrement, j'ai entrepris d'étudier ce fort couplage entre les évolutions microstructurales et les modèles de plasticité, qui tiennent compte des effets de taille, en utilisant le modèle de champ de phase pour traiter ce genre de problématique. En effet, la méthode des champs de phase s'est avérée la plus adaptée pour étudier les évolutions microstructurales accompagnées de changements topologiques complexes, notamment en présence de contraintes générées par les désaccords entre les réseaux cristallins des phases impliquées. D'autre part, ils reposent sur une formulation thermodynamique qui permet d'inclure de manière cohérente de nombreux phénomènes physiques, dont la plasticité.

Durant mes travaux de recherche, j'ai suivi une démarche progressive en couplant à la méthode de champ de phase des modèles de plasticité de complexité croissante. Dans un premier temps, nous avons consolidé le couplage avec des modèles phénoménologiques de plasticité «macroscopique» continue, déjà développés durant ma thèse, et qui nous a permis de clarifier les différentes stratégies de couplage en vue de leur mise en œuvre au cours des étapes suivantes. Dans une deuxième étape, nous avons travaillé sur le couplage avec les modèles de plasticité dits à gradients, qui tiennent compte des effets d'échelle et qui font apparaître des

lois de comportement dépendant directement ou indirectement du gradient de déformation. La troisième étape a consisté à étendre les couplages précédents aux modèles de plasticité cristalline, reposant sur des densités de dislocations, plus réalistes à l'échelle de la microstructure dans la mesure où la déformation plastique est anisotrope et contrôlée par les systèmes de glissement cristallins des phases en présence.

Le chapitre 3 est consacrée à l'étude du couplage cohérent champ de phase/plasticité continue «macroscopique». Une première application, présentée dans la section 3.3, vise à étudier les interactions entre la plasticité et les transformations de phase diffusives et comprendre un tel couplage fort en analysant le processus de dissolution des précipités assisté par chargement de cisaillement. Le rôle possible de la plasticité sur la bifurcation de la forme des précipités lors du chargement mécanique est étudié, à condition que le temps caractéristique de diffusion soit de la ordre du chargement en régime plastique

En plus, La description de la plasticité dans les interfaces diffuses par des modèles continus s'est avérée un problème particulièrement délicat, associé en particulier à la question de l'héritage de la déformation plastique par une phase qui croît dans une matrice se plastifiant. La comparaison de ces deux formulations a été présentée dans la section 3.4 et a surtout souligné des comportements très différents, suivant l'approche adoptée, lorsqu'une interface progresse dans un volume déjà plastifié : la phase fille hérite ou non de la déformation plasticité de la matrice. En effet, ces deux formulations nous ont permis de traiter deux cas limites, à savoir l'héritage complet de la plasticité lors du passage des interfaces lorsque on choisit l'interpolation des propriétés mécanique et l'effacement complet dans le cas de l'interpolation des comportements. En réalisant des calculs de validation dans le cas d'une interface mobile, tels que la croissance et la dissolution d'un précipité avec des formes de complexités croissantes, dans diverses configurations (conditions aux frontières, sollicitations...), nous avons mis en évidence l'importance de l'héritage de la plasticité d'une phase par une autre lors des changements de phase en montrant que la plasticité peut jouer sur l'évolution de la forme, ainsi que sur la cinétique de croissance suivant le traitement de l'héritage (héritage complet ou effacement complet de la plasticité)

Le couplage entre le modèle des champs de phase avec la plasticité continue, réalisé dans le chapitre 3, est une étape très intéressantes, permettant de bien souligner l'importance du choix de la description de la plasticité dans les interfaces diffuses et sa conséquence primordial sur le traitement de l'héritage, ainsi sur l'évolution microstructurale. Cependant, ce couplage reste phénoménologique et insuffisant pour étudier les évolutions microstructurales à l'échelle du micromètre. Pour prendre en compte les effets de taille de la plasticité, un modèle alternatif de plasticité à gradient à été développé et détaillé dans le chapitre 4, permettant d'intégrer à la fois l'évolution des microstructures et les effets de taille de la plasticité.

Pour étudier les évolutions microstructurales dans lesquelles l'effet de taille est susceptible de jouer un rôle significatif, nous avons utilisé les modèles résultant pour la simulation de la mise en radeaux dans les superalliages base nickel, utilisés notamment dans l'industrie aéronautique. Nous avons montré que l'impact de la plasticité sur l'évolution microstructurale était très grand, mais que celui des effets de taille de la plasticité était plus important sur le comportement mécanique que sur l'évolution microstructurale. En effet, Il s'est avéré que le comportement mécanique évolue significativement pendant le fluage quand on prend en compte les effets de taille de la plasticité, et ce parce que la taille des couloirs de phase γ évolue au cours du temps. En revanche, les effets de taille n'ont que des conséquences modérées sur l'évolution morphologique des précipités.

Cependant, les modèles de plasticité à gradient, s'ils corrigent un certain nombre de problèmes que rencontrent les modèles classiques à l'échelle de la microstructure, restent fortement phénoménologiques. Notamment, les termes de gradient sont souvent proposés à partir d'arguments qualitatifs qui limitent le pouvoir de prévision des modèles. En effet, il est ap-

paru au cours de mes travaux de recherche sur le couplage transformation de phase/plasticité, que l'héritage de la plasticité représente un problème très important pour des modèles mésoscopiques manipulant des quantités moyennées sur un grand nombre d'atomes et de dislocations. Ce problème ne peut être résolu qu'en s'appuyant sur des études aux échelles plus basses (atomiques, dislocations) en dérivant des modèles de plasticité en partant de l'échelle des dislocations et en mettant en œuvre une démarche de changement d'échelle rigoureuse. Par conséquent, le chapitre 5 a été consacré à étendre les couplages précédents aux modèles de plasticité cristalline, reposant sur des densités de dislocations, plus réalistes à l'échelle de la microstructure dans la mesure où la déformation plastique est anisotrope et contrôlée par les systèmes de glissement cristallins des phases en présence. Nous avons suivi les deux voies proposées dans la littérature : d'une part en adoptant un modèle de plasticité «macroscopique» projeté sur les systèmes de glissement des structures cristallines impliquées et d'autre part en s'inspirant des modèles de plasticité cristalline reposant sur des densités de dislocations. Ce couplage a été utilisé pour l'étude du mécanisme de la croissance interne d'une couche d'oxyde Cr_2O_3 dans un substrat composé d'un acier austénitique monocristallin ainsi que la modélisation de l'oxydation inter-granulaire dans les aciers inoxydables polycristallins.

L'ensemble des travaux numériques sont développés dans l'environnement offert par le logiciel Z-Set software

Le chapitre 6 explicite mes perspectives et mon projet scientifique que j'envisage développer au cours des prochaines années en poursuivant ma carrière au sein au Centre des Matériaux MINES ParisTech, mais toujours avec des collaborations fructueuses avec les partenaires académiques et industriels. Je souhaiterais vivement étendre ma thématique de recherche en visant d'autres défis et thématiques tels que l'étude de la recristallisation, La modélisation multiphysique de la rupture dynamique de matériaux fragiles par un modèle d'endommagement à gradient ainsi que l'étude de l'optimisation topologique de matériaux hétérogènes.

Phase Field and Isotropic Continuum Plasticity

Contents

3.1	Introduction	43
3.2	Model description	44
3.2.1	Helmholtz free energy density	44
3.2.1.1	Partition of free energy	44
3.2.1.2	Chemical contribution	44
3.2.1.3	Mechanical contribution	45
3.2.2	Coupling between phase-field model and plasticity	45
3.2.2.1	Interpolation model	45
3.2.2.2	Multiphase approach : homogenisation method	47
3.2.3	Governing equations	51
3.3	Application : Splitting of dissolving precipitates during plastic shear	52
3.3.1	Introduction	52
3.3.2	Parameters and conditions for FE calculations	53
3.3.3	Results	54
3.3.4	Conclusion	66
3.4	Inheritance of plastic deformation during migration of phase boundaries	67
3.4.1	Introduction	67
3.4.2	Parameters and conditions for FE calculations	68
3.4.3	Results	69
3.4.3.1	Growth of a spherical precipitate	69
3.4.3.2	Microstructural evolution coupled to plastic activity	75
3.4.4	Conclusion	75

3.1 Introduction

Phase transformations most often generate internal stresses coming from eigenstrains associated with changes in crystalline structure and in chemical composition. In the case of coherent precipitation (in the absence of plasticity) these stresses induce very anisotropic long range interactions between precipitates at the origin of complex patterns ([Khachatryan, 1983]). However, in many industrial materials, plasticity is likely to partially relax stresses when those reach the yield stress. This indeed may happen in three cases : (i) First, internal stresses can reach significant magnitudes as in bainites or martensites in steels where plasticity is responsible for the change in their morphologies ([Li et al., 1998]). (ii) Second, yield stresses are generally small at high temperature where diffusive phase transformations generally proceed. Hence, even rather small eigenstresses may be relaxed as during the late stage of γ' precipitation in superalloys ([Yang et al., 2007]). (iii) Finally, in service, materials are often submitted to external loadings and temperature changes. In that case, the microstructure evolution and the plastic activity are also obviously coupled. Despite some early attempts ([Ganghoffer et al., 1994, Wen et al., 1996, Ganghoffer et al., 1991, Su et al., 2006]) the coupling of plastic relaxation with phase transformations has not been extensively investigated so far from a modeling point of view, because this requires efficient methods to handle microstructure evolution.

These last two decades, the phase field method (PFM) has emerged as the most powerful method for such a task, especially when stresses are involved in solids. Indeed, this method has been able : (i) to explain the formation of complex microstructures, such as cuboidal microstructures in Ni-base superalloys ([Wang et al., 1998, Boisse et al., 2007, Boussinot et al., 2009]), twin structures in martensites ([Wang et al., 2004, Finel et al., 2010]), chessboard structures ([Le Bouar et al., 1998]) or hydrides precipitation in zirconium ([Thuinet and Legris, 2010]); (ii) to capture subtle kinetic processes such as the slow down of coarsening in the presence of high elastic inhomogeneity ([Onuki and Nishimori, 1991]) or transitions between growth modes in ternary alloys involving slow and fast diffusing species ([Viardin, 2010]). So, it appears natural to include plasticity into a PFM to investigate its role in phase transformations.

Recent advances in phase field modelling include the description of elastoviscoplastic material behaviour of the phases combined with diffusion and phase transformation [Guo et al., 2005a, Gaubert et al., 2008, Ammar et al., 2009c, Gaubert et al., 2010, Ammar et al., 2011, Spatschek and Eidel, 2013]. In [Guo et al., 2005b], a PFM has been coupled to an isotropic plasticity model to study stress fields around defects such as holes and cracks. In [Ubachs et al., 2005], a general formalism incorporating phase field and isotropic viscoplasticity with non linear hardening has been proposed to investigate tin-lead solder joints undergoing thermal cycling. Since these pioneering works, similar approaches including isotropic plasticity models have been developed to study crystal growth ([Uehara et al., 2007]), martensites ([Yamanaka et al., 2008]), superalloys ([Gaubert et al., 2008]) and kinetics issues in diffusion controlled growth ([Ammar et al., 2009c, Ammar et al., 2011]). In the context of rafting in Ni-base superalloys, a few works have extended PFM with *anisotropic* plasticity model, either in a perfectly plastic model ([Zhou, 2010]) or in a crystal plasticity framework including both hardening and viscosity ([Gaubert et al., 2010]). the yield stress as well as any hardening effects are not included.

The corresponding models, that are interested in the coupling between elastoviscoplasticity and the phase field approach, can be classified into two main classes of theories, referred to as interpolation and homogenisation models in the present chapter. In the first one, called the "interpolation model" in the present work, all material points are endowed with the same set of mechanical constitutive equations (including elasticity, von Mises plasticity or crystal plasticity, etc.) but the material parameters (including the elasticity moduli, the yield stress, the hardening modulus, etc.) differ in the phases and are interpolated within the diffuse interfaces [Guo et al., 2005a, Gaubert et al., 2010]. In the second model class, the phase field method is

combined with the homogenisation approach well-known in the mechanics of heterogeneous materials [Steinbach and Apel, 2006, Steinbach and Apel, 2007, Ammar et al., 2009c, Ammar et al., 2011, de Rancourt et al., 2016]. Arbitrary constitutive equations can then be used for each phase and homogenisation rules are applied to the free energy densities and dissipation potentials.

This chapter is organized as follows : The first section 3.2 is devoted to describe the phase field approach, coupled with diffusion and isotropic continuum plasticity for alloys. The two main classes of theories, which are “interpolation models” and “homogenization schemes” are presented. To understand such strong coupling between diffusion controlled phase transformation and mechanics at the solid state, the possible role of plasticity on the shape bifurcation of hard precipitates during mechanical loading at high temperatures is investigated in section 3.3. In particular, we will show that the concomitant actions of both plasticity and dissolution are necessary for splitting precipitates into smaller ones. The question of inheritance of plastic deformation during migration of phase boundaries is discussed in section 3.4, in order to compare the implication of the choice of two proposed models “interpolation” and “homogenization” in the diffuse interface region. It is shown that both approaches strongly differ concerning the inheritance of plastic deformation, after an interface sweeps a plastified zone of bulk phase, during phase transformation.

3.2 Model description

3.2.1 Helmholtz free energy density

3.2.1.1 Partition of free energy

In the phase field approach, the total free energy F of the body is defined as the integral over the volume V of a free energy density f , which is split into a chemical free energy density contribution f^{ch} , a coherent mechanical energy density f^{u} , and a quadratic gradient contribution. Assuming that the free energy density depends on the order parameter ϕ , its gradient $\underline{\nabla}\phi$, the concentration c , the elastic strain tensor $\underline{\boldsymbol{\varepsilon}}^e$ and the set of internal variables V_k associated to material hardening, we have

$$\begin{aligned} F(\phi, \underline{\nabla}\phi, c, \underline{\boldsymbol{\varepsilon}}^e, V_k) &= \int_V f(\phi, \underline{\nabla}\phi, c, \underline{\boldsymbol{\varepsilon}}^e, V_k) dv \\ &= \int_V \left[f^{\text{ch}}(\phi, c) + f^{\text{u}}(\phi, c, \underline{\boldsymbol{\varepsilon}}^e, V_k) + \frac{\epsilon}{2} |\underline{\nabla}\phi|^2 \right] dv \end{aligned} \quad (3.1)$$

where the usual quadratic isotropic Ginzburg term was chosen with respect to the gradient of the order parameter ϕ .

The total strain tensor $\underline{\boldsymbol{\varepsilon}}$ is the symmetric part of the gradient of the displacement field. It is partitioned into the elastic strain $\underline{\boldsymbol{\varepsilon}}^e$, the eigenstrain $\underline{\boldsymbol{\varepsilon}}^*$ due to phase transformation and the plastic strain $\underline{\boldsymbol{\varepsilon}}^p$:

$$\underline{\boldsymbol{\varepsilon}} = \frac{1}{2} (\underline{\nabla}\underline{\mathbf{u}} + \underline{\nabla}\underline{\mathbf{u}}^T) = \underline{\boldsymbol{\varepsilon}}^e + \underline{\boldsymbol{\varepsilon}}^* + \underline{\boldsymbol{\varepsilon}}^p \quad (3.2)$$

3.2.1.2 Chemical contribution

Considering a two-phase binary alloy, the chemical free energy density f^{ch} of the binary alloy is a function of the order parameter ϕ and of the concentration field c . In order to guarantee the coexistence of both phases α and β discriminated by ϕ , f^{ch} must be non-convex with

respect to ϕ . Following [Kim et al., 1998], f^{ch} is built with the free energy densities of the two individual phases f_α and f_β as follows :

$$f^{\text{ch}}(\phi, c) = h(\phi)f_\alpha^{\text{ch}}(c) + \bar{h}(\phi)f_\beta^{\text{ch}}(c) + W\Psi(\phi) \quad (3.3)$$

The subscripts α and β indicate the two coexisting phases. Here, the function $h(\phi) = 1 - \bar{h}(\phi)$ is taken as $h(\phi) = \phi^2(3 - 2\phi)$, and $\Psi(\phi) = \phi^2(1 - \phi)^2$ is the double well potential accounting for the free energy penalty of the interface. The height W of the potential barrier is related to the interfacial energy Λ and the interfacial thickness δ as $W = 6Z\Lambda/\delta$. Assuming that the interface region ranges from $\phi = \theta$ to $\phi = 1 - \theta$, then $Z = \log((1 - \theta)/\theta)$. In the present work $\theta = 0.05$ following [Kim et al., 1998, Ammar et al., 2009a].

The densities f_α and f_β are chosen to be quadratic functions of the concentration only :

$$f_\alpha(c) = \frac{1}{2}k_\alpha(c - a_\alpha)^2 \quad \text{and} \quad f_\beta(c) = \frac{1}{2}k_\beta(c - a_\beta)^2 \quad (3.4)$$

The parameters k_α, k_β are the free energy curvatures with respect to concentration. They are assumed to be identical in the present study : $k_\alpha = k_\beta = k$. a_α and a_β are the equilibrium concentrations for α and β phases respectively [Ammar et al., 2009a].

3.2.1.3 Mechanical contribution

The second contribution to the free energy density in Eq. (3.1) is due to mechanical effects. Assuming that elastic behaviour and hardening are uncoupled, the mechanical part of the free energy density f^{u} is decomposed into a coherent elastic energy density f^e and a plastic part f^p as :

$$f^{\text{u}}(\phi, c, \boldsymbol{\epsilon}^e, V_k) = f^e(\phi, c, \boldsymbol{\epsilon}^e) + f^p(\phi, c, V_k) \quad (3.5)$$

The specific form of $f^{\text{u}}(\phi, c, \boldsymbol{\epsilon}^e, V_k)$ will be detailed in the next sections.

3.2.2 Coupling between phase-field model and plasticity

There are essentially two ways of introducing linear or nonlinear mechanical constitutive equations into the standard phase field approach, that are presented in the following.

3.2.2.1 Interpolation model

The material behaviour is described by a unified set of constitutive equations including material parameters that explicitly depend on the concentration or on the phase field variable. Each material parameter is usually interpolated between limit values known for each phase. This is the formulation adopted in the finite element simulations of Cahn-Hilliard like equations coupled with viscoplasticity by [Ubachs et al., 2004, Ubachs et al., 2005, Weinberg et al., 2009, Anders and Weinberg, 2011] for tin-lead solders, also derived in [Forest, 2008a, Forest, 2009]. The same methodology is used in [Gaubert et al., 2008, Gaubert et al., 2010] to simulate the rôle of viscoplasticity on rafting of γ' precipitates in single crystal nickel base superalloys under load. For instance, when an elastic phase coexists with an elastic-plastic one, the plastic yield threshold is interpolated between the actual value in the plastic phase and a very high unreachable value in the elastic phase, e.g. [Cha et al., 2009].

The diffuse interface behaviour resulting from this procedure can be compared to the ones commonly used in phase field models, as popularized by Khachaturyan and co-workers, e.g.

[Wang and Khachaturyan, 1995]. According to the latter, mixture rules are adopted respectively for eigenstrain and the tensor of elasticity moduli :

$$\underline{\boldsymbol{\varepsilon}}^* = h(\phi) \underline{\boldsymbol{\varepsilon}}_\alpha^* + \bar{h}(\phi) \underline{\boldsymbol{\varepsilon}}_\beta^* \quad , \quad \underline{\boldsymbol{C}} = h(\phi) \underline{\boldsymbol{C}}_\alpha + \bar{h}(\phi) \underline{\boldsymbol{C}}_\beta \quad (3.6)$$

where $\underline{\boldsymbol{\varepsilon}}_{\alpha,\beta}^*$ and $\underline{\boldsymbol{C}}_{\alpha,\beta}$ respectively are the eigenstrain and elasticity tensors of the individual phases. Hooke's law then relates the strain to the stress tensors by the following relations :

$$\begin{aligned} \underline{\boldsymbol{\sigma}} &= \underline{\boldsymbol{C}} : (\underline{\boldsymbol{\varepsilon}} - \underline{\boldsymbol{\varepsilon}}^*) \\ &= (h(\phi) \underline{\boldsymbol{C}}_\alpha + \bar{h}(\phi) \underline{\boldsymbol{C}}_\beta) : (\underline{\boldsymbol{\varepsilon}} - h(\phi) \underline{\boldsymbol{\varepsilon}}_\alpha^* - \bar{h}(\phi) \underline{\boldsymbol{\varepsilon}}_\beta^*) \end{aligned} \quad (3.7)$$

In that way, the elastic energy of the effective homogeneous material at a material point cannot be interpreted as the average of energy densities of both phases [Ammar et al., 2009c, Ammar et al., 2011]. The elastic energy is then postulated as :

$$f^e(c, \underline{\boldsymbol{\varepsilon}}^e) = \frac{1}{2} \underline{\boldsymbol{\varepsilon}}^e(c) : \underline{\boldsymbol{C}}(c) : \underline{\boldsymbol{\varepsilon}}^e(c) = \frac{1}{2} (\underline{\boldsymbol{\varepsilon}} - \underline{\boldsymbol{\varepsilon}}^p - \underline{\boldsymbol{\varepsilon}}^*(c)) : \underline{\boldsymbol{C}}(c) : (\underline{\boldsymbol{\varepsilon}} - \underline{\boldsymbol{\varepsilon}}^p - \underline{\boldsymbol{\varepsilon}}^*(c)) \quad (3.8)$$

where the explicit concentration dependence of material parameters has been introduced. The second term f^p in (3.5) accounts for mechanical energy contributions due to hardening effects. Plastic or viscoplastic deformation is generally associated with dislocation storage and therefore energy storage to be included in the free energy density. We consider here that the system consists of a two-phase elastoplastic binary alloy with one non-linear isotropic hardening and one non-linear kinematic hardening in each phase, following standard formulations of elastoviscoplastic constitutive equations [Lemaître and Chaboche, 1985, Besson et al., 2001]. The specific plastic free energy is chosen as a quadratic function of all state variables :

$$f^p(\phi, c, \underline{\boldsymbol{\alpha}}, r) = \frac{1}{3} C(\phi, c) \underline{\boldsymbol{\alpha}} : \underline{\boldsymbol{\alpha}} + \frac{1}{2} b(\phi, c) Q(\phi, c) r^2 \quad (3.9)$$

where $\underline{\boldsymbol{\alpha}}$ and r respectively are a tensorial kinematic and a scalar isotropic hardening variable, and C, Q and b are material parameters. In particular, C represents a plastic kinematic hardening modulus whereas the meaning of Q and b will become apparent at the end of this section. Each parameter is interpolated between limit values known for each phase as follows :

$$\begin{cases} C = h(\phi) C_\alpha + \bar{h}(\phi) C_\beta \\ b = h(\phi) b_\alpha + \bar{h}(\phi) b_\beta \\ Q = h(\phi) Q_\alpha + \bar{h}(\phi) Q_\beta \end{cases} \quad (3.10)$$

A yield criterion $g(\phi, c)$ is introduced :

$$g(\underline{\boldsymbol{\sigma}}, \underline{\boldsymbol{X}}, R, \phi) = J_2(\underline{\boldsymbol{\sigma}}, \underline{\boldsymbol{X}}) - R^0 - R(\phi) \quad \text{with} \quad R^0(\phi) = h(\phi) R_\alpha^0 + \bar{h}(\phi) R_\beta^0 \quad (3.11)$$

where R^0 is the initial yield stress and R subsequent isotropic hardening according to

$$R = \frac{\partial f^p}{\partial r} = b Q r \quad (3.12)$$

As a result, $R^0 + R$ is the radius of the elasticity domain. The function J_2 is chosen as the von Mises equivalent stress measure :

$$J_2 = \sqrt{\frac{3}{2} (\underline{\boldsymbol{s}} - \underline{\boldsymbol{X}}) : (\underline{\boldsymbol{s}} - \underline{\boldsymbol{X}})} \quad , \quad \text{with} \quad \underline{\boldsymbol{s}} = \underline{\boldsymbol{\sigma}} - \frac{1}{3} (\text{trace}(\underline{\boldsymbol{\sigma}})) \mathbf{1} \quad (3.13)$$

The tensors \underline{s} and \underline{X} respectively are the deviatoric stress tensor and the back-stress tensor accounting for kinematic hardening :

$$\underline{X} = \frac{\partial f^p}{\partial \underline{\alpha}} = \frac{2}{3} C \underline{\alpha} \quad (3.14)$$

According to the normality rule, the plastic flow rule takes the form

$$\dot{\underline{\epsilon}}^p = \dot{\lambda} \frac{\partial g}{\partial \underline{\sigma}} = \dot{\lambda} \underline{n} \quad (3.15)$$

where the direction of plastic flow is $\underline{n} = \partial g / \partial \underline{\sigma} = \frac{3}{2} \frac{\underline{s} - \underline{X}}{J_2(\underline{\sigma} - \underline{X})}$ in the case of the von Mises criterion and $\dot{\lambda}$ is the plastic multiplier. The evolution laws for isotropic and kinematic variables can be taken, for instance, from Chaboche model [Besson et al., 2001] :

$$\dot{r} = \dot{\lambda} \left(1 - \frac{R}{Q} \right) = \dot{\lambda} (1 - br), \quad \text{and} \quad \dot{\underline{\alpha}} = \dot{\lambda} \left(\underline{n} - \frac{3D}{2C} \underline{X} \right) \quad (3.16)$$

Nonlinear kinematic hardening is characterized by the additional material parameter D .

In the case of rate-independent plasticity considered here for simplicity, the plastic multiplier $\dot{\lambda}$ is determined from the consistency condition $dg/dt = 0$ and $g = 0$ under plastic loading condition ¹

3.2.2.2 Multiphase approach : homogenisation method

An alternative approach for formulating mechanical constitutive equations within a phase field framework is to resort to the multiphase approach as initially proposed in [Steinbach and Apel, 2006, Steinbach, 2009, Steinbach and Shchyglo, 2011]. Within this framework, it is possible to apply some results of the homogenisation theory developed in the mechanics of heterogeneous materials [Sanchez-Palencia and Zaoui, 1987, Zaoui, 2002, Besson et al., 2001] as demonstrated in [Ammar et al., 2009c, Ammar et al., 2011, Durga et al., 2013, de Rancourt et al., 2016].

One distinct set of constitutive equations is attributed to each individual phase α, β . Each phase at a material point then possesses its own stress/strain tensors $\underline{\sigma}_{\alpha, \beta}, \underline{\epsilon}_{\alpha, \beta}$. The overall strain and stress quantities $\underline{\sigma}, \underline{\epsilon}$ at this material point are defined as the averages of the corresponding tensors attributed to each phase. This is particularly important for points inside the smooth interface zone. At this stage, several homogenisation rules are available to perform the averaging. This homogenisation rule can also be interpreted as specific interpolation relations since there is generally no clear physical picture of the distribution of phases at the atomic scale underlying each material point of the diffuse interface. The advantage of the approach is that it makes it possible to mix strongly different types of constitutive equations for each phase, like hyperelastic nonlinear behaviour for one phase and conventional elasto-plastic model with internal variables for the other one. No correspondence of material parameters is needed between the respective constitutive laws of the phases. This is the approach proposed in [Steinbach and Apel, 2006] for incorporating elasticity in a multi-phase field model. For that purpose, the authors resorted to a well-known homogeneous stress hypothesis (Reuss model) taken from homogenisation theory in the mechanics of heterogeneous materials [Nemat-Nasser and Hori, 1999, Qu and Cherkaoui, 2006]. This approach has been applied to compute the effect of chemically induced strain on pearlite growth kinetics in [Steinbach and Apel, 2007].

1. The first condition, $g = 0$, means that the state of stress is on the actual yield surface, the second $\dot{g} = 0$ is the continuing plastic loading condition. Elastic unloading occurs when $g < 0$ or $\dot{g} < 0$, the internal variables then keeping a constant value.

It must be emphasised that this procedure is very similar to what has already been proposed for handling diffusion in phase field models [Kim et al., 1999]. Two concentration fields c_α and c_β are indeed introduced, and the real concentration field is obtained by a mixture rule together with an internal constraint on the diffusion potentials, called quasi-equilibrium constraint in [Eiken et al., 2006]. Introducing two concentration fields gives an additional degree of freedom for controlling the energy of the interface with respect to its thickness. Furthermore, the chemical and mechanical coupling inside the diffuse interface sometimes leads to spurious effects like too high stresses or stress fluctuation, due to the often unrealistic interface thickness that one is forced to use in practical applications. Adding additional degrees of freedom like fictitious concentration or other state variables for describing the stress/strain behaviour within a diffuse interface can be useful to get rid of such unwanted behaviour.

The homogenisation procedure in the mechanics of heterogeneous materials consists in replacing an heterogeneous medium by an equivalent homogeneous one, which is defined by an effective constitutive law relating the macroscopic variables, namely macroscopic stress $\boldsymbol{\sigma}$ and strain $\boldsymbol{\varepsilon}$ tensors, which are obtained by averaging the corresponding non-uniform local stress and strain in each phase. In the case of two-phase materials :

$$\boldsymbol{\varepsilon} = \frac{1}{\mathcal{V}} \sum_{k=\alpha,\beta} \int_{\mathcal{V}_k} \boldsymbol{\varepsilon}_k dv \quad \text{and} \quad \boldsymbol{\sigma} = \frac{1}{\mathcal{V}} \sum_{k=\alpha,\beta} \int_{\mathcal{V}_k} \boldsymbol{\sigma}_k dv \quad (3.17)$$

where $\mathcal{V} = \mathcal{V}_\alpha \cup \mathcal{V}_\beta$ is the underlying material representative volume element (RVE). In many cases, the actual geometry of the RVE is left unspecified but, for instance, the homogenisation scheme used in the phase-field/microelasticity approach in [Durga et al., 2013], corresponds to a laminate microstructure of the interface. Following a simple representation depicted in Figure 3.1, each material point, i.e. \mathcal{V} , within a diffuse interface can be seen as a local mixture of the two abutting phases α and β with proportions fixing \mathcal{V}_α and \mathcal{V}_β given by complementary functions of ϕ .

In the case of a two-phase material, the strain and stress at each material point are defined by the following mixture laws which would proceed from space averaging in a conventional homogenisation problem, but which can be seen as interpolations in the present case :

$$\boldsymbol{\varepsilon} = h(\phi) \boldsymbol{\varepsilon}_\alpha + \bar{h}(\phi) \boldsymbol{\varepsilon}_\beta \quad \text{and} \quad \boldsymbol{\sigma} = h(\phi) \boldsymbol{\sigma}_\alpha + \bar{h}(\phi) \boldsymbol{\sigma}_\beta \quad (3.18)$$

where $\boldsymbol{\varepsilon}_\alpha$, $\boldsymbol{\varepsilon}_\beta$ are the local strains and $\boldsymbol{\sigma}_\alpha$, $\boldsymbol{\sigma}_\beta$ are the local stresses attributed, at a material point, to the α and β phases respectively, and $h(\phi)$ is a polynomial function varying in a monotonic way from 0 to 1 between both phases, as usual in phase field approaches. Note that in homogenisation theory, one has $h(\phi) = \phi$ which turns out to be insufficient for the modelling of evolving microstructures.

According to the homogenisation theory, the effective elastic and plastic free energy densities are given by the rule of mixtures as follows :

$$f^e(\phi, c, \boldsymbol{\varepsilon}_\alpha^e, \boldsymbol{\varepsilon}_\beta^e) = h(\phi) f_\alpha^e(c, \boldsymbol{\varepsilon}_\alpha^e) + \bar{h}(\phi) f_\beta^e(c, \boldsymbol{\varepsilon}_\beta^e) \quad (3.19)$$

$$f^p(\phi, c, V_{k\alpha}, V_{k\beta}) = h(\phi) f_\alpha^p(c, V_{k\alpha}) + \bar{h}(\phi) f_\beta^p(c, V_{k\beta}) \quad (3.20)$$

All state and internal variables are therefore duplicated and corresponding variables $\boldsymbol{\varepsilon}_{\alpha,\beta}^e$ and $V_{k\alpha,\beta}$ are introduced.

In the proposed model, the reversible mechanical behaviour of each individual phase is governed by a convex mechanical free energy potential, which can be decomposed, using Eq. (3.5), into the contributions of each phase.

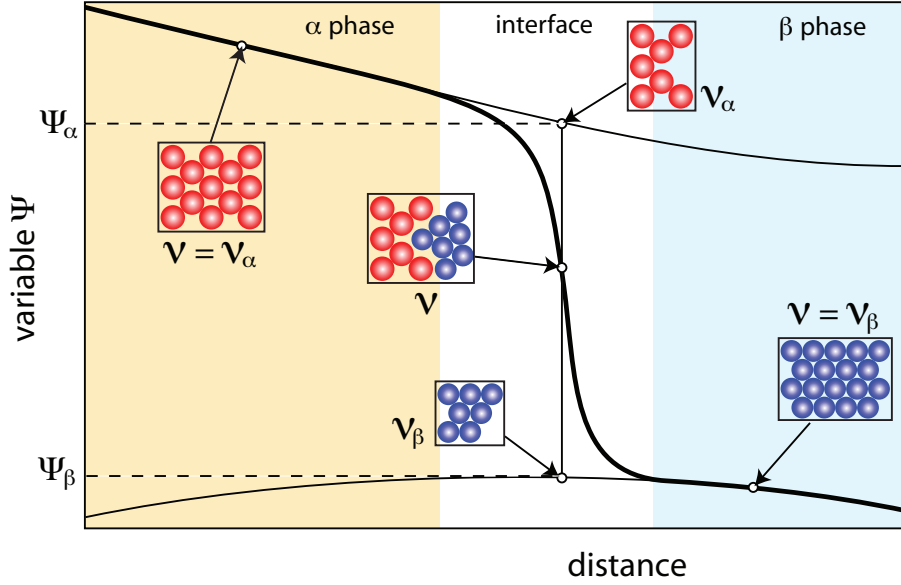


FIGURE 3.1 – Schematic illustration of the underlying material representative volume element \mathcal{V} at each material point of a diffuse interface : The real effective variable Ψ appears with a thick line, whereas the variables attached to each phase Ψ_α and Ψ_β are with thinner lines

Elastic energy density :

The effective elastic energy is expressed in terms of the elastic energies of both phases weighted by the complementing functions $h(\phi)$ and $\bar{h}(\phi)$. The corresponding free energy densities f_α^e, f_β^e are introduced as quadratic potentials with respect to the elastic strain contributions of the different phases :

$$f^e = h(\phi) f_\alpha^e + \bar{h}(\phi) f_\beta^e \quad (3.21)$$

with

$$f_\alpha^e(\boldsymbol{\epsilon}_\alpha^e) = \frac{1}{2} \boldsymbol{\epsilon}_\alpha^e : \underset{\approx}{\mathbf{C}}_\alpha : \boldsymbol{\epsilon}_\alpha^e \quad \text{and} \quad f_\beta^e(\boldsymbol{\epsilon}_\beta^e) = \frac{1}{2} \boldsymbol{\epsilon}_\beta^e : \underset{\approx}{\mathbf{C}}_\beta : \boldsymbol{\epsilon}_\beta^e \quad (3.22)$$

where the fourth-order tensors of elasticity moduli, $(\underset{\approx}{\mathbf{C}}_\alpha, \underset{\approx}{\mathbf{C}}_\beta)$, of the individual phases are introduced.

The total strains, $(\boldsymbol{\epsilon}_\alpha, \boldsymbol{\epsilon}_\beta)$, the eigenstrains, $(\boldsymbol{\epsilon}_\alpha^*, \boldsymbol{\epsilon}_\beta^*)$ and the plastic strain tensors $(\boldsymbol{\epsilon}_\alpha^p, \boldsymbol{\epsilon}_\beta^p)$ are introduced for both phases at each material point of the whole body. The partition hypothesis, already used for the effective total strain tensor in (3.2), requires, in a similar way, a decomposition of the total strain in each phase into elastic, eigenstrain and plastic parts :

$$\boldsymbol{\epsilon}_\alpha = \boldsymbol{\epsilon}_\alpha^e + \boldsymbol{\epsilon}_\alpha^* + \boldsymbol{\epsilon}_\alpha^p \quad \text{and} \quad \boldsymbol{\epsilon}_\beta = \boldsymbol{\epsilon}_\beta^e + \boldsymbol{\epsilon}_\beta^* + \boldsymbol{\epsilon}_\beta^p \quad (3.23)$$

The eigenstrains and tensors of elastic moduli at each point may then depend on the local concentration c , but not on the order parameter ϕ .

At this stage, the Voigt/Taylor assumption from homogenisation theory is introduced stating that

$$\boldsymbol{\epsilon}_\alpha = \boldsymbol{\epsilon}_\beta = \boldsymbol{\epsilon} \quad (3.24)$$

so that the local Hooke laws take the form

$$\underline{\underline{\sigma}}_{\alpha} = \underline{\underline{C}}_{\alpha} : (\underline{\underline{\epsilon}} - \underline{\underline{\epsilon}}_{\alpha}^{\star} - \underline{\underline{\epsilon}}_{\alpha}^p), \quad \underline{\underline{\sigma}}_{\beta} = \underline{\underline{C}}_{\beta} : (\underline{\underline{\epsilon}} - \underline{\underline{\epsilon}}_{\beta}^{\star} - \underline{\underline{\epsilon}}_{\beta}^p) \quad (3.25)$$

The resulting global Hooke law follows from the averaging rule (3.18) :

$$\underline{\underline{\sigma}} = h(\phi) \underline{\underline{C}}_{\alpha} : (\underline{\underline{\epsilon}} - \underline{\underline{\epsilon}}_{\alpha}^{\star} - \underline{\underline{\epsilon}}_{\alpha}^p) + \bar{h}(\phi) \underline{\underline{C}}_{\beta} : (\underline{\underline{\epsilon}} - \underline{\underline{\epsilon}}_{\beta}^{\star} - \underline{\underline{\epsilon}}_{\beta}^p) \quad (3.26)$$

It can be rewritten in the following form :

$$\underline{\underline{\sigma}} = \underline{\underline{C}}_{\text{eff}} : (\underline{\underline{\epsilon}} - \underline{\underline{\epsilon}}^p - \underline{\underline{\epsilon}}^{\star}) \quad (3.27)$$

where the effective elasticity moduli $\underline{\underline{C}}_{\text{eff}}$, effective eigenstrain $\underline{\underline{\epsilon}}^{\star}$ and effective plastic strain $\underline{\underline{\epsilon}}^p$ are defined as

$$\underline{\underline{C}}_{\text{eff}} = h(\phi) \underline{\underline{C}}_{\alpha} + \bar{h}(\phi) \underline{\underline{C}}_{\beta} \quad (3.28)$$

$$\underline{\underline{\epsilon}}^{\star} = \underline{\underline{C}}_{\text{eff}}^{-1} : (h(\phi) \underline{\underline{C}}_{\alpha} : \underline{\underline{\epsilon}}_{\alpha}^{\star} + \bar{h}(\phi) \underline{\underline{C}}_{\beta} : \underline{\underline{\epsilon}}_{\beta}^{\star}) \quad (3.29)$$

$$\underline{\underline{\epsilon}}^p = \underline{\underline{C}}_{\text{eff}}^{-1} : (h(\phi) \underline{\underline{C}}_{\alpha} : \underline{\underline{\epsilon}}_{\alpha}^p + \bar{h}(\phi) \underline{\underline{C}}_{\beta} : \underline{\underline{\epsilon}}_{\beta}^p) \quad (3.30)$$

which are the well-known Voigt effective properties. Note that (3.29) and (3.30) differ from usual phase field schemes as discussed in [Ammar et al., 2009c].

Plastic energy density :

Based on the application of the homogenization scheme inside the smooth interface zone as proposed in [Ammar et al., 2009c, de Rancourt et al., 2016], the (visco)-elasto-plastic behaviour of each phase is treated independently, where plastic strain and hardening state of α and β phases at a given time are completely described by a finite number of local internal variables, defined at each point for each phase. Considering the case of a two-phase elastoplastic alloy, it is considered that energy can be stored due to non-linear isotropic hardening and non-linear kinematic hardening in each phase. The hardening components are modelled by means of internal variables attributed to each phase. The set of internal variables V_k , of scalar or tensorial nature, represents the state of hardening of phase k : for instance, a scalar isotropic hardening variable r_k , and a tensorial kinematic hardening variable $\underline{\underline{\alpha}}_k$

$$V_k = \{r_{\alpha}, r_{\beta}, \underline{\underline{\alpha}}_{\alpha}, \underline{\underline{\alpha}}_{\beta}\} \quad (3.31)$$

The associated thermodynamic driving forces are

$$R_{\alpha} = \frac{\partial f_{\alpha}^p}{\partial r_{\alpha}}, \quad R_{\beta} = \frac{\partial f_{\beta}^p}{\partial r_{\beta}}, \quad \underline{\underline{X}}_{\alpha} = \frac{\partial f_{\alpha}^p}{\partial \underline{\underline{\alpha}}_{\alpha}}, \quad \underline{\underline{X}}_{\beta} = \frac{\partial f_{\beta}^p}{\partial \underline{\underline{\alpha}}_{\beta}} \quad (3.32)$$

A simple quadratic potential is adopted for the plastic part of the free energy density :

$$f_{\alpha}^p = \frac{1}{3} C_{\alpha} \underline{\underline{\alpha}}_{\alpha} : \underline{\underline{\alpha}}_{\alpha} + \frac{1}{2} b_{\alpha} Q_{\alpha} r_{\alpha}^2, \quad f_{\beta}^p = \frac{1}{3} C_{\beta} \underline{\underline{\alpha}}_{\beta} : \underline{\underline{\alpha}}_{\beta} + \frac{1}{2} b_{\beta} Q_{\beta} r_{\beta}^2 \quad (3.33)$$

thus assuming that each phase exhibits the same kind of isotropic elastoplastic behaviour, which is a simplification but not a real restriction in the approach. These potentials are similar to the function (3.9) chosen in the multiphase approach but different values of the constant

material parameters $b_{\alpha,\beta}$, $Q_{\alpha,\beta}$ and $C_{\alpha,\beta}$ are attributed to each phase. These parameters may depend on the concentration c but they do not depend on ϕ . It follows from (3.33) and (3.32) that

$$\begin{aligned} R_\alpha &= b_\alpha Q_\alpha r_\alpha, & R_\beta &= b_\beta Q_\beta r_\beta \\ \underline{\mathbf{X}}_\alpha &= \frac{2}{3} C_\alpha \underline{\boldsymbol{\alpha}}_\alpha, & \underline{\mathbf{X}}_\beta &= \frac{2}{3} C_\beta \underline{\boldsymbol{\alpha}}_\beta \end{aligned} \quad (3.34)$$

Still assuming that the elastoplastic behaviour of each phase is treated independently, distinct yield functions are introduced for both phases as

$$g_\alpha(\sigma_\alpha, \underline{\mathbf{X}}_\alpha, R_\alpha) = J_{2\alpha} - R_\alpha - R_\alpha^0, \quad g_\beta(\sigma_\beta, \underline{\mathbf{X}}_\beta, R_\beta) = J_{2\beta} - R_\beta - R_\beta^0 \quad (3.35)$$

The parameters $R_{\alpha,\beta}^0$ represent the initial yield stress of each phase. In the present work, a von Mises criterion is adopted for both phases :

$$J_{2\alpha} = \sqrt{\frac{3}{2}(\underline{\mathbf{s}}_\alpha - \underline{\mathbf{X}}_\alpha) : (\underline{\mathbf{s}}_\alpha - \underline{\mathbf{X}}_\alpha)} \quad \text{where} \quad \underline{\mathbf{s}}_\alpha = \underline{\boldsymbol{\sigma}}_\alpha - \frac{1}{3}(\text{trace}(\underline{\boldsymbol{\sigma}}_\alpha))\underline{\mathbf{1}} \quad (3.36)$$

$$J_{2\beta} = \sqrt{\frac{3}{2}(\underline{\mathbf{s}}_\beta - \underline{\mathbf{X}}_\beta) : (\underline{\mathbf{s}}_\beta - \underline{\mathbf{X}}_\beta)} \quad \text{where} \quad \underline{\mathbf{s}}_\beta = \underline{\boldsymbol{\sigma}}_\beta - \frac{1}{3}(\text{trace}(\underline{\boldsymbol{\sigma}}_\beta))\underline{\mathbf{1}} \quad (3.37)$$

where the deviatoric stress tensors $\underline{\mathbf{s}}_{\alpha,\beta}$ are introduced.

The plastic flow rules and the evolution equations for the internal variables are the following :

$$\dot{\underline{\boldsymbol{\epsilon}}}_\alpha^p = \dot{\lambda}_\alpha \underline{\mathbf{n}}_\alpha, \quad \text{with} \quad \underline{\mathbf{n}}_\alpha = \frac{\partial g_\alpha}{\partial \underline{\boldsymbol{\sigma}}_\alpha} \quad (3.38)$$

$$\dot{\underline{\boldsymbol{\epsilon}}}_\beta^p = \dot{\lambda}_\beta \underline{\mathbf{n}}_\beta, \quad \text{with} \quad \underline{\mathbf{n}}_\beta = \frac{\partial g_\beta}{\partial \underline{\boldsymbol{\sigma}}_\beta} \quad (3.39)$$

$$\dot{r}_\alpha = \dot{\lambda}_\alpha \left(1 - \frac{R_\alpha}{Q_\alpha}\right), \quad \dot{r}_\beta = \dot{\lambda}_\beta \left(1 - \frac{R_\beta}{Q_\beta}\right) \quad (3.40)$$

$$\dot{\underline{\boldsymbol{\alpha}}}_\alpha = \dot{\lambda}_\alpha \left(\underline{\mathbf{n}}_\alpha - \frac{3D_\alpha}{2C_k} \underline{\mathbf{X}}_\alpha\right), \quad \dot{\underline{\boldsymbol{\alpha}}}_\beta = \dot{\lambda}_\beta \left(\underline{\mathbf{n}}_\beta - \frac{3D_\beta}{2C_k} \underline{\mathbf{X}}_\beta\right) \quad (3.41)$$

As a result, two distinct plastic multipliers $\dot{\lambda}_\alpha$ and $\dot{\lambda}_\beta$ are required in the theory. They are determined independently for each phase using the consistency condition in rate-independent elastoplasticity.

3.2.3 Governing equations

Considering diffusion-controlled phase transformations in alloys, the present model belongs to the class of diffuse interface models, where the basic fields describing the inhomogeneous microstructure are (i) the non-conservative phase field $\phi(\underline{\mathbf{r}}, t)$ discriminating the precipitate (α phase) and the matrix (β phase), and (ii) the conservative concentration $c(\underline{\mathbf{r}}, t)$ of an alloying species (here arbitrarily taken as α -stabilizer, although the model can easily be extended to multicomponent alloys).

Because mechanics is involved, displacement field $\underline{\mathbf{u}}(\underline{\mathbf{r}}, t)$ is the third degree of freedom in the model.

The evolution equations of the coupled diffusion–phase transformation–mechanical problem are governed by the diffusion equation for the concentration field $c(\underline{\mathbf{x}}, t)$ and the Ginzburg-Landau equation for the order parameter $\phi(\underline{\mathbf{x}}, t)$, relating the rates to their corresponding driving forces as follows :

$$\frac{1}{M} \frac{\partial \phi}{\partial t} = - \frac{\partial f}{\partial \phi} = - \frac{\partial f_{\text{ch}}(\phi, c)}{\partial \phi} + \epsilon \Delta \phi \quad (3.42)$$

$$\frac{\partial c}{\partial t} = \nabla \cdot \left[L(\phi) \left(\nabla \frac{\partial f}{\partial c} \right) \right] \quad (3.43)$$

where f is the total free energy density which is the relevant thermodynamic potential in isothermal conditions.

The mobilities M and L are strictly positive real numbers (isotropy of the corresponding properties are assumed for simplicity). The Onsager coefficient $L(\phi)$ can be related to the interdiffusion coefficient D as follows $L = D/(\partial^2 f/\partial c^2)$ where f is the free energy density, so as to recover usual diffusion equations in the bulk phases.

The stress tensor $\underline{\boldsymbol{\sigma}}$, defined as the functional derivative with respect to the strain tensor $\underline{\boldsymbol{\epsilon}}$, fulfills mechanical static equilibrium in the absence of volume forces :

$$\nabla \cdot \underline{\boldsymbol{\sigma}} = \nabla \cdot \frac{\partial f}{\partial \underline{\boldsymbol{\epsilon}}} = 0 \quad (3.44)$$

3.3 Application : Precipitate shape bifurcations induced by plasticity

3.3.1 Introduction

The influence of elasticity on diffusion controlled phase transformations at the solid state has been extensively investigated. Besides its effect on thermodynamic equilibrium and its consequence on phase diagrams [Cahn and Larché, 1984], the role of elasticity on morphologies has been largely demonstrated (e.g. [Voorhees et al., 1988, Thompson et al., 1994, Le Bouar et al., 2003, Cottura et al., 2015b, Cottura et al., 2014] to cite a few works among many others). However, it has often been claimed that at high homologous temperatures plasticity is likely to relax completely any elastic contribution, such that the diffusive phase transformations can be investigated without accounting for mechanics. It is only recently, with the development of phase field models coupled with continuum plasticity [Ammar et al., 2009c, Gaubert et al., 2010, Ammar et al., 2011, Schneider et al., 2014, Cottura et al., 2015a, Vattré and Denoual, 2016, Hektor et al., 2016, Cheng et al., 2017, Hermann et al., 2018, Basak and Levitas, 2019], that it has become possible to show that the effect of elasticity cannot be discarded even at high temperatures. Indeed, due to the fact that stress relaxation is only partial, plasticity may increase the sizes of the microstructures without changing the nature of the shapes [Cottura et al., 2015a]. The impact of plasticity on the patterns formed by assemblies of precipitates can be more spectacular [Cottura et al., 2016, Cottura et al., 2021]. Moreover, plasticity has been shown to feature non trivial effects on kinetics, either promoting [Ammar et al., 2009c] or impeding [Ammar et al., 2011] interface migration depending on the morphology and loading. Finally, when plasticity displays some viscous character, the evolution is dependent on the ratio of time scales between visco-plasticity and diffusion [de Rancourt et al., 2016].

Along this line, we address in the present work the possible role of plasticity on shape bifurcation of hard precipitates during mechanical loading at high temperatures, a feature that

has never been put into evidence although it can be of interest in hot working of two phase alloys. Indeed, beside the interest for understanding such strong coupling between diffusion controlled phase transformation and plasticity, our work aims at bringing some possible explanation for microstructure evolutions observed commonly during adiabatic shear banding in two-phase Ti alloys. It is indeed not clear whether the small precipitates observed in shear bands results from the deformation process alone or from some partial dissolution due to the local temperature increase. In particular, we will show that the concomitant actions of both plasticity and dissolution are necessary for splitting precipitates into smaller ones. For that purpose, we have used a phase field coupled with an isotropic plasticity model as proposed in [Ammar et al., 2009c], that is recalled briefly in the following section. After providing the data and settings of the calculations, we analyze the process of dissolution assisted by shear loading, and on the basis of this analysis, we propose a possible new scenario for explaining the evolution of microstructures in adiabatic shear bands in Ti alloys.

Regarding notations, tensors of first, second and fourth rank are respectively denoted by \underline{u} , $\underline{\varepsilon}$ and $\underline{\underline{C}}$.

3.3.2 Parameters and conditions for FE calculations

Eqs. (3.42)-(3.44) have been recast into balances of microforces, following [Fried and Gurtin, 1996, Ammar et al., 2009a], and implemented in the finite element software Z-Set [Z-set package, 2013], where balances and constitutive laws are separated. The values of the parameters entering the model are reported in non-dimensional form in Tab. 3.1, where length, time and energy scales are respectively the size L of the system (typically the average distance between precipitates), diffusion time $\tau = M/k$, and the curvature k of the free energies with respect to concentration, which is chosen to be the same for both phases ($k_\alpha = k_\beta = k$), see Eq. (3.3). The rescaled quantities are denoted with tilde.

c_α^e	0.7	c_β^e	0.3
$\tilde{\Lambda} = \Lambda/(kL)$	5×10^{-4}	$\tilde{\delta} = \delta/L$	5×10^{-2}
$\tilde{D}_\alpha = D_\alpha \tau/L^2$	1×10^{-4}	$\tilde{D}_\beta = D_\beta \tau/L^2$	1×10^{-4}
$\tilde{E}_\alpha = E_\alpha/k$	14×10^{10}	$\tilde{E}_\beta = E_\beta/k$	7×10^{10}
$\nu_\alpha = \nu_\beta$	0.3	$\tilde{R}_\beta^0 = R_\beta^0/k$	50
$\underline{\underline{\varepsilon}}^*$	$3 \times 10^{-4} \mathbf{1}$		

TABLE 3.1 – Parameters in non-dimensional form.

Although most of the values have been selected in order to comply at least qualitatively with metallic alloys and in particular with Ti alloys, different quantities have been selected so as to enhance the effects of the coupling between the $\alpha \rightarrow \beta$ transformation and plasticity with moderate strains in the validity range of the small strain framework.

In order to enhance the variations of concentrations (commensurate with $c_\alpha^e - c_\beta^e$) associated with curvature and strain/stress changes, the equilibrium concentrations are set arbitrarily to the values in the middle of range $[0; 1]$. Moreover, both phases are considered as elastically isotropic for simplicity, with α twice stiffer than β , i.e. $E_\alpha = 2E_\beta$. This ratio is likely to be greater than the real one [Fisher and Renken, 1964], although there is a large scatter of the elastic moduli reported in the literature. But this significant contrast has been chosen to promote the

heterogeneity of strain and stress fields in the dual phase microstructure even for moderate imposed strains. Finally, it can be noticed that a very small and isotropic eigenstrain $\boldsymbol{\epsilon}^*$ has been assigned to α so as to mimic α nodules in Ti alloys [Semiatin et al., 2003] which generally do not feature any orientation relationships with the β matrix.

We have considered a $L \times L$ square domain composed of a single α circular precipitate of initial radius $R^0/L = \zeta$ with $\zeta = 0.8$, surrounded by the β matrix. The system has been discretized by a regular grid with 161×161 linear elements. The initial concentration in the precipitate has been set at the equilibrium concentration ($c^{\alpha 0} = c_\alpha^e$), whereas β is undersaturated with $c_\beta^0 = 0.2 < c_\beta^e$ (non-dimensional initial supersaturation $\Omega^0 = (c_\beta^0 - c_\beta^e)/\Delta c^e = 0.25$, with $\Delta c^e = c_\alpha^e - c_\beta^e = 0.4$). This situation corresponds to an instantaneous heating from some temperature in the $\alpha + \beta$ field where the initial precipitate is at equilibrium up to some higher temperature still in the two-phase domain.

At the boundaries, zero fluxes are imposed for ϕ and c , i.e. $\nabla c \cdot \mathbf{n}^{\text{ext}} = 0$ and $\nabla \phi \cdot \mathbf{n}^{\text{ext}} = 0$ where \mathbf{n}^{ext} are the normals to the system boundaries pointing outward. Moreover, the mechanical load is applied by keeping the boundaries planar.

The loading sequences are as follows : (i) during $\Delta \tilde{t}_1 = 1 \times 10^{-2}$, there is no load applied. (ii) Then the imposed average shear strain $\langle \epsilon_{12} \rangle$ is increased linearly during $\Delta \tilde{t}_2 = 1 \times 10^{-1}$, up to some prescribed homogeneous shear E_{12} . (iii) This shear is sustained for a duration sufficient for the system to achieve an equilibrium state (under load). The loading sequences are shown in the inset of Fig. 3.2 with stage (ii) differentiated with the grey vertical slab.

3.3.3 Results

Three finite element simulations have been performed. First, a reference calculation discarding mechanics was performed. Then, two other calculations have been performed by mechanical loading for $\Delta \tilde{t}_2 = 1 \times 10^{-1}$ up to $E_{12} = 1 \times 10^{-2}$ (shear rate $\langle \dot{\tilde{\epsilon}}_{12} \rangle = 1 \times 10^{-1}$), considering an elastic behavior for both matrix and precipitate phases for the first case and an ideal isotropic plasticity in β matrix for the second.

The time evolution of the precipitate fraction and the concentration field of the α precipitate during the dissolution of the α precipitate are respectively shown in Fig. 3.2 and Fig. 3.3 for different cases.

As expected, for pure chemical calculations the precipitate remains circular during the whole dissolution with a decrease of the radius following a \sqrt{t} law at the beginning of the process. Then, dissolution stops when the equilibrium phase fraction is reached. This equilibrium given by the lever rule $f^e = \Omega + \pi \zeta^2 (1 - \Omega)$ where $\Omega = (c_\beta^0 - c_\beta^e(\tilde{R}))/\Delta c^e$ is the undersaturation accounting for the Gibbs-Thomson effect that changes the equilibrium concentrations at curved interfaces as follows $c_\beta^e(\tilde{R}) = c_\beta^e + \tilde{\Lambda}/(\tilde{R}\Delta c^e)$. Hence, considering the average concentration and the final radius, the precipitate volume fraction at equilibrium is $f_\alpha = 0.38$ (upper horizontal dashed line in Fig. 3.2).

For the calculation where both phases are elastic, the precipitate dissolves totally during the loading stage (ii), as shown in Figs. 3.2 and 3.3a-d (middle column). The precipitate displays rapidly a nut shape with symmetry axes corresponding to the diagonals of the square system, with the long (resp. short) axis along the upper (resp. lower) diagonal. Indeed, as shown in Fig. 3.4, the aspect ratio l/L (short over long) of the precipitate decreases when the imposed shear strain increases linearly during the loading step. When the load is sustained, the precipitate size is sufficiently small so that the minimization of the interface energy drives the dissolution process : the aspect ratio tends to increase sharply until complete disappearance of the precipitate.

Contrary to the elastic case, the precipitate in a matrix with plastic relaxation does not dissolve totally and reaches stable size and shape on a time scale similar to the chemical case. As shown

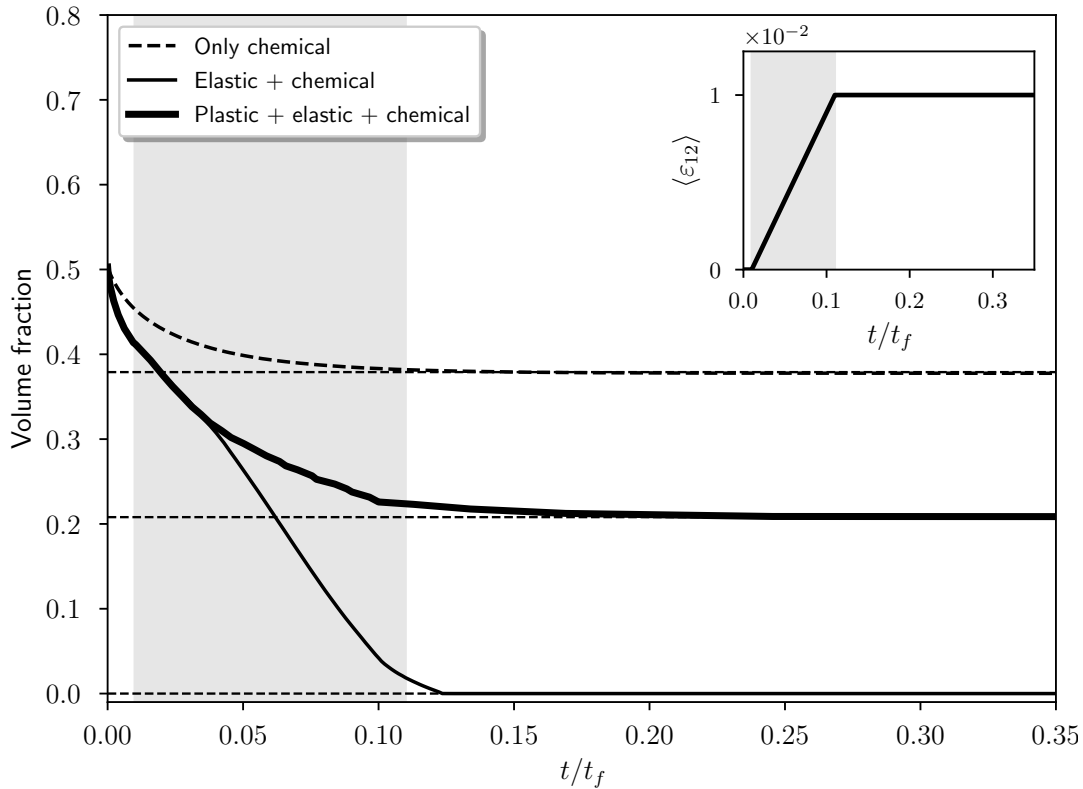


FIGURE 3.2 – Precipitate fraction vs time for chemical (dashed line), elastic (thin continuous line) and plastic (thick continuous line) cases. Inset shows the average shear strain loading sequence.

in Fig. 3.2, the dissolution rate is the same as in the elastic case at the beginning of the loading. Then, a deviation between both cases is observed at the middle of stage (ii). This difference in the evolutions is also clearly visible in Fig. 3.3 when comparing snapshots of the microstructure at same times. Starting from the same initial precipitate (top row), the shapes are already different (second row) at the middle of the loading stage (ii), i.e. at the onset of the deviation between the phase fraction curves ($\tilde{t} = 0.04$): whereas the precipitate becomes elliptical in the elastic case, it displays a lemon shape with flat sides connected by curved segments along the diagonals. It can also be noticed that the concentration fields in α and β phases are more heterogeneous when plastic relaxation is accounted for in β . At the end of the loading stage (ii), the shapes in both cases display sharper tips along the upper diagonal (third row), with a thinner and shorter precipitate in the elastic case, in agreement with the phase fraction (Fig. 3.2). In both cases, the precipitates are homogeneous in concentration when the β matrices are still heterogeneous. Finally, at the end of stage (iii), when the precipitate has already disappeared in the elastic case, the precipitate has kept the shape achieved at the end of stage (ii) with a smaller size in the plastic case. It is worth stressing that the concentration fields are homogeneous in both phases, indicating that chemical equilibrium has been achieved. Moreover, in the plastic case, the aspect ratio l/L in Fig. 3.4 decreases almost linearly with time during the loading stage (ii), before stopping around 0.58 with a very slow evolution towards the equilibrium value ≈ 0.55 .

For the plastic case, we have plotted in Fig. 3.5 snapshots of the cumulative plastic strain p as well as the hydrostatic pressure taken here as one third of the trace of the stress tensor at different times. Plastic relaxation starts in the first part of the loading stage (ii), with bands forming

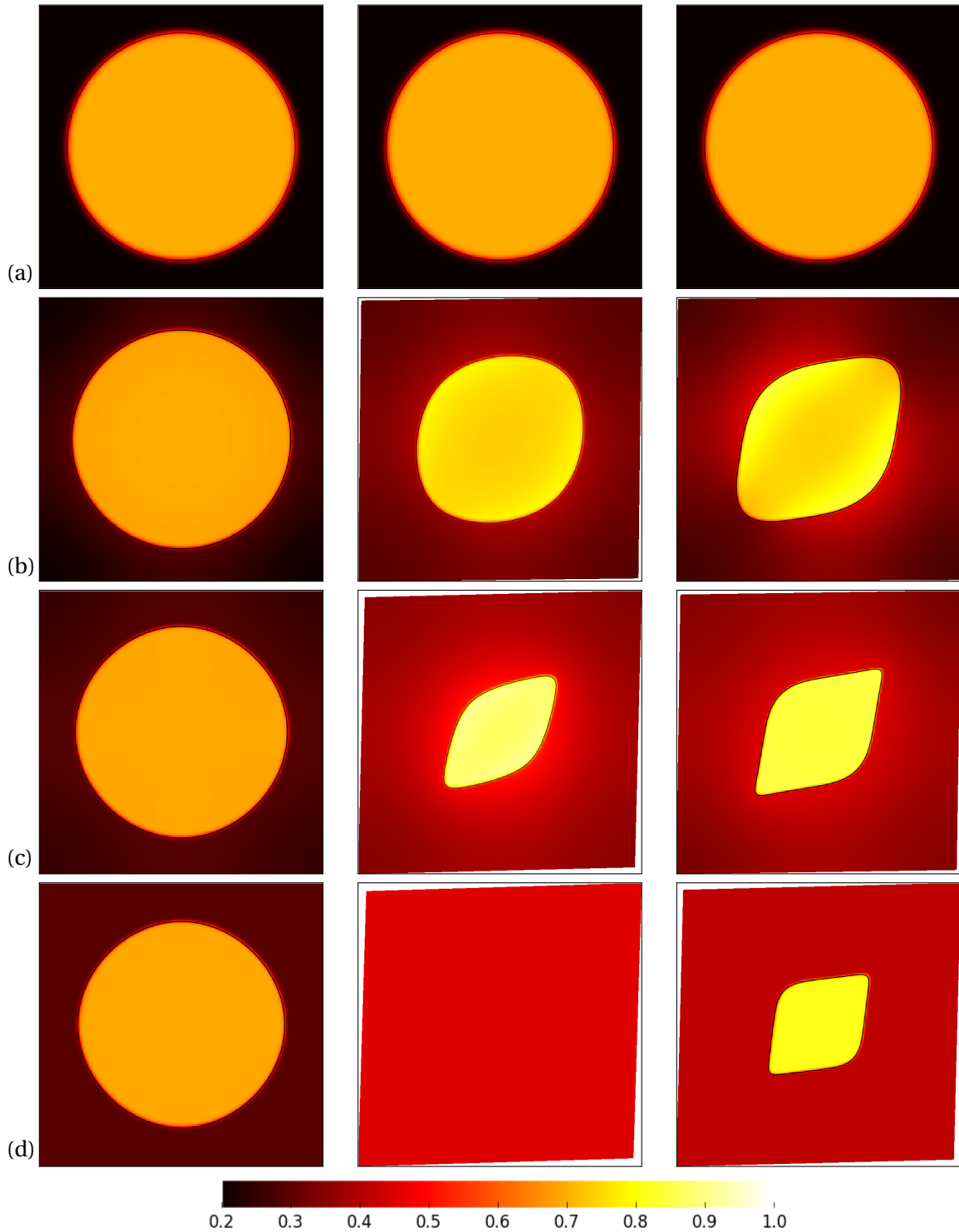


FIGURE 3.3 – Snapshots of the concentration field during the dissolution of the α precipitate in the chemical (first column), elastic (middle column) and plastic (last column) cases at (a) $\tilde{t} = 10^{-3}$, (b) $\tilde{t} = 4 \times 10^{-2}$, (c) $\tilde{t} = 10^{-1}$, and (d) $\tilde{t} = 1$; with $\tilde{t} = t/t_f$.

approximately parallel to the system boundaries, in agreement with previous works in nonlinear composites [Moulinec and Suquet, 2003, Chaboche et al., 2001]. They are more intense

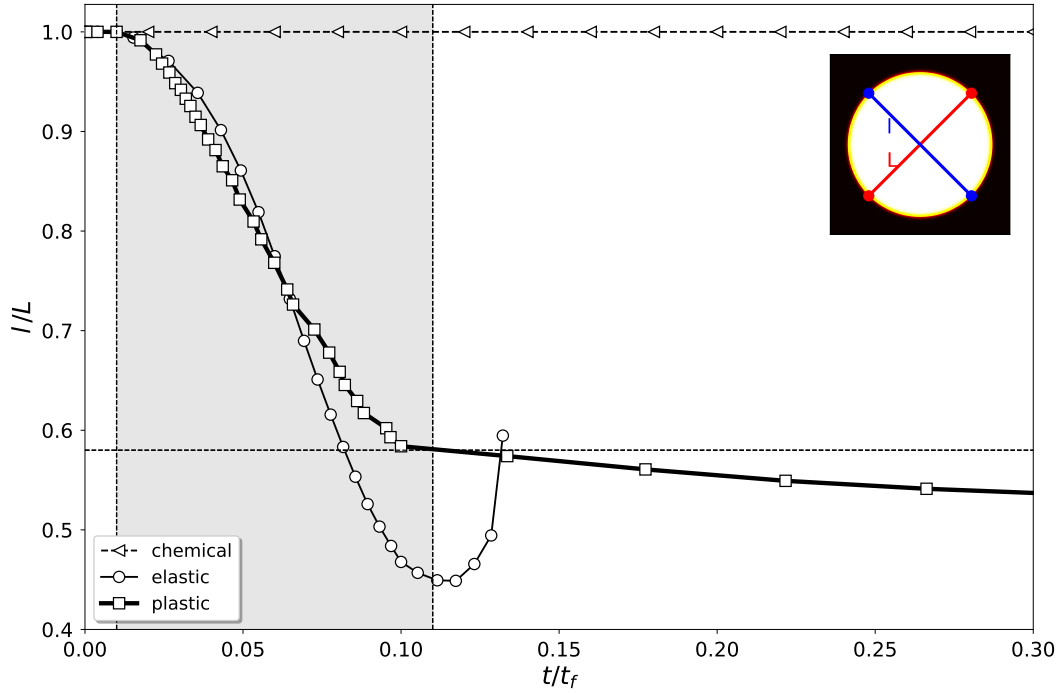


FIGURE 3.4 – Aspect ratio of the precipitate l/L vs. time for the chemical, elastic and plastic cases.

close to the precipitate tips along the upper diagonal due to the asymmetrical shape of the precipitate (Fig. 3.5b). At the end of the loading stage, the bands are thicker due to the dissolution of the precipitate, with "hot spots" where $p \approx 2\%$ along the upper diagonals. At the end of stage (iii), the four bands enclosing the precipitate are thick with large "hot spots" ($p \approx 3\%$) along the upper diagonal. During the last stage where the evolution of the precipitate is minor, small "hot spots" appear also along the lower diagonal. It is clear that the patterning of plasticity is tightly coupled to the microstructure evolution. The pressure distribution is characterised by significant but realistic values with maximal values concentrated at regions close to highly curved precipitate boundaries. These locations are correlated with intense strain localization zones.

The shape evolutions can be understood by analyzing the evolution of the concentration fields. Indeed, the local interface velocity is related to the difference of flows between α and β phases as stated by the interface solute balance :

$$\Delta c v = D(\nabla c_\beta - \nabla c_\alpha) \cdot \underline{n} \quad (3.45)$$

with all quantities considered at the α/β interface, $\Delta c = c_\alpha - c_\beta$ where \underline{n} denotes the normal vector pointing from α to β .

Hence, we have plotted the concentration profiles at different time steps in Fig. 3.6 (c to e corresponding to the loading stage (ii)), along the left and right diagonals of the system drawn respectively with red and blue lines in the upper left snapshot. The elastic and plastic cases are plotted with dashed and continuous lines respectively.

It can be noted that the concentration field becomes rapidly heterogeneous in α and β . At the beginning of the shear loading ($\bar{t} = 3.0 \times 10^{-2}$, Fig. 3.6a), the concentrations are higher than in the bulks, such that diffusion in α and β phases promotes the dissolution according to the interfacial solute balance Eq. (3.45) ($\nabla c_\alpha \cdot \underline{n} > 0$ and $\nabla c_\beta \cdot \underline{n} < 0$). The circular symmetry is slightly broken as illustrated by the differences between the left and right profiles corresponding to the

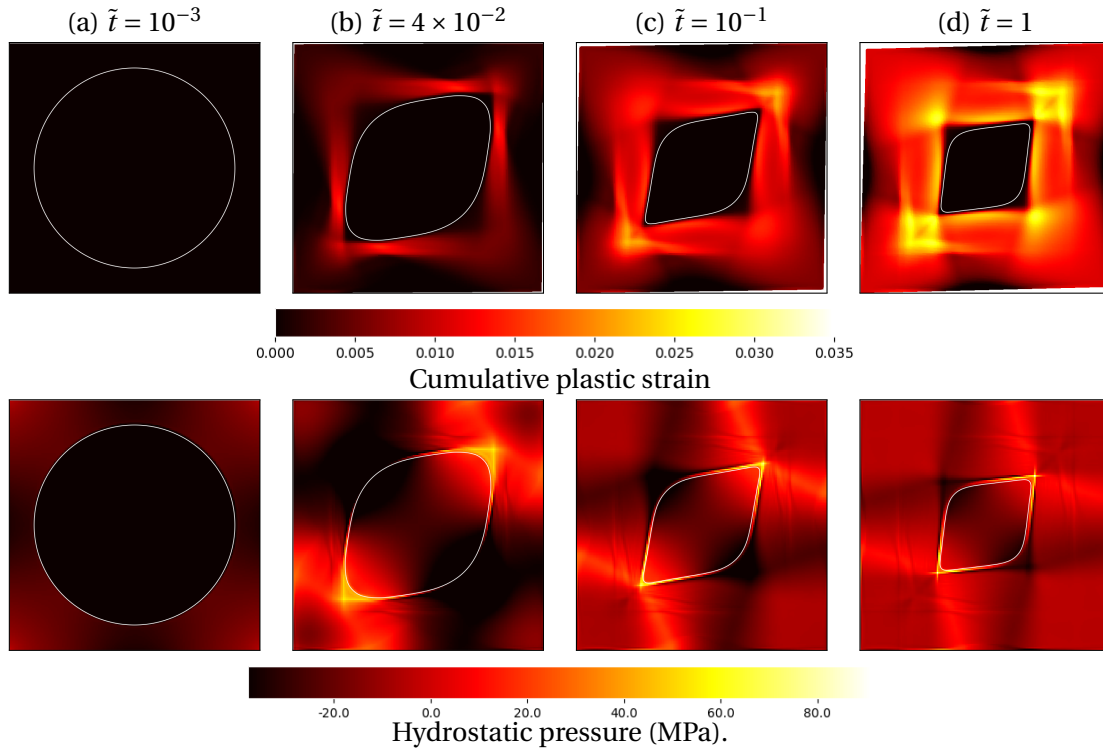


FIGURE 3.5 – Snapshots of cumulative plastic strain and hydrostatic pressure during shear loading at rate $\langle \dot{\epsilon}_{12} \rangle = 0.1$

two diagonals. The gradients are steeper along the lower diagonal (right) in agreement with the shape evolutions ensuing from a faster dissolution along this diagonal. Moreover, the plastic case is more asymmetrical than the elastic case, with slightly higher interfacial concentrations. It can also be noticed that the interface concentrations are higher than the equilibrium concentrations at flat interfaces (horizontal dashed lines at 0.3 and 0.7 for respectively β and α). Finally, due to the initial undersaturation of the β matrix, the concentration gradients are steeper in β and are likely to drive the dissolution process at this stage.

During stage (ii), elastic and plastic cases exhibit different evolutions of the concentration profiles. First, at the middle of the loading stage $\tilde{t} = 7.5 \times 10^{-2}$ (Fig. 3.6b), when the size of the precipitates are still similar, the asymmetry becomes much stronger in the plastic case. Whereas concentration gradients are still in a configuration promoting dissolution in the elastic case, the plastic case features two different behaviors depending on the diagonal. Hence, along the upper diagonal, one can observe the inversion of ∇c_α (i.e. $\nabla c_\alpha \cdot \underline{n} < 0$) and the drastic lowering of $|\nabla c_\beta|$. Quantitatively, $(\nabla c_\beta - \nabla c_\alpha) \cdot \underline{n} \approx 0$ such that the interface along the upper diagonal does not migrate any longer. On the contrary, the profiles along the lower diagonal remain favorable to the dissolution with $\nabla c_\alpha \cdot \underline{n} > 0$ and $\nabla c_\beta \cdot \underline{n} < 0$. As the shear load increases (Fig. 3.6c-e, in the elastic case, the concentration in the α precipitate increases continuously as well as the interface concentration in β . Consequently, the gradients increase such that the dissolution rate increases with time to end up with the total disappearance of the precipitate at the end of stage (ii). In the plastic case, the asymmetry between the profiles along the diagonal decreases during stage (ii). When the profile evolves only slowly and slightly along the upper diagonal, so that the interface migration is negligible, the profiles become flatter along the lower diagonal with an enrichment of the β matrix, so that dissolution along this diagonal slows down progressively. At the end of stage (iii), the profiles in the plastic case are flat in the bulks with concentrations higher than the equilibrium concentrations for flat interfaces (Fig. 3.6e).

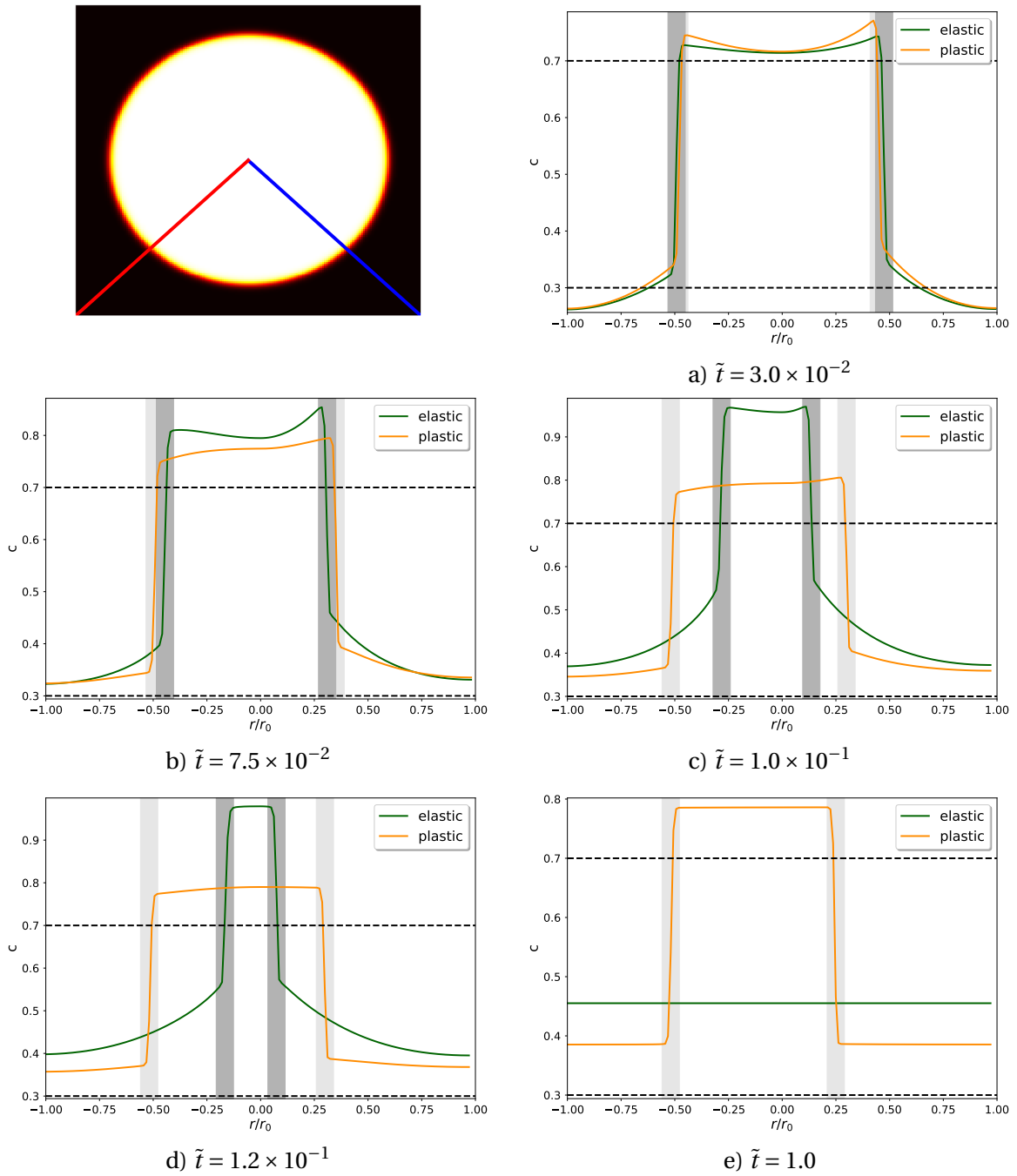


FIGURE 3.6 – Concentration profiles along the left and right diagonals at different time steps in the elastic (dashed line) and plastic (continuous line) cases. The plot axis is drawn in the upper left snapshot by the red and blue lines, respectively for left and right diagonals. Equilibrium concentrations $c_{\alpha}^e = 0.7$ and $c_{\beta}^e = 0.3$ of flat interfaces are plotted with dashed horizontal lines.

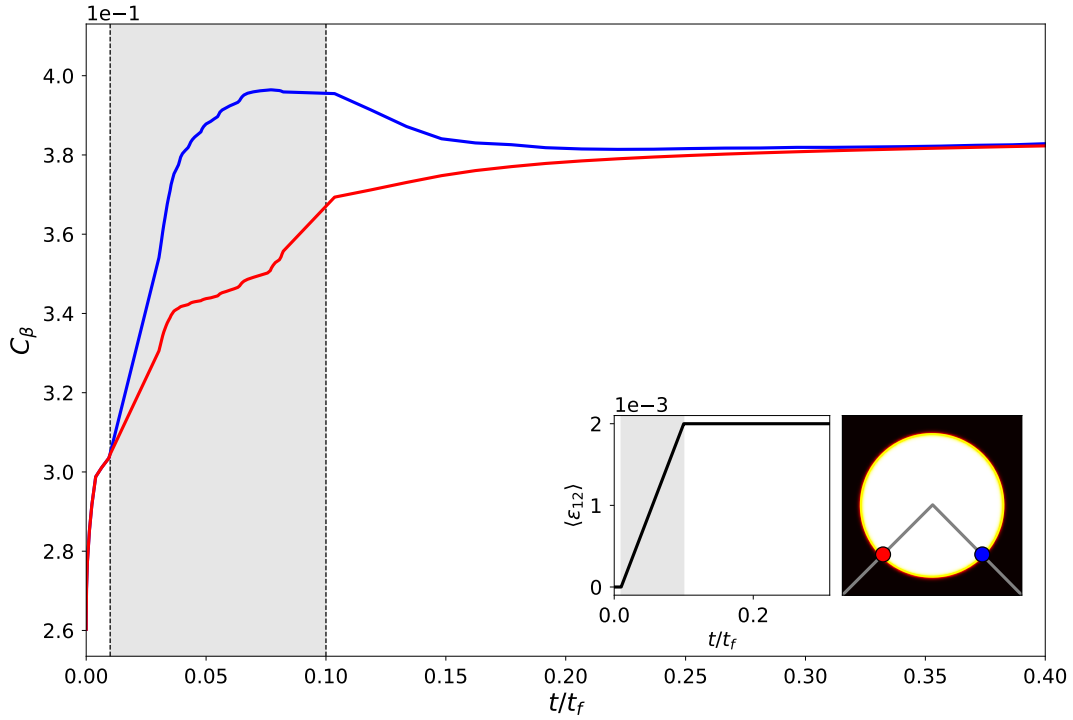


FIGURE 3.7 – Time evolution of the concentrations in β at the interfaces crossing respectively the left (blue) and right (red) diagonals, in the plastic case.

The previous analysis suggests that the interfacial concentrations are a key parameter controlling the shape evolutions through the concentration fields. Indeed, we have mentioned that the amplitude and sign of the solute flows are driven by the evolution of these concentrations. Thus, we have determined the interfacial concentrations by extrapolating the bulk profiles (typically close to $\phi = 0.05$ or 0.95) into the diffuse interface and extracting the values at $\varphi = 0.5$.

We have plotted in Fig. 3.7 the concentration in β at the interfaces crossing the upper (red) and lower (blue) diagonals respectively, in the plastic case. It must be stressed that the small irregularities observed in the curves should be attributed to some numerical problems but rather to the sensitivity of the extraction method to the order and support of the extrapolation from the bulks. After a transient regime, shorter than $\tilde{t} = 10^{-2}$ during the load free stage (i), the interface concentration reaches its equilibrium value accounting for the Gibbs-Thomson effect, i.e. with a value slightly above 0.3 increasing with the local curvature. When the shear load is applied, the concentrations at the two different interfaces increase with different rates that do not involve only the change in local curvatures. Indeed, whereas the interface crossing the lower diagonal is flatter than the interface crossing the upper diagonal (Fig. 3.3b last column), its concentration increases the fastest. When the concentration of the sharper tips (red) with the slow migration rate increases continuously, with a sudden deceleration around $\tilde{t} \approx 0.04$, the evolution of the concentration on the flatter sides (blue) displays a maximum by the end of stage (ii). Then, during stage (iii) the concentrations at both interfaces converge slowly towards the same value of about 0.38.

To understand these evolutions, we have proceeded as in [Ammar et al., 2014, Cottura et al., 2015a] by comparing the interfacial concentrations with their expressions at a sharp interface in local equilibrium, accounting for mechanics. Following [Voorhees and Johnson, 2004], these concentrations can be obtained using the equilibrium conditions holding at a coherent sharp

interface :

$$\Delta\mu = 0 \quad (3.46)$$

$$\Delta\omega = E^{\text{coh}} - \Lambda\kappa \quad (3.47)$$

where Δ denotes as previously the difference between the α and β sides of the interface (i.e. $\Delta A = A^\alpha - A^\beta$ for any A), $\mu = \partial f / \partial c$ the diffusion potential, $\omega = f - \mu c$ the grand potential, κ the local curvature (positive for convex α), and $E^{\text{coh}} = \sigma_\beta : \Delta\varepsilon$ the coherence energy, representing the elastic energy necessary to keep both lattices coherent across the interface [Larché and Cahn, 1973, Johnson and Alexander, 1986]. It is worth noting that Eqs. (3.46)-(3.47) reduce to the usual equality of the chemical potentials between both phases when elasticity and curvature can be neglected.

As introduced in the phase field model Section 3.2.1.1, the free energy densities f can be split into chemical and elastic contributions. Because it is assumed that the elastic energy does not depend on c , the diffusion potentials are independent of stress and the grand potential can be rewritten as $\omega = f^{\text{ch}} + f^e - \mu c$. Then, expanding Eqs. (3.46)-(3.47) to first order in c with respect to the chemical equilibrium holding at flat interfaces (where the right-hand side of Eq. (3.47) is null), one obtains :

$$\Delta \left(\frac{\partial \mu_{\text{ch}}}{\partial c} (c - c^e) \right) = 0 \quad (3.48)$$

$$\Delta \left(-c^e \frac{\partial \mu_{\text{ch}}}{\partial c} (c - c^e) + f^e \right) = E^{\text{coh}} - \Lambda\kappa \quad (3.49)$$

Using the fact that the curvatures of f with respect to c (i.e. $\partial \mu_{\text{ch}} / \partial c$) are the same for α and β , Eqs. (3.48)-(3.49) become :

$$c_\alpha^e - c_\beta^e = \Delta c^e \quad (3.50)$$

$$c_\psi - c_\psi^e = \frac{\tilde{\mathcal{E}} + \tilde{\Lambda}\tilde{\kappa}}{\Delta c^e} \quad \forall \psi \in \{\alpha, \beta\} \quad (3.51)$$

where the non-dimensional mechanical contribution to the change in the interfacial concentrations reads :

$$\tilde{\mathcal{E}} = \frac{\Delta f^e - E^{\text{coh}}}{k} \quad (3.52)$$

We have shown in [Ammar et al., 2011] that this expression still holds when plastic strain is accounted for, and that plastic strain directly contributes to the change in the local equilibrium through the jump of strain $\Delta\varepsilon$ across the interface. It must be emphasized that the presence of the coherency term discard any simple explanations based only on the distribution of the elastic energy density.

Following the same procedure as for the interfacial concentrations, we have extrapolated all the quantities involved in Eq. (3.52) in the bulks near the interface up to $\phi = 0.5$, namely Δf^e and E^{coh} to determine the evolution of the mechanical contribution $\tilde{\mathcal{E}}$. In this way, we have checked that the evolution of the interfacial concentrations (Fig. 3.7) can be explained by the modification of the local equilibrium by elasto-visco-plasticity. Although the extraction method of the interfacial quantities is not robust enough to verify precisely Eq. (3.51), we have checked that the order of magnitude of the variations are consistent with this expression. Figure 3.8 shows the evolution with respect to time of the two contributions f^e/k and E^{coh}/k in insets as well as the resulting $\tilde{\mathcal{E}}$. First, it can be noticed that the variations of the coherence energy are larger than the variations of the jump in elastic energy. Moreover, the coherence energy is almost

always negative, thus contributing positively to the mechanical term $\tilde{\mathcal{E}}$ (Eq. 3.52). Second, two very different behaviors are observed at the two kinds of interfaces, crossing the upper (red) and lower (blue) diagonals, corresponding respectively to the tips and to the rounded sides (Fig. 3.3 last column). At the "red" interface, both Δf^e and E^{coh} evolve in the same direction during the loading stage (ii), with a first increase from negative values to positive ones, followed by large drops to negative values. Consequently, the evolution of $\tilde{\mathcal{E}}$ displays two steps during stage (ii) : a first drop to around zero when plastic "hot spots" are not visible yet ahead of the tips (Fig. 3.5b), followed by a large increase when the "hot spots" intensify (Fig. 3.5c). Hence, these two steps can explain the evolution of the interfacial concentration. When $\tilde{t} \lesssim 0.04$, the increase of c_β can be attributed to the combined effect of $\tilde{\mathcal{E}}$ and curvature with the appearance of the nut shape with tips along the upper diagonal (Fig. 3.5b). Then the sudden slowdown is likely due to $\tilde{\mathcal{E}} < 0$ that cancels the curvature term although the tips sharpen significantly (Fig. 3.5c). Finally, when $\tilde{\mathcal{E}}$ has increased again sufficiently, it takes over and the increase of c_β accelerates again. During stage (iii), all contributions evolve only slightly and slowly. It can be observed that the tips do not sharpen any longer and the slight increase of the interface concentrations can be attributed to the slight plastic relaxation at constant shear load. At the "blue" interface, the coherence energy E_{coh} remains negative and always overcomes the jump in elastic energy density Δf^e . This is why the evolution of $\tilde{\mathcal{E}}$ follows mainly that of $-E_{\text{coh}}$, with a steep increase in the first half of stage (ii), followed by a progressive slowdown. Finally, during stage (iii) all evolutions are slow and moderate resulting in a slight decrease of $\tilde{\mathcal{E}}$. As for the "red" interface, the overall evolution of $\tilde{\mathcal{E}}$ can explain the evolution of c_β : a steep increase at the beginning of stage (ii), followed by a slight decrease during stage (iii), although the max of c_β is achieved before the end of stage (ii) whereas $\tilde{\mathcal{E}}$ is maximal at the transition between stages (ii) and (iii). In conclusion, this analysis has shown that the two different dissolution rates along the upper and lower diagonals result from the particular pattern of plastic strain : the plastic case is not a tempered elastic case, but plastic relaxation plays a significant role in the morphological evolution of the precipitates in the particular situation investigated.

Finally, the previous calculations may give clues about what can happen in adiabatic shear bands in Ti forged parts where globular precipitates are observed to be much smaller than in other parts. Indeed, they are usually attributed to either the complete dissolution followed by nucleation of new small precipitates on defects, or the splitting of surviving precipitates. Nonetheless, the splitting process is never explained and it is not clear how dissolution and mechanics interact.

Using the previous calculation accounting for plasticity as a reference, we have considered higher loading rates and a higher sustained shear (thereafter, referred to as cases 1 and 2 respectively) :

- $\langle \dot{\tilde{\epsilon}}_{12} \rangle = 1$ during $\Delta \tilde{t}_2 = 10^{-2}$ up to $E_{12} = 10^{-2}$;
- $\langle \dot{\tilde{\epsilon}}_{12} \rangle = 10$ during $\Delta \tilde{t}_2 = 10^{-3}$ up to $E_{12} = 10^{-2}$.

Indeed, we can expect that increasing the shear magnitude will enhance dissolution, and that increasing the shear rates, the time scale of mechanics will compete with the time scale of diffusion.

In Fig. 3.9, we have plotted snapshots of concentration and accumulated plastic strain during the dissolution, for the first rate $\langle \dot{\tilde{\epsilon}}_{12} \rangle = 1$. Because the loading rate is larger than in the reference case, the second snapshot at $\tilde{t} = 0.015$ is already in stage (iii). This second snapshot exhibits the same shape evolution as in the reference case, the precipitate adopting a lemon shape with tips along the upper diagonal. The overall pattern of cumulative plastic strain is similar to the reference case, with two sets of bands aligned with the system boundaries and more intense close to the tips. Due to the higher sustained shear load, p reaches higher values with respect to Fig. 3.5. Contrary to the reference case, p extends also off the horizontal and vertical bands,

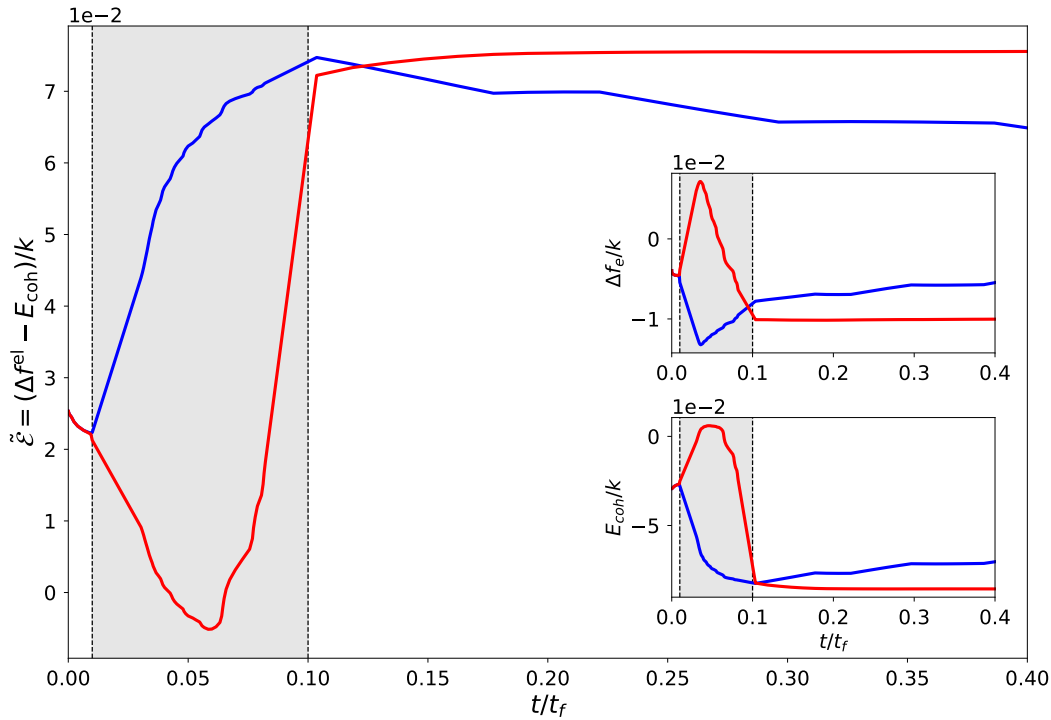


FIGURE 3.8 – Time evolution of the mechanical energy contribution to the interfacial local equilibrium at interfaces crossing respectively the left (blue) and right (red) diagonals (see inset in Fig. 3.7), in the plastic case.

along the two diagonals in the matrix. At the same time, the heterogeneity in concentration is more pronounced with rich regions close to the interfaces oriented in the same direction as the upper diagonal. Nonetheless, comparing Fig. 3.9b and Fig. 3.3b (last column), the difference seems only to be quantitative rather than qualitative. This is why, the elongated shape at $\tilde{t} = 0.1$ can appear as unexpected. In fact, this shape results from the same differentiated dissolution as in the reference case, i.e. fast dissolution along the lower diagonal and pinning of the interfaces along the upper diagonal by the particular configuration of solute profiles. Plastic patterning remains qualitatively similar to earlier times, with bands slightly thicker and more intense. Then, the dissolution continues along the lower diagonal only so that the precipitate pinches off (Fig. 3.9c) to finally split into two precipitates (Fig. 3.9d). It is worth noticing that the pattern of cumulative plastic strain remains almost the same during this process ($\tilde{t} \geq 0.1$): the size of the square with no plastic strain is related to the most distant interfaces along the upper diagonal. Nonetheless, very thin plastic bands can be observed at the center of the system.

The evolution of the microstructure during the second intense shear loading with the fastest rate $\langle \tilde{\epsilon}_{12} \rangle = 10$ is plotted in Fig. 3.10. In this case, the shape at $\tilde{t} = 0.015$ is different from the previous cases. Smooth corners, visible at about 30° from the upper diagonal, separate the interface into two parts: segments with normal vectors closer to the lower diagonal with large solute gradients; segments with normal vectors closer to the upper diagonal with vanishing solute gradients. The corresponding cumulative plastic strain displays a pattern similar to case 1, with more intense values and additional bands at 45° . As shown in Fig. 3.9c, contrary to case 1, dissolution is not the fastest along the lower diagonal but next to the smooth corners. This process results in splitting the initial precipitate into three parts. The precipitate at the center features a shape reminiscent of the reference case. It displays a very high concentration and is

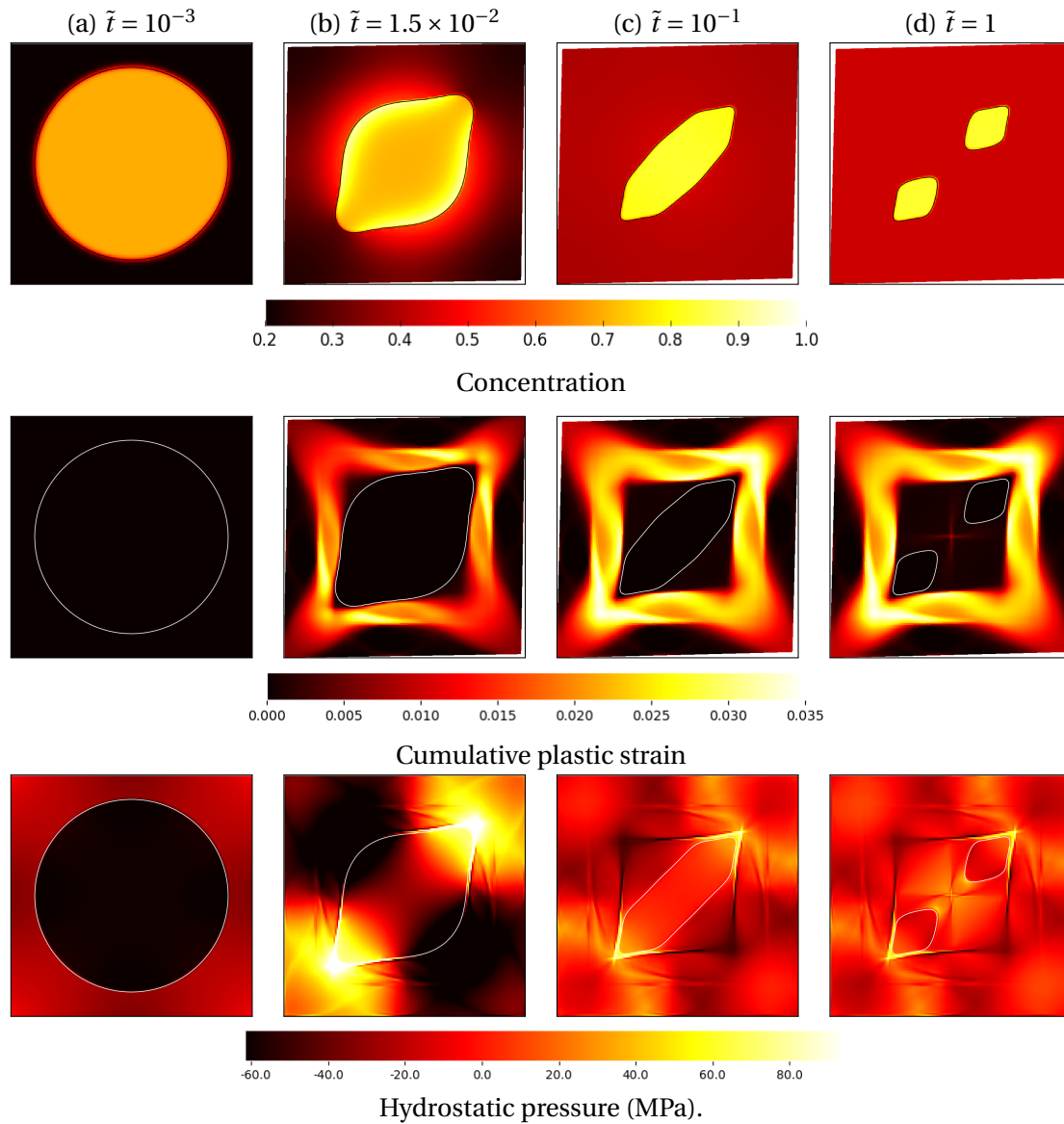


FIGURE 3.9 – Snapshots of concentration, cumulative plastic strain and hydrostatic pressure during intense shear loading at rate $\langle \dot{\epsilon}_{12} \rangle = 1$.

surrounded by an enriched zone coming from the fast dissolution process, that will drive its complete dissolution. The two other precipitates display asymmetrical shapes with the longest axis along the lower diagonal. The configuration of the solute field in the matrix with almost no gradient oriented normal to their interfaces explains why they will survive (Fig. 3.9d). The complete dissolution of the central precipitate is fast so that only thin and slight plastic bands enclosing it have time to develop.

To understand why increasing the shear load and the shear rate promotes the splitting of precipitates, it is important to have in mind the analysis based on the solute balance Eq. (3.45) and the local equilibrium condition Eqs. (3.51)-(3.52).

- First, increasing the shear load increases locally the concentration at the interfaces making significant angles with the lower diagonal, but does not change the situation at the interfaces crossing the upper diagonal. Indeed, the pattern of plastic relaxation remains qualitatively the same with a major localization along the upper diagonal, responsible for

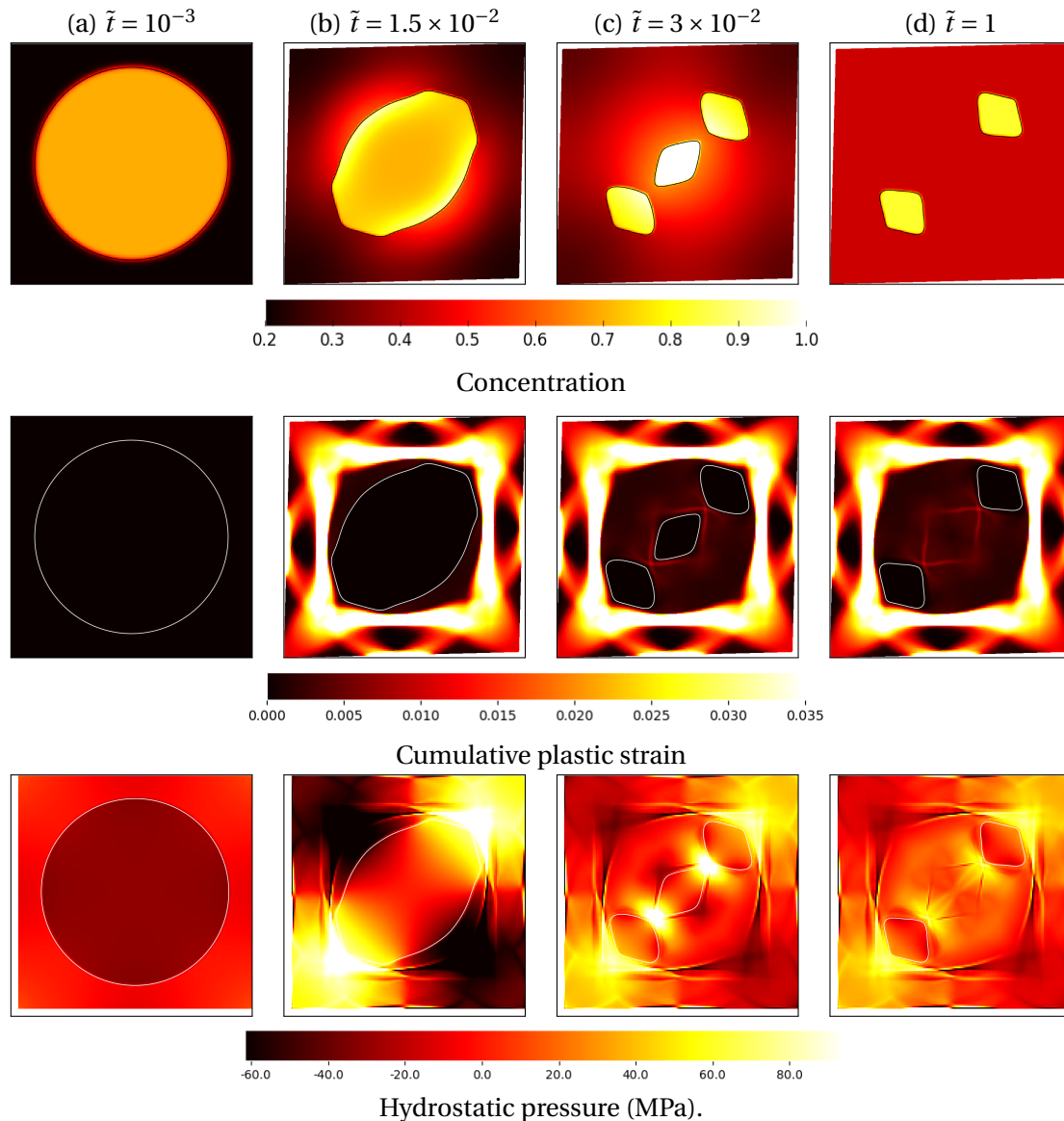


FIGURE 3.10 – Snapshots of concentration, cumulative plastic strain and hydrostatic pressure during intense shear loading at rate $\langle \dot{\epsilon}_{12} \rangle = 10$.

the pinning of the neighboring interfaces. Thus, the differential dissolution is not changed with respect to the reference case.

- Second, increasing sufficiently the shear rate implies that diffusion becomes too slow to mitigate the concentration gradients enhanced by the change in the interfacial concentrations. Hence, contrary to the reference case, dissolution in the direction of the lower diagonal can proceed to completion and splits the precipitate.

With these calculations, we have shown that the production of small precipitates from large ones is possible by plasticity-assisted dissolution provided that the ratio of the loading time scale over the diffusion time scale is lowered. The precise value of the critical ratio beyond which splitting is possible has not been determined because it is very dependent on the configuration considered. Further work is obviously needed to obtain more quantitative information, in particular by considering 3D, different spatial distributions and more complex loadings. Moreover, it is likely that work-hardening, plasticity within the precipitates, and anisotropy as-

sociated with crystal plasticity, which were not considered in the present work, will definitely play a role. These considerations also bring the question of inheritance of plastic activity and dislocation hardening. Indeed, in the case of growth some aspects of this question have been addressed in [Ammar et al., 2014] and have been shown to change the morphological evolutions.

3.3.4 Conclusion

We have investigated the influence of plasticity on the dissolution of precipitates at high temperatures in the case of shear loading. We have shown that plasticity is able to stabilize precipitates that dissolve completely when only elasticity is accounted for. Moreover, we have deeply investigated the process giving rise to the nut shapes, whose symmetry reflects those of the precipitate arrangement and loading. In particular, we have demonstrated that plasticity modifies the local equilibrium at the interface and consequently the local dissolution rate. In the investigated configuration, strong localization of plastic strain in the matrix tends to pin the neighboring interface so that the initial circular symmetry is broken. It remains to analyse more in detail the relative contributions of various terms in the driving force responsible for precipitate evolution. They include the impact of heterogeneous elasticity, of phase transformation eigenstrain and of plastic eigenstrain tensors. Preliminary calculations have shown that different non isotropic shapes can be obtained depending on these different contributions to the driving force.

Finally, we have studied intense and rapid shear loadings. When diffusion is not sufficiently fast to homogenize the concentration field generated by the change in interfacial concentrations associated with mechanics, dissolution that proceeds at different rates along the interface leads to the splitting of the initial precipitate into several ones. Hence, our work may give clues about the process explaining the presence of small precipitates in adiabatic shear bands in forged parts in titanium alloys, although further work is needed to obtain more quantitative predictions.

3.4 Inheritance of plastic deformation during migration of phase boundaries

3.4.1 Introduction

The choice of the mixture rule has a significant influence on the behaviour of the diffuse interfaces, as recently discussed in [Ammar et al., 2009c, Durga et al., 2013]. The question then arises of the evolution of plasticity-related variables at a material point after the passing of a phase transformation front. The question of inheritance of plastic deformation and hardening existing prior to phase transformation has already been addressed, although insufficiently, from the experimental perspective, for instance in the context of thermomechanical treatments [Greenberg et al., 2001] or the behaviour of TRIP steels [Kouznetsova and Geers, 2007]. But the question is largely open from the modelling point of view in the context of phase field approaches, despite preliminary attempts e.g. [Kundin et al., 2011, Abrivard et al., 2012b, Abrivard et al., 2012a].

The question of inheritance of internal variables associated with plastic deformation when an interface sweeps a plasticized zone of bulk phase, during migration of phase boundaries has not been discussed in most existing phase field models involving nonlinear material behaviour.

The inheritance is likely to depend on the nature of the interface, but the question : “Does coherent and incoherent interface motion favor recovery of the hardening of the mother phase?” has no obvious answer, and will deserve a particular attention in the model development in order to reach realistic comparison with experimental results. Indeed, it is essential to know if the newly formed phase inherits all or part of the plastic strain or strain hardening of the parent phase, in order to predict the existence of residual stresses by structural calculations for instance.

It is first necessary to distinguish the question of inheritance of plastic deformation from that of strain hardening. Plastic deformation is associated with the motion of dislocations that do not necessarily stay in the material volume element and lead to a change of the local reference configuration for the calculation of elastic stresses. In contrast hardening is accompanied by the storage of dislocations that can be destroyed by the passing of a phase boundary or that can leave debris contributing to the hardening of the new phase. Alternatively, dislocations may be repelled by the moving interface. The mentioned previous references deal with the question of inheritance of strain hardening, i.e. of dislocation structures. In contrast, the question of inheritance of plastic deformation itself has not been addressed yet in the context of the recent advanced phase field models. The present work is limited to the consideration of this question, leaving the consideration of inheritance of strain hardening to future work. That is why the analysis is performed in the absence of hardening in the constitutive model.

The objective of this section is to investigate the properties of existing phase field models with respect to the question of inheritance of plastic deformation during phase transformation. It will turn out that both classes of phase field models, which are the interpolation and homogenisation models, display strongly different plastic strain inheritance behaviours. The development of plastic deformation in the mother phase can be due to prior mechanical loading of the material or to local stresses induced by the misfit strain accompanying the motion of the phase transformation front. Inheritance can be total, partial or absent if the plastic strain tensor at the material point after the passing of the transformation front, is equal to that of the mother phase at that particular point, a portion of it or simply vanishing, respectively. In the case of total or partial inheritance the plastic residual shape of the structure is left totally or partially unchanged after the passing of a moving phase boundary. The objective is then to study the impact of the choice of interpolation schemes on the inheritance of plastic deformation during phase transformation, depending on the particular class of phase field models. The

analysis is limited to the small deformation framework for the sake of simplicity.

In order to illustrate the inheritance behaviour of each class of models, Two simple situations are then considered in this section, defined by the growth of elastic misfitting precipitates embedded in a rate-independent elastoplastic matrix material, described by associated von Mises plasticity in the absence of hardening. For the same intrinsic nonlinear behaviour of individual phases, the concentration, plastic strain and stress fields will be shown to differ after precipitate growth depending on the phase field formulation. In fact, Finite element simulations reveal that the interpolation model allows for total inheritance of plastic deformation in contrast to the homogenisation model. The residual stress field and the growth kinetics are shown to be impacted by this essential property of the models. The results suggest that new models should be designed that allow for partial and controlled inheritance. The analysis is performed in the absence of hardening in the constitutive model.

3.4.2 Parameters and conditions for FE calculations

The two presented phase field approaches, namely the interpolation and homogenisation models, have been applied to study the mechanical effect on the diffusion-controlled growth of α -precipitates embedded in a supersaturated β -matrix phase. The particles and matrix are separated by a coherent diffuse interface endowed with the constitutive properties described in the previous sections. The case of a single spherical precipitate is considered first, before studying the coalescence of a collection of initially circular precipitates. Internal stresses are generated by the transformation eigenstrains. To ease the interpretation of the results, the α phase displays a purely elastic behaviour whereas the β phase is assumed to be elastic-perfectly plastic with a yield stress R_β^0 . Homogeneous isothermal isotropic mechanical behaviour is considered for both phases.

The previous models have been implemented into the finite element code Z-set [Z-set package, 2013]. The variational formulation corresponding to the field equations (3.42, 3.43 and 3.44) and the implicit resolution schemes based on a monolithic framework are described in [Ammar et al., 2009c, Ammar et al., 2011].

All chemical and mechanical material data values are dimensionless and scaled with the chemical free energy curvature, which is chosen to be the same for both phases ($k_\alpha = k_\beta = k$), a mesoscopic system length r_0 , where r_0 is the initial radius of the precipitates, and the characteristic time $\tau = 1/Mk$. Identical chemical diffusivities $D_{\alpha,\beta}$ are assumed in the two phases. They are taken such that $D\tau/r_0^2 = 1 \cdot 10^{-4}$. The interfacial energy is isotropic, $\Lambda/(kr_0) = 5 \cdot 10^{-3}$. The corresponding interface thickness has been chosen to be about 0.5% of the total size of the system $\delta/r_0 = 0.25$. The equilibrium concentrations at incoherent state for both phases are $a_\alpha = 0.7$ and $a_\beta = 0.3$. Both phases possess the same isotropic normalized elastic moduli, corresponding to a Young modulus $E/k = 7 \cdot 10^{10}$ and a Poisson ratio $\nu = 0.3$. For the sake of simplicity, the eigenstrains in both phases are spherical tensors independent of concentration. Taking the β phase as the stress free reference state ($\boldsymbol{\varepsilon}_\beta^* = \mathbf{0}$), the eigenstrain in the α phase is a spherical tensor ($\boldsymbol{\varepsilon}_\alpha^* = \varepsilon_\alpha^* \mathbf{1} = 6 \cdot 10^{-4} \mathbf{1}$).

The normalized yield stress for the β phase is $R_\beta^0/k = 12$.

Circular nuclei of α phase are introduced in the β -matrix as initial conditions for the phase field ϕ . The initial condition for the concentration field is a uniform equilibrium value of c_α in the nuclei and the precipitate grows under a matrix supersaturation ($c_\beta^\infty - c_\beta^{int}$). Neglecting effects of interfacial curvature and in complete absence of stress field, the interfacial concentrations c_α^{int} and c_β^{int} correspond to the equilibrium concentrations for the specified phase obtained from the phase diagram. A typical composition profile is shown schematically in Figure 3.11 for the single precipitate studied in the next section.

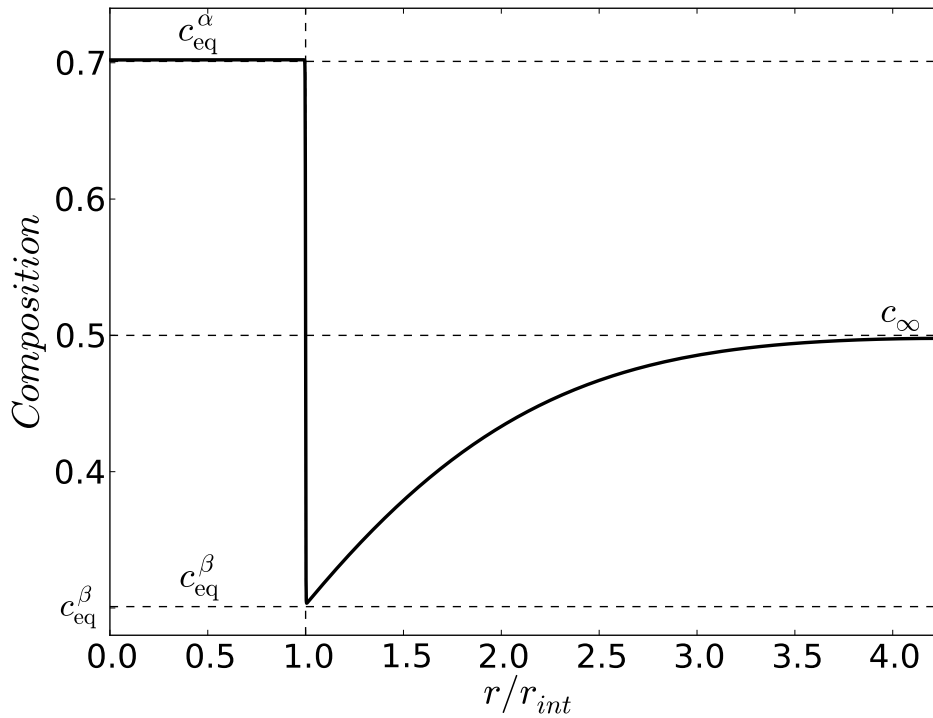


FIGURE 3.11 – Schematic illustration of the composition profile at a given time associated with the growth of an isolated coherent precipitate into a supersaturated matrix. The matrix/precipitate interface lies at $r/r_{int} = 1$, r_{int} being the current position of the interface.

The concentration field within the matrix is given in [Bourne et al., 1994], verifying the following interface/boundary conditions for the composition field :

$$\begin{aligned} c_{\beta} &= c_{\beta}^{int} & \text{when} & \quad x = x_{int}^{+} \\ c_{\beta} &= c_{\infty} & \text{when} & \quad x \rightarrow \infty \end{aligned} \quad (3.53)$$

c_{β}^{∞} is the far-field matrix concentration, which is assumed to be independent of time in the case of the isolated precipitate.

3.4.3 Results

3.4.3.1 Growth of a spherical precipitate

In this section, the case of an isolated misfitting spherical precipitate in a supersaturated matrix is chosen in order to compare the proposed phase field mechanical models and examine the stored mechanical energy effect on the interfacial compositions and the diffusion-controlled growth. Interfacial conditions for mechanical equilibrium in two-phase crystals separated by a curved interface are deduced.

The geometry of the problem is that of two concentric spheres, the central one delimiting the α precipitate, the outer one corresponding to the outer surface of the β matrix. The computation is made by means of axisymmetric finite elements with a finite element mesh corresponding to one sector $0 \leq \theta \leq \theta_0 = 10^{\circ}$. The initial spherical nucleus has a radius r_0 whereas the outer boundary of the matrix is at $r = R$. The finite element mesh is composed of linear 4-node axisymmetric quadrangular elements.

Profiles of ϕ and c as tanh functions along one direction have been set initially, which correspond to coexistence of an initial misfitting spherical precipitate of initial radius $r_0/R = 0.02$, and a β matrix of outer radius R and separated by a curved diffuse interface with a thickness roughly equal to δ . Let us call \mathcal{S} the union of the surfaces $r = R$, $\theta = 0$ and $\theta = \theta_0$. The following boundary conditions have been applied to the system :

$$\begin{aligned} \underline{\xi} \cdot \underline{n} = 0, \quad \underline{J} \cdot \underline{n} = 0 & \quad \text{on the surface } \mathcal{S} \\ \sigma_{rr}(r = R) = 0 & \quad \text{free surface condition} \\ u_\theta = 0 & \quad \text{on the surface } \mathcal{S} \end{aligned} \quad (3.54)$$

where \underline{n} is the normal vector to the considered surface. The generalized stress vector $\underline{\xi} = \epsilon \underline{\nabla} \phi$ is defined in [Gurtin, 1996, Ammar et al., 2009c].

Figure 3.12 compares the stress distributions in a misfitting spherical precipitate, obtained in the case of ideal plastic deformation in the matrix according to the interpolation and homogenisation methods. The radial stress σ_{rr} and hoop stress $\sigma_{\theta\theta}$ are normalized to the yield stress and are plotted as functions of the radial distance r divided by the outer radius R . These distributions are illustrated at four different time increments. The initial nucleus is shown by a white strip. The brown domain corresponds to the grown part of the α precipitate whereas the blue strip indicates the zone of plastic activity in the matrix phase. The domains are delimited by vertical dotted lines. The plastic zone size can be seen to increase as the precipitate grows. The hoop stress exhibits a steep increase at the $\alpha - \beta$ interface, $r = r_{int}$, which is the phase field counterpart of the discontinuity expected in the sharp interface model. The main feature of the stress distributions is that stresses as predicted by the interpolation and Voigt homogenisation almost coincide in the β matrix and strongly differ inside the precipitate. The homogenisation model predicts constant stress values inside the inclusion, in contrast to the strongly varying stress field provided by the interpolation model.

This can be understood by looking at the distribution of the plastic strain components ϵ_{rr}^p , $\epsilon_{\theta\theta}^p$. According to the interpolation model, the plastic strain components are obtained by integrating the flow rule (3.15). In contrast, the plastic strain is defined by Eq. (3.30) in the homogenisation model. When the α phase starts growing, the stress level increases in the matrix due to the eigenstrain of the particle. The von Mises equivalent stress reaches the threshold value R_β^0 and plasticity starts flowing in the blue domain around the particle. As the particle continues growing, the interface propagates through the plastic zone of the matrix. As a result the α phase inherits (or not, depending on the model) some plastic deformation from the matrix phase. According to the interpolation scheme, a unique variable ϵ^p is defined and is therefore "transmitted" from one phase to the other. This explains why residual plastic deformation is observed within the α phase, even though it behaves purely elastically, as illustrated by the top part of figure 3.13. The amount of plastic strain inherited by the α phase from the matrix can be seen to increase when the particle size increases.

In contrast, according to the homogenisation model, the mixture rule (3.29) for the plastic strain in the precipitate implies that plastic strain inherited from the β matrix is progressively forgotten when ϕ asymptotically reaches the value 0. This explains why the plastic strain value inherited from the matrix is only visible in the diffuse interface region and in the β phase, and steeply decreases when leaving the interface in the α phase, as illustrated by the profiles in the bottom part of figure 3.13.

The radial strain profiles are shown in figure 3.14 according to the interpolation and homogenisation models. The latter predicts constant strain inside the precipitate. The solutions of the two models are found to be very close in the matrix. The difference in total strain on both sides of the interfaces is responsible for a difference in the so-called coherence energy \mathcal{E}_{coh} defined as the elastic energy necessary to keep both lattices coherent across the interface

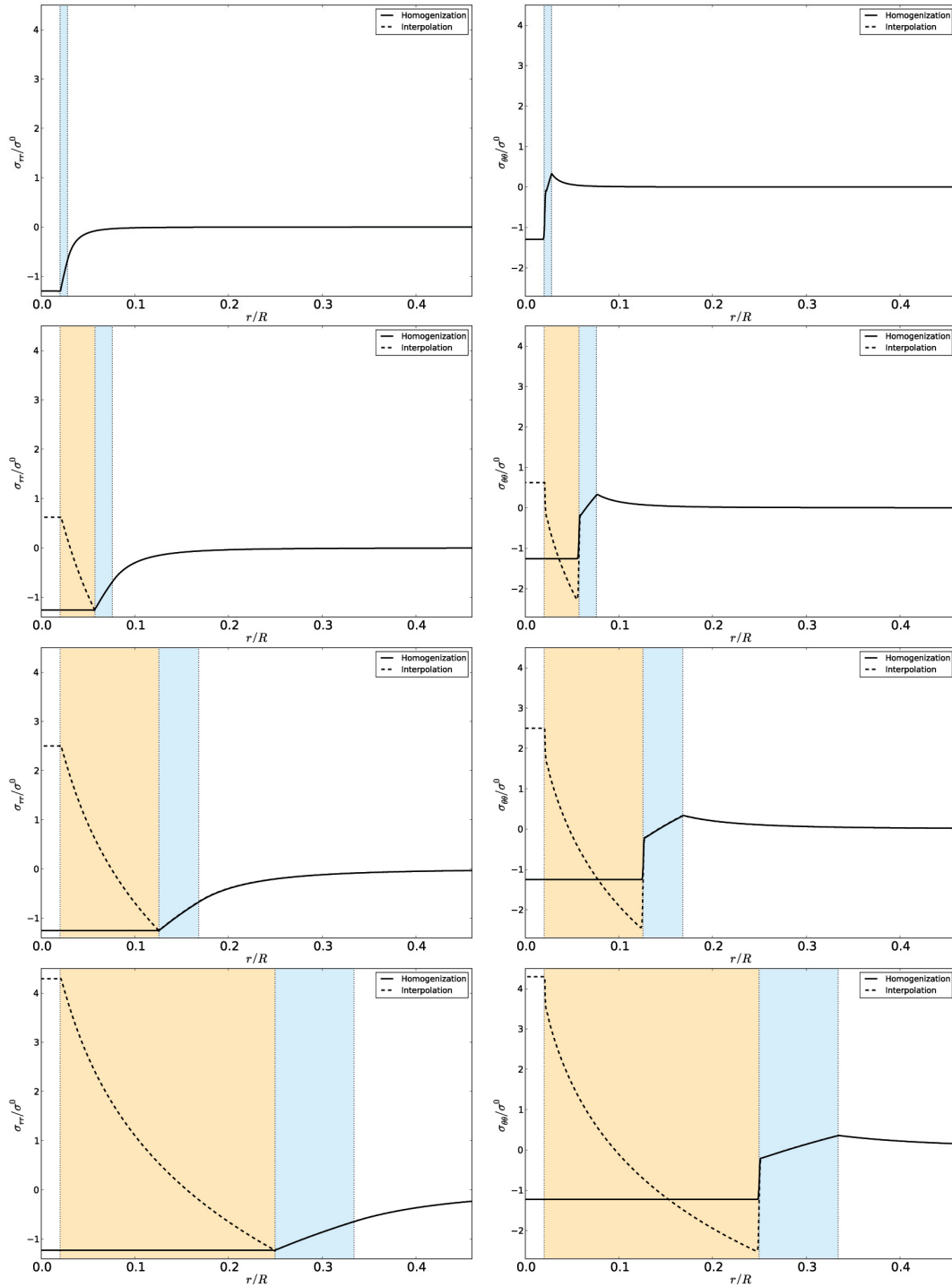


FIGURE 3.12 – Normal σ_{rr} and tangential $\sigma_{\theta\theta}$ stress distributions in a radial direction from the center of the particle with both interpolation and homogenisation methods, at four stages of the growth process. Stresses are normalized with respect to the yield stress R_{β}^0 . The matrix precipitate interface lies at $r/r_{int} = 1$. The white, brown and blue colors respectively correspond to the initial nucleus, grown α phase domain, and active plastic zone in the matrix.

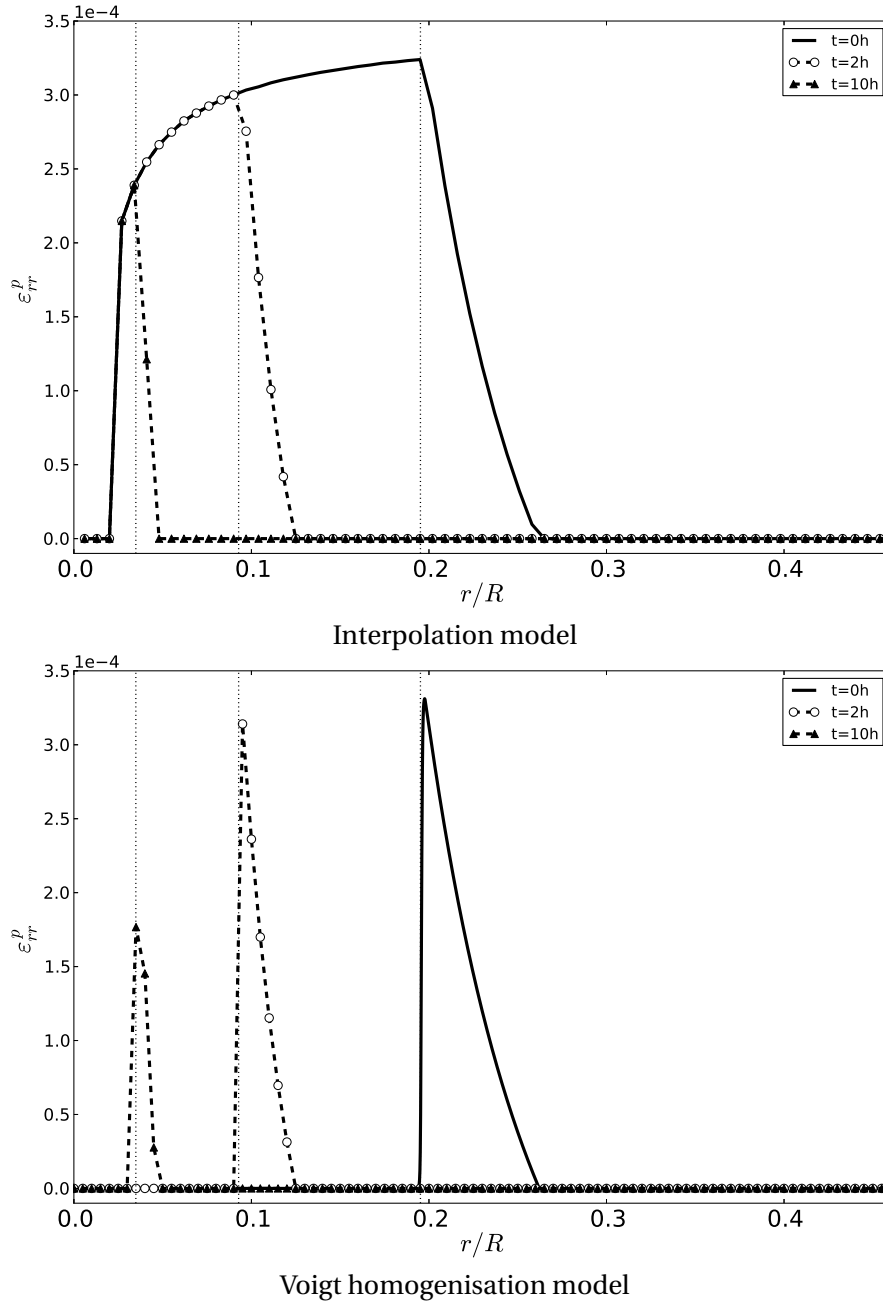


FIGURE 3.13 – Plastic deformation distribution in a spherical precipitate embedded in a concentric spherical matrix as a function of the normalized radial distance r/R as computed at three different time steps for the interpolation model (top) and for the Voigt homogenisation model (bottom).

[Johnson and Alexander, 1986, Ammar et al., 2011]. Its analytical expression and the evolution of the coherence energy with time during growth is shown in the upper right corner of Fig. 3.14.

The corresponding concentration profiles are given in figure 3.15. They show slight differences found in the precipitate according to the phase field model. They remain very close to each other in the matrix phase. The differences in elastic and coherence energies for both models illustrated in the upper right corner of figure 3.15 lead to different jumps of concentrations

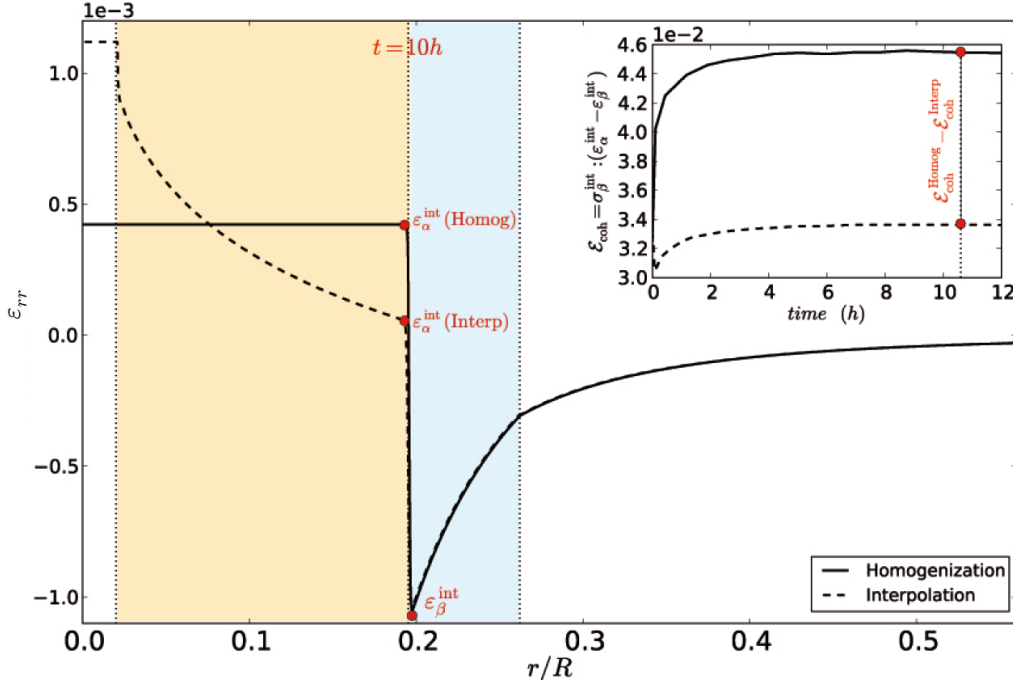


FIGURE 3.14 – Total strain distribution in a spherical precipitate embedded in a concentric spherical matrix as a function of the normalized radial distance r/R as computed at $t = 10$ hours for the interpolation model (dotted line) and for the Voigt homogenisation model (dark line).

on each side of the interface in the form

$$c_{\alpha,\beta}^{int} = a_{\alpha,\beta} + (\mathcal{E} + \frac{\Lambda}{R}) / (k(a_\alpha - a_\beta)) \quad (3.55)$$

where

$$\mathcal{E} = f_\alpha^e - f_\beta^e - \mathcal{E}_{coh}, \quad \text{with} \quad \mathcal{E}_{coh} = \sigma_\beta : (\epsilon_\alpha^{int} - \epsilon_\beta^{int}) \quad (3.56)$$

In particular, c_β^{int} is found to be slightly higher in the interpolation model than in the homogenisation model which induces a slightly less steep concentration gradient in the matrix, as shown in figure 3.15.

In order to examine the effect of stored elastic energy on the diffusional growth of a coherent spherical precipitate into a supersaturated matrix, the time evolution of the precipitate radius, normalized by the matrix radius r_{int}/R , is shown in Fig. 3.16 for the two models. A parabolic law describes the particle growth in both cases but with two different kinetic constants. The square of the precipitate radius increases linearly with time $\Delta e = K\sqrt{t}$. The found values for the coefficient K are : $K = 1.38 \cdot 10^{-9} \text{ m.s}^{-1}$ for the purely elastic model, $K = 1.12 \cdot 10^{-9} \text{ m.s}^{-1}$ for the elastoplastic homogenization model and $K = 10^{-9} \text{ m.s}^{-1}$ for the elastoplastic interpolation model. The reason for such different kinetics stems from the difference in stored elastic energy close to the interface induced by different plastic strain values. As shown in [Ammar et al., 2011] for a dilatational misfit in the particle, plastic deformation leads to a slowdown of the growth kinetics compared to sole elasticity due to a flattening of the concentration profile in the matrix induced by relaxed stresses, as discussed before. The strain jump at the interface shown in figure 3.14 is higher according to the homogenisation model than in the interpolation model which explains the faster kinetics predicted by the former model. In other words, the higher stored elastic energy obtained with the homogenisation model leads to faster kinetics.

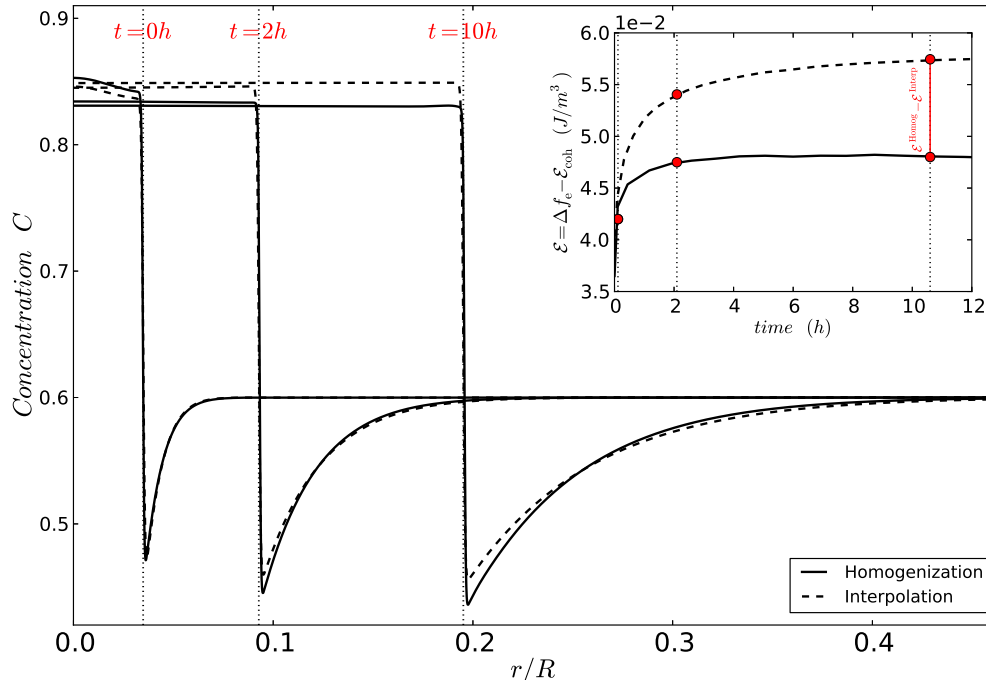


FIGURE 3.15 – Composition profile associated with the growth of an isolated coherent precipitate into a supersaturated matrix, according to the interpolation (dotted line) and homogenisation models (dark line) at three distinct time steps. The matrix/precipitate interface lies at $r/r_{int} = 1$ indicated by the vertical dotted line.

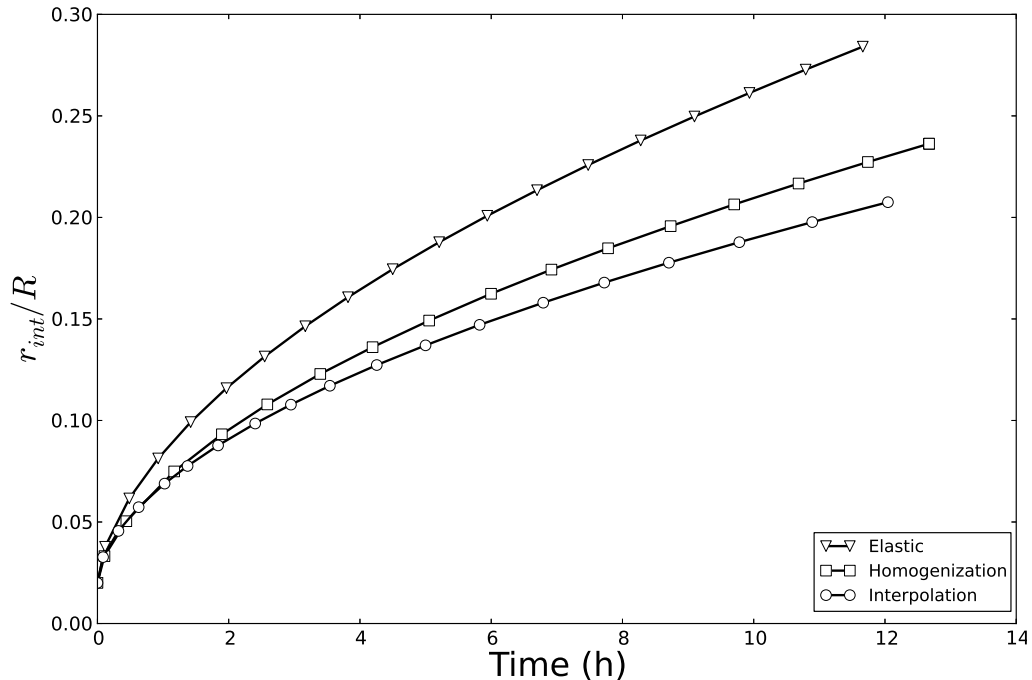


FIGURE 3.16 – Growth kinetics of a misfitting spherical precipitate in an isotropic infinite matrix. Two finite element calculations have been performed according to the interpolation and homogenisation models.

3.4.3.2 Microstructural evolution coupled to plastic activity

The phase field simulation of Ostwald ripening of a population of α precipitates embedded in a β -matrix is considered in this section, including the impact of elastoplastic deformation on the process. Ostwald ripening is a process related to the coarsening of one phase dispersed in a matrix phase. It is generally the last stage of a first-order phase transition in a two-phase region. The first stage is nucleation when a new phase forms from the mother phase, maintained in a supersaturated state. As the supersaturation decreases due to particle growth, the nucleation barrier and the stable cluster size increase. The system usually forms a microstructure with particles in a matrix. Even after full exhaustion of the driving force, the particles in the matrix are not in thermodynamic equilibrium. The system can further decrease its total free energy by decreasing the overall interface area between the particles and the matrix. The decrease of total interface area progresses by a process where the large particles grow at the expense of the smaller particles. The average size of the particles of the dispersed phase increases during coarsening due to diffusion through the matrix phase, and their total number decreases.

A square area has been meshed with 250×250 linear quadrangular elements. Several solid particles ($\phi = 1$) of different shapes and radii were randomly distributed in the matrix ($\phi = 0$). The initial solute compositions of both phases are homogeneous and set to be equal to $c_0 = 0.5$. The simulations are performed under plane strain conditions. Periodic boundary conditions are applied to the concentration and phase fields. Periodicity is also enforced to the mechanical variables ensuring here a vanishing mean stress, by means of a special finite element described in [Besson et al., 2009].

The simulated results for the Ostwald-ripening process are shown in Fig. 3.17 and 3.18, for the interpolation and homogenisation models respectively. In each case, the top figures illustrate the coarsening of the particles, i.e. the growth and coalescence of some particles and the disappearance of other ones. In both simulations, only two particles remain after 5 hours. The kinetics is slightly faster for the homogenization than for the interpolation model.

The simulations also provide the field of cumulative plastic strain p defined as :

$$\dot{p} = \sqrt{\frac{2}{3} \dot{\boldsymbol{\epsilon}}^p : \dot{\boldsymbol{\epsilon}}^p} \quad (3.57)$$

at different time steps, see the bottom images of Fig. 3.17 and 3.18. At the final stage, the homogenisation model predicts very limited zones of residual plastic strain due to the sweeping of plastic strain by the interface. In contrast a complex field of plastic deformation is found to pertain according to the interpolation model. As a result, the material swept by the phase transformation front is full of residual stresses. Residual stresses are much more limited for the homogenisation model. In particular, when the α phase will have spread over the whole domain, it is expected that the interpolation model will predict residual plastic strains and stresses inside the domain whereas the homogenisation will predict a new virgin state in the domain. This represents a major difference between both approaches. The relevance of both situations to the physical reality could be investigated by means of residual stress or strain field measurements with sufficient accuracy.

3.4.4 Conclusion

Recent advances in phase field modeling involve the nonlinear mechanical behaviour of materials during phase transformation. Two main classes of such models have been distinguished, namely the interpolation models relying on a single set of constitutive equations and interpolation of material parameters, and the homogenisation models that are based on the mixture of free energy and dissipation potentials associated with distinct behaviours of the phases. The two model classes have been shown to exhibit opposite behaviour regarding the

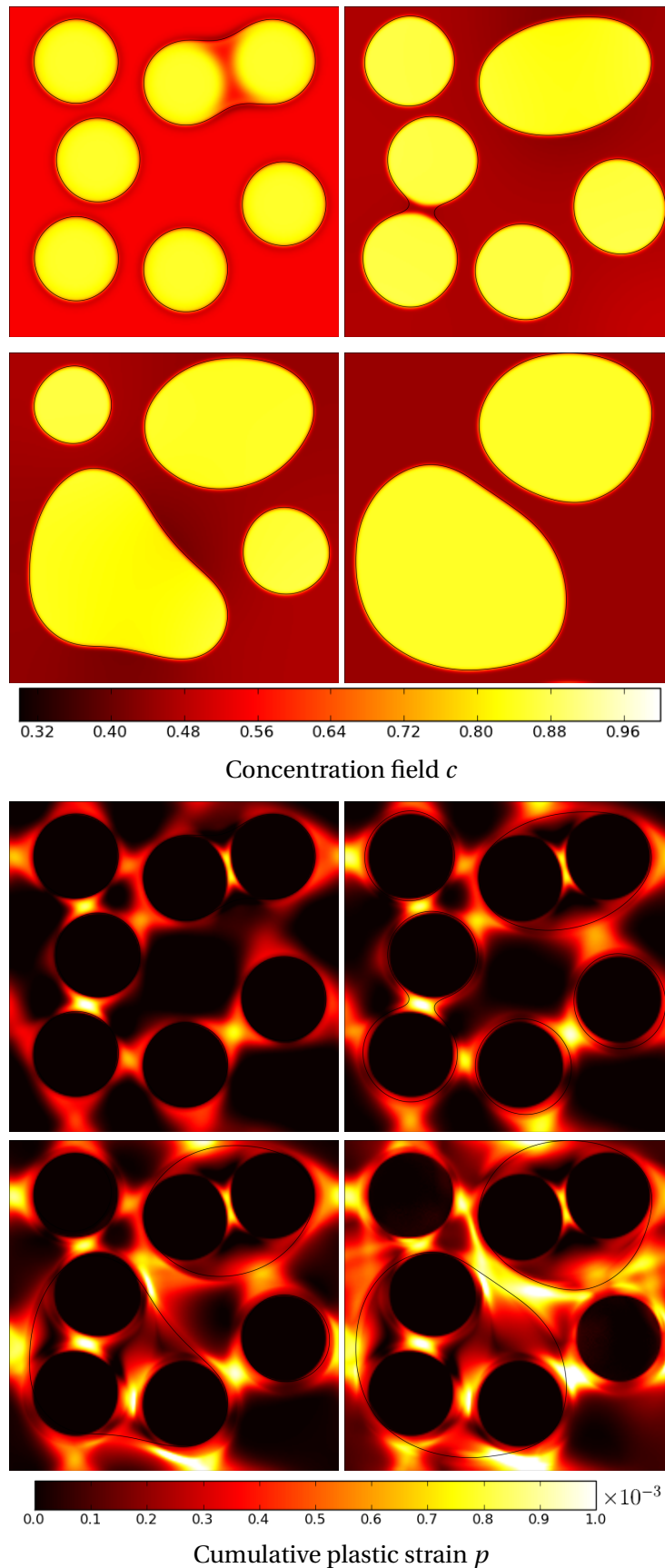


FIGURE 3.17 – Time history of Ostwald ripening process in the case of total inheritance between the new elastic formed phase and the parent plastic phase (interpolation model) : phase field and field of cumulative plastic strain at the time steps $t = 0h, 1.7h, 2.5h, 5h$. The black lines in the bottom part denote the $\phi = 0.5$ iso-lines.

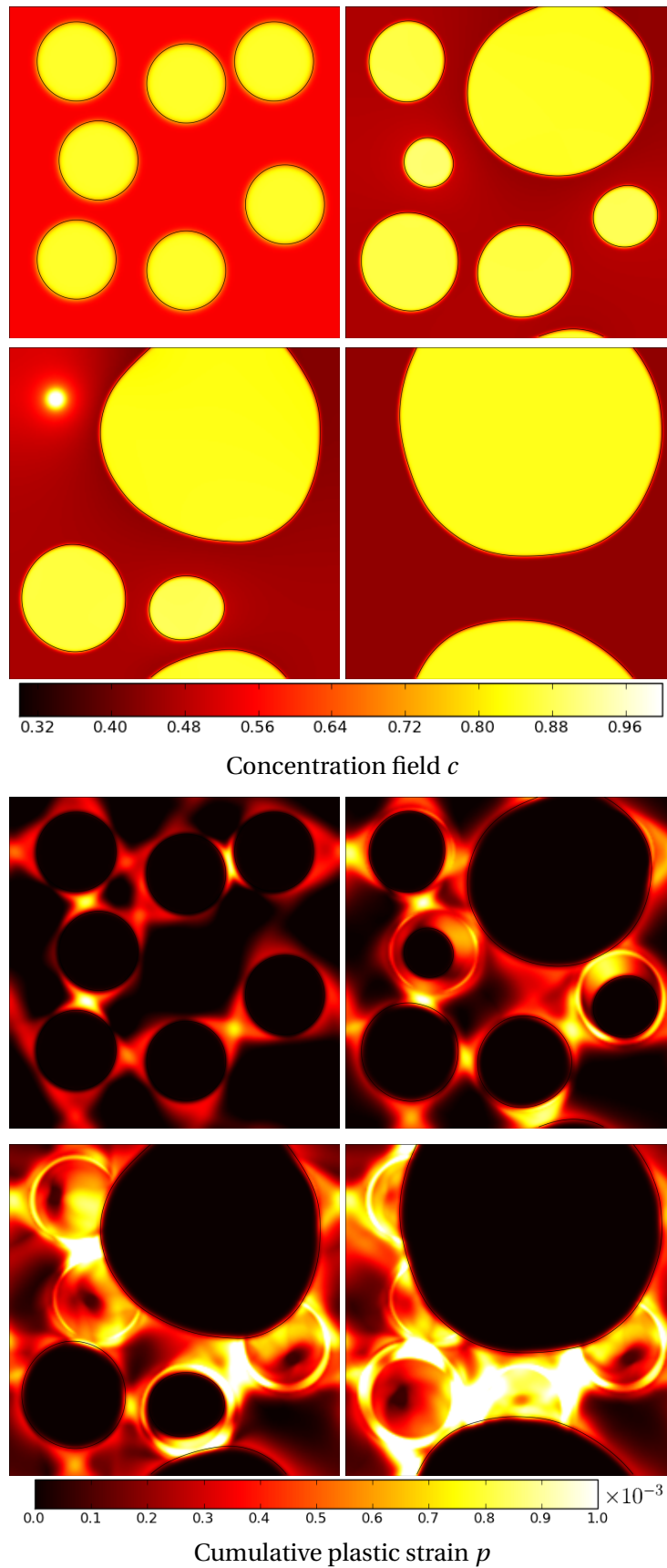


FIGURE 3.18 – Time history of Ostwald ripening process in the absence of inheritance between the new elastic formed phase and the parent plastic phase (homogenisation model) : phase field and field of cumulative plastic strain at the time steps $t = 0h, 0.25h, 1h, 5h$.

question of inheritance of plastic deformation during phase transformation. As a rule, according to interpolation models, the plastic strain that occurred in the mother phase due to prior straining or induced by the local stresses arising at the vicinity of the interface, was shown to be inherited by the new phase after the passing of the interface. This means that the new reference state for computing elastic stresses is that of the parent phase. In contrast, according to homogenisation models, fading memory of plastic strain is observed due to the fact that the plastic strain tensor is expressed as an explicit weighted function of the plastic strain tensors attributed to each phase at each material point. This distinct behaviour of each model class has been shown to result in different residual plastic strain and stress fields after transformation. Residual stresses are minimized when using homogenisation models. Interpolation models lead to a non-vanishing residual plastic strain field, even after complete phase transformation. This residual plastic strain field reflects the history of growth and coalescence of precipitates embedded in an elastoplastic matrix.

Finite element simulation results were given in the case of a misfitting elastic precipitate phase growing within an elastoplastic von Mises matrix. A slowdown of transformation kinetics due to plasticity compared to purely elastic behaviour was observed and related to the strain relaxation induced by plasticity close to the interface [Ammar et al., 2011]. The homogenisation was shown to lead to a slightly faster kinetics than the interpolation models due to the fact that the inheritance of plastic deformation in the latter model allows for higher strain relaxation. This slowdown in the growth kinetics does not reflect the pipe diffusion effects induced by dislocations which would rather lead to significant acceleration of the kinetics in alloys. Pipe diffusion effects could be introduced in the modelling by means of a dependence of diffusion coefficients on dislocation density. Although only two-dimensional axisymmetric or plane strain simulations were provided in this work, the fundamental difference in the resulting inheritance behaviour of the two classes of models remains in the 3D case, because it lies in the mathematical formulation of the models. The axisymmetric example already addresses spherical precipitate shape but random distributions of growing second phase in an elastoplastic matrix must be considered in the future.

It is anticipated that the actual behaviour of engineering materials lies between that of total inheritance of plastic deformation and no inheritance at all. It will therefore be necessary to develop phase field models combining features of both model classes investigated in this work and leading to the possibility of partial inheritance.

Hardening laws were formulated in the constitutive models but not used in the simulation because the existence of hardening raises the question of inheritance of dislocation microstructures after the passing of an interface, which is a different question from that of the inheritance of plastic deformation. The latter solely represents a change in the reference local configuration for the computation of elastic stresses. The question of inheritance of hardening microstructures will be the subject of future work both in the case of the phenomenological constitutive equations presented in the present work and for phase field dislocation models proposed in [Geslin et al., 2014]. Also, rate-independent plasticity only was considered in the present work to avoid mixing too many phenomena in the discussion. The presented model formulations are general and include viscoplastic behaviour that is more realistic for diffusional phase transformation and will be used in the future.

The question of inheritance of plastic strain gradients, i.e. accumulation of geometrically necessary dislocations close to boundaries could also be modelled within a coupled phase field / strain gradient plasticity approach as proposed in [Cottura et al., 2012].

Phase field and strain gradient visco-plasticity

Contents

4.1	Introduction	81
4.2	Model description	81
4.2.1	Ginzburg-Landau free energy	81
4.2.1.1	Chemical free energy	82
4.2.1.2	Elastic energy	82
4.2.1.3	Evolution equations	83
4.2.2	Strain gradient Mesoscale Plasticity Model	83
4.3	Results	85
4.3.1	Plasticity in a static microstructure	85
4.3.1.1	1D : Analytical solution	85
4.3.1.2	Global mechanical behavior	87
4.3.2	Microstructural evolution coupled to a viscoplastic activity	89
4.3.2.1	Initial cuboidal microstructure and elastic parameters	89
4.3.2.2	Rafting under creep	90
4.3.2.3	Influence of the plastic length scale	90
4.4	Conclusion	95

4.1 Introduction

Despite significant successes achieved by the models, which couple a diffuse interface model with an continuum plasticity, they miss an important feature of the plastic behavior : the so-called *size effect*, also known as the Hall-Petch effect in polycrystals ([Hall, 1951]) : the smaller the domains involved by plasticity, the harder the material. This size effect becomes significant when sizes involved are below a few microns, which is typically the case in an evolving microstructure.

The aim of the present chapter is precisely to demonstrate how a phase field method can be coupled to a mesoscale viscoplastic model accounting for the size effect of the plastic behavior. The formulation of a phase field model accounting for size-dependent viscoplasticity is developed to study materials in which microstructure evolution and viscoplastic behavior are strongly coupled. This size effect can only emerge from a viscoplastic model in which an intrinsic length is included and therefore, the viscoplastic model has to be chosen within the framework of the mechanics of generalized continua, where plasticity is introduced using a continuum strain gradient formalism ([Gurtin et al., 2010, Forest and Sievert, 2003]).

The chapter is divided as follows : In a first section, the phase field method and the viscoplastic model are presented, as well as their coupling within a coherent thermodynamic framework. In a second section, the predictions of the coupled model are analyzed. We first analyze static microstructures and we explain how the size effect modifies plastic activity and the resulting macroscopic mechanical behavior. Finally, the dynamic coupling between microstructure evolution and viscoplastic activity is addressed and illustrated by the rafting of the microstructure observed in Ni-base superalloys under creep conditions. It is found that the plastic size effect has only a moderate impact on the shape of the rafts but is crucial to reproduce the macroscopic mechanical behavior of that particular material. This chapter is based on the work proposed in [Cottura et al., 2012]

4.2 Model description

4.2.1 Ginzburg-Landau free energy

The coupling between phase field method and mesoscale viscoplastic model is presented in the context of the microstructural evolution in Ni-base superalloys. In these alloys, the disordered γ phase and the ordered γ' phase coexist at equilibrium. Following [Boussinot et al., 2010], the superalloy is modeled as an effective binary alloy. In that case, in addition to the local concentration field $c(\underline{r}, t)$, three non-conservative structural fields $\phi_{i=1,3}(\underline{r}, t)$ are introduced to account for the degeneracy of the low temperature γ' phase. The four translational variants of γ' are described by the following long-range order parameters : $\{\phi_1, \phi_2, \phi_3\} = \phi_0\{1, 1, 1\}, \phi_0\{\bar{1}, \bar{1}, 1\}, \phi_0\{\bar{1}, 1, \bar{1}\}, \phi_0\{1, \bar{1}, \bar{1}\}$.

The main ingredient of phase field modeling is a mesoscopic free energy functional F relating the concentration and order parameters to the total free energy. This free energy, which is defined as the integral over the volume V of a free energy density f , is given by a standard Ginzburg-Landau functional, which is usually defined as the integral over the volume V of several contributions : chemical free energy f^{ch} , interface energies and elastic energy f^e , detailed in the next subsections. As usually done in mesoscale viscoplastic model, the free energy func-

tional may also contain a viscoplastic contribution f^{vp} . Hence,

$$\begin{aligned} F &= \int_V f(c, \underline{\nabla} c, \{\phi_i\}, \underline{\nabla} \phi_i, \underline{\boldsymbol{\varepsilon}}^e, \underline{\boldsymbol{\alpha}}, p) dV \\ &= \int_V f^{\text{ch}}(c, \{\phi_i\}) + f^e(c, \{\phi_i\}, \underline{\boldsymbol{\varepsilon}}^e) + f^{vp}(\underline{\boldsymbol{\alpha}}, p) + \frac{\epsilon}{2} \sum_i |\underline{\nabla} \phi_i|^2 + \frac{\beta}{2} |\underline{\nabla} c|^2 dV \end{aligned} \quad (4.1)$$

where V is the volume, ϵ and β are gradient energy coefficients and $\underline{\boldsymbol{\varepsilon}}^e$ is the elastic strain tensor.

The viscoplastic contribution f^{vp} , as well as the new fields necessary to describe hardening ($\underline{\boldsymbol{\alpha}}, p$) will be introduced in section 4.2.2.

4.2.1.1 Chemical free energy

The chemical free energy $f^{\text{ch}}(c, \{\phi_i\})$ accounts for the free energy density of an homogeneous system, associated with phase transformation, which is characterized by the concentration c and order parameters ϕ_i . As usual, $f^{\text{ch}}(c, \{\phi_i\})$ is approximated by a Landau polynomial expansion with respect to the order parameters. Its form is dictated by the symmetry loss during the $\gamma \rightarrow \gamma'$ phase transformation. Following [Boussinot et al., 2010], the lowest possible order of the expansion has been chosen :

$$f^{\text{ch}}(c, \{\phi_i\}) = \Delta f \left[\frac{1}{2} (c - c_\gamma)^2 + \frac{\mathcal{B}}{6} (c_2 - c) \sum_{i=1,3} \phi_i^2 - \frac{\mathcal{C}}{3} \phi_1 \phi_2 \phi_3 + \frac{\mathcal{D}}{12} \sum_{i=1,3} \phi_i^4 \right] \quad (4.2)$$

where Δf is an energy density scale and c_2 an arbitrary concentration chosen between the equilibrium concentrations c_γ and $c_{\gamma'}$ of the coexisting phases. \mathcal{B} , \mathcal{C} and \mathcal{D} are constants related to c_2 , c_γ , $c_{\gamma'}$ and to the equilibrium long-range order parameter ϕ_0 . In all the subsequent calculations, we have used the equilibrium concentrations $c_\gamma = 0.15$ and $c_{\gamma'} = 0.231$, as well as $c_2 = 0.18$. Following [Boussinot et al., 2010], forcing ϕ_0 to saturate at 1 gives $\mathcal{B} = 0.162$, $\mathcal{C} = 0.01458$ and $\mathcal{D} = 0.022842$ and the non dimensional coefficients : $\tilde{\epsilon} = \epsilon / (\Delta f d^2)$ and $\tilde{\beta} = \beta / (\Delta f d^2)$, where d is the grid spacing, are chosen to be $\tilde{\epsilon} = 9.75 \cdot 10^{-4}$ and $\tilde{\beta} = 0.21$.

4.2.1.2 Elastic energy

The elastic energy density in the framework of linear elasticity reads :

$$f^e(\underline{\boldsymbol{\varepsilon}}^e) = \frac{1}{2} \underline{\boldsymbol{\varepsilon}}^e : \underline{\mathbb{C}} : \underline{\boldsymbol{\varepsilon}}^e dV \quad (4.3)$$

where $\underline{\mathbb{C}}$ stands for the local elastic moduli tensor. Assuming that the local concentration is the relevant field for discriminating the elastic properties, $\underline{\mathbb{C}}$ is chosen as a linear function of c and is thus space dependent ([Boussinot et al., 2010]).

Accounting for plasticity in the small strain framework, the total strain $\underline{\boldsymbol{\varepsilon}}$ can be divided into three contributions :

$$\underline{\boldsymbol{\varepsilon}} = \underline{\boldsymbol{\varepsilon}}^e + \underline{\boldsymbol{\varepsilon}}^* + \underline{\boldsymbol{\varepsilon}}^p \quad (4.4)$$

where $\underline{\boldsymbol{\varepsilon}}^p$ is the plastic strain tensor with time evolution detailed in section 4.2.2. $\underline{\boldsymbol{\varepsilon}}^*$ is the stress-free strain tensor associated with the lattice parameter change during the $\gamma \rightarrow \gamma'$ transformation. Assuming Vegard's law :

$$\underline{\boldsymbol{\varepsilon}}^* = \lambda / (c_{\gamma'} - c_\gamma) \Delta c \mathbf{1} \quad (4.5)$$

where $\underline{\mathbf{1}}$ is the identity matrix. The misfit is related to the lattice parameters a_γ and $a_{\gamma'}$ of the stress-free γ and γ' phases $\lambda = 2(a_{\gamma'} - a_\gamma)/(a_{\gamma'} + a_\gamma)$.

In the case of diffusion controlled phase transformations, static mechanical equilibrium can be assumed since relaxation of the elastic waves is by orders of magnitude faster than the evolution of concentration, order parameters, and plastic strain governed by viscoplasticity. Therefore, at any time, elastic strain can be computed by solving mechanical equilibrium assuming stress-free strain and constant plastic strain. This can be done by minimizing the potential elastic energy with respect to displacements accounting for given boundary conditions. When the elastic constants of the coexisting phases differ, mechanical equilibrium has to be solved iteratively as in [Boussinot et al., 2010].

4.2.1.3 Evolution equations

The time evolution of the concentration and order parameters is governed by kinetic equations relating time derivatives to the corresponding driving forces, defined as the functional derivatives of free energy density f with respect to the fields. Assuming linear constitutive relationships, the Cahn-Hilliard equation is recovered for the conserved concentration field and the Allen-Cahn equation for the non-conserved order parameter ones :

$$\frac{\partial c}{\partial t}(\underline{\mathbf{r}}, t) = L \nabla^2 \frac{\partial f}{\partial c(\underline{\mathbf{r}}, t)} \quad (4.6)$$

$$\frac{\partial \phi_i}{\partial t}(\underline{\mathbf{r}}, t) = -M \frac{\partial f}{\partial \phi_i(\underline{\mathbf{r}}, t)} \quad (4.7)$$

The kinetic coefficients L and M , related to diffusion and structural relaxation respectively, are assumed constant. Following [Gaubert et al., 2010], L is such as to recover the interdiffusion coefficient $D = D_0 \exp(-\Delta U/k_B T)$ with $D_0 = 1.45 \cdot 10^{-4} \text{ m}^2\text{s}^{-1}$ and $\Delta U = 2.8 \text{ eV}$ ([Fujiwara et al., 1999]). We have used $M = 100 L d^{-2}$, where d is the grid spacing, to ensure that kinetics is much faster for the order parameter than for the concentration field.

4.2.2 Strain gradient Mesoscale Plasticity Model

The mesoscale viscoplastic model coupled to the phase field method is presented in this section. As explained in the introduction, the key point is that the size effect due to the plastic behavior has to be taken into account. Within the framework of continuum mechanics, this size effect can only emerge from a plastic model in which an intrinsic length is included.

Size-dependent constitutive models can be obtained by resorting to the mechanics of generalized continua, like second gradient and micromorphic theories ([Mindlin and Eshel, 1968, Eringen and Suhubi, 1964]). Isotropic strain gradient plasticity models have been developed since the early 1980s to account for size effect and deformation patterning observed in metals ([Aifantis, 1987]). Secondly, size dependent crystal plasticity models have been proposed by Fleck and Forest using second gradient ([Fleck et al., 1994]) and Cosserat ([Forest et al., 1997]) theories. More recently the microforce approach put forward by Gurtin was applied to crystal plasticity as an alternative ([Gurtin, 2002, Svendsen, 2002]). The curl of the plastic strain tensor or, equivalently, the lattice curvature tensor (gradient of the deformation induced lattice rotation) are directly related to the notion of geometrically necessary dislocations well-known in physical metallurgy ([Ashby, 1970, Steinmann, 1996]). Constitutive equations involving functions of the plastic strain gradient or, equivalently, of the densities of geometrically necessary dislocations introduce internal length scales that are responsible for a size effect in the resulting behavior. In the present work, we have chosen to use a strain gradient viscoplastic model

similar to the one proposed in [Aifantis, 1987] and [Forest, 2008b] which has the advantage of simplicity and in which the intrinsic plastic length is easily controlled through the value of a single parameter. The framework used below will be similar to the one developed in [Gaubert et al., 2010] but with the addition of an heterogeneous component in the viscoplastic free energy density. Also, for the sake of simplicity, the present formulation is limited to isotropic viscoplasticity even though the extension to an anisotropic viscoplastic behavior could be obtained by explicitly introducing an appropriate set of slip systems. The derivation of the simple isotropic model within a coherent thermodynamic framework is presented in this section.

The plastic state of the material is described classically with two internal variables $\underline{\alpha}$ and p related to kinematic and isotropic hardening, respectively ([Lemaitre and Chaboche, 1994]). They enter the free energy as follow :

$$f^{vp}(\underline{\alpha}, p) = \frac{1}{3} C \underline{\alpha} : \underline{\alpha} + \frac{1}{2} H p^2 + \frac{1}{2} A |\underline{\nabla} p|^2 \quad (4.8)$$

A simple quadratic form is assumed for the contribution of $\underline{\alpha}$. The contribution of p has also a quadratic part describing linear isotropic hardening, which can be easily extended to the case of a non linear isotropic hardening ([Lemaitre and Chaboche, 1994]). The last term in (4.8), proportional to the square gradient of p introduces an intrinsic length scale in the plastic model. A dimension analysis shows that this intrinsic length is proportional to the square root of the gradient coefficient A .

The evolution of the material leads to an energy dissipation. The local intrinsic dissipation is given by :

$$\underline{\sigma} : \dot{\underline{\epsilon}}^p - \underline{X} : \dot{\underline{\alpha}} - R \dot{p} \geq 0 \quad (4.9)$$

where the thermodynamic forces associated with the internal variables are given by :

$$\underline{X} = \frac{\delta F}{\delta \underline{\alpha}} = \frac{2}{3} C \underline{\alpha} \quad (4.10)$$

$$R = \frac{\delta F}{\delta p} = H p - A \Delta p \quad (4.11)$$

These thermodynamic forces correspond to the hardening variables defining the elastic domain and the corresponding plastic/viscoplastic potential ([Lemaitre and Chaboche, 1994]). More precisely, \underline{X} is the back-stress, i.e. the center of the elastic domain, and R is its radius. In this formulation, we assume that all strain gradient effects are attributed to the free energy (4.8), following [Gurtin et al., 2010] and [Forest, 2008b]. More general models could also incorporate some dissipative contributions associated with strain gradients.

The kinetic equations of the viscoplastic model are obtained within a thermodynamic framework by postulating the existence of a convex dissipation potential Ω which depends on stress $\underline{\sigma}$ and on the thermodynamic forces in the following way ([Lemaitre and Chaboche, 1994]) :

$$\Omega(\underline{\sigma}, \underline{X}, R) = g(\underline{\sigma}, \underline{X}, R) + \frac{3D}{4C} \underline{X} : \underline{X} \quad (4.12)$$

J_2 defining a distance in stress space is given by $J_2(\underline{\sigma}) = \sqrt{\frac{3}{2}(\underline{s} : \underline{s})}$ where $\underline{s} = \underline{\sigma} - \frac{1}{3} Tr(\underline{\sigma}) \underline{1}$ is the deviatoric stress and R^0 , C and D are coefficients which may depend on temperature. $g(\underline{\sigma}, \underline{X}, R)$ is a yield functional, defined as :

$$g(\underline{\sigma}, \underline{X}, R) = J_2(\underline{\sigma} - \underline{X}) - (R^0 + R)$$

The normal dissipative laws are then expressed as :

$$\dot{p} = -\frac{\delta\Omega}{\delta R} \quad (4.13)$$

$$\dot{\boldsymbol{\varepsilon}}^p = \frac{\delta\Omega}{\delta\boldsymbol{\sigma}} = \dot{p} \mathbf{n} \quad (4.14)$$

$$\dot{\boldsymbol{\alpha}} = -\frac{\delta\Omega}{\delta\mathbf{X}} = (\mathbf{n} - D\boldsymbol{\alpha})\dot{p} = \dot{\boldsymbol{\varepsilon}}^p - D\boldsymbol{\alpha}\dot{p} \quad (4.15)$$

where $\mathbf{n} = \partial g / \partial \boldsymbol{\sigma} = \frac{3}{2} \frac{\underline{\mathbf{s}} - \mathbf{X}}{J_2(\boldsymbol{\sigma} - \mathbf{X})}$ is the normal to the yield surface and defines the flow direction.

Combining these expressions, it is found that p is the cumulative plastic strain since $\dot{p} = \sqrt{\frac{2}{3} \dot{\boldsymbol{\varepsilon}}^p : \dot{\boldsymbol{\varepsilon}}^p}$.

Finally, the following dissipation potential density has been assumed :

$$\tilde{\Omega}(f) = \frac{K}{N+1} \left\langle \frac{g}{K} \right\rangle^{N+1} \quad (4.16)$$

where $\langle a \rangle$ stands for the positive part of a and N, K are positive parameters. This choice leads to a Norton type flow rule :

$$\dot{p} = \left\langle \frac{g}{K} \right\rangle^N \quad (4.17)$$

where R^0 appears now to be the initial yield stress and R the isotropic hardening. It is worth noting that R includes both linear isotropic hardening and the strengthening resulting from the plastic size effect (4.11).

In heterogeneous materials, the viscoplastic parameters C, D, H, A, N, K and R^0 depend on position \mathbf{r} . In the particular case of γ/γ' superalloys under creep loading, only γ undergoes plastic strain while γ' behaves elastically. To reproduce this behavior all the viscoplastic parameters have been set at their value in the γ phase, except the initial yield stress R^0 which is interpolated between R_γ^0 and $R_{\gamma'}^0$ as follows :

$$R^0 = \bar{R}_0 + R'_0 \tanh \left[\theta \left(\frac{1}{3\phi_0^2} \sum_{i=1,3} \phi_i^2 - \frac{1}{2} \right) \right] \quad (4.18)$$

with $\bar{R}_0 = (R_\gamma^0 + R_{\gamma'}^0)/2$, $R'_0 = (R_{\gamma'}^0 - R_\gamma^0)/2$ and θ a parameter controlling plasticity in the interface.

In all the calculations, we have used $\theta = 100$ which leads to variations of the parameters over a grid spacing d , a distance smaller than the interface width. Other values have been tested to check that the influence on the microstructural evolution is negligible. Moreover, for purely numerical reasons, the value of $R_{\gamma'}^0$ is chosen large enough (100GPa) to prevent any plastification of γ' even in presence of a characteristic plastic length.

4.3 Results

4.3.1 Plasticity in a static microstructure

4.3.1.1 1D : Analytical solution

At first, we have investigated the viscoplastic model in a simple static microstructure so as to make a clear link between its parameters and a characteristic plastic length.

For that purpose, a 1D configuration has been chosen which mimics a periodic arrangement of elastic γ' layers with thickness ℓ and plastic γ channels with thickness s along the x direction (Fig. 4.1). This two phases laminate is submitted to a tensile strain along x . This configuration was also analyzed by [Cordero et al., 2010] in the context of single crystal strain gradient plasticity under shear loading conditions. We have considered cubic homogeneous elasticity, isotropic hardening and no kinematic hardening. Moreover the misfit between γ and γ' has been neglected.

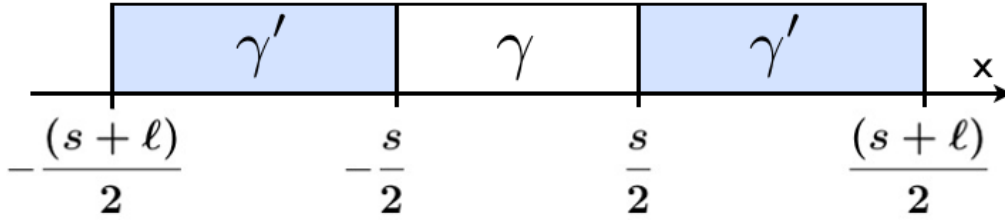


FIGURE 4.1 – Configuration used to derive the analytical solution.

In the limit of time independent plasticity ($\dot{\epsilon}_{11} \rightarrow 0$), an analytical solution for the cumulative plastic strain p can be found along the following lines (see Appendix for details). First the J_2 yield surface is expressed for the specific 1D geometry considered here : $J_2(\boldsymbol{\sigma}) = |\sigma_{11} - \sigma_{22}(x)|$, where σ_{11} is homogeneous to fulfill mechanical equilibrium. Using von Mises criterion in γ , we have :

$$R^0 + Hp(x) - A\Delta p(x) = |\sigma_{11} - \sigma_{22}(x)| \quad (4.19)$$

Using Hooke's law $\sigma_{22}(x)$ can be written in terms of σ_{11} and p and replaced in Eq. (4.19) to give a second order differential equation. Integrating this equation with the boundary conditions leads to :

$$p(x) \propto 1 - \frac{\cosh(\omega x)}{\cosh(\omega s/2)} \quad \text{with} \quad \omega^2 = \frac{1}{A} \left(H + \frac{1}{2} \frac{E}{1-\nu} \right) \quad (4.20)$$

where E and ν are Young's modulus and Poisson's ratio in the x direction.

The characteristic plastic length $L_p = 1/\omega$ can be identified, which varies as \sqrt{A} as expected. L_p depends on the isotropic hardening modulus H and on Young's modulus E . In a simplified approach H and E can be linked to the slopes of plastic and elastic parts of the σ vs. ϵ curve, respectively. Provided that H is much smaller than E , a good estimate of the plastic length is $\tilde{L}_p = \sqrt{A/E}$.

Typical profiles of p are shown in Fig. 4.2 for different values of L_p at the same average strain $\bar{\epsilon}_{11} = 5 \cdot 10^{-3}$, using parameters in Tab. 4.1 and $H = 4.3$ GPa. Analytical solutions obtained with Eq. (4.20) are plotted with continuous lines. Plastic deformation is of course confined in the γ channel. Its gradients are located at the γ/γ' interfaces and extend over L_p . When $L_p \ll s$, p is homogeneous in almost the whole γ channel, and tends to the value given by conventional plasticity ($L_p \rightarrow 0$). The homogeneous region of the plastic strain starts to disappear when L_p is about 15% of channel thickness. For $L_p \approx s/3$, p exhibits an almost parabolic profile with a significant decrease in the maximum cumulative plastic strain at $x = 0$. As a consequence, the elastic strain as well as σ_{11} become higher as L_p increases for a given $\bar{\epsilon}_{11}$. It must be noted that for the γ' volume fraction $\tau_{\gamma'} = 0.7$ used in Fig. 4.2, the influence of L_p on σ_{11} remains moderate (for $L_p = 0.1$ nm, $\sigma_{11} = 292$ MPa; for $L_p = 38$ nm, $\sigma_{11} = 350$ MPa).

In Fig. 4.2, the corresponding numerical calculations are plotted with symbols. The kinetic coefficients L and M in Eqs. (4.6) and (4.7) are set to zero to freeze the microstructure. $\bar{\epsilon}_{11}$ has been applied at a very small rate $\dot{\epsilon}_{11} = 10^{-10} \text{ s}^{-1}$ in order to match the conditions used to

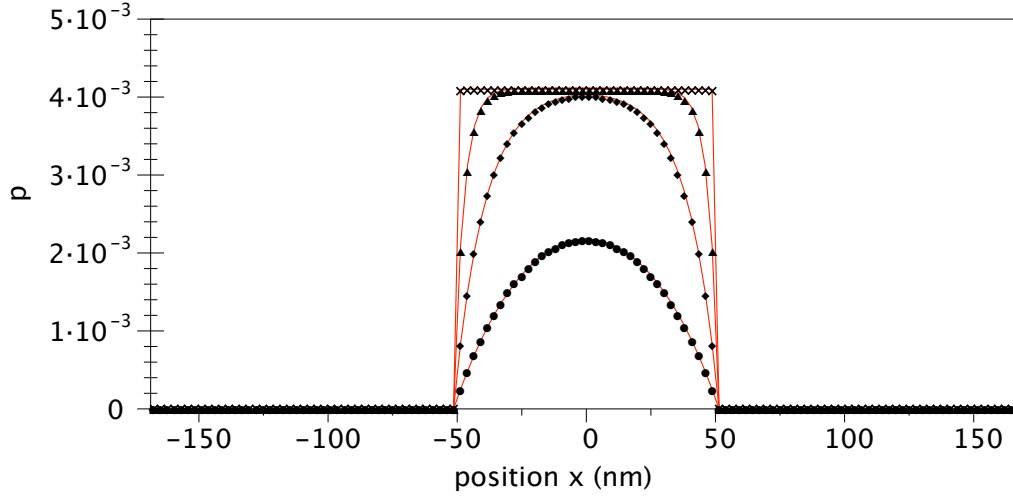


FIGURE 4.2 – Profiles of cumulative plastic strain for different values of L_p at $\bar{\varepsilon}_{11} = 5 \cdot 10^{-3}$ in a 1D configuration of two phases : γ channel (plastic) of thickness $s = 102$ nm and γ' precipitates (elastic) of thickness $\ell = 235$ nm. The red curves are the analytical solutions corresponding to the simulations with (\times) $L_p = 0.1$ nm, (\blacktriangle) $L_p = 3.8$ nm, (\blacklozenge) $L_p = 12$ nm, (\bullet) $L_p = 38$ nm.

derive the analytical solution. A perfect match between the analytical solution and numerical simulation is found, which validates the numerical implementation of our model.

4.3.1.2 Global mechanical behavior

Aiming at investigating microstructure evolutions coupled to viscoplasticity in Ni-base superalloys, the first step is to properly assess the size effect as predicted by the viscoplastic model on the mechanical behaviour of a static real microstructure. For that purpose, we have studied an AM1-type superalloy under loading for which data concerning its mechanical behavior are available in the literature. More specifically, we have used tensile curves σ vs. ε obtained with a tensile strain rate $\dot{\varepsilon}_{11} = 10^{-3} \text{ s}^{-1}$, in conditions where the microstructure is known not to evolve significantly.

The simulations have been performed considering a 3D periodic model configuration : a cube-shaped precipitate inside a cubic matrix. It mimics a periodic array of identical γ' precipitates aligned along the cubic orientations separated by narrow γ channels. To reproduce the features of realistic microstructures observed in AM1 ([Diologent, 2002]), such as the volume fraction $\tau_{\gamma'} = 0.7$ and the average precipitate size ~ 450 nm, we have considered γ' precipitates 456 nm large and γ channels 56 nm wide. We used a discretization of 256^3 nodes and a node spacing of $d = 2$ nm. Moreover, the fields identifying the microstructure have been relaxed so as to obtain diffuse interfaces. All the model parameters have been selected from experimental measurements. According to [Royer et al., 1998] and [Diologent et al., 2003], the lattice mismatch is $\lambda = -0.1\%$. The elastic moduli and the viscoplastic parameters have been taken from [Gaubert et al., 2010] (Tab. 4.1). For AM1, it has been shown that isotropic hardening is small ([Hanriot, 1993]) and therefore we neglect the hardening modulus H in our simulations.

In Fig. 4.3, the curve σ vs. ε predicted with the parameters in Tab. 4.1 for the γ bulk phase is compared to the experimental tensile curve of [Espíe, 1996], with $\dot{\varepsilon}_{11} = 9 \cdot 10^{-4} \text{ s}^{-1}$. As expected, an excellent agreement is achieved. Assuming a perfectly elastic behavior for γ' , and using the viscoplasticity parameters for γ without plastic length ($\tilde{L}_p = 0$), the calculations (dashed black) underestimate the mechanical behaviour of the two-phase alloy as compared to experiments

	C_{11} (GPa)	C_{12} (GPa)	C_{44} (GPa)	C (GPa)	D	N	K (MPa.s $^{\frac{1}{N}}$)	R^0 (MPa)
γ	197	144	90	150	1900	5	150	86
γ'	193	131	97	150	1900	5	150	$1.05 \cdot 10^5$

TABLE 4.1 – Elastic moduli ([Gaubert et al., 2010]) and viscoplastic parameters at $T = 950^\circ\text{C}$. The parameters of γ have been identified from macroscopic experiments ([Espíe, 1996, Gaubert et al., 2010]).

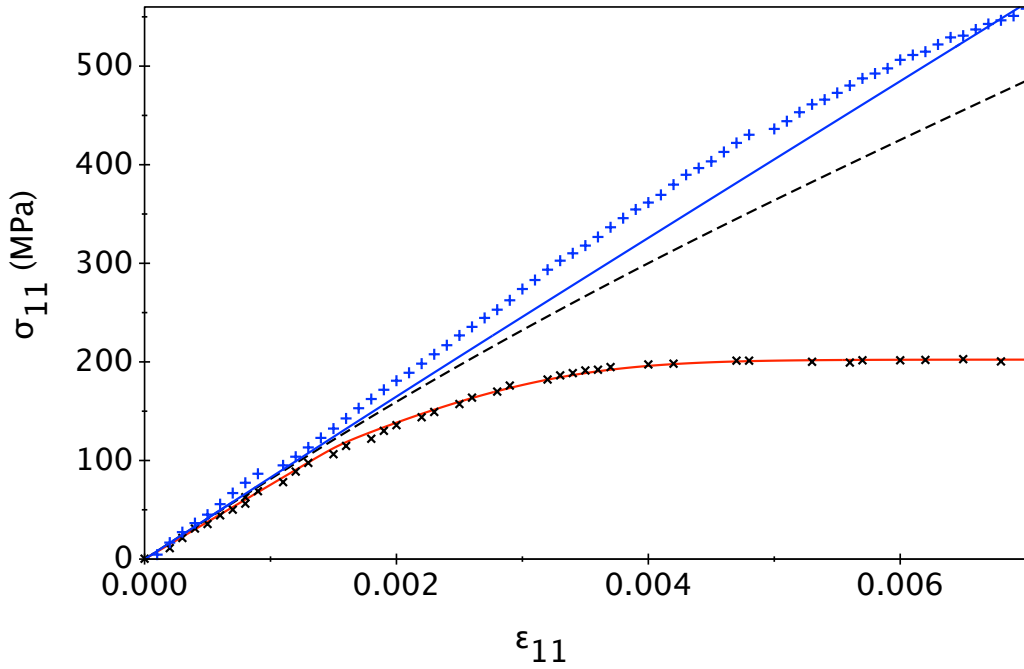


FIGURE 4.3 – Stress-strain curves at $T = 950^\circ\text{C}$ of the bulk γ phase ($\dot{\epsilon}_{11} = 9 \cdot 10^{-4} \text{ s}^{-1}$) and of the AM1 superalloy ($\dot{\epsilon}_{11} = 10^{-3} \text{ s}^{-1}$). The tensile axis is parallel to the [100] crystallographic direction. Experimental measurements are represented by \times symbols for pure γ and by blue $+$ symbols for AM1 ([Espíe, 1996, Gaubert et al., 2010]). PFM results with lines in red for pure γ ; in dashed black ($\tilde{L}_p = 0$) or blue ($\tilde{L}_p = 26 \text{ nm}$) for AM1.

(blue $+$) : at $\epsilon = 0.07\%$, $\sigma \approx 480 \text{ MPa}$ is below the experimental value $\sigma \approx 560 \text{ MPa}$. This difference can be attributed to the confinement of plasticity in γ which strengthens the material. This demonstrates the necessity of including a plastic size effect to predict more quantitatively the flow stress curve of AM1 superalloys.

This strengthening is introduced in the viscoplastic model by tuning the additional parameter A . We have chosen $A = 5 \cdot 10^7 \text{ MPa.nm}^2$ corresponding to $\tilde{L}_p = 26 \text{ nm}$, which is half the γ channel width. For such a value, a better agreement is achieved with the measurements as shown in Fig. 4.3. It is worth noting that increasing \tilde{L}_p such that $\tilde{L}_p \gg s$ makes γ behave purely elastically : the mechanical behavior of the two-phase alloy becomes closer to a linear elastic behavior with a slope corresponding to the slope at the beginning of the tensile curves in Fig. 4.3. The present method could be used to identify \tilde{L}_p , provided that the elastic constants of the γ and γ' phases have been accurately obtained.

Finally, the softening effect, characterized by a decrease of the flow stress shortly after the beginning of yielding often observed in single crystal Ni-base superalloys, is not accounted

for in our model ([Levkovitch et al., 2006]). However, in the service conditions studied in the present work (small deformation rate), this softening is hardly visible for the AM1 superalloy ([Espíe, 1996, Gaubert et al., 2010]).

4.3.2 Microstructural evolution coupled to a viscoplastic activity

In this section, the rafting (directional coarsening) of γ' precipitates in AM1-type superalloy under creep loading is investigated with the coupled phase field method/viscoplastic model. In particular, the question of whether the size effect has an influence or not on the transformation kinetics and on the morphological evolution is addressed. It must be stressed that this alloy is particularly well suited for this purpose because plastic activity is only observed within the γ channels, at temperatures around 950°C - 1050°C . We have proceeded in two steps : (i) first, a typical cuboidal microstructure is generated accounting for elasticity only, with no applied stress. (ii) Second, the evolution of this microstructure during the creep experiment is investigated.

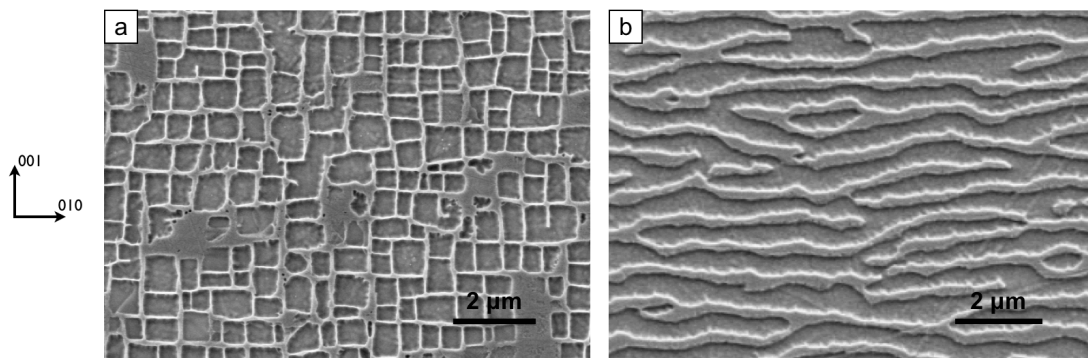


FIGURE 4.4 – SEM observations of AM1 : (a) - before aging (b) - after a 72 h creep experiment under 150 MPa along the [001] axis at $T = 1050^\circ\text{C}$ ([Gaubert et al., 2010]).

4.3.2.1 Initial cuboidal microstructure and elastic parameters

The cuboidal microstructure is achieved using the PFM presented in §4.2. The only required input parameters are the interfacial energy ($\sigma_{\text{exp}} = 2 \text{ mJ/m}^2$), the misfit ($\lambda = -0.1\%$) and the elastic constants. The choice of the elastic constants is detailed in the following paragraph. As shown in [Gaubert et al., 2010], if we use the γ/γ' elastic moduli available in the literature for the AM1 at $T = 950^\circ\text{C}$ (Tab. 4.1), the PFM predicts the formation of an anisotropic microstructure where the γ/γ' interfaces are aligned along the cubic directions. However, this microstructure contains many γ' precipitates of irregular shape which are rarely observed in AM1. A systematic study in [Hu and Chen, 2001] has shown the importance of the inhomogeneity of the shear elastic constant $C' = (C_{11} - C_{12})/2$ on the microstructure formed. Microstructures made of well aligned cuboidal precipitates, as observed in AM1, can be generated only when the inhomogeneity of C' is large enough. This suggests that the difference of about 10% in C' between γ and γ' obtained in ([Gaubert et al., 2010]) is underestimated. The inaccuracy of the measurements can be attributed to the inverse process used to infer the elastic constants of each phase from the behaviour of the two-phase alloy ([Fahrman et al., 1999, Sieborger et al., 2001]). For that reason, we have increased the inhomogeneity of C' up to 40% while keeping the same elastic anisotropy $2C_{44}/(C_{11} - C_{12}) = 3.3$. This has been carried out by changing $C_{12}^{\gamma'}$ to 118 GPa and $C_{44}^{\gamma'}$ to 124 GPa, keeping all other moduli in Tab. 4.1 unchanged.

The initial cuboidal microstructure was generated in the elastic regime from an initial disordered γ phase with stress-free boundary conditions. The total size of the 2D system is $2.3 \times 2.3 \mu\text{m}^2$ discretized with 512^2 nodes. The last stage of the formation process is shown in Fig. 4.5.(0) where the grey corresponds to the γ matrix and the different colors are related to the four translational variants of the γ' phase. After 16 h at 950°C , the microstructure consists of cuboidal precipitates, well aligned along the cubic directions, separated by well defined γ channels (Fig. 4.5.(0)). The initial volume fraction of γ' precipitates is 0.63 and their average size is 319 nm. The γ channels have an average size of 78 nm. This microstructure is in good agreement with microstructures observed in AM1. Finally, it is worth mentioning that slight modifications of the C' inhomogeneity has significant consequences on the microstructure. The necessity of a large enough C' inhomogeneity could be used in the future as a new ingredient to improve the inverse process designed for the determination of the elastic constants of the γ and γ' phases.

4.3.2.2 Rafting under creep

In the second step, a constant stress $\sigma^a = 150 \text{ MPa}$ has been applied to the microstructure in Fig. 4.5.(0) along the horizontal axis, while holding temperature at 950°C . In order to test the influence of the plastic characteristic length on the microstructure evolution, three different creep simulations have been performed. First, a purely elastic case has been considered (Fig. 4.5.(a)-(d)). Second, an elasto-viscoplastic one without size effect (Fig. 4.5.(h)-(j)) was completed to make a full comparison with the last one where the plastic size effect are accounted for (Fig. 4.5.(e)-(g)). As in Section 4.3.1.2, \tilde{L}_p is set to 26 nm. This value corresponds to one third of the initial average channel width.

For all evolutions in Fig. 4.5, the microstructure tends towards a morphology of rafts aligned along the same direction perpendicular to the tensile axis. This is in agreement with previous studies of creep along one cubic direction showing that the elastic and plastic driving forces lead to the same raft orientation ([Boussinot et al., 2010, Zhou et al., 2008]). Comparing the elastic and plastic cases clearly shows that viscoplasticity has two major impacts on the evolution. First, it influences the kinetics : the formation of the rafts is faster when plastic activity is accounted for. This behavior is clearly demonstrated by the splitting of the larger precipitate observed in the first and row in Fig. 4.5. The splitting happens at $t = 3.5 \text{ h}$ with viscoplasticity (Fig. 4.5.(h)) and at $t = 5.8 \text{ h}$ without viscoplasticity (Fig. 4.5.(b)).

Second, at a stage where straight rafts are observed in the elastic case, the microstructure in the plastic simulation is still wavy. This feature is in agreement with a previous study using an anisotropic viscoplastic model ([Gaubert et al., 2010]). Furthermore, in the late stage of the viscoplastic simulation, the evolution becomes hardly noticeable and the microstructure is almost frozen (last column in Fig. 4.5), while in the elastic case it is still evolving to give flat rafts after $t = 72.6 \text{ h}$ (Fig. 4.5.(d)). Finally, it can be noted that the volume fraction of γ' decreases slightly with viscoplasticity : at $t = 36.3 \text{ h}$, $\tau_{\gamma'} = 0.59$ in the elastic case whereas $\tau_{\gamma'} = 0.57$ and $\tau_{\gamma'} = 0.55$ in the viscoplastic cases with $\tilde{L}_p = 26 \text{ nm}$ and $\tilde{L}_p = 0$, respectively.

4.3.2.3 Influence of the plastic length scale

The comparison between the middle and right columns shows the influence of the characteristic plastic length \tilde{L}_p . Again, the kinetics of rafting is estimated with the time necessary for the large precipitate to split into two smaller precipitates. When $\tilde{L}_p = 26 \text{ nm}$, splitting occurs at a later time ($t = 4 \text{ h}$) than when $\tilde{L}_p = 0$ ($t = 3.5 \text{ h}$). Therefore, the plastic length slows down the raft formation and gives a kinetics closer to the elastic case. This behavior is expected because the plastic length leads to an increase in flow stress and therefore to a decrease of plastic

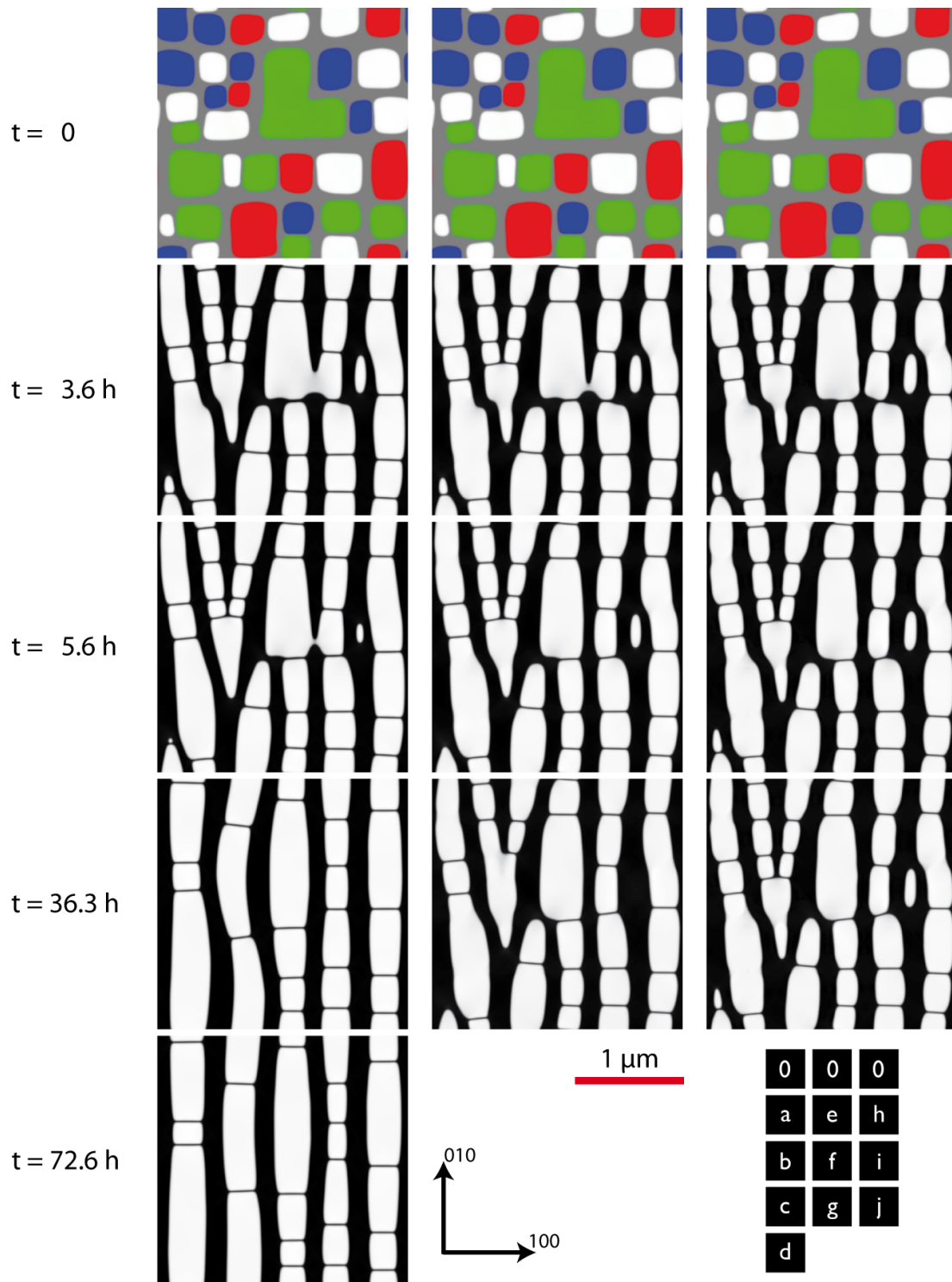


FIGURE 4.5 – Starting from the initial microstructure generated under stress-free conditions (0), microstructure evolutions under a constant tensile stress along the [100] axis (150 MPa) predicted by : (a)-(d) the elastic PFM; (e)-(g) the elasto-viscoplastic PFM including size effect ($\tilde{L}_p = 26$ nm); (h)-(j) the elasto-viscoplastic PFM ($\tilde{L}_p = 0$). The shade of grey are in accordance with the value of the concentration field $c(\underline{r}, t)$; the white and black areas represent the γ' and γ phase, respectively. The nomenclature of the images is indicated in the lower right corner.

activity. Furthermore, as already noted when $\tilde{L}_p = 0$, the microstructure evolution predicted with $\tilde{L}_p = 26$ nm is almost frozen after the formation of the rafts (Fig. 4.5.(g)). The frozen configurations obtained in the two viscoplastic cases (Fig. 4.5.(g) and 4.5.(j)) are rather similar : the plastic length has moderate consequences on the morphological evolution at long time for the particular evolution considered. Still, a few differences are noticeable. Some small precipitates have dissolved when $\tilde{L}_p \neq 0$ but they can still be observed when $\tilde{L}_p = 0$. Moreover, as already mentioned, $\tau_{\gamma'}$ is slightly larger with plastic length than without, resulting in slightly smaller γ channels.

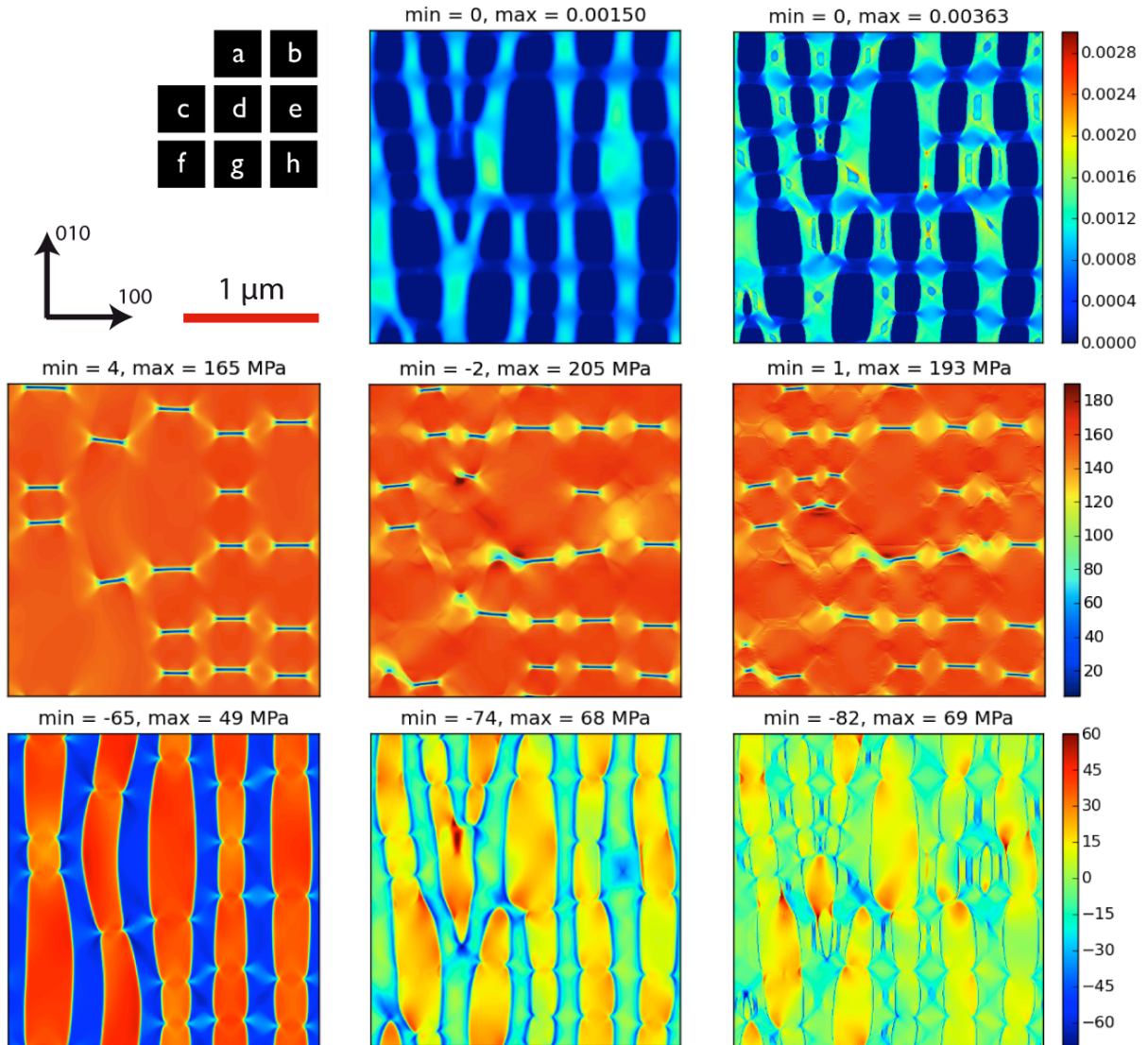


FIGURE 4.6 – Plastic and elastic fields obtained at $t = 36.3$ h in the elastic model (first column), in the elasto-viscoplastic model including size effect (middle column) and in the elasto-viscoplastic model where $\tilde{L}_p = 0$ (last column). The first row is the cumulative plastic strain field p and the second and third row are the stress components σ_{11} and σ_{22} , respectively. The nomenclature of the images is indicated in the upper left corner.

The difference between the two viscoplastic cases is more obvious when considering the plastic fields, e.g. the cumulated plastic strain p at $t = 36.3$ h (first row in Fig. 4.6). As expected, plastic activity is confined in γ , mainly in the vertical channels in both cases. When $\tilde{L}_p = 0$,

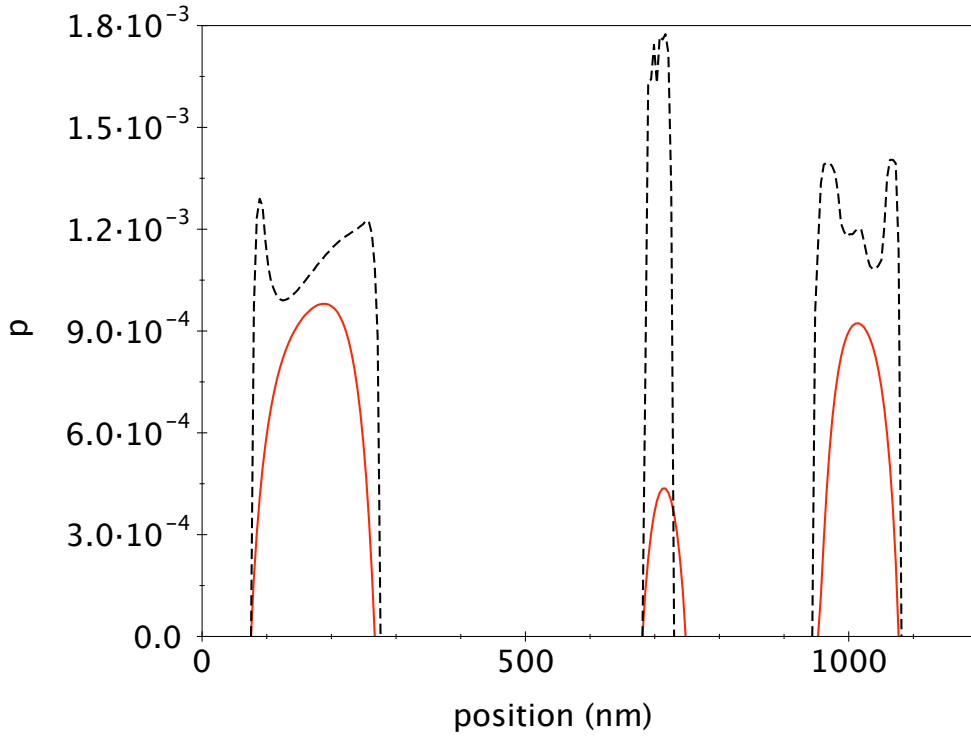


FIGURE 4.7 – Profiles of the cumulative plastic strain perpendicular to the rafts at $t = 1$ h: $\tilde{L}_p = 0$ (dashed line); $\tilde{L}_p = 26$ nm (full red line).

p is almost homogeneous in all the vertical γ channels (Fig. 4.6.(b)). The plastic length introduces several differences with conventional viscoplasticity (Fig. 4.6.(a)-(b)). (i) Plastic activity becomes weaker due to the increase in flow stress. (ii) The decrease of p is more pronounced in the thin channels than in the large ones (Fig. 4.6.(a)). (iii) p varies more smoothly. These features are also clearly observed with the profile of p perpendicular to the rafts (Fig. 4.7). The variations of p along the profile are smoother and smaller when $\tilde{L}_p = 26$ nm (full red line) than when $\tilde{L}_p = 0$ (dashed line). Large channels are less sensitive to the plastic length than small ones : when $\tilde{L}_p = 0$, $p \approx 1.2 \cdot 10^{-3}$ in all the channels; when $\tilde{L}_p = 26$ nm, $p \approx 9.8 \cdot 10^{-4}$ in the center of channels 190 nm wide, and decreases to $p \approx 4.9 \cdot 10^{-4}$ in channels 75 nm wide. Finally, it can be noticed that small regions at the center of the vertical channels (Fig. 4.6.(b) and 4.7) display plastic singular behaviors. The origin of their formation will be discussed at the end of the section.

Maps of the stress components σ_{11} (Fig. 4.6.(c)-(e)) and σ_{22} (Fig. 4.6.(f)-(h)) for the three different situations at $t = 36.3$ h are presented in Figure 4.6. For the elastic model, the σ_{11} component is nearly homogeneous through all the material with a value close to the applied stress σ_{11}^a . The homogeneity of σ_{11} is nothing but the consequence of mechanical equilibrium in a microstructure whose interfaces are perpendicular to the [100] direction. The only small heterogeneities of the σ_{11} field are in the horizontal channels where the value of σ_{11} is much smaller. Since the horizontal channels accommodate the misfit between the two phases ($\lambda < 0 \rightarrow a_\gamma > a_\gamma'$) they are submitted to smaller local stresses. This point is also true in the viscoplastic simulations because, as detailed above, plastic activity is negligible in the horizontal γ channels. Their behavior can be considered as an elastic one. Contrary to the σ_{11} maps, the σ_{22} maps are very different in the three simulations. $|\sigma_{22}|$ has a much higher value in the elastic simulation. For both viscoplastic simulations, after a sufficient time, we observe a relaxation of

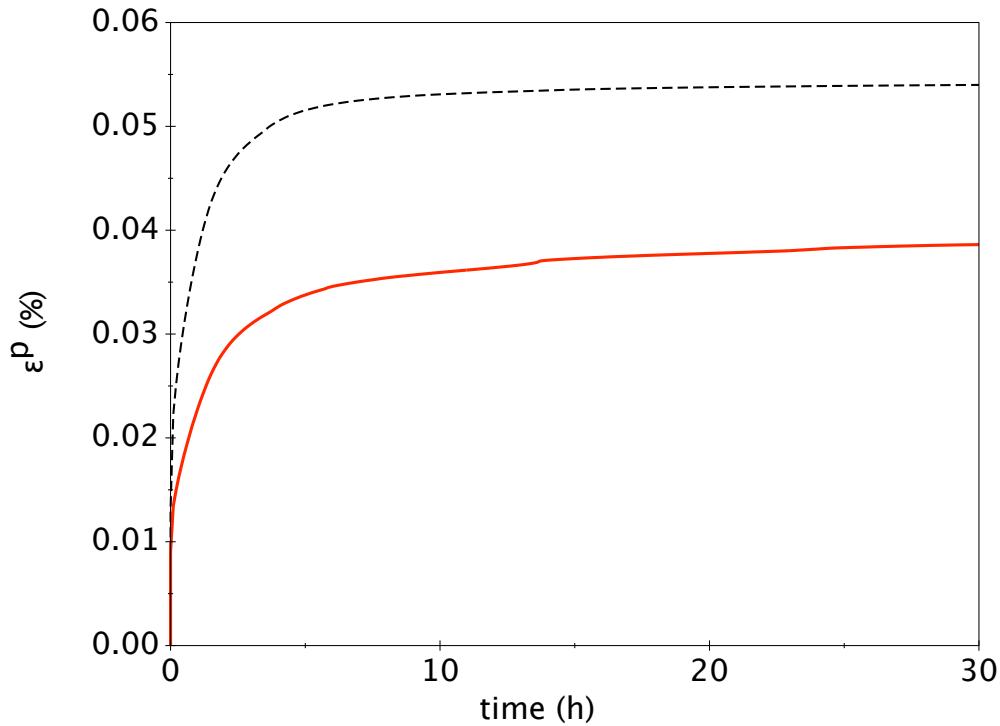


FIGURE 4.8 – Average plastic strain vs. to time obtained from simulated creep experiment at $T = 950^\circ\text{C}$ under 150 MPa : $\tilde{L}_p = 0$ (dashed line) ; $\tilde{L}_p = 26$ nm (full red line).

the σ_{22} stress component (Fig. 4.6.(f)-(h)) resulting from the plastic deformation of the γ channels. The behavior of σ_{33} (not shown) is qualitatively the same. These differences in σ_{22} and σ_{33} are the result of the previously described differences in the plastic field p and they explain the variations in kinetics observed between the three simulations in Figure 4.5.

In Fig. 4.8, the average plastic strain $\underline{\epsilon}^p$ is plotted vs. time for the two viscoplastic cases. In both cases, a primary creep stage featuring a rapid increase of $\underline{\epsilon}^p$ is observed when $t < 5$ h. At the end of this stage, a rafted microstructure can be observed (Fig. 4.5.(e)-(h)). For $t > 5$ h, the evolution of $\underline{\epsilon}^p$ becomes slow and almost linear. During this secondary creep stage, the microstructure remains stable in time (Fig. 4.5.(g)-(j)). The time at which the secondary creep stage begins as well as the value of the plastic strain plateau are consistent with experiments on AM1 superalloys obtained in similar creep conditions ([Diologent, 2002]). As expected, introducing the size effect results in a strengthening of the material : $\underline{\epsilon}^p$ is smaller with $\tilde{L}_p = 26$ nm (full red line) than with $\tilde{L}_p = 0$ (dashed line). The difference is more important during the primary creep stage when the microstructure still features a large distribution of γ channels widths. During the secondary creep stage, the microstructure exhibits well defined rafts. Plastic activity develops inside rather large vertical γ channels which are barely affected by the size effect. This explains the rather similar plastic behavior of the two viscoplastic models in the secondary creep stage.

During the creep experiment, a widening of the γ channels is observed leading to a decrease of the plastic size effects, in accordance with 1D calculations (§4.3.1.1). In addition, the kinematic hardening variable X evolves rapidly during the first stages of the experiment and reaches a plateau after 5 h in both simulations. The saturation value is found very close to the value $2C/3D$ expected in a 1D configuration. Note finally that after 5 h a slow evolution of both ϵ_{11}^p and X_{11} can still be observed for $\tilde{L}_p \neq 0$ but not for $\tilde{L}_p = 0$.

Note that in Fig. 4.8, there is no tertiary creep stage since the physical mechanisms responsible

of the phenomenon are not included : the shearing of the γ' precipitates and the internal crack initiation resulting from porosity ([Maclachlan et al., 2001]).

Finally, we discuss the origin of the slight differences in plastic behavior which can be observed at the center of the γ channels. These regions are visible in Figure 4.6.(b) (also in Figure 4.7) when $\tilde{L}_p = 0$ and subsist during microstructure evolution. The plastic strain inside these regions remains rather constant and the ulterior plasticity takes place around these areas. Note that the presence of these areas does not seem to impact significantly microstructure evolution, probably because they are not located close to the γ/γ' interfaces. These regions are not observed in experiments. These artifacts disappear when a plastic size effect, which regularises the plastic rate, is operating.

4.4 Conclusion

An extension of a phase field model has been proposed, which captures microstructure evolutions coupled to viscoplasticity. In particular, the model accounts for the size effect of the plastic behavior beyond the volume fraction effect, i.e. for the hardening (resp. softening) induced by the decrease (resp. increase) of the size of the plastic regions. This effect may be rather important in heterogeneous materials because the size and the shape of the plastic regions evolve during thermo-mechanical treatments. To our knowledge, the plastic size effect had never been introduced in a phase field model using a continuous approach. The viscoplastic behavior is introduced at mesoscale using a strain gradient approach and is coupled to a phase field model within a thermodynamic consistent framework. The model has been applied to the microstructural evolution in Ni-base superalloys in creep conditions during which plasticity only proceeds inside the γ phase. The parameters of the model have been selected to mimic the behavior of the AM1 monocrystalline superalloy. We have assumed that plasticity in the γ channels can be described by continuum strain gradient viscoplasticity, in spite of their very small width. Several important physical phenomena, such as the ordered character of the γ' phase, the elastic inhomogeneity and anisotropy, the misfit, the hardening and the viscosity of the plasticity are included in the model.

Static configurations have first been used to emphasize the influence of the plastic size effect on the mechanical behavior of heterogeneous materials and to properly define the internal length scale of the plastic model. Then, two dimensional simulations have been performed to investigate the influence of the plastic size effect on the microstructural evolution during creep loading along a cubic axis. It has been found that plastic activity accelerates the formation of the rafts and leads to an almost frozen configuration of wavy rafts. Comparing the simulation results including or ignoring the plastic size effect, we have shown that, *in these alloys*, the size effect has only a moderate impact on the morphological evolution but is crucial to reproduce the macroscopic mechanical behavior of the material.

The model proposed in this chapter will be extended to include plastic anisotropy and three dimensional simulations will be performed. In particular, in the context of Ni-base superalloys, this extension will open the possibility to investigate the microstructural evolution during creep experiments along complex loading axis.

Phase field and Crystal Plasticity : Application to oxidation of austenitic strainless steels single crystals under mechanical load

Contents

5.1	Introduction	99
5.2	Oxidation induced damage	100
5.3	Stress oxidation phase field model	101
5.3.1	Phase field variables	101
5.3.2	Free energy potential	102
5.3.3	Grain boundary description	103
5.3.4	Mechanical contribution to the free energy potential	103
5.3.5	Damage strain	104
5.3.6	Homogenisation and evolution equations	105
5.4	Simulation of intergranular oxide growth	107
5.4.1	Initial and boundary conditions	107
5.4.2	Materials parameters	108
5.4.3	Accelerated growth along a grain boundary	108
5.4.4	Concentration fields of oxygen and chromium	109
5.5	Intergranular oxide growth, and crack initiation	111
5.5.1	Oxidation-induced internal stresses	111
5.5.2	Effect of a creep load on the damage behaviour	115
5.6	Conclusions	115

5.1 Introduction

The present work, which provides an original consistent framework for combining different nonlinear constitutive laws by homogenization rather than by mixing the material parameters, is suitable for the material evolution at a mesoscale. It typically applies at the grain scale in a polycrystal where the continuum crystal plasticity has proved in many cases to provide a reliable description of slip processes. Individual dislocations are not resolved but rather represented by suitable densities.

In fact, the crystal plasticity theory that accounts for grain boundaries, crystal orientations and anisotropic nonlinear response of single crystals and polycrystal materials is essential to improve the evaluation of local strain and stress heterogeneities that develop in the grains of a polycrystal during overall homogeneous deformation. In order to account for a variety of additional phenomena, like damage, precipitation, diffusion-creep, dislocation pile-ups, grain boundary sliding, etc..., an extension of the present model was proposed by incorporating the continuum crystal viscoplastic framework in the diffuse interface approach.

In the case of multi-phase metallic alloys, The description of crystals plasticity is very difficult because slip systems of dislocations usually differ from one phase to the other, and because the microstructure evolution and the dislocations dynamics are in principle coupled through the stress fields generated in the material. The introduction of crystal plasticity into phase field models goes back to works by [Gaubert et al., 2008, Gaubert et al., 2010, Cottura et al., 2012] for single crystals and by [Abrivard et al., 2012b, Abrivard et al., 2012a] for polycrystals, including grain boundary migration. Because plasticity in crystals is mainly due to the movement of one-dimensional crystal defects called dislocations, several works have explicitly introduced mobile dislocations in a PFM ([Rodney et al., 2003, Wang et al., 2001, Koslowski et al., 2002]) using an analogy between a dislocation loop and a thin precipitate. Dislocations are described with continuous fields for each slip system. The main advantage of this framework is that the elastic interactions between dislocations and/or precipitates are automatically accounted for. But it has two major flaws : (i) first, the dislocations cores spread over several grid spacings : consequently realistic short-range interactions between dislocations require either subnanometer grid spacings, or a discrete description as in [Rodney et al., 2003]. (ii) Second, mechanisms other than dislocations glides (e.g. climb and cross slips at high temperatures, or twinning in materials with low stacking faults energy) are not accounted for currently.

To circumvent these drawbacks, crystal plasticity theory can be rather easily incorporated in the phase field approach [Gaubert, 2009], using the general framework, proposed in this work. Plasticity can be introduced into PFMs through plastic strain field defined at mesoscale, where additional internal hardening variables and scalar dislocation densities are introduced to describe the slips on crystallographic systems. As usual in continuum mechanics, evolution equations in the form of ordinary differential equations are postulated to describe plastic flow and hardening the material volume element with parameters identified from experimental data. This approach has the advantage to phenomenologically include all the physical processes at the origin of plasticity. Works along this route have been only very recently proposed by several groups using mesoscale plasticity models differing by their descriptions of hardening, viscosity and plastic anisotropy.

The present chapter has been devoted to the formulation of a generic multicomponent-stress phase field framework, which accounts for the viscoplastic deformation of the phases using the homogenisation based phase field modelling framework [de Rancourt et al., 2016], in order to model phase transformation coupled with crystal plasticity and multicomponent diffusion. The framework accounts for several microstructural phenomena : multi-component diffusion, diffusion short circuits and anisotropy, grain boundary, surface energies, isotropic and anisotropic viscoplastic relaxation and damage.

The model is used to simulate the growth of oxide intrusions along grain boundaries. The framework allows the investigation of stress relaxation within oxide layers, which phenomenon can be induced by diffusion. The finite element simulations show that tensile stresses appear progressively at the free surface of oxide intrusions. Such tensile stresses appear to be able to generate cracks at the free surface of oxidised grain boundaries. It appears that such cracks are frequently observed in the field of stress corrosion cracking and yet remain not well explained.

The model results in a possible and new stress intergranular oxidation induced failure mechanism. Finally, the damage initiation time is shown to depend on the applied tensile creep load. The structure of the present chapter is as follows : a multiphysics framework based on [de Rancourt et al., 2016] is first briefly described, then numerical simulations of the growth of oxide intrusions are performed. The results are finally discussed.

5.2 Oxidation induced damage

Oxidation-induced damage is a crucial phenomenon that must be accounted for to ensure the long-term safety of critical equipment or parts such as those found in the nuclear, aeronautic, oil and gas industries, etc. Corrosion resistant alloys can be used to mitigate such a delayed damage. However, stress corrosion cracking can still occur. Stress corrosion cracks are often observed to appear in the continuity of grain boundaries. Two main embrittlement mechanisms can be inferred. The first one is known as dynamic embrittlement [Krupp et al., 2014] where the grain boundary is rapidly opened by pushing the oxide intrusion – this cracking can be enhanced by the diffusion of spurious elements such as hydrogen – and the second is the brittle failure – possibly with low cracking rates – of the oxide intrusion. The latter has not been well understood up to now. This problem involves complex physics such as phase transformations and strong couplings between mechanics and multicomponent diffusion.

Oxide intrusions along grain boundaries and possibly slip bands as well – surface defects in general – act as the precursors of micro-cracks for which the causes are not well identified up to now. Under mechanical loads, they can act as stress increases in the metal phase [Evans, 1983, Morra, 1995]. The present work is devoted to the simulation of oxide intrusion growth.

Understanding stress corrosion cracking is challenging and would enable transport and industry to progress in terms of safety. Scientific challenges in this area are found in both experimental and modelling work. The typical crack growth curve, illustrated in Fig. 5.1, exhibits the following steps [Lee et al., 1988] : an incubation time during which cracking conditions are progressively generated, a crack initiation step during which the cracks are mostly nucleated on the free surface, and finally a propagation phase during which dominant cracks grow rapidly in the metal.

The incubation time has been shown to be thermally activated [Laghoutaris, 2009], which underlines the importance of diffusion. Understanding the growth and failure of oxide intrusions is therefore a key element in predicting stress-corrosion cracking. It has also been inferred that power-law creep phenomena could also be responsible for the initiation of cracks [Krupp et al., 2014] but to the knowledge of the author, no firm experimental evidence has yet been found.

To date, modeling of the propagation phase has been performed at the macroscopic scale [Shoji et al., 2010]. The incubation phase has been first investigated by [Fisher, 1951] and followers [Mishin and Yurovitskii, 1991, Balluffi, 1992, Mishin and Herzig, 1999, Mishin, 2001] while tackling the problem of grain boundary diffusion. The initiation phase has been discussed in [Evans, 1983].

In parallel, stress-diffusion coupled problems have been investigated, *e.g.* [Krishnamurthy and Srolovitz, 2003, Beke et al., 2004, Favergeon et al., 2005, Krishnamurthy and Srolovitz, 2004, Zhou, 2010, Zhou et al., 2010a, Zhou et al., 2010b, Zhou et al., 2010c], which mainly rely on

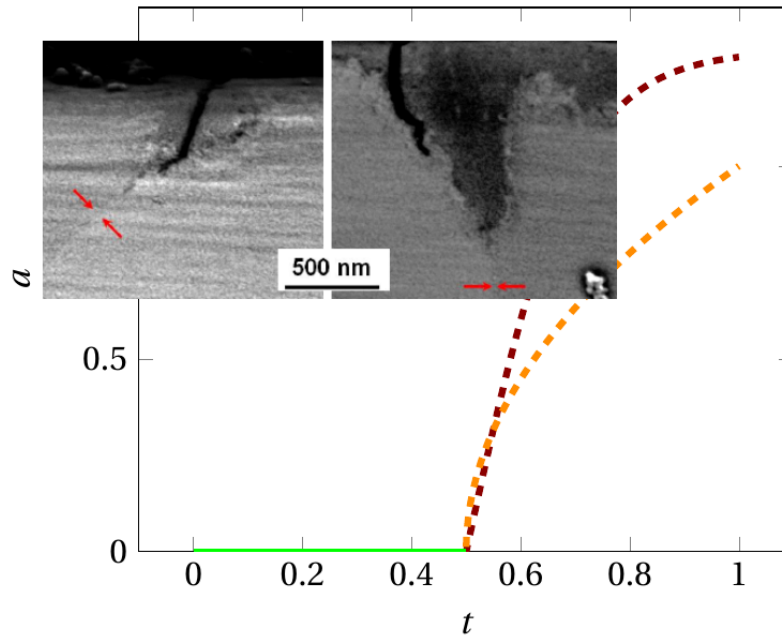


FIGURE 5.1 – Schematic representation of crack growth curves in the vicinity of intergranular oxides intrusions [Wehbi, 2014]. The initiation time is arbitrary set to 0.5.

the theory of [Larché and Cahn, 1985]. The mechanical behaviour of the oxide layers has been investigated by [Huntz et al., 1993, Goedjen et al., 1994, Huntz et al., 1998, Mougín et al., 2001, Huntz et al., 2002, Mougín et al., 2003].

Nevertheless, no model is yet able to describe the complexity of the growth and failure of oxide intrusions. Further understanding will therefore be the result of the comprehensive constitutive modelling of oxidation at the grain scale, which has been initiated by [Zhou et al., 2010c][Auinger et al., 2011] and [Zhou, 2010]. The present work is in continuity with these works.

Thus, this chapter aims to simulate both incubation and initiation stages of intergranular oxidation embrittlement by means of the phase field method applied to oxide growth, [Ammar et al., 2009a]. The growth of chromia in polycrystalline austenitic stainless steel is modelled by means of a phase field variable ϕ , which is coupled with multi-component diffusion, stresses and an additional static grain boundary phase field η

5.3 Stress oxidation phase field model

5.3.1 Phase field variables

A phase field ϕ is used to simulate the growth of an oxide phase within a polycrystalline metallic phase. ϕ is set to 1 in the oxide phase and 0 in the metal phase and varies continuously and rapidly at the metal-oxide interface hence resulting in a so-called diffuse interface. The evolution of ϕ is governed by the Allen-Cahn equation, which enforces the chemical equilibrium between the oxide and metal phases. Additional static phase field variables, η and θ [Abrivard et al., 2012b, Abrivard et al., 2012a], are also used to account for the grain boundary and will further be coupled with diffusion and stresses. The field η represents the loss of crystallinity within the grain boundary; it is equal to 1 inside the grain boundary and zero inside a grain. The field θ represents the in-plane tilt angle. Finally, a single diffuse interface width is used throughout

the work for simplicity.

Due to the complexity and variety of oxide phases usually reported in austenitic stainless steels, *e.g.* [Kjellqvist et al., 2008], this work is necessarily restricted to the growth of chromia, which is the oxide phase of interest within austenitic stainless steels, on austenite. In such a case, oxide growth is driven by the transport of oxygen anions and the supply of chromium cations from the free surface and the base metal, respectively, at the metal-oxide interface. Such components are therefore explicitly accounted for, while the remaining iron and additional alloying components such as nickel are included in the complementary concentration.

5.3.2 Free energy potential

The evolution equations within the phase field modelling are derived from an enhanced free energy potential, which depends on both the phase field and its gradient coupled with different physics, diffusion and mechanics, *etc.* The free energy potential is defined as follows,

$$f = f^\phi(\phi) + f^{\text{ch}}(\phi, c_\psi) + f^{\text{u}}(\phi, \boldsymbol{\varepsilon}_\psi) + f^{\text{GB}}(\phi, \eta), \quad (5.1)$$

where f^ϕ is the interface free energy, that stems from the regularisation of the interface energy [Kim et al., 1999], which embeds a double well function and a gradient energy term :

$$f^\phi = 3\Lambda \left(\frac{2z}{\delta} W + \frac{\delta}{2z} \nabla\phi \cdot \nabla\phi \right), \quad (5.2)$$

where $W = \phi^2(1-\phi)^2$ is the double well function, Λ is the interface energy, δ is the interface thickness and z a parameter set to $\log(0.95/0.05)$ [Kim et al., 1999]. Finally, f^{ch} and f^{u} are the bulk free energies for chemistry and mechanics, respectively. Such bulk free energies rely on a homogenization-based framework [Ammar et al., 2009b, Ammar et al., 2014, de Rancourt et al., 2016]. In such models, state variables and thermodynamic forces are extended over the whole volume of the study domain, resulting in virtual fields outside the considered phase. Then, non-linear mixture rules are postulated to obtain volume-averaged quantities. Bulk potentials are obtained as follows :

$$f^{\text{ch, u}} = h(\phi) f_{\text{ox}}^{\text{ch, u}} + \bar{h}(\phi) f_\gamma^{\text{ch, u}} \quad (5.3)$$

where $f_{\text{ox}}^{\text{ch, u}}$ and $f_\gamma^{\text{ch, u}}$ are the potentials of the individual phases for the chemical and mechanical free energies. $h(\phi) = \phi^2(3-2\phi)$ is the mixture rule used in the model and $\bar{h}(\phi) = 1 - h(\phi)$.

The chemical bulk free energies of the individual phases are taken as quadratic potentials for simplicity :

$$f_\psi^{\text{ch}} = \frac{1}{2} \sum_{i=\{\text{Cr, O}\}} k_\psi^i \left(c_\psi^i - a_\psi^i \right)^2. \quad (5.4)$$

The field $\psi = \{\text{ox}, \gamma\}$ is used throughout this work to refer to the oxide and metal phases. k^i are the energy curvature parameters and a^i are the concentration at stoichiometry. This assumption along with the homogenization approach greatly simplifies the numerical solving of the diffusion problem [Kim et al., 1999]. Logarithmic chemical free energy densities are more accurate, but the quadratic potentials are suitable if local concentrations are limited to small variations. It has been verified that the present two phase system, Oxide- γ , was in good agreement with experimental and calculated phase phase diagrams [Laheij et al., 1980, Kjellqvist et al., 2008, Kjellqvist and Selleby, 2009].

5.3.3 Grain boundary description

Two additional static phase fields η and θ are used to describe the grain boundary [Abrivard et al., 2012b, Abrivard et al., 2012a]. The grain boundary field η is based on a smoothed version of Fisher's grain boundary model [Fisher, 1951]. The orientation field θ accounts for the change of orientation throughout the grain boundary. Their thicknesses are equal to the interface thickness of the phase field for simplicity. Diffusivities within both metallic and oxide phase are then coupled with the field η . They are greater in such a diffuse grain boundary. The normal vector of the grain boundary $\underline{n}^{\text{GB}} = \frac{\nabla\theta}{\|\nabla\theta\|}$ is also used to take the diffusion anisotropy inside the grain boundary into account by equating the normal diffusivity to the bulk diffusivity of the alloy and the diffusivities in the plane with the grain boundary diffusivities, thus improving the description of the crystalline structure of the grain boundaries [Mishin and Yurovitskii, 1991]. The grain boundary free energy finally reads :

$$f^{\text{GB}} = \bar{h}(\phi)\chi\eta, \quad (5.5)$$

where χ accounts for the grain boundary excess energy in the form of an energy density. Future works may include a dependency of the grain boundary energy on the grain boundary orientation mismatch and segregation [Prokoshkina et al., 2013, Raabe et al., 2014].

5.3.4 Mechanical contribution to the free energy potential

First, a strain partitioning intrinsic to each phase ψ is assumed as follows,

$$\underline{\epsilon}_\psi = \underline{\epsilon}_\psi^e + \underline{\epsilon}_\psi^p + \underline{\epsilon}_\psi^* + \underline{\epsilon}_\psi^d, \quad (5.6)$$

where $\underline{\epsilon}$ is the total strain tensor, $\underline{\epsilon}^e$ the elastic strain tensor, $\underline{\epsilon}^p$ the plastic strain tensor, $\underline{\epsilon}^*$ the eigenstrain tensor related to the phase transformation and $\underline{\epsilon}^d$ a damage related strain tensor.

An additional anisotropic transformation strain analogous to [Clarke, 2002, Huntz et al., 2002] is included in the strain partitioning of the oxide phase, while the transformation strain of the metal phase is set to zero. It reads :

$$\underline{\epsilon}_{\text{ox}}^* = \begin{pmatrix} 0.02 & 0 & 0 \\ 0 & 0.01 & 0 \\ 0 & 0 & 0.01 \end{pmatrix}, \quad (5.7)$$

Where the x axis is normal to the free surface. It describes the ability of the oxide phase to expand more in a unconstrained direction and to reduce the elastic energy induced by the volume expansion of the oxide.

A viscoplastic power law is adopted in the oxide phase to reproduce a diffusion-creep-based stress relaxation phenomenon, while a crystal plasticity framework is used in the metal phase as metal grains are explicitly modelled.

The driving force for plasticity in the oxide phase is the deviatoric stress, $\underline{\sigma}^{\text{dev}}$. The evolutionary equation of $\underline{\epsilon}_{\text{ox}}^p$ reads,

$$\dot{\underline{\epsilon}}_{\text{ox}}^p = \left\langle \frac{J2_{\text{ox}} - R_{\text{ox}}^0}{K_{\text{ox}}} \right\rangle^{n_{\text{ox}}} \frac{3}{2} \frac{\underline{\sigma}_{\text{ox}}^{\text{dev}}}{J2_{\text{ox}}}, \quad (5.8)$$

where

$$J2_{\text{ox}} = \sqrt{\frac{3}{2} \underline{\sigma}_{\text{ox}}^{\text{dev}} : \underline{\sigma}_{\text{ox}}^{\text{dev}}}, \quad (5.9)$$

is the second stress invariant – the von Mises stress.

$\underline{\sigma}_{\text{ox}}^{\text{dev}}$ is the deviatoric stress, n_{ox} and K_{ox} are viscosity related parameters and R_{ox}^0 is the yield stress.

The driving force for slip in the metal phase is the resolved shear stress $\tau_{\gamma}^s = \underline{\sigma}_{\gamma} : \underline{m}_{\gamma}^s$ for each slip system s with Schmid tensor \underline{m}_{γ}^s . The slip rate $\dot{\gamma}_{\gamma}^s$ reads [Cailletaud, 1992, Busso and Cailletaud, 2005],

$$\dot{\gamma}_{\gamma}^s = \left\langle \frac{|\tau_{\gamma}^s - x_{\gamma}^s| - R_{\gamma}^s}{K_{\gamma}} \right\rangle^{n_{\gamma}} \text{sign}(|\tau_{\gamma}^s - x_{\gamma}^s| - R_{\gamma}^s), \quad (5.10)$$

where $x_{\gamma}^s = C_{\gamma} \alpha_{\gamma}^s$, with C_{γ} a parameter, α_{γ}^s is the non linear kinematic hardening. Its evolutionary equation reads,

$$\dot{\alpha}_{\gamma}^s = \dot{\gamma}_{\gamma}^s - d_{\gamma}^v \alpha_{\gamma}^s |\dot{\gamma}_{\gamma}^s| \quad (5.11)$$

where d_{γ}^v is a parameter. The isotropic hardening is then provided by the following expression,

$$R_{\gamma}^s = S_{\gamma}^0 + \Delta S_{\gamma} \sum_r h_{\gamma}^{sr} [1 - \exp(-b_{\gamma} (\dot{\gamma}_{\gamma}^r)^{\text{acc}})] \quad (5.12)$$

where S_{γ}^0 , ΔS_{γ} and b_{γ} are the initial critical resolved shear stress and the hardening parameters; h_{γ}^{sr} is the interaction matrix accounting for both self and latent hardening induced by accumulated slip at slip systems. The accumulated slip is defined as follows,

$$(\dot{\gamma}_{\gamma}^s)^{\text{acc}} = |\dot{\gamma}_{\gamma}^s|. \quad (5.13)$$

Finally, the plastic strain rate is defined as follows,

$$\dot{\underline{\epsilon}}_{\gamma}^p = \sum_s \dot{\gamma}_{\gamma}^s \underline{m}_{\gamma}^s, \quad (5.14)$$

where,

$$\underline{m}_{\gamma}^s = \frac{1}{2} (\underline{l}_{\gamma}^s \otimes \underline{n}_{\gamma}^s + \underline{n}_{\gamma}^s \otimes \underline{l}_{\gamma}^s), \quad (5.15)$$

is the orientation tensor while \underline{l}_{γ}^s and \underline{n}_{γ}^s are respectively the glide direction and the normal direction for each slip system s . Within a two dimensional framework, fcc crystals can be reduced on a set of three effective slip systems [Flouriot et al., 2003, Shishvan et al., 2011] as described in Tab. 5.1 in the framework of the fcc crystal lattice,

\underline{n}_{γ}^s	\underline{l}_{γ}^s
(0, 1)	[1, 0]
$(\frac{1}{\sqrt{3}}, \frac{2}{\sqrt{3}})$	$[-\frac{2}{\sqrt{3}}, \frac{1}{\sqrt{3}}]$
$(\frac{1}{\sqrt{3}}, -\frac{2}{\sqrt{3}})$	$[\frac{2}{\sqrt{3}}, \frac{1}{\sqrt{3}}]$

TABLE 5.1 – Effective slip systems of a fcc crystal lattice in a two dimensional framework

5.3.5 Damage strain

Brittle damage is considered inside grain boundaries. It is modelled *via* a damage strain tensor $\underline{\epsilon}^d$. The driving force is chosen as the grain boundary opening traction [Dugdale et al.,

2013]. The damage framework stems from [Aslan et al., 2011]. The damage rate is defined as follows,

$$\dot{\boldsymbol{\epsilon}}_{\psi}^d = \dot{d}_{\psi} \underline{\mathbf{n}}^{\text{GB}} \otimes \underline{\mathbf{n}}^{\text{GB}}, \quad (5.16)$$

where $\underline{\mathbf{n}}^{\text{GB}}$ is the grain boundary normal vector already discussed and d a damage internal variable. The damage internal variable rate is in the form of a power law,

$$\dot{d}_{\psi} = \eta \left\langle \frac{|\boldsymbol{\sigma}_{\psi} : \underline{\mathbf{n}}^{\text{GB}} \otimes \underline{\mathbf{n}}^{\text{GB}}| - Y_{\psi}^d}{K^d} \right\rangle^{n^d} \text{sign}(\boldsymbol{\sigma}_{\psi} : \underline{\mathbf{n}}^{\text{GB}} \otimes \underline{\mathbf{n}}^{\text{GB}}), \quad (5.17)$$

where K^d and n^d are viscous regularisation parameters, η is the grain boundary phase field and Y_{ψ}^d is the fracture stress that decreases with increasing damage,

$$Y_{\psi}^d = \langle Y_{\psi}^{d0} + H_{\psi}^d \mathbf{d}_{\psi}^{\text{acc}} \rangle, \quad (5.18)$$

where H_{ψ}^d is a negative hardening modulus related to an embrittlement mechanism. The accumulated damage is finally calculated as follows,

$$\mathbf{d}^{\text{acc}} = |\dot{d}| \quad (5.19)$$

5.3.6 Homogenisation and evolution equations

Homogenisation rules are necessary to eliminate the additional degrees of freedom that are present in the current framework. Namely, either the two strain or the two stress tensors $\boldsymbol{\epsilon}_{\text{ox}}$, $\boldsymbol{\epsilon}_{\gamma}$, $\boldsymbol{\sigma}_{\text{ox}}$ and $\boldsymbol{\sigma}_{\gamma}$ must be reduced to a single unknown to then be solved by Cauchy's static equilibrium. As well, either the two concentration or the two diffusion potentials c_{ox}^i , c_{γ}^i , μ_{ox}^i and μ_{γ}^i of each component i must be reduced to a single unknown to then enable the solving of the mass balance. One can finally eliminate such additional degrees of freedom by assuming a relationship between the two thermodynamic forces or the two state variables. In mechanics, the Voigt and Reuss bounds can be used for instance.

For the concentration fields, one can use the pseudo-equilibrium relationship of [Kim et al., 1999] as a bound as follows,

$$\mu = \frac{\partial f}{\partial c} = \mu_{\text{ox}} = \mu_{\gamma}. \quad (5.20)$$

The pseudo-equilibrium along with quadratic chemical potentials is convenient in the sense that it leads to a straight relationship between the concentration fields c_{ox} and c_{γ} when quadratic chemical potentials are used. In the computation, only one of such field comes then as a degree of freedom.

Regarding mechanics, the Voigt scheme is chosen,

$$\boldsymbol{\epsilon} = \boldsymbol{\epsilon}_{\text{ox}} = \boldsymbol{\epsilon}_{\gamma}. \quad (5.21)$$

In such case, the two stress tensors $\boldsymbol{\sigma}_{\text{ox}}$ and $\boldsymbol{\sigma}_{\gamma}$ are independent, which allows the uncoupling of mechanical behaviours inside the interface and therefore eases the integration of nonlinear constitutive laws [de Rancourt et al., 2016].

Finally, the system of equations reduces into the Allen-Cahn equation as follows,

$$\dot{\phi} = M_{\psi} \left[3\Lambda \left(\frac{\delta}{z} \Delta \phi - \frac{2z}{\delta} W'(\phi) \right) + h'(\phi) \Delta \omega \right], \quad (5.22)$$

where

$$\Delta\omega = \left(f_{\text{ox}} - \sum c_{\text{ox}}^i\right) - \left(f_{\gamma} - \sum c_{\gamma}^i\right), \quad (5.23)$$

is the phase transformation driving force under the form of a grand potential difference between the oxide phase and metal phase, M_{ψ} is the interface mobility.

The total concentrations are subjected to the local balance of mass in the form :

$$\dot{c}^i + \nabla \cdot \underline{J}^i = 0, \quad (5.24)$$

The flux averaging relations are :

$$\underline{J}^i = -\left(h(\phi) L_{\text{ox}}^i + \bar{h}(\phi) L_{\gamma}^i\right) \nabla \mu^i, \quad (5.25)$$

so that effective mobilities can be defined as the average of the bulk diffusivities of the phases :

$$L^i(\phi) = h(\phi) L_{\text{ox}}^i + \bar{h}(\phi) L_{\gamma}^i. \quad (5.26)$$

where the diffusion mobilities L_{ψ}^i can be related to the diffusivities D_{ψ}^i as follows, in order to retrieve the generalized Fick law of diffusion :

$$L_{\psi}^i = D_{\psi}^i \left(\frac{\partial^2 f_{\psi}}{\partial c_{\psi}^i{}^2} \right)^{-1}. \quad (5.27)$$

where D^i are the diffusivities; in the current homogenisation framework, the mass balance can be solved only regarding the concentrations of the oxyde related concentrations.

The Cauchy static equilibrium reads,

$$\nabla \cdot \underline{\sigma} = 0. \quad (5.28)$$

The system of equations is solved in a monolithic way using the Newton-Raphson algorithm over a finite element discretisation [de Rancourt et al., 2016].

The diffusivity tensor is found below,

$$\underline{D} = D^{\text{B}} \underline{I} + \eta (D^{\text{GB}} - D^{\text{B}}) (\underline{I} - \underline{n}^{\text{GB}} \otimes \underline{n}^{\text{GB}}), \quad (5.29)$$

where \underline{I} is the identity tensor, D^{B} the bulk diffusivity, D^{GB} the grain boundary diffusivity. Furthermore, diffusion anisotropy with respect to the cristal orientation can be accounted for but is here neglected for simplicity.

Finally in (5.29), D^{GB} can be replaced by its damaged counterpart $D^{\text{GB}}(d)$ for modelling diffusion-damage coupled phenomena, *i.e.* breakaway oxidation,

$$D^{\text{GB}}(d) = D_0^{\text{GB}} \left[1 + N \left(1 - \exp\left(-\frac{d}{\tau^d}\right) \right) \right], \quad (5.30)$$

where D_0^{GB} is the undamaged grain boundary diffusivity, N and τ^d are parameters. In the present work, N is chosen to be equal to 100.

5.4 Simulation of intergranular oxide growth

5.4.1 Initial and boundary conditions

Two dimensional finite element simulations of oxide growth within a bicrystal are performed. The Fig. 5.2 displays a growing oxide intrusion in the zone of interest (ZoI). At the left hand side, the oxide phase is displayed in dark blue. The grain boundary is displayed with a dashed horizontal black line. In two dimensions, fcc cubic slip systems can be reduced to three slip systems – denoted A, B and C in this work. Slip systems orientations are displayed in black in the Figure.

The initial conditions of such simulations are further described. Initially, at $t = 0$, a thin and planar oxide layer of thickness $e \ll L$ is introduced at the free surface of the substrate as the model cannot handle oxide nucleation phenomena.

Chromium is initially homogeneous within each phase close to stoichiometry within the oxide and supersaturated within the base metal. Oxygen is not initially homogeneous and varies linearly throughout the oxide layer from a prescribed surface concentration to stoichiometry at the metal oxide interface. There is no oxygen in the metal phase.

Vertical displacements of the bottom surface and horizontal displacements of the right hand side surface are prescribed to zero. Stress at the top surface can be zero or can be positive.

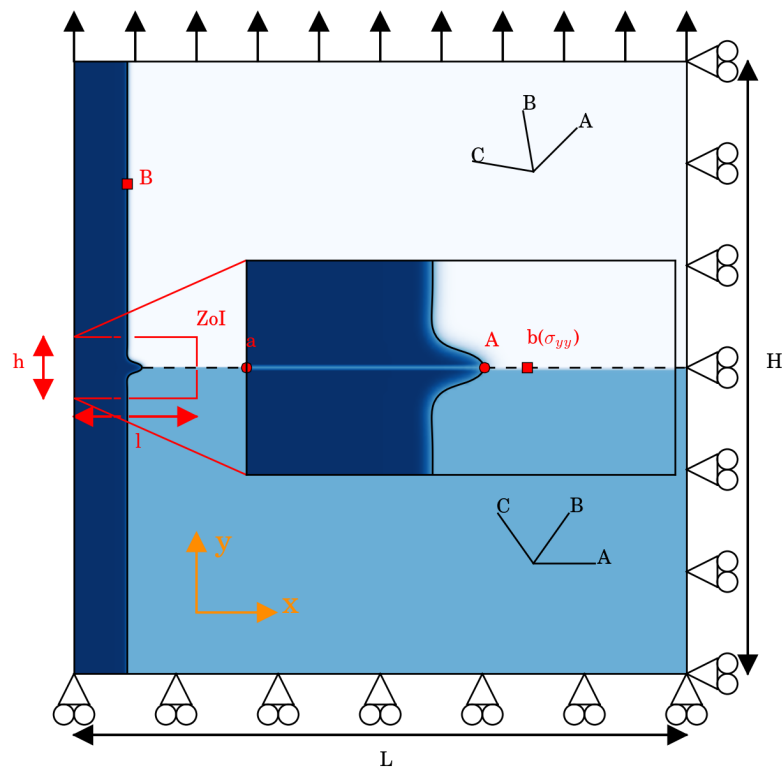


FIGURE 5.2 – Bi-crystalline sample used for finite element simulations. The mesh contains a refined Zone of Interest (ZoI) in the red dashed rectangle, which encompasses the oxide intrusion. Furthermore, points of interest are also defined for the local analyses of growth kinetics (A and B) and for the grain boundary opening tractions (a and $b(\sigma^{yy})$).

5.4.2 Materials parameters

Simulation parameters are defined at 900°C on the basis of a widespread literature review on stainless steels. They are summarised in Tab. 5.2 and 5.3. The choice of such a high temperature has been constrained by the lack of thermodynamic and diffusion data at moderate temperatures. The data shows relatively high contrasts between the oxide and metal phases. For instance, a 3 :2 Young's modulus ratio is found regarding the mechanical properties.

Metal-oxide interface properties are first discussed. The interface length and the mobility, respectively 10 nm and $10^{-8} \text{ J}^{-1} \cdot \text{m}^3 \cdot \text{s}^{-1}$, have been chosen from preliminary parametric studies so that the phase field kinetics is independent of the interface mobility and is diffusion controlled. The interface energy comes from density functional calculations performed by [Punkkinen et al., 2013] and is equal to $1 \text{ J} \cdot \text{m}^{-2}$.

Two square-shaped grains of stainless steel are superimposed in the simulations. The grain orientation of the upper grain is rotated of 10° counter-clockwise with respect to that of the lower one. The diffuse grain boundary thickness equals the metal-oxide thickness. The grain boundary energy is high enough to induce wetting. Such a grain boundary energy is lightly overestimated with regards to common experimental results [Fultz, 2014]. Nevertheless, preliminary parametric studies – which are not shown here – have shown a negligible effect of the grain boundary energy on the growth of the oxide intrusion.

Chemical energy curvatures are inferred from ternary phase diagrams [Laheij et al., 1980] and [Kjellqvist et al., 2008], respectively at 1200°C and 1600°C. Diffusion parameters are obtained from a re-assessment of the experimental results of [Sabioni et al., 2012] according to the present model. Diffusion short circuits are chosen greater – up to three order of magnitude – than bulk diffusivities.

Further, crystal plasticity parameters for the austenitic substrate are extrapolated from a mono-crystalline law obtained at 360°C by [Couvant et al., 2009]. It overestimates the mechanical behaviour at 900°C. Nevertheless, such steels can be hardened through plastic deformations, e.g. for bolts, which allows the retaining of significant mechanical properties in high temperature prior to the triggering of restoration. Restoration is not considered in this study.

It is assumed that the substrate retains high mechanical properties during oxidation. In this work, less than one hour of high temperature oxidation is considered. It is worth stressing that lower mechanical properties of the substrate would not change the conclusions of the study. Mechanical parameter of the oxide phase are taken from [Huntz et al., 2002] at 900°C.

Damage parameters can be reasonably extrapolated on the basis of recent experimental observations, e.g. [Dugdale et al., 2013]. 150 MPa and 1000 MPa opening stresses are assumed respectively for oxidised grain boundary and for the substrate grain boundary.

5.4.3 Accelerated growth along a grain boundary

Diffusion short-circuits have been reported in the literature [Weiss and Pineau, 1993]. Here, the oxide phase growth is driven by anionic diffusion – diffusion of oxygen from the free surface to the metal-oxide interface. Preliminary simulations have shown that the diffusion short-circuit nature of the grain boundary drives the growth of the oxide intrusion.

The materials parameters are provided in Tab. 5.2-5.3 and the boundary conditions in Fig. 5.3. As expected, the oxide intrusion grows faster than the oxide in the bulks because of the larger diffusivities along the grain boundaries. Early studies have suggested that grain boundary diffusion results in $t^{1/4}$ to $t^{1/2}$ growth laws [Irving, 1964, Fisher, 1951], while planar growth follows a \sqrt{t} law. However, with the selected parameters our calculations predict that the growth process is still in its transient stage. Nonetheless, the growth rates seem to tend at longer times towards the analytical power laws suggested by the early works.

Metal oxide Interface					
δ	10			nm	
Λ	1			J.m^{-2}	[Punkkinen et al., 2013]
M_ψ	10^{-8}			$\text{J}^{-1}.\text{m}^3.\text{s}^{-1}$	
Grain boundary					
δ	10			nm	
Λ	2			J.m^{-2}	
Diffusion					
	oxide		γ		
	O	Cr	O	Cr	
k_ψ	10^{11}	10^{11}	10^{11}	10^9	J.m^{-3}
a_ψ	0.5	0.33	0.01	0.01	-
D_ψ	240	0.47	56	56	$10^{-18} \text{m}^2.\text{s}^{-1}$
$(D_\psi^{\text{GB}})_x$	1200	0.47	56	56	$10^{-16} \text{m}^2.\text{s}^{-1}$
$(D_\psi^{\text{GB}})_y$	240	0.47	56	56	$10^{-18} \text{m}^2.\text{s}^{-1}$
m_ψ	10^3		10^3		-

TABLE 5.2 – Interface and diffusion parameters. $(D_\psi^{\text{GB}})_x$ and $(D_\psi^{\text{GB}})_y$ are the grain boundary diffusivities along the x and y axes, respectively and the x axis is normal to the free surface

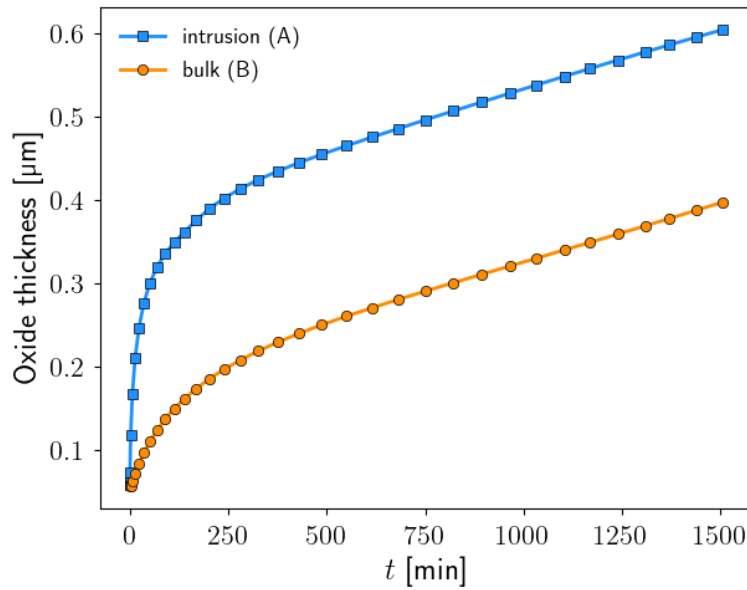


FIGURE 5.3 – Growth curves (B) away from the grain boundary and (A) along the grain boundary (A and B are displayed on Fig. 5.2).

5.4.4 Concentration fields of oxygen and chromium

Generalised oxide growth and more particularly the growth of oxide intrusions result in chemical heterogeneities in both the oxide and the metal phase, *e.g.* Fig. 5.4 and 5.5 respectively for oxygen and chromium. The figures display concentration fields with isovalues. Oxygen gradients are found only within the oxide as no oxygen cross the interface. Chromium gradients are found in the substrate in the vicinity of the metal-oxide interface. Significant curvature ef-

Elasticity			
E_ψ	oxyde	γ	
	215	145	GPa
ν_ψ	0.3	0.3	[Huntz et al., 1998]
Viscoplasticity			
K_ψ	7784	1000	MPa.s ^{1/n}
n_ψ	5	5	
R_ψ^0, S_ψ^0	200	65	MPa
ΔS_γ		45	MPa
h_γ^{ij}		1	-
b_γ		3	-
C_γ		600	MPa
d_γ^v		20	-
Damage			
K_ψ^d	100	100	MPa.s ^{1/n}
n_ψ^d	5	5	
Y_ψ^{d0}	150	1000	MPa
H_ψ^d	10	10	GPa
m_ψ^d	100	100	-
τ_ψ^d	0.03	0.03	-

TABLE 5.3 – Mechanical parameters

fects on the chromium concentration are shown in Fig. 5.5 [Li and Wang, 2020, Sherman and Voorhees, 2017, Schreiber et al., 2013].

It is worth noting that Whipple's solution – in comparison with the present finite element simulations – results in broader and shallower oxygen ingress, *viz.* oxide penetration levels, despite similar shapes of the oxygen concentration isolines. Such differences lie mainly in the fact that oxygen does not ingress into the base metal. To the knowledge of the authors, no measurements of oxygen concentrations in the vicinity of oxide intrusions are available for comparison.

Depleted chromium areas are critical as less protective oxide phase can nucleate instead of chromia. A high chromium depletion can also lead to additional stresses [Zhao et al., 1986], which are neglected in the present work. In the simulations, the chromium flux towards the metal oxide interface is rather high and lead to a small chromium depletion so that the substrate would maintain its oxidation resistance throughout the simulation. Such a chromium depleted area can be shown to follow a parabolic growth rate away from the grain boundary. It is mainly kept above the critical chromium content of 10.5%, which is necessary for the formation of a full barrier of chromia. Isovalues of the chromium field are displayed in Fig. 5.5. Along the metal-oxide interface, they reveal that the lowest chromium concentration levels are located at the shoulders of the oxide intrusion whereas highest chromium concentrations are found at the tip of the oxide intrusion, indicating strong curvature effects. Finally, the chromium depletion in the vicinity of the metal oxide interface has been reported in [Couvant et al., 2009, Kruska et al., 2012, Marrier et al., 2013] up to a zero chromium concentration at the metal oxide interface but by mean of an extrapolation.

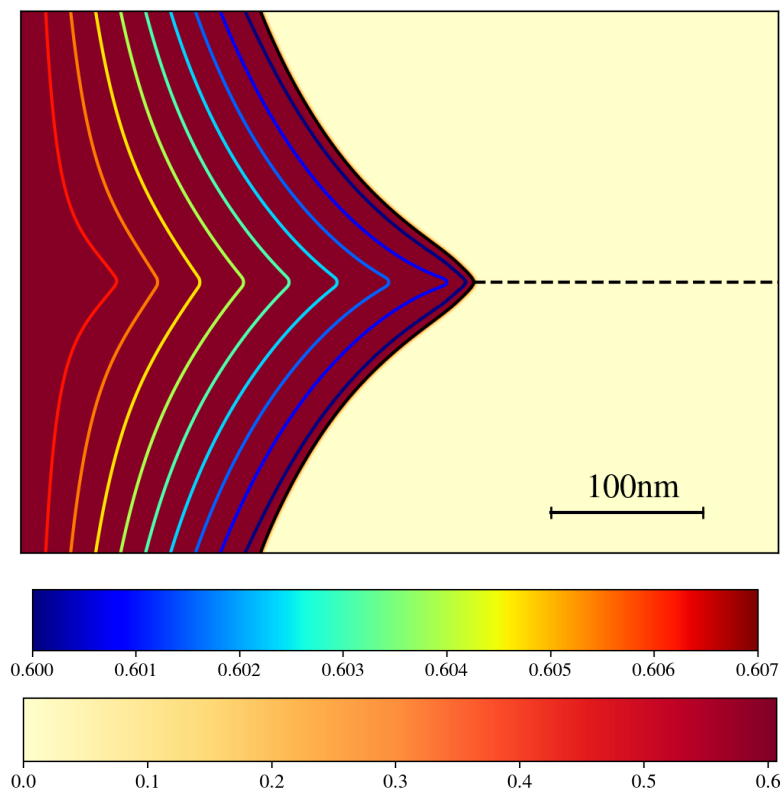


FIGURE 5.4 – Oxygen concentration field after 12 min of oxidation.

5.5 Intergranular oxide growth, and crack initiation

5.5.1 Oxidation-induced internal stresses

Volumetric changes occur during oxidation. They are considered here under the form of eigenstrains, which leads to internal stresses [Pilling and Bedworth, 1923]. They can be inferred from the well-known Pilling-Bedworth ratio – PBR, which consists in the ratio between the molar volumes of oxide and metal. Nevertheless, eigenstrains inferred from the PBR lead most likely to unrealistic internal stresses. This is due to the fact that the PBR is limited to pure anionic growth and does not consider mass losses. Therefore, the anisotropic effective eigenstrain ϵ^* , which is used here encompasses additional phenomena, e.g. [Krishnamurthy and Srolovitz, 2004]. Such kind of eigenstrain has already been used by [Clarke, 2002]. Nevertheless, the mechanical behaviour of oxides could be reasonably thought to be similar to the one of ceramics, *viz.* brittle and creep sensitive. The present simulations feature the volumetric expansion of the oxide matrix in the form of an effective eigenstrain along with viscoplastic stress relaxation mechanisms, e.g. [Clarke, 2002] and [Huntz et al., 1993].

Away from the oxide intrusion, similar stress fields as the ones described in [Huntz et al., 1993] are obtained. Maxima of compressive stresses are found within the oxide along the metal-oxide interface. The oxide compressive stresses then gradually decrease from the metal oxide interface to the free surface. Inside the metal phase, stresses can be shown to be homogeneous far from the intrusion. In the unidimensional case, it is worth noting that creep of the metal phase under tensile stresses would lead to the tensile deformation of the oxide. The compressive stress would then slowly vanish and become tensile firstly at the free surface with respect to the non-homogeneous stress field in the oxide phase. Surface cracks are therefore most likely to be generated.

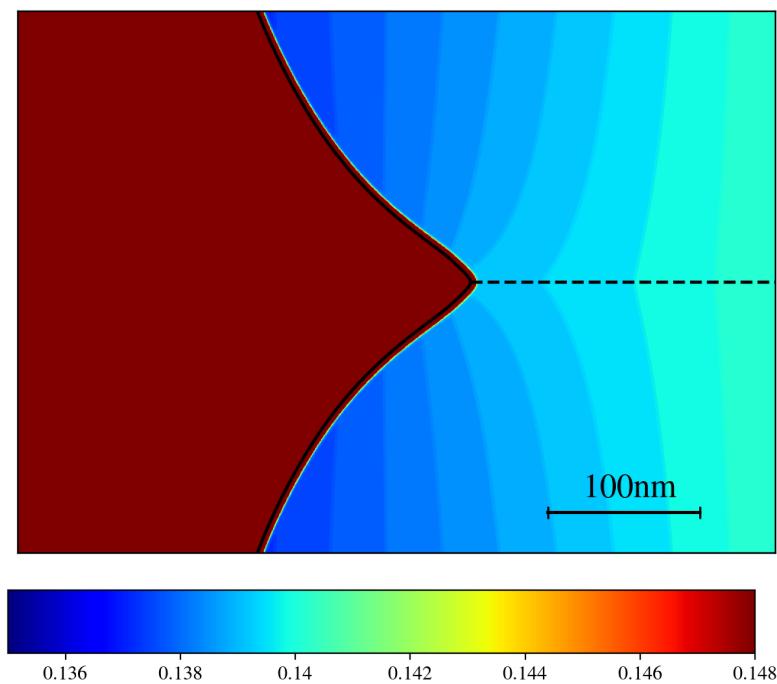


FIGURE 5.5 – Chromium concentration field after 12 min of oxidation.

In the vicinity of the oxide intrusion, the relaxation of compressive stresses within the oxide is followed by an increase of stresses – up to tensile stresses – on the free surface. The Fig. 5.6 shows σ^{yy} and the hydrostatic stress field σ^H in the vicinity of the oxide intrusion up to significant oxide intrusion levels. Tensile stresses are found ahead of the oxide intrusion tip, echoing the early works of [Evans, 1983] and [Ploc and Christodoulou, 1990]. Nevertheless, such tensile stresses are slightly shifted due to the viscoplastic relaxation – leading to a few percents of plastic deformations – of the base metal at the tip of the oxide intrusion. Compressive stresses accompanied by a few percents of plastic deformations are also found in the base metal on each side of the oxide intrusion. It is worth noting that the combination of tensile stresses and tensile hydrostatic stresses in the grain boundary at the tip of the oxide intrusion can potentially lead to the segregation of deleterious species, such as hydrogen, oxygen, phosphorus, *etc.* [Guedes et al., 2014].

During oxide growth, heterogeneous stresses are found around the oxide intrusion. The hydrostatic stress field displayed in Fig. 5.6 reveals two zones of interest. They are found at the oxide intrusion tip and at the intersection between the free surface and the oxidised grain boundary. It can be found that the grain boundary opening traction is the main contributor to the hydrostatic stress – see bottom plot of Fig. 5.6. Further, the von-Mises stress in Fig. 5.7 reveals high deviatoric stresses around the oxide intrusion and along the oxidised grain boundary.

Along the grain boundary, it can be shown that tensile tractions along the ghost grain boundary – also visible in 5.7 – appear progressively within the oxide layer at the free surface and also ahead of the oxide intrusion tip. This feature was quite unexpected and represents a major finding in the present work. Such tensile tractions are displayed in Fig. 5.8 and can result in the failure of the oxidised grain boundary. The evolution of the grain boundary opening traction is displayed in Fig. 5.8. It is worth noting that prior to the generation of the oxide intrusion, compressive stresses are initially found inside the oxide layer, which are rapidly relaxed due to viscoplastic deformation. This is clearly displayed on the bottom plot of Fig. 5.7. After-

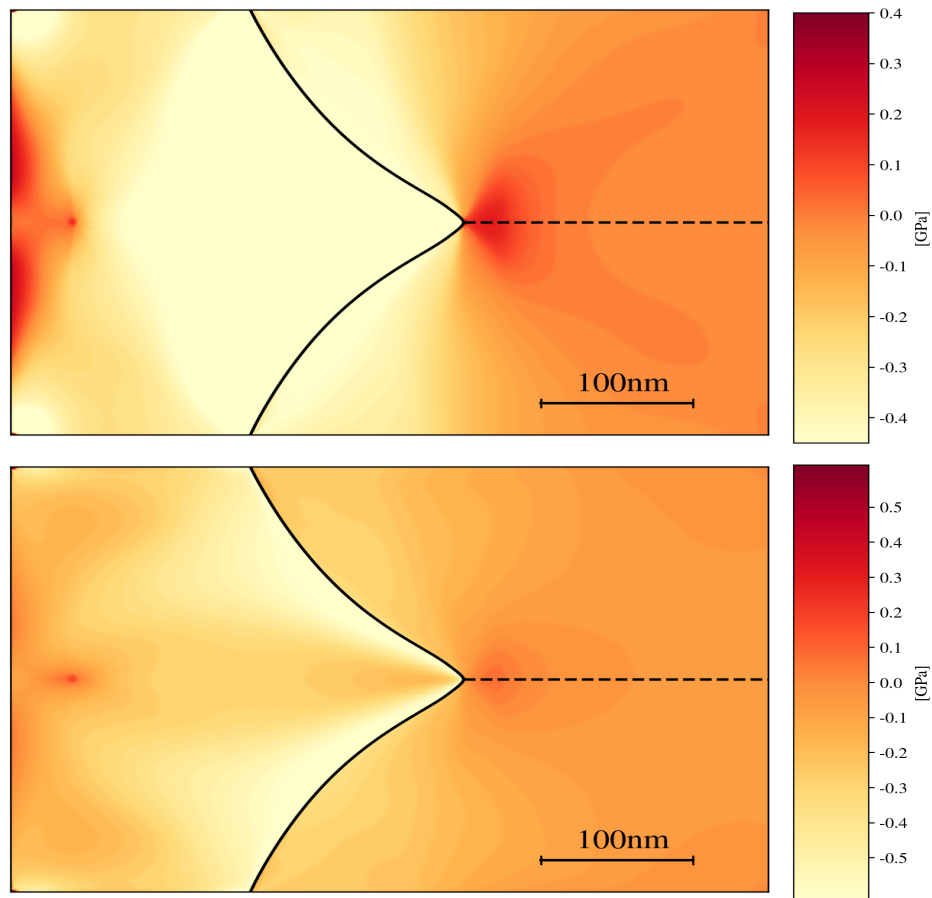


FIGURE 5.6 – The top plot represents the σ^{yy} field that corresponds to the grain boundary opening traction along the grain boundary and the bottom plot represents the hydrostatic stress $\sigma^H = \frac{1}{3}\sigma^{kk}$ after an oxidation time of 14 min.

wards and during the growth of the oxide intrusion, plastic deformation within the oxide layer concentrates along the ghost grain boundary axis. Fig. 5.8 shows the rapid relaxation of stresses in the vicinity of the free surface, while additional tractions are formed at the tip of the oxide intrusion. The figure shows then a progressive reversal of grain boundary positive tractions at the free surface. Such a phenomenon could explain crack initiation at the free surface and the delayed failure within oxide intrusions.

The Fig. 5.9 displays the damage field during oxidation. Damage is first initiated at the free surface and propagates throughout the oxide layer. This result is of fundamental importance. It highlights the ability of the current model to predict the initiation time and the growth kinetics of such short cracks.

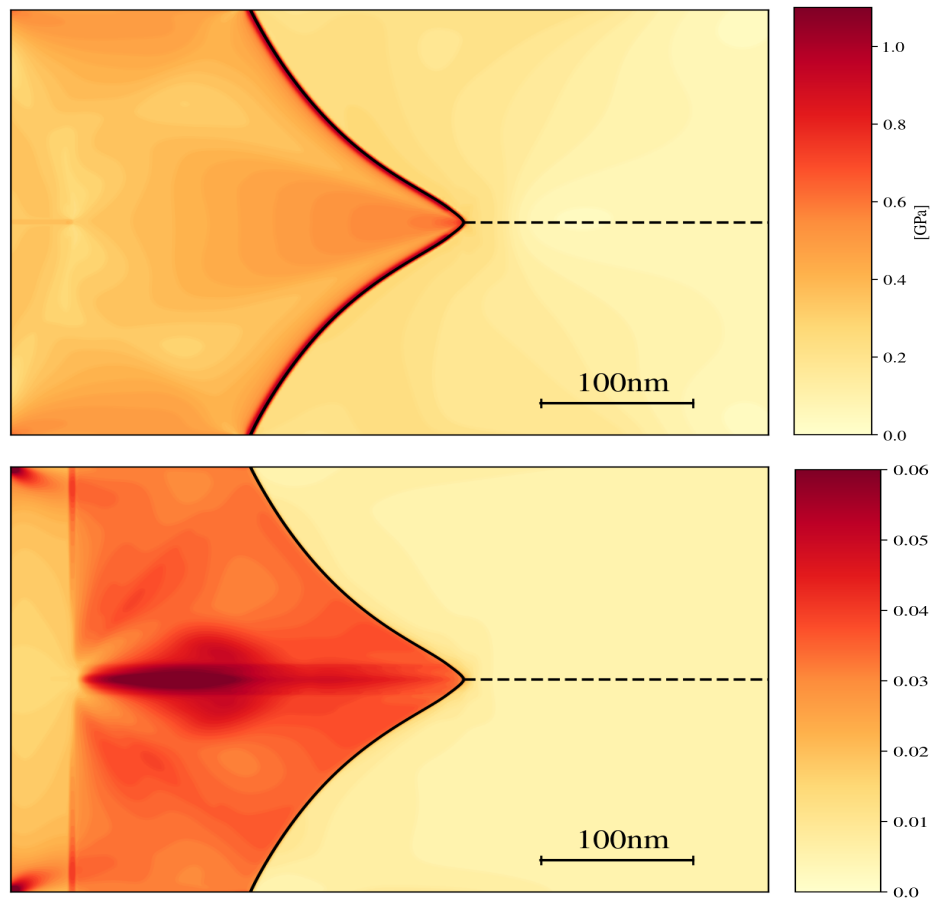


FIGURE 5.7 – The top plot represents the von Mises stress σ^{eq} and the bottom plot combines together the accumulated plastic strain in the oxide and the accumulated slip in the substrate after an oxidation time of 14 min.

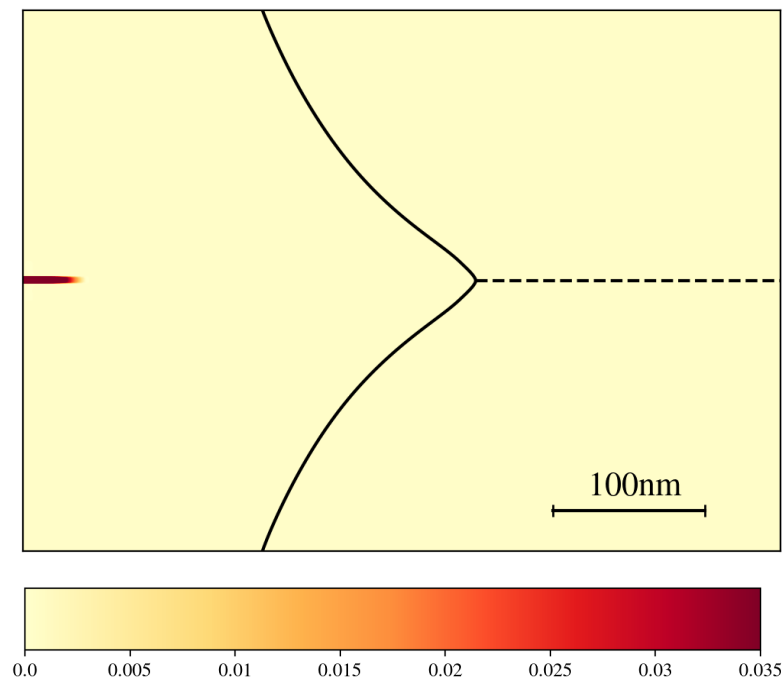


FIGURE 5.9 – Crack initiation at the free surface.

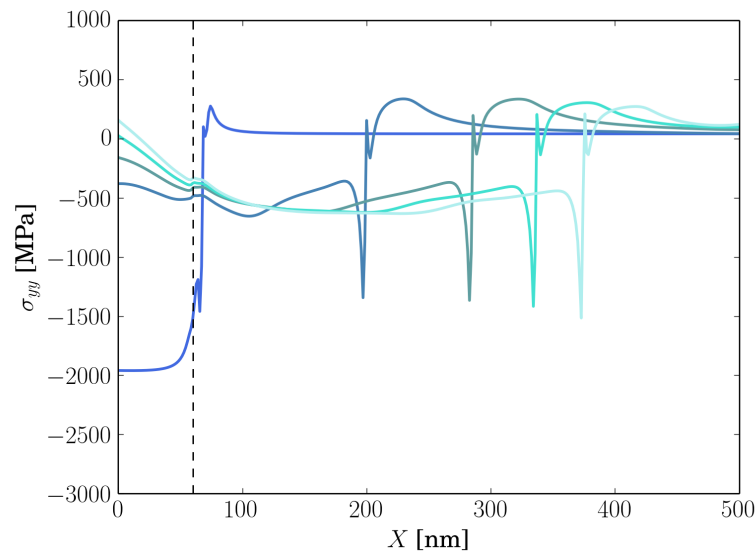


FIGURE 5.8 – Grain boundary normal tractions at different times : 4 s, 12 min, 41 min, 1 h 11 min, 1 h 40 min. The traction at the free surface goes to positive values with time, while a almost constant opening traction is found at the oxide intrusion tip.

It is worth noting that simplistic oxide intrusions are here modelled although much more complex patterns can be observed. It is thought that the highest tensile stress areas should be shifted in general – when the grain boundary is not normal to the free surface – resulting in similar cracking mechanisms but slightly shifted from the ghost grain boundary, which has been observed in [Wehbi, 2014].

5.5.2 Effect of a creep load on the damage behaviour

Finally, creep loading is considered with loads up to 300 MPa in the y -direction as illustrated in Fig. 5.3. Brittle failure of the oxide intrusion occurs at the free surface, which is here followed by a steady growth shown in Fig. 5.10. This figure shows a series of crack growth kinetics for different creep loads. The creep load is shown to be firstly beneficial as it can delay the crack initiation time. Nevertheless, it becomes then detrimental after reaching a certain level and accelerate the crack initiation mechanism. The first case can be explained by the decrease of the creep rate of the oxide phase while the second case can be explained by the increase of the creep rate of the metal phase. The coupling between damage and diffusion is also clearly visible in Fig. 5.10 as the cubic growth – displayed in Fig. 5.3 – rapidly becomes close to a quasi-linear growth; such an effect is also known as breakaway oxidation [Busso et al., 2010, Pujilaksono et al., 2011].

Finally, Fig. 5.11 highlights also the – beneficial and detrimental – effects of the creep load on crack initiation time. Such effects are namely : a delay induced by a slower relaxation of the compressive stresses within the oxide and a catalysis induced by the creep deformation of the base metal.

5.6 Conclusions

An extended phase field modelling framework was presented, which is able to simulate the growth of oxide intrusions along grain boundaries, including elasto-viscoplastic relaxation and

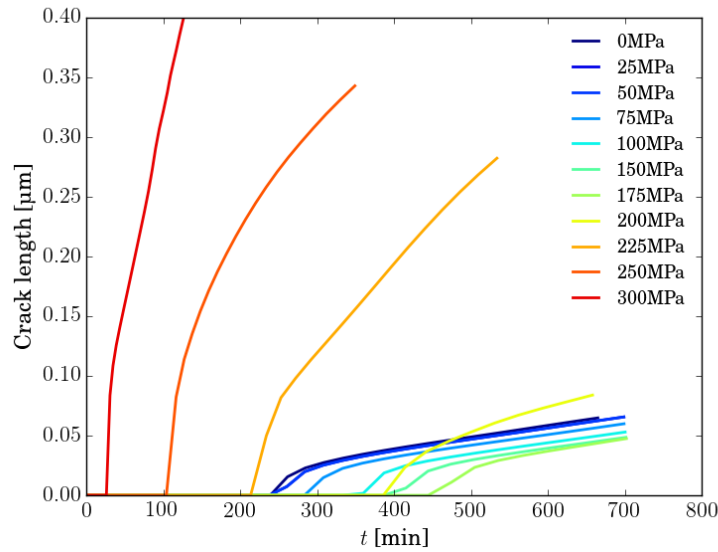


FIGURE 5.10 – Intergranular crack growth kinetics for different creep loads.

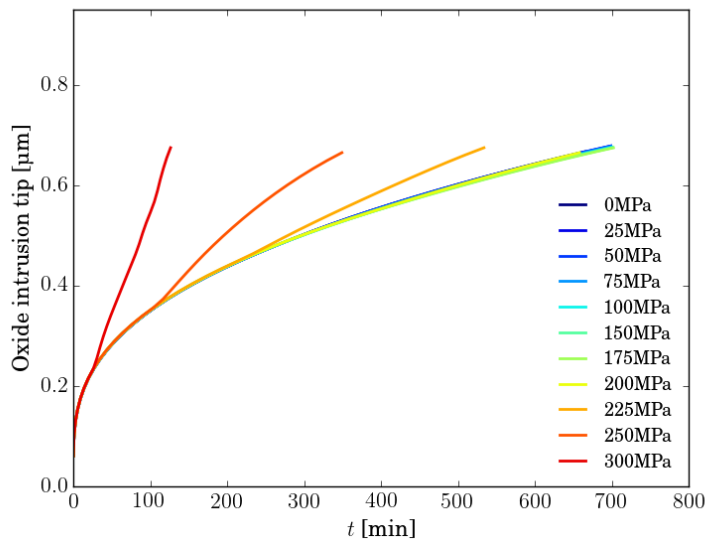


FIGURE 5.11 – Intergranular oxide growth for different creep loads.

crystal plasticity. The framework allows the investigation of stress relaxation within oxide layers, which phenomenon can be induced by diffusion. The chromium depletion evolution in the vicinity of an oxide intrusion and The heterogeneous oxide growth kinetics were study. Finite element simulations of growing oxide intrusions taking into account stress relaxation within oxide layers show that tensile stresses appear progressively at the free surface of oxide intrusions. Such tensile stresses appear to be able to generate delayed positive opening normal traction along the grain boundary at the free surface and at the tip of oxide intrusion, which can lead to the appearance of cracks. It appears that such cracks are frequently observed in the field of stress corrosion cracking and yet remain not well explained. The effect of creep loads on the failure behaviour of an oxide intrusion was investigated. The present work opens the way to

new assumptions in the field of stress corrosion cracking.

Many work perspectives can be extracted from such results in both numerical and experimental domains :

- the analysis of more realistic oxide intrusion shapes;
- The effect of ambipolar diffusion and external growth;
- The analysis of the growth kinetics of oxidation induced short cracks.

Perspectives - Mon projet de recherche

Le programme de recherche que je souhaite développer au cours des prochaines années s'appuie sur les deux thèmes suivants :

Modélisation de la recristallisation

Une thématique de recherche que j'ai commencée à aborder plus récemment est la modélisation de la recristallisation en utilisant la méthode de champs de phases.

La recristallisation est un phénomène complexe que l'on rencontre dans la plupart des procédés de transformation des alliages métalliques, et qui a pour effet majeur de transformer totalement la microstructure du matériau et notamment son degré d'anisotropie. Elle modifie donc les propriétés d'emploi des alliages métalliques, qu'ils s'agissent de propriétés mécaniques, physiques ou couplées. Avec la complexité croissante des procédés de transformation et des états microstructuraux des nouveaux matériaux, l'exigence sans cesse renouvelée de propriétés améliorées pour des matériaux que l'on souhaite de plus en plus multifonctionnels, à durée de vie plus longue, plus légers, la compréhension, la modélisation et la prévision de ces mécanismes sont nécessaires pour un contrôle rigoureux et une meilleure amélioration des propriétés finales d'emploi des matériaux lors des procédés de transformation et de leur optimisation notamment par le biais du formage.

Cette tâche est particulièrement complexe surtout que la recristallisation se produit généralement en même temps que d'autres sources de modification de l'état microstructural du matériau comme la déformation plastique, la précipitation, la transformation de phase, la restauration statique et dynamique, et la croissance de grains. Ces sont des phénomènes, qui impliquent tous les défauts des structures cristallines monophasées, lacunes, dislocations, joints de grains, et ce à toutes les échelles. Il est ainsi nécessaire de prendre en compte le mouvement des dislocations, que ce soit par glissement ou par montée impliquant la diffusion des lacunes, leur auto-organisation, leur interaction avec les joints grains, et le mouvement de ces derniers qui présente une grande variabilité suivant leur nature. En outre, les mécanismes essentiels intervenant lors de la recristallisation sont la germination et la croissance. La plupart des modèles actuels de recristallisation, reposant sur une modélisation à l'échelle du grain, ont été utilisés en premier lieu pour simuler l'étape de croissance seulement. Cette dernière est plus simple à simuler en se basant sur une description plus ou moins simplifiée des joints de grains pouvant se déplacer, de leur courbure, des orientations et des distributions d'énergie stockée de part et d'autres.

Cependant, la germination recouvre une réalité très complexe, fortement dépendante des conditions de recristallisation, de déformation préalable, très difficile à étudier car débutant nécessairement à une échelle très locale et très petite (de la taille d'une cellule de dislocations par exemple, ou même parfois plus petite) et donc encore finalement fort mal connue et modélisée.

Dans la littérature, la modélisation de la recristallisation peut être classée en deux grandes catégories :

- les modèles reposant sur des grandeurs moyennes et scalaires qui restent qualitatifs.
- les modèles en champ complet dont l'objectif est de saisir la complexité de l'évolution de la microstructure et qui sont butés sur la difficulté de définir des lois de germination et de migration. L'origine est l'absence de cadre thermodynamique permettant de décrire tous les phénomènes impliqués dans la recristallisation.

La description de la recristallisation durant les évolutions microstructurales complètes, couplée avec les déformations des grains d'un polycrystal et la mobilité des joints de grains dues à la courbure et l'énergie du joint de grains et à l'énergie stockée de part et d'autre du joint représente un déficit important permettant d'aboutir à la modélisation d'un procédé de transformation complet et c'est précisément le cœur de mes futures travaux que je souhaiterais développer. L'objectif sera donc de définir un cadre de modélisation, formulé comme une théorie des champs mécaniques et physiques sur une base thermodynamique cohérente et intégrant les mécanismes principaux impliqués dans la recristallisation, à savoir la déformation viscoplastique, la restauration et les mouvements des joints de grains.

Du côté de la modélisation des évolutions microstructurales lors de la recristallisation, nous proposons d'appliquer la méthode de champs de phase, dans le domaine de la recristallisation, qui à l'inverse des méthodes précédentes considère des interfaces diffuses et non plus discrètes, ce qui dans certains cas, peut permettre une meilleure description de l'état déformé et qui doit donc être explorée. Les modèles de champs de phases pour les polycristaux et les joints de grains ont généralement recours à deux champs de variables : une variable d'orientation cristalline et un paramètre d'ordre, parfois appelé taux de cristallinité et mesure le désordre atomique aux joints de grains. Il s'agit d'une représentation frustrée de la réalité atomique mais déjà plus riche que dans les approches précédentes.

Nos travaux s'appuieront sur une démarche à deux échelles : d'une part en enrichissant un modèle de champ de phase par un modèle de Cosserat à l'échelle mésoscopique; d'autre part en recourant à une nouvelle approche permettant d'étudier l'auto-organisation des dislocations à une échelle plus fine, afin de guider la construction du modèle mésoscopique.

Modélisation de la rupture statique de matériaux fragiles par un modèle d'endommagement à gradient.

Un autre thème, que je suis entrain de développer en collaboration avec le CEA Saclay, est consacré à la modélisation de la rupture des matériaux fragiles, qui constitue un enjeu majeur de l'évaluation de la durée de vie de nombreux composants industriels. L'objectif principal est de fournir les outils de modélisation adéquats, pour décrire la propagation des fissures dans les matériaux solides.

Le fondement théorique de la mécanique de la rupture repose sur le travail de Griffith (1921), qui s'appuie sur un formalisme énergétique pour décrire les conditions de propagation d'une fissure. En effet, l'approche énergétique de la rupture proposée par Griffith postule qu'une fissure se propage dès que le taux de libération d'énergie au sommet de la fissure atteint

une énergie critique, nécessaire à la création d'une nouvelle surface. À partir de ce concept fondamental, plusieurs outils décrivant les conditions de propagation et permettant de prédire la direction des fissures dans des matériaux homogènes ont été développés

La simulation de l'initiation et de la propagation des fissures dans le cadre de la rupture fragile fait encore aujourd'hui l'objet de nombreux développements, tant au niveau des modèles mathématiques que des méthodes numériques, du fait de la complexité de décrire les trajets de fissuration. Il est bien connu que la localisation de l'endommagement et la dégradation de matériaux, qui sont caractérisées par un adoucissement du comportement, entraînant généralement une perte d'ellipticité du système d'équations différentielles décrivant le processus de déformation. Par conséquent, la description mathématique d'un modèle d'endommagement est donc mal posée en ce sens qu'elle n'a pas une solution unique avec une dépendance continue des données matériau. Les conditions initiales et les conditions aux limites, qui ont été correctement définies dans le cas elliptique, deviennent inadaptées pour le cas hyperbolique. D'un point de vue numérique, les modèles locaux classiques de la mécanique de la rupture conduisent à une forte dépendance des résultats par rapport à la finesse et à l'orientation du maillage.

Pour palier cette déficience du modèle, plusieurs stratégies de régularisation ont été proposées pour enrichir la description mécanique du milieu de manière à pouvoir introduire un aspect non local dans les relations constitutives et éviter la sensibilité de la solution au maillage durant la phase d'adoucissement. L'idée générale consiste à introduire une échelle de longueur interne, liée aux interactions entre les défauts. Parmi les méthodes proposées dans la littérature, on trouve les théories non-locales continues [Pijaudier-Cabot and Bazant, 1987], les modèles d'endommagement à gradient [Peerlings et al., 1996, Francfort and Marigo, 1998] et la méthode du champ de phase (PFM) [Borden et al., 2012, Hofacker and Miehe, 2013].

Pour mener à bien ce sujet, on compte se baser sur le modèle à gradient d'endommagement (approche champ de phases), où le matériau est décrit par une variable continue d'endommagement (paramètre d'ordre) qui vaut zéro dans la phase saine intact, et un là où le matériau est rompu et ne peut plus supporter de charge mécanique. Cette variable varie continûment entre ces valeurs à travers des interfaces diffuses d'épaisseur non nulle. À l'inverse des approches de type "suivi interface", représentées par une interface discrète, la représentation continue d'une fissure par une interfaces diffuses offre une alternative intéressante dans laquelle il n'est pas nécessaire de suivre explicitement la topologie de la fissure ni d'en contraindre le trajet a priori. Par conséquent, un modèle théorique et numérique, qui repose sur une approche, bénéficiant du cadre variationnel bien défini des matériaux standards généralisés, sera développé en se basant sur la méthode de champs de phase, permettant de prédire la trajectoire de fissures tridimensionnelles ainsi que l'amorçage de nouvelles fissures, et d'aborder les problématiques de multi-fissuration (faïençage sous refroidissement rapide, fragmentation sous impact, branchement de fissures...). L'évolution du trajet de la fissure est dictée par un principe de minimum global de l'énergie sous des conditions d'irréversibilité d'évolution de la variable d'endommagement.

Modélisation des interactions entre la plasticité et l'environnement

Je souhaiterais élargir mes travaux à court terme, à l'étude de la modélisation numérique des interactions entre la mécanique, et en particulier la plasticité, et l'environnement. L'oxydation [de Rancourt et al., 2016, Wang et al., 2023] et la corrosion [Imanian and Amiri, 2022, Kovacevic et al., 2023], et la fragilisation par l'oxygène [Le Saux et al., 2015, Xia et al., 2019] sont des exemples courants d'interactions entre la mécanique et l'environnement, dont ils peuvent avoir un impact considérable sur la durabilité des structures.

L'étude du couplage et de l'interaction entre la mécanique et l'environnement est un domaine de recherche multidisciplinaire, qui contribue activement à la résolution des défis majeurs dans la mécanique et la science des matériaux. Les facteurs environnementaux physico-chimique, parfois extrêmes (haute température, haute pression, irradiations, concentration chimique, contraintes mécaniques), peuvent être des précurseurs, des catalyseurs ou des amplificateurs de l'endommagement d'un matériau et mènent à des propriétés dégradées et à des pertes de tenue ou d'intégrité du composant et de la structure. Par conséquent, la compréhension de l'influence de différents facteurs environnementaux sur les propriétés mécaniques des matériaux est une étape cruciale pour améliorer les performances des matériaux et des procédés de production dans des applications telles que la métallurgie, la mécanique des matériaux et la production d'énergie et permet de concevoir des matériaux plus résistants et plus durables.

Une partie de mes travaux de recherches sera consacrée à l'étude de la fragilisation par l'oxygène, qui peut conduire à une dégradation accélérée des matériaux et des composants utilisés dans diverses industries, telles que l'aérospatiale, l'énergie nucléaire, la production d'électricité et dans d'autres domaines impliquant des structures en métal. La compréhension des mécanismes de fragilisation par l'oxygène peut aider à développer des stratégies efficaces afin de minimiser ou prévenir ce phénomène, ce qui peut entraîner une amélioration de la fiabilité et de la sécurité des équipements et des installations.

En combinant les résultats expérimentaux avec des simulations numériques et en s'appuyant sur des modèles thermodynamiques et physico-chimiques, mes activités visent à comprendre les interactions procédés-microstructure/architecture-propriétés et leurs évolutions dans les environnements complexes (haute température, oxydation/corrosion, durée de vie,...). Le couplage plasticité-environnement peut être simulé de manière efficace en utilisant la méthode de champs de phase et en intégrant les équations de la plasticité avec des équations de l'environnement. La modélisation numérique en utilisant le champs de phases est très performante pour ces phénomènes complexes, fortement couplées (multi-physique) à des échelles spatiales étendues (multi-échelle), permettant de prendre en compte de nombreux facteurs d'ordre mécanique, métallurgique, physico-chimique, électrochimique,... dans la description des propriétés mécaniques des matériaux exposés à un environnement donné. Cette méthode peut ainsi fournir des informations précieuses sur les comportements des matériaux sous différentes conditions environnementales, ce qui peut permettre ainsi à une meilleur analyse et à une optimisation des processus et des procédés de production.



Bibliographie

- [Abrivard et al., 2012a] Abrivard, G., Busso, E., Forest, S., and Appolaire, B. (2012a). Phase field modelling of grain boundary motion driven by curvature and stored energy gradients. Part I : Theory and numerical implementation. *Philosophical Magazine*, 92(28-30) :3618–3642.
- [Abrivard et al., 2012b] Abrivard, G., Busso, E., Forest, S., and Appolaire, B. (2012b). Phase field modelling of grain boundary motion driven by curvature and stored energy gradients. Part II : Application to recrystallisation. *Philosophical Magazine*, 92(28-30) :3643–3664.
- [Aifantis, 1987] Aifantis, E. (1987). The physics of plastic deformation. *Int. J. Plasticity*, 3 :211.
- [Ammar et al., 2009a] Ammar, K., Appolaire, B., Cailletaud, G., Feyel, F., and Forest, S. (2009a). Finite element formulation of a phase field model based on the concept of generalized stresses. *Computational Materials Science*, 45(3) :800–805.
- [Ammar et al., 2009b] Ammar, K., Appolaire, B., Cailletaud, G., Feyel, F., and Forest, S. (2009b). Modélisation du couplage changement de phase-mécanique par la méthode des champs de phases et les techniques d’homogénéisation. In *Giens*.
- [Ammar et al., 2009c] Ammar, K., Appolaire, B., Cailletaud, G., and Forest, S. (2009c). Combining phase field approach and homogenization methods for modelling phase transformation in elastoplastic media. *European Journal of Computational Mechanics*, 18 :485–523.
- [Ammar et al., 2011] Ammar, K., Appolaire, B., Cailletaud, G., and Forest, S. (2011). Phase field modeling of elasto-plastic deformation induced by diffusion controlled growth of a misfitting spherical precipitate. *Philosophical Magazine Letters*, 91(3) :164–172.
- [Ammar et al., 2014] Ammar, K., Appolaire, B., Forest, S., Cottura, M., Le Bouar, Y., and Finel, A. (2014). Modelling inheritance of plastic deformation during migration of phase boundaries using a phase field method. *Meccanica*, 49(11) :2699–2717.
- [Anders and Weinberg, 2011] Anders, D. and Weinberg, K. (2011). Numerical simulation of diffusion induced phase separation and coarsening in binary alloys. *Computational Materials Science*, 50 :1359–1364.
- [Ashby, 1970] Ashby, M. F. (1970). The deformation of plastically non-homogeneous materials. *The Philosophical Magazine : A Journal of Theoretical Experimental and Applied Physics*, 21(170) :399–424.
- [Aslan et al., 2011] Aslan, O., Quilici, S., and Forest, S. (2011). Numerical modeling of fatigue crack growth in single crystals based on microdamage theory. *International Journal of Damage Mechanics*, 20(5) :681–705.

- [Auinger et al., 2011] Auinger, M., Naraparaju, R., Christ, H.-J., and Rohwerder, M. (2011). Modelling high temperature oxidation in iron-chromium systems : combined kinetic and thermodynamic calculation of the long-term behaviour and experimental verification. *Oxidation of Metals*, 76(3-4) :247–258.
- [Balluffi, 1992] Balluffi, R. (1992). Grain boundary diffusion mechanisms in metals. *Journal of Electronic Materials*, 21(1) :527–553.
- [Basak and Levitas, 2019] Basak, A. and Levitas, V. I. (2019). Finite element procedure and simulations for a multiphase phase field approach to martensitic phase transformations at large strains and with interfacial stresses. *Computational Methods in Applied Mechanical Engineering*, 343 :368–406.
- [Beke et al., 2004] Beke, D., Szabó, I., Erdélyi, Z., and Opposits, G. (2004). Diffusion-induced stresses and their relaxation. *Materials Science and Engineering : A*, 387–389(0) :4–10.
- [Besson et al., 2001] Besson, J., Cailletaud, G., Chaboche, J.-L., and Forest, S. (2001). *Mécanique non linéaire des matériaux*. Hermès Sciences, France.
- [Besson et al., 2009] Besson, J., Cailletaud, G., Chaboche, J.-L., Forest, S., and Blétry, M. (2009). *Non-Linear Mechanics of Materials*. Series : Solid Mechanics and Its Applications, Vol. 167, Springer, ISBN : 978-90-481-3355-0, 433 p.
- [Boisse et al., 2007] Boisse, J., Lecoq, N., Patte, R., and Zapolsky, H. (2007). Phase-field simulation of coarsening of γ precipitates in an ordered γ' matrix. *Acta Materialia*, 55 :6151–6158.
- [Borden et al., 2012] Borden, M., Verhoosel, C., Scott, M., Hughes, T., and Landis, C. (2012). A phase-field description of dynamic brittle fracture. *Computer Methods in Applied Mechanics and Engineering*, 217–220 :77–95.
- [Bourne et al., 1994] Bourne, J., Atkinson, C., and Reed, R. (1994). Diffusion controlled growth in ternary systems. *Metallurgical and Materials Transactions A*, 25 :2683–2694.
- [Boussinot et al., 2009] Boussinot, G., Finel, A., and Le Bouar, Y. (2009). Phase-field modeling of bimodal microstructures in nickel-based superalloys. *Acta Materialia*, 57 :921–931.
- [Boussinot et al., 2010] Boussinot, G., Le Bouar, Y., and Finel, A. (2010). Phase-field simulations with inhomogeneous elasticity : Comparison with an atomic-scale method and application to superalloys. *Acta Materialia*, 58(12) :4170–4181.
- [Busso and Cailletaud, 2005] Busso, E. and Cailletaud, G. (2005). On the selection of active slip systems in crystal plasticity. *International Journal of Plasticity*, 21(11) :2212–2231.
- [Busso et al., 2010] Busso, E., Evans, H., Qian, Z., and Taylor, M. (2010). Effects of breakaway oxidation on local stresses in thermal barrier coatings. *Acta Materialia*, 58(4) :1242–1251.
- [Cahn and Larché, 1984] Cahn, J. and Larché, F. (1984). A simple model for coherent equilibrium. *Acta Metall.*, 32(11) :1915–1923.
- [Cailletaud, 1992] Cailletaud, G. (1992). A micromechanical approach to inelastic behaviour of metals. *International Journal of Plasticity*, 8(1) :55 – 73.
- [Cha et al., 2009] Cha, P.-R., Kim, J., Kim, W.-T., and Kim, S. (2009). Effect of transformation induced stress and plastic deformation on austenite/ferrite transition in low carbon steel. In *Plasticity 2009*, pages 376–378.
- [Chaboche et al., 2001] Chaboche, J., Kruch, S., Maire, J., and Pottier, T. (2001). Towards a micromechanics based inelastic and damage modeling of composites. *International Journal of Plasticity*, 17 :411–439.

- [Cheng et al., 2017] Cheng, T., Wen, Y. H., and Hawk, J. A. (2017). Modeling elasto-viscoplasticity in a consistent phase field framework. *International Journal of Plasticity*, 96 :242–263.
- [Clarke, 2002] Clarke, D. (2002). Stress generation during high-temperature oxidation of metallic alloys. *Current Opinion in Solid State and Materials Science*, 6(3) :237–244.
- [Cordero et al., 2010] Cordero, N., Gaubert, A., Forest, S., Busso, E., Gallerneau, F., and Kruch, S. (2010). Size effects in generalised continuum crystal plasticity for two-phase laminates. *Journal of The Mechanics and Physics of Solids*, 58 :1963–1994.
- [Cottura et al., 2014] Cottura, M., Appolaire, B., Finel, A., and Le Bouar, Y. (2014). Phase field study of acicular growth : Role of elasticity in Widmanstätten structure. *Acta Materialia*, 72 :200–210.
- [Cottura et al., 2015a] Cottura, M., Appolaire, B., Finel, A., and Le Bouar, Y. (2015a). Plastic relaxation during diffusioncontrolled growth of Widmanstätten plates. *Scripta Materialia*, 108 :117–121.
- [Cottura et al., 2016] Cottura, M., Appolaire, B., Finel, A., and Le Bouar, Y. (2016). Coupling the phase field method for diffusive transformations with dislocation density-based crystal plasticity : Application to Ni-based superalloys. *Journal of the Mechanics and Physics of Solids*, 94 :473–489.
- [Cottura et al., 2021] Cottura, M., Appolaire, B., Finel, A., and Le Bouar, Y. (2021). Microstructure evolution under [110] creep in Ni-base superalloys. *Acta Materialia*, 212 :116851.
- [Cottura et al., 2015b] Cottura, M., Le Bouar, Y., Appolaire, B., and Finel, A. (2015b). Rôle of elastic inhomogeneity in the development of cuboidal microstructures in Ni-based superalloys. *Acta Materialia*, 94 :15–25.
- [Cottura et al., 2012] Cottura, M., Le Bouar, Y., Finel, A., Appolaire, B., Ammar, K., and Forest, S. (2012). A phase field model incorporating strain gradient viscoplasticity : Application to rafting in Ni-base superalloys. *Journal of the Mechanics and Physics of Solids*, 60(7) :1243–1256.
- [Couvant et al., 2009] Couvant, T., Legras, L., Herbelin, A., Musienko, A., Ilevbrev, G., Delafosse, D., Cailletaud, G., and Hickling, J. (2009). Development of understanding of the interaction between localized deformation and SCC of austenitic stainless steel exposed to primary PWR environment. In *Proceedings of the Fourteenth International Conference on Environmental Degradation of Materials in Nuclear Power Systems Water Reactors*, pages 182–194. American Nuclear Society (ANS).
- [de Rancourt et al., 2016] de Rancourt, V., Ammar, K., Appolaire, B., and Forest, S. (2016). Homogenization of viscoplastic constitutive laws within a phase field approach. *Journal of the Mechanics and Physics of Solids*, 88 :291–319.
- [Diologent, 2002] Diologent, F. (2002). *Comportement en fluage et en traction de superalliages monocristallins à base de nickel*. Thèse de doctorat, Université Paris XI-Orsay.
- [Diologent et al., 2003] Diologent, F., Caron, P., d’Almeida, T., Jacques, A., and Bastie, P. (2003). The $\gamma - \gamma'$ mismatch in ni based superalloys : In situ measurements during a creep test. *Nuclear Instruments & Methods in Physics Research Section B-beam Interactions With Materials and Atoms*, 200 :346–351.
- [Dugdale et al., 2013] Dugdale, H., Armstrong, D., Tarleton, E., Roberts, S., and Lozano-Perez, S. (2013). How oxidized grain boundaries fail. *Acta Materialia*, 61(13) :4707–4713.

- [Durga et al., 2013] Durga, A., Wollants, P., and Moelans, N. (2013). Evaluation of interfacial excess contributions in different phase-field models for elastically inhomogeneous systems. *Modelling and Simulation in Material Science and Engineering*, 21 :055018.
- [Eiken et al., 2006] Eiken, J., Böttger, B., and Steinbach, I. (2006). Multiphase-field approach for multicomponent alloys with extrapolation scheme for numerical application. *Physical Review E*, 73.
- [Eringen and Suhubi, 1964] Eringen, A. and Suhubi, E. (1964). Nonlinear theory of simple micro-elastic solids—i. *International Journal of Engineering Science*, 2 :189 – 203.
- [Espíé, 1996] Espíé, L. (1996). *Etude expérimentale et modélisation numérique du comportement de monocristaux de superalliages*. Thèse de doctorat, Ecole des Mines de Paris.
- [Evans, 1983] Evans, H. (1983). The role of oxide grain boundaries in the development of growth stresses during oxidation. *Corrosion Science*, 23(5) :495–506.
- [Fahrman et al., 1999] Fahrman, M., Hermann, W., Fahrman, E., Boegli, A., Pollock, T., and Sockel, H. (1999). Determination of matrix and precipitate elastic constants in $(\gamma-\gamma')$ ni-base model alloys, and their relevance to rafting. *Materials Science and Engineering : A*, 260(1) :212 – 221.
- [Favergeon et al., 2005] Favergeon, J., Montesin, T., and Bertrand, G. (2005). Mechano-chemical aspects of high temperature oxidation : A mesoscopic model applied to zirconium alloys. *Oxidation of Metals*, 64(3-4) :253–279.
- [Finel et al., 2010] Finel, A., Le Bouar, Y., Gaubert, A., and Salman, U. (2010). Phase field methods : Microstructures, mechanical properties and complexity. *Comptes Rendus Physique*, 11 :245–256.
- [Fisher and Renken, 1964] Fisher, E. and Renken, C. (1964). Single-crystal elastic moduli and the hcp \rightarrow bcc transformation in Ti, Zr, and Hf. *Physical Review*, 135(2A) :482–494.
- [Fisher, 1951] Fisher, J. C. (1951). Calculation of diffusion penetration curves for surface and grain boundary diffusion. *Journal of Applied Physics*, 22(1) :74–77.
- [Fleck et al., 1994] Fleck, N., Muller, G., Ashby, M., and Hutchinson, J. (1994). Strain gradient plasticity : Theory and experiment. *Acta Metallurgica et Materialia*, 42 :475 – 487.
- [Flouriot et al., 2003] Flouriot, S., Forest, S., Cailletaud, G., Koster, A., Rémy, L., Burgardt, B., Gros, V., Mosset, S., and Delautre, J. (2003). Strain localization at the crack tip in single crystal CT specimens under monotonous loading : 3D finite element analyses and application to nickel-base superalloys. *International Journal of Fracture*, 124(1-2) :43–77.
- [Forest, 2008a] Forest, S. (2008a). The micromorphic approach to plasticity and diffusion. In Jeulin, D. and Forest, S., editors, *Continuum Models and Discrete Systems 11, Proceedings of the international conference CMDS11*, pages 105–112, Paris, France. Les Presses de l’Ecole des Mines de Paris.
- [Forest, 2008b] Forest, S. (2008b). Some links between cosserat, strain gradient crystal plasticity and the statistical theory of dislocations. *Philosophical Magazine*, 88 :3549–3563.
- [Forest, 2009] Forest, S. (2009). The micromorphic approach for gradient elasticity, viscoplasticity and damage. *ASCE Journal of Engineering Mechanics*, 135 :117–131.
- [Forest et al., 1997] Forest, S., Cailletaud, G., and Sievert, R. (1997). A cosserat theory for elastoviscoplastic single crystals at finite deformation. *Archives of Mechanics*, 49.

- [Forest and Sievert, 2003] Forest, S. and Sievert, R. (2003). Elastoviscoplastic constitutive frameworks for generalized continua. *Acta Mechanica*, 160 :71–111.
- [Francfort and Marigo, 1998] Francfort, G. and Marigo, J.-J. (1998). Revisiting brittle fracture as an energy minimization problem. *Journal of the Mechanics and Physics of Solids*, 46 (8) :1319–1342.
- [Fried and Gurtin, 1996] Fried, E. and Gurtin, M. (1996). A phase-field theory for solidification based on a general anisotropic sharp-interface theory with interfacial energy and entropy. *Physica D : Nonlinear Phenomena*, 91(1–2) :143–181.
- [Fujiwara et al., 1999] Fujiwara, F., Watanabe, M., Nemoto, Z., and Noumi, K. and Simozaki, T. (1999). International conference on solid-solid transformations, in jmic-3.
- [Fultz, 2014] Fultz, B. (2014). *Phase Transitions in Materials*. Cambridge University Press.
- [Ganghoffer et al., 1994] Ganghoffer, J., Simonsson, K., Denis, S., Gautier, E., Sjöström, S., and Simon, A. (1994). Martensitic transformation plasticity simulations by finite elements. *Journal de Physique IV (France)*, 4 :C3–215–220.
- [Ganghoffer et al., 1991] Ganghoffer, J.-E., Denis, S., Aeby-Gautier, E., Simon, A., SIMONSSON, K., and Sjöström, S. (1991). Micromechanical simulation of a martensitic transformation by finite elements. <http://dx.doi.org/10.1051/jp4:1991411>, 1.
- [Gaubert, 2009] Gaubert, A. (2009). *Modelisation des effets de l'évolution microstructurale sur le comportement mécanique du superalliage monocristallin AM1*. PhD thesis, Mines ParisTech.
- [Gaubert et al., 2008] Gaubert, A., Finel, A., Le Bouar, Y., and Boussinot, G. (2008). Viscoplastic phase field modelling of rafting in Ni-base superalloys. In Jeulin, D. and Forest, S., editors, *Continuum Models and Discrete Systems CMDS11*, pages 161–166. Mines Paris Les Presses.
- [Gaubert et al., 2010] Gaubert, A., Le Bouar, Y., and Finel, A. (2010). Coupling phase field and viscoplasticity to study rafting in Ni-based superalloys. *Philosophical Magazine*, 90(1-4) :375–404.
- [Geslin et al., 2014] Geslin, P., Appolaire, B., and Finel, A. (2014). Investigation of coherency loss by prismatic punching with a nonlinear elastic model. *Acta Materialia*, 71 :80–88.
- [Goedjen et al., 1994] Goedjen, J., Stout, J., Guob, Q., and Shores, D. (1994). Evaluation of stresses in Ni-NiO and Cr-Cr₂O₃ during high temperature oxidation by in situ X-ray diffraction. *Materials Science and Engineering : A*, 177(1–2) :115–124.
- [Greenberg et al., 2001] Greenberg, B., Volkov, A., and Kruglikov, N. (2001). Composite-like behavior of alloys ordered after severe cold deformation. *Physics of Metals and Metallography*, 92 :167–178.
- [Guedes et al., 2014] Guedes, D., Oudriss, A., Frappart, S., Courlit, G., Cohendoz, S., Girault, P., Creus, J., Bouhattate, J., Metsue, A., Thebault, F., Delattre, L., Koschel, D., and Feaugas, X. (2014). The influence of hydrostatic stress states on the hydrogen solubility in martensitic steels. *Scripta Materialia*, 84–85(0) :23–26.
- [Guo et al., 2005a] Guo, X., Shi, S., and Ma, X. (2005a). Elastoplastic phase field model for microstructure evolution. *Applied Physics Letters*, 87 :221910–1–3.
- [Guo et al., 2005b] Guo, X., Shi, S., and Ma, X. (2005b). Elastoplastic phase field model for microstructure evolution. *Applied Physics Letters*, 87(22).
- [Gurtin, 1996] Gurtin, M. (1996). Generalized Ginzburg-Landau and Cahn-Hilliard equations based on a microforce balance. *Physica D : Nonlinear Phenomena*, 92(3-4) :178–192.

- [Gurtin, 2002] Gurtin, M. (2002). A gradient theory of single-crystal viscoplasticity that accounts for geometrically necessary dislocations. *Journal of the Mechanics and Physics of Solids*, 50 :5–32.
- [Gurtin et al., 2010] Gurtin, M., Fried, E., and Anand, L. (2010). *The Mechanics and Thermodynamics of Continua*. The Mechanics and Thermodynamics of Continua. Cambridge University Press.
- [Hall, 1951] Hall, E. O. (1951). The deformation and ageing of mild steel : III discussion of results. *Proceedings of the Physical Society. Section B*, 64(9) :747–753.
- [Hanriot, 1993] Hanriot, F. (1993). *Comportement du superalliage monocristallin AM1 sous sollicitations cycliques*. Thèse de doctorat, Ecole des Mines de Paris ENSMP.
- [Hektor et al., 2016] Hektor, J., Ristinmaa, M., Hallberg, H., Hall, S. A., and Iyengar, S. (2016). Coupled diffusion-deformation multiphase field model for elastoplastic materials applied to the growth of Cu_6Sn_5 . *Acta Materialia*, 108 :98–109.
- [Hermann et al., 2018] Hermann, C., Schoof, E., and Schneider, D. (2018). Multiphase-field model of small strain elasto-plasticity according to the mechanical jump conditions. *Computational Mechanics*, pages 1–14.
- [Hofacker and Miehe, 2013] Hofacker, M. and Miehe, C. (2013). A phase field model of dynamic fracture : Robust field updates for the analysis of complex crack patterns. *International Journal for Numerical Methods in Engineering*, 93 :276–301.
- [Hu and Chen, 2001] Hu, S. Y. and Chen, L. Q. (2001). A phase field model for evolving microstructures with strong elastic inhomogeneity. *Acta Metallurgica*, 49 :1879–1890.
- [Huntz et al., 2002] Huntz, A., Calvarin Amiri, G., Evans, H., and Cailletaud, G. (2002). Comparison of oxidation-growth stresses in NiO film measured by deflection and calculated using creep analysis or finite-element modeling. *Oxidation of Metals*, 57(5-6) :499–521.
- [Huntz et al., 1993] Huntz, A., Liu, C., Kornmeier, M., and Lebrun, J. (1993). The determination of stresses during oxidation of Ni : in situ measurements by XRD at high temperature. *Corrosion Science*, 35(5–8) :989–997.
- [Huntz et al., 1998] Huntz, A., Piant, A., Lebrun, J., and Daghigh, S. (1998). Evidence of stress relaxation in thermally grown oxide layers – experiments and modelling. *Materials Science and Engineering : A*, 248(1–2) :44–55.
- [Imanian and Amiri, 2022] Imanian, A. and Amiri, M. (2022). Phase field modeling of corrosion damage. *Corrosion Reviews*, 40(4) :343–354.
- [Irving, 1964] Irving, B. A. (1964). Effect of grain boundaries on the diffusional growth of oxides on metals. *Nature*, 204(4963) :1083–1083.
- [Johnson and Alexander, 1986] Johnson, W. C. and Alexander, J. I. D. (1986). Interfacial conditions for thermomechanical equilibrium in two-phase crystals. *Journal of Applied Physics*, 9 :2735–2746.
- [Khachaturyan, 1983] Khachaturyan, A. (1983). *Theory of Structural Transformations in Solids*. John Wiley & Sons, New York.
- [Kim et al., 1998] Kim, M., Baek, S., and Paik, U. (1998). Electrical conductivity and oxygen diffusion in nonstoichiometric TiO_{2-x} . *Journal of the Korean Physical Society*, 32 :1127–1130.
- [Kim et al., 1999] Kim, S., Kim, W., and Suzuki, T. (1999). Phase-field model for binary alloys. *Phys. Rev. E*, 60 :7186–7197.

- [Kjellqvist and Selleby, 2009] Kjellqvist, L. and Selleby, M. (2009). Adding C to the thermodynamic description of the Cr-Fe-Ni-O system. *Calphad*, 33(2) :393–397. Tools for Computational Thermodynamics.
- [Kjellqvist et al., 2008] Kjellqvist, L., Selleby, M., and Sundman, B. (2008). Thermodynamic modelling of the Cr-Fe-Ni-O system. *Calphad*, 32(3) :577–592.
- [Koslowski et al., 2002] Koslowski, M., Cuitino, A., and Ortiz, M. (2002). A phase-field theory of dislocation dynamics, strain hardening and hysteresis in ductile single crystals. *Journal of the Mechanics and Physics of Solids*, 50 :2597–2635.
- [Kouznetsova and Geers, 2007] Kouznetsova, V. and Geers, M. (2007). Modeling the interaction between plasticity and the austenite-martensite transformation. *International Journal for Multiscale Computational Engineering*, 5 :129–140.
- [Kovacevic et al., 2023] Kovacevic, S., Ali, W., Martínez-Pañeda, E., and LLorca, J. (2023). Phase-field modeling of pitting and mechanically-assisted corrosion of mg alloys for biomedical applications. *Acta Biomaterialia*, 164 :641–658.
- [Krishnamurthy and Srolovitz, 2003] Krishnamurthy, R. and Srolovitz, D. (2003). Stress distributions in growing oxide films. *Acta Materialia*, 51(8) :2171–2190.
- [Krishnamurthy and Srolovitz, 2004] Krishnamurthy, R. and Srolovitz, D. (2004). Stress distributions in growing polycrystalline oxide films. *Acta Materialia*, 52(13) :3761–3780.
- [Krupp et al., 2014] Krupp, U., Giertler, A., Söker, M., Fu, H., Dönges, B., Christ, H.-J., Istomin, K., Hüsecken, A., Pietsch, U., Fritzen, C.-P., and Ludwig, W. (2014). Significance and mechanism of the crack initiation process during very high cycle fatigue of duplex stainless steel. *Procedia Engineering*, 74 :143 – 146. XVII International Colloquium on Mechanical Fatigue of Metals (ICMFM17).
- [Kruska et al., 2012] Kruska, K., Lozano-Perez, S., Saxey, D., Terachi, T., Yamada, T., and Smith, G. (2012). Nanoscale characterisation of grain boundary oxidation in cold-worked stainless steels. *Corrosion Science*, 63(0) :225–233.
- [Kundin et al., 2011] Kundin, J., Raabe, D., and Emmerich, H. (2011). A phase-field model for incoherent martensitic transformations including plastic accommodation processes in the austenite. *Journal of the Mechanics and Physics of Solids*, 59 :2082–2102.
- [Laghoutaris, 2009] Laghoutaris, P. (2009). *Corrosion sous contrainte de l'alliage 600 en milieu primaire des réacteurs à eau sous pression : apport à la compréhension des mécanismes*. PhD thesis, Mines ParisTech.
- [Laheij et al., 1980] Laheij, M., Loo, F., and Metselaar, R. (1980). Phase relations in the Fe-Cr-O system at 1200°C investigated by means of a diffusion couple technique. *Oxidation of Metals*, 14(3) :207–215.
- [Larché and Cahn, 1973] Larché, F. and Cahn, J. (1973). A linear theory of thermochemical equilibrium of solids under stress. *Acta Metallurgica*, 21 :1051–1063.
- [Larché and Cahn, 1985] Larché, F. and Cahn, J. (1985). Overview no. 41 the interactions of composition and stress in crystalline solids. *Acta Metallurgica*, 33(3) :331–357.
- [Le Bouar et al., 2003] Le Bouar, Y., Loiseau, A., and Finel, A. (2003). Origin of the complex wetting behavior in Co-Pt alloys. *Physical Review B*, 68 :224203.
- [Le Bouar et al., 1998] Le Bouar, Y., Loiseau, A., and Khachatryan, A. (1998). Origin of chessboard-like structures in decomposing alloys. Theoretical model and computer simulation. *Acta Metallurgica*, 46(8) :2777–2788.

- [Le Saux et al., 2015] Le Saux, M., Besson, J., and Carassou, S. (2015). A model to describe the mechanical behavior and the ductile failure of hydrided zircaloy-4 fuel claddings between 25 °c and 480 °c. *Journal of Nuclear Materials*, 466 :43–55.
- [Lee et al., 1988] Lee, S.-M., Kim, K.-T., and Pyun, S.-I. (1988). Kinetics of intergranular corrosion and separation between initiation and propagation of stress corrosion crack in mild steel. *Scripta Metallurgica*, 22(1) :31–34.
- [Lemaître and Chaboche, 1985] Lemaître, J. and Chaboche, J.-L. (1985). *Mécanique des Matériaux Solides*. Dunod.
- [Lemaitre and Chaboche, 1994] Lemaitre, J. and Chaboche, J.-L. (1994). *Mechanics of Solid Materials*. University Press, Cambridge, UK.
- [Levkovitch et al., 2006] Levkovitch, V., Sievert, R., and Svendsen, B. (2006). Simulation of deformation and lifetime behavior of a fcc single crystal superalloy at high temperature under low-cycle fatigue loading. *International Journal of Fatigue*, 28 :1791–1802.
- [Li et al., 1998] Li, D., Zhang, X., Gautier, E., and Zhang, J. (1998). Morphology transitions of deformation-induced thin-plate martensite in fe-ni-c alloys. *Acta Materialia*, 46(13) :4827 – 4834.
- [Li and Wang, 2020] Li, Z. and Wang, J. (2020). A diffusion–reaction continuum damage model for the oxidation behaviors of high-cr steels in supercritical water. *Oxidation of Metals*, 94.
- [Maclachlan et al., 2001] Maclachlan, D., Wright, L., Gunturi, S., and Knowles, D. (2001). Constitutive modelling of anisotropic creep deformation in single crystal blade alloys srr99 and cmsx-4. *International Journal of Plasticity*, 17 :441–467.
- [Marrier et al., 2013] Marrier, E., Ganster, P., Moulin, N., and Wolski, K. (2013). Substrate depletion analysis and modeling of the high temperature oxidation of binary alloys. *Oxidation of Metals*, 79(1-2) :81–91.
- [Mindlin and Eshel, 1968] Mindlin, R. and Eshel, N. (1968). On first strain-gradient theories in linear elasticity. *International Journal of Solids and Structures*, 4(1) :109–124.
- [Mishin, 2001] Mishin, Y. (2001). 50 years of grain boundary diffusion : What do we know about it today? *Defect and Diffusion Forum*, 194-199 :1113–1126.
- [Mishin and Herzig, 1999] Mishin, Y. and Herzig, C. (1999). Grain boundary diffusion : recent progress and future research. *Materials Science and Engineering : A*, 260(1–2) :55–71.
- [Mishin and Yurovitskii, 1991] Mishin, Y. and Yurovitskii, I. (1991). A generalized model of grain boundary diffusion. *Philosophical Magazine A*, 64(6) :1239–1249.
- [Morra, 1995] Morra, M. (1995). *Stress assisted intergranular oxidation cracking of incoloy alloy 908*.
- [Mougin, 2001] Mougin, J. (2001). *Tenue mécanique de couches d'oxyde thermique générées sur le chrome et sur quelques aciers inoxydables ferritiques étude des contraintes et de l'adhérence*. PhD thesis, Institut National Polytechnique de Grenoble.
- [Mougin et al., 2003] Mougin, J., Dupeux, M., Antoni, L., and Galerie, A. (2003). Adhesion of thermal oxide scales grown on ferritic stainless steels measured using the inverted blister test. *Materials Science and Engineering : A*, 359(1–2) :44–51.
- [Mougin et al., 2001] Mougin, J., Rosman, N., Lucazeau, G., and Galerie, A. (2001). In situ Raman monitoring of chromium oxide scale growth for stress determination. *Journal of Raman Spectroscopy*, 32 :739–744.

- [Moulinec and Suquet, 2003] Moulinec, H. and Suquet, P. (2003). Intraphase strain heterogeneity in nonlinear composites : a computational approach. *European Journal of Mechanics A/Solids*, 22 :751–770.
- [Nemat-Nasser and Hori, 1999] Nemat-Nasser, S. and Hori, M. (1999). *Micromechanics : Overall Properties of heterogeneous Solids*. Elsevier Science Publishers, 2nd edition edition.
- [Onuki and Nishimori, 1991] Onuki, A. and Nishimori, H. (1991). Anomalous slow domain growth due to a modulus inhomogeneity in phase-separating alloys. *Phys. Rev. B*, 43 :13649–13652.
- [Peerlings et al., 1996] Peerlings, R., Borst, de, R., Brekelmans, W., and Vree, de, J. (1996). Gradient enhanced damage for quasi-brittle materials. *International Journal for Numerical Methods in Engineering*, 39(19") :3391–3403.
- [Pijaudier-Cabot and Bazant, 1987] Pijaudier-Cabot, G. and Bazant, Z. (1987). Nonlocal damage theory. *Journal of Engineering Mechanics*, 113(10) :1512–1533.
- [Pilling and Bedworth, 1923] Pilling, N. and Bedworth, R. (1923). The oxidation of metals at high temperatures. *Journal of the Institute of Metals*, 29 :529–582.
- [Ploc and Christodoulou, 1990] Ploc, R. and Christodoulou, N. (1990). Stress patterns around hemispherical oxide intrusions. *Journal of Nuclear Materials*, 175(1) :107–116.
- [Prokoshkina et al., 2013] Prokoshkina, D., Esin, V., Wilde, G., and Divinski, S. (2013). Grain boundary width, energy and self-diffusion in nickel : Effect of material purity. *Acta Materialia*, 61 :5188–5197.
- [Pujilaksono et al., 2011] Pujilaksono, B., Jonsson, T., Heidari, H., Halvarsson, M., Svensson, J.-E., and Johansson, L.-G. (2011). Oxidation of binary FeCr alloys (Fe-2.25Cr, Fe-10Cr, Fe-18Cr and Fe-25Cr) in O₂ and in O₂+H₂O environment at 600°C. *Oxidation of Metals*, 75(3-4) :183–207.
- [Punkkinen et al., 2013] Punkkinen, M., Kokko, K., Levämäki, H., Ropo, M., Lu, S., Delczeg, L., Zhang, H., Delczeg-Czirjak, E., Johansson, B., and Vitos, L. (2013). Adhesion of the iron-chromium oxide interface from first-principles theory. *Journal of Physics : Condensed Matter*, 25(49) :495501.
- [Qu and Cherkaoui, 2006] Qu, J. and Cherkaoui, M. (2006). *Fundamentals of micromechanics of solids*. John Wiley & Sons Inc, Hoboken.
- [Raabe et al., 2014] Raabe, D., Herbig, M., Sandlöbes, S., Li, Y., Tytko, D., Kuzmina, M., Ponge, D., and Choi, P.-P. (2014). Grain boundary segregation engineering in metallic alloys : A pathway to the design of interfaces. *Current Opinion in Solid State and Materials Science*, 18(4) :253–261. Slip Localization and Transfer in Deformation and Fatigue of Polycrystals.
- [Rodney et al., 2003] Rodney, D., Le Bouar, Y., and Finel, A. (2003). Phase field methods and dislocations. *Acta Materialia*, 51 :17–30.
- [Royer et al., 1998] Royer, A., Bastie, P., and Veron, M. (1998). In situ determination of γ' phase volume fraction and of relations between lattice parameters and precipitate morphology in ni-based single crystal superalloy. *Acta Materialia*, 46(15) :5357–5368.
- [Sabioni et al., 2012] Sabioni, A., Ramos, R., Ji, V., Jomard, F., Macedo, W., Gastelois, P., and Trindade, V. (2012). About the role of chromium and oxygen ion diffusion on the growth mechanism of oxidation films of the AISI 304 austenitic stainless steel. *Oxidation of Metals*, 78(3-4) :211–220.

- [Sanchez-Palencia and Zaoui, 1987] Sanchez-Palencia, E. and Zaoui, A. (1987). *Homogenization techniques for composite media*. Lecture Notes in Physics No. 272, Springer, Berlin.
- [Schneider et al., 2014] Schneider, D., Schmid, S., Selzer, M., Böhlke, T., and Nestler, B. (2014). Small strain elasto-plastic multiphase-field model. *Computational Mechanics*.
- [Schreiber et al., 2013] Schreiber, D., Olszta, M., Saxey, D., Kruska, K., Moore, K., Lozano-Perez, S., and Bruemmer, S. (2013). Examinations of oxidation and sulfidation of grain boundaries in alloy 600 exposed to simulated pressurized water reactor primary water. *Microscopy and Microanalysis*, 19 :676–687.
- [Semiatin et al., 2003] Semiatin, S., Knisley, S., Fagin, P., Zhang, F., and Barker, D. (2003). Microstructure evolution during alpha-beta heat treatment of Ti-6Al-4V. *Metallurgical and Materials Transactions A*, 34 :2377–2386.
- [Sherman and Voorhees, 2017] Sherman, Q. C. and Voorhees, P. W. (2017). Phase-field model of oxidation : Equilibrium. *Phys. Rev. E*, 95 :032801.
- [Shishvan et al., 2011] Shishvan, S., Mohammadi, S., Rahimian, M., and Van der Giessen, E. (2011). Plane-strain discrete dislocation plasticity incorporating anisotropic elasticity. *International Journal of Solids and Structures*, 48(2) :374–387.
- [Shoji et al., 2010] Shoji, T., Lu, Z., and Murakami, H. (2010). Formulating stress corrosion cracking growth rates by combination of crack tip mechanics and crack tip oxidation kinetics. *Corrosion Science*, 52(3) :769–779.
- [Sieborger et al., 2001] Sieborger, D., Knake, H., and Glatzel, U. (2001). Temperature dependence of the elastic moduli of the nickel-base superalloy cmsx-4 and its isolated phases. *Materials Science and Engineering : A*, 298 :26–33.
- [Spatschek and Eidel, 2013] Spatschek, R. and Eidel, B. (2013). Driving forces for interface kinetics and phase field models. *International Journal of Solids and Structures*, 50(14–15) :2424–2436.
- [Steinbach, 2009] Steinbach, I. (2009). Phase field models in materials science. *Modelling and Simulation in Materials Science and Engineering*, 17 :1–31.
- [Steinbach and Apel, 2006] Steinbach, I. and Apel, M. (2006). Multi phase field model for solid state transformation with elastic strain. *Physica D : Nonlinear Phenomena*, 217(2) :153–160.
- [Steinbach and Apel, 2007] Steinbach, I. and Apel, M. (2007). The influence of lattice strain on pearlite formation in Fe–C. *Acta Materialia*, 55 :4817–4822.
- [Steinbach and Shchyglo, 2011] Steinbach, I. and Shchyglo, O. (2011). Phase-field modelling of microstructure evolution in solids : Perspectives and challenges. *Current Opinion in Solid State and Materials Science*, 15 :87–92.
- [Steinmann, 1996] Steinmann, P. (1996). Views on multiplicative elastoplasticity and the continuum theory of dislocations. *International Journal of Engineering Science*, 34(15) :1717–1735.
- [Su et al., 2006] Su, T., Aeby-Gautier, E., and Denis, S. (2006). Morphology changes in bainite formed under stress. *Scripta Materialia*, 54 :2185–2189.
- [Svendsen, 2002] Svendsen, B. (2002). Continuum thermodynamic models for crystal plasticity including the effects of geometrically-necessary dislocations. *Journal of the Mechanics and Physics of Solids*, 50 :1297–1329.

- [Thompson et al., 1994] Thompson, M., Su, C., and Voorhees, P. (1994). The equilibrium shape of a misfitting precipitate. *Acta Metallurgica and Materialia*, 42(6) :2107–2122.
- [Thuinet and Legris, 2010] Thuinet, L. and Legris, A. (2010). Elastically driven morphology of coherent trigonal precipitates inside a close-packed hexagonal matrix. *Acta Materialia*, 58(6) :2250 – 2261.
- [Ubachs et al., 2004] Ubachs, R., Schreurs, P., and Geers, M. (2004). A nonlocal diffuse interface model for microstructure evolution of tin–lead solder. *Journal of the Mechanics and Physics of Solids*, 52 :1763–1792.
- [Ubachs et al., 2005] Ubachs, R., Schreurs, P., and Geers, M. (2005). Phase field dependent viscoplastic behaviour of solder alloys. *International Journal of Solids and Structures*, 42 :2533–2558.
- [Uehara et al., 2007] Uehara, T., Tsujino, T., and Ohno, N. (2007). Elasto-plastic simulation of stress evolution during grain growth using a phase field model. *Journal of Crystal Growth*, 300 :530–537.
- [Vattré and Denoual, 2016] Vattré, A. and Denoual, C. (2016). Polymorphism of iron at high pressure : A 3D phase-field model for displacive transitions with finite elastoplastic deformations. *Journal of the Mechanics and Physics of Solids*, 92 :1–27.
- [Viardin, 2010] Viardin, A. (2010). *Modélisation par champ de phases de la croissance de la ferrite allotriomorphe dans les aciers Fe-C-Mn*. Thèse de doctorat, INPL.
- [Voorhees and Johnson, 2004] Voorhees, P. and Johnson, W. (2004). The thermodynamics of elastically stressed crystals. In Ehrenreich, H. and Spaepen, F., editors, *Solid State Physics*, volume 59 of *Solid State Physics*, pages 1–201. Academic Press.
- [Voorhees et al., 1988] Voorhees, P., McFadden, G., Boisvert, R., and Meiron, D. (1988). Numerical simulation of morphological development during Ostwald ripening. *Acta Metallurgica*, 36(1) :207–222.
- [Wang et al., 2023] Wang, R., Ji, Y., Cheng, T.-L., Xue, F., Chen, L.-Q., and Wen, Y.-H. (2023). Phase-field modeling of alloy oxidation at high temperatures. *Acta Materialia*, 248 :118776.
- [Wang et al., 1998] Wang, Y., Banerjee, D., Su, C., and Khachaturyan, A. (1998). Field kinetic model and computer simulation of precipitation of L1₂ ordered intermetallics from F.C.C. solid solution. *Acta Metallurgica*, 46(9) :2983–3001.
- [Wang et al., 2001] Wang, Y., Jin, Y., Cuitinõa, and Khachaturyan, A. (2001). Nano-scale phase field microelasticity theory of dislocations : Model and 3D simulations. *Acta Metallurgica*, 49 :1847–1857.
- [Wang and Khachaturyan, 1995] Wang, Y. and Khachaturyan, A. (1995). Shape instability during precipitate growth in coherent solids. *Acta Metall. mater.*, 43(5) :1837–1857.
- [Wang et al., 2004] Wang, Y. U., Jin, Y. M., and Khachaturyan, A. G. (2004). The effects of free surfaces on martensite microstructures : 3D phase field microelasticity simulation study. *Acta Materialia*, 52 :1039–1050.
- [Wehbi, 2014] Wehbi, M. (2014). *Modélisation de l'amorçage de la Corrosion Sous Contrainte dans les alliages base nickel 182 et 82 en milieu primaire des Réacteurs à Eau sous Pression*. PhD thesis, Mines ParisTech.
- [Weinberg et al., 2009] Weinberg, K., Böhme, T., and Müller, W. (2009). Kirkendall voids in the intermetallic layers of solder joints in MEMS. *Computational Materials Science*, 45 :827–831.

- [Weiss and Pineau, 1993] Weiss, J. and Pineau, A. (1993). Fatigue and creep-fatigue damage of austenitic stainless steels under multiaxial loading. *Metallurgical and Materials Transactions A*, 24 :2247–2261.
- [Wen et al., 1996] Wen, Y. H., Denis, S., and Aeby-Gautier, E. (1996). Computer simulation of martensitic transformation under stress. *J. Phys. IV*, 6 :C1–475.
- [Xia et al., 2019] Xia, Z., Zhang, J., Tong, Q., and Ding, S. (2019). Multi-physics modeling of delayed hydride cracking in zirconium alloys. *Journal of the Mechanics and Physics of Solids*, 132 :103677.
- [Yamanaka et al., 2008] Yamanaka, A., Takaki, T., and Tomita, Y. (2008). Elastoplastic phase-field simulation of self- and plastic accommodations in cubic→tetragonal martensitic transformation. *Materials Science & Engineering A*, 491 :378–384.
- [Yang et al., 2007] Yang, J., Zheng, Q., Sun, X., Guan, H., and Hu, Z. (2007). Morphological evolution of γ' phase in k465 superalloy during prolonged aging. *Materials Science and Engineering : A*, 457(1) :148 – 155.
- [Z-set package, 2013] Z-set package (2013). Non-linear material & structure analysis suite, www.zset-software.com.
- [Zaoui, 2002] Zaoui, A. (2002). Continuum micromechanics : Survey. *ASCE Journal of Engineering Mechanics*, 128 :808–816.
- [Zhao et al., 1986] Zhao, J., Huntz, A., Couffin, P., and Baron, J. (1986). An investigation of oxidation internal stresses in nicr alloy by x-ray diffraction. *Acta Metallurgica*, 34(7) :1351–1357.
- [Zhou et al., 2010a] Zhou, C., Ma, H., and Wang, L. (2010a). Comparative study of oxidation kinetics for pure nickel oxidized under tensile and compressive stress. *Corrosion Science*, 52(1) :210–215.
- [Zhou, 2010] Zhou, H. (2010). *Stress-diffusion interaction during oxide-scale growth on metallic alloys*. PhD thesis, Georgia Institute of Technology.
- [Zhou et al., 2010b] Zhou, H., Qu, J., and Cherkaoui, M. (2010b). Finite element analysis of oxidation induced metal depletion at oxide-metal interface. *Computational Materials Science*, 48(4) :842–847.
- [Zhou et al., 2010c] Zhou, H., Qu, J., and Cherkaoui, M. (2010c). Stress-oxidation interaction in selective oxidation of Cr-Fe alloys. *Mechanics of Materials*, 42(1) :63–71.
- [Zhou et al., 2008] Zhou, N., Shen, C., Mills, M., and Wang, Y. (2008). Contributions from elastic inhomogeneity and from plasticity to γ' rafting in single-crystal Ni-Al. *Acta Materialia*, 56(20) :6156–6173.

Appendices

Analytical solution of the model in 1D

In the case of a 1D configuration (Fig. 4.1 §4.3.1.1), displacement reads :

$$\begin{cases} u_1(x) &= \bar{\varepsilon}_{11} x + u(x) \\ u_2(y) &= \varepsilon_{22} y \\ u_3(z) &= \varepsilon_{22} z \end{cases} \quad (\text{A.1})$$

where $u(x)$ is the periodic fluctuation displacement and $\bar{\varepsilon}_{11}$ the average tensile strain field. Strain and stress tensors are :

$$\boldsymbol{\varepsilon} = \begin{pmatrix} \bar{\varepsilon}_{11} + u_{,1}(x) & 0 & 0 \\ 0 & \varepsilon_{22} & 0 \\ 0 & 0 & \varepsilon_{22} \end{pmatrix} \quad \boldsymbol{\sigma} = \begin{pmatrix} \sigma_{11} & 0 & 0 \\ 0 & \sigma_{22}(x) & 0 \\ 0 & 0 & \sigma_{22}(x) \end{pmatrix} \quad (\text{A.2})$$

where $f_{,1}$ denotes the derivative of f with respect to the x coordinate. For this 1D geometry, coherency of the γ/γ' interface implies that ε_{22} is homogeneous. In addition, σ_{11} is also homogeneous to fulfill mechanical equilibrium. Under these conditions, the J_2 yield surface can be defined in stress space as :

$$J_2(\boldsymbol{\sigma}) = |\sigma_{11} - \sigma_{22}(x)| \quad (\text{A.3})$$

Hooke's law holding in γ and γ' , we have :

$$\begin{cases} \sigma_{11}^{\gamma'} &= C_{11} [\bar{\varepsilon}_{11} + u_{,1}^{\gamma'}(x)] + 2C_{12} \varepsilon_{22} \\ \sigma_{11}^{\gamma} &= C_{11} [\bar{\varepsilon}_{11} + u_{,1}^{\gamma}(x) - p(x)] + 2C_{12} [\varepsilon_{22} + p(x)/2] \end{cases} \quad (\text{A.4})$$

$$\begin{cases} \sigma_{22}^{\gamma'}(x) &= C_{12} [\bar{\varepsilon}_{11} + u_{,1}^{\gamma'}(x)] + (C_{11} + C_{12}) \varepsilon_{22} \\ \sigma_{22}^{\gamma}(x) &= C_{12} [\bar{\varepsilon}_{11} + u_{,1}^{\gamma}(x) - p(x)] + (C_{11} + C_{12}) [\varepsilon_{22} + p(x)/2] \end{cases} \quad (\text{A.5})$$

Since σ_{11} is homogeneous, we get :

$$\sigma_{11}^{\gamma} = \sigma_{11} = C_{11} [\bar{\varepsilon}_{11} + u_{,1}^{\gamma}(x) - p(x)] + 2C_{12} [\varepsilon_{22} + p(x)/2] = \text{Cst} \quad (\text{A.6})$$

We consider a situation where the γ phase undergoes time independent plastic deformation. Using von Mises criterion, we get :

$$R_0 + Hp(x) - A\Delta p(x) = |\sigma_{11} - \sigma_{22}^{\gamma}(x)| \quad (\text{A.7})$$

Using Eq. (A.5) into Eq. (A.7) gives :

$$\left[H + \frac{1}{2} \frac{E}{1-\nu} \right] p(x) - A \Delta p(x) = T - R_0 \quad (\text{A.8})$$

where $E/(1-\nu) = (C_{11} - C_{12})(C_{11} + 2C_{12})/C_{11}$ and $T = (C_{11} - C_{12})/C_{11} [\sigma_{11} - (C_{11} + 2C_{12}) \varepsilon_{22}]$.

Eq. (A.8) is a second order differential equation. Integrating this equation leads to :

$$p(x) = \mathcal{M} \left(1 - \frac{\cosh(\omega x)}{\cosh(\omega s/2)} \right) \quad (\text{A.9})$$

where $\omega^2 = \frac{H + \frac{1}{2} \frac{E}{1-\nu}}{A}$ and $\mathcal{M} = \frac{T - R_0}{H + \frac{1}{2} \frac{E}{1-\nu}}$.

The two unknown constants σ_{11} and ε_{22} are determined using the following boundaries conditions $\langle \sigma_{11} \rangle = \sigma_{11}$ and $\langle \sigma_{22} \rangle = 0$. We obtain :

$$\begin{cases} \sigma_{11} &= (C_{11} + 2C_{12})(\bar{\varepsilon}_{11} + 2\varepsilon_{22}) \\ \varepsilon_{22} &= \frac{B}{B \frac{E}{1-\nu} - (C_{11} + C_{12})} R_0 - \frac{B \frac{E}{1-\nu} - C_{12}}{B \frac{E}{1-\nu} - (C_{11} + C_{12})} \bar{\varepsilon}_{11} \end{cases} \quad (\text{A.10})$$

where $B = \frac{(C_{12} - C_{11})}{2(\ell + s)(H + \frac{1}{2} \frac{E}{1-\nu})} \left[s - \frac{2}{\omega} \tanh(\omega s/2) \right]$.

The continuity of plastic strain $p(x)$ and the continuity of displacement at the interface $x_1 = s/2$ can be used to determine the heterogeneous displacement field $u(x)$.

RÉSUMÉ

MOTS CLÉS

ABSTRACT

KEYWORDS

